# A SYSTEMS APPROACH TO DEVELOPMENT AND EVALUATION OF GEOTHERMAL ENERGY UTILIZATION SYSTEMS

A Dissertation

Presented to the Faculty of the Graduate School

of Cornell University

in Partial Fulfillment of the Requirements for the Degree of

Doctor of Philosophy

by

Maciej Zbigniew Lukawski

January 2017

# A SYSTEMS APPROACH TO DEVELOPMENT AND EVALUATION OF GEOTHERMAL ENERGY UTILIZATION SYSTEMS

Maciej Zbigniew Lukawski, Ph. D.

Cornell University 2017

A successful design and operation of geothermal energy systems require a multidisciplinary approach combining engineering, geoscience and economics. The complex interactions between individual geothermal system components can be captured using techno-economic models. An example of such model is the GEOPHIRES software developed at the Cornell Energy Institute, which allows users to determine the optimal configurations of geothermal systems and quantify their technical and economic performance. The main objective of this work was to improve the competitiveness of geothermal energy by developing improved energy conversion and distribution technologies and by providing well cost models used for the GEOPHIRES software.

The first part of this work focused on the development of organic Rankine cycle (ORC) power plants used in geothermal applications. This goal was addressed in multiple ways. First, the efficiency of ORCs was correlated with the molecular structure of working fluids. The developed methodology can be used to evaluate performance of ORCs using less common working fluids, for which no accurate equations of state (EOS) exist. This dissertation also supported the development of more accurate EOS models for next-generation working fluids by providing measurements of isobaric heat capacity ($C_p$) of pure fluids and mixtures. To expand the thermodynamic data library for these fluids, a flow calorimeter for measuring $C_p$ in

liquid, vapor, and supercritical phases was developed. Lastly, this work evaluated the ways to effectively incorporate geothermal utilization systems into the existing energy infrastructure. A feasibility study of a hybrid geothermal-biomass-natural gas energy system for Cornell University campus was done to analyze the opportunities for improving the integration of low-temperature geothermal systems.

In addition to the work on geothermal utilization systems, this dissertation quantified the costs and uncertainties associated with drilling and completion of geothermal wells. The well cost correlations were developed using a predictive well cost model and the records of recently drilled geothermal wells. The presented analysis can reduce the financial risk involved in geothermal systems by quantifying the well cost uncertainty and its impact on the project economics.

## BIOGRAPHICAL SKETCH

Maciej Lukawski was born and raised in Kielce, Poland. He graduated cum laude with a M.S. degree in Energy Engineering from the University of Science and Technology in Krakow, Poland. Maciej has done his Master's thesis research as a visiting student at Lund University in Sweden, where he worked on numerical modeling and optimization of space heating systems. During the course of his college education, Maciej developed interest in geothermal energy. To pursue these interests, he enrolled in a geothermal energy program at the RES School for Renewable Energy Science in Iceland. He graduated cum laude with an M.S. degree in Renewable Energy Science in 2009. His M.S. thesis looked at design and optimization of modular Organic Rankine Cycle (ORC) power plants and was written under the supervision of Prof. Pall Valdimarsson at the University of Iceland. Following his education in Poland and Iceland, Maciej received a Fulbright Scholarship to pursue his Ph.D. in Chemical Engineering at Cornell University in Ithaca, NY. At Cornell, Maciej has worked under the supervision of Prof. Jefferson Tester on a range of projects described in this dissertation. He has also enjoyed working on a number of extracurricular projects throughout his involvement in the Earth-Energy IGERT program, Cornell Energy Club at the Johnson Graduate School of Management, and Cornell University President's Sustainable Campus Committee.

**ACKNOWLEDGMENTS**

I would like express my gratitude to all the people who helped me in my journey through the graduate school and made it such a wonderful learning experience.

First and foremost, I would like to thank my adviser, Dr. Jeff Tester for his continued support, positive attitude, and creating a great work environment. I feel that I learned as much from him about how to approach problems and work with people as I have about energy and thermodynamics.

I am sincerely grateful to my thesis committee members, Dr. Abraham Stroock and Dr. Lawrence Cathles for their constructive feedback, support, and encouragement to follow interesting research ideas.

I am also thankful for the invaluable advice I received from Dr. Ron DiPippo, Dr. Brian Anderson, Dr. Chad Augustine, Louis Capuano Jr., Dr. Michal Moore, and Dr. Bill Livesay. Ron DiPippo deserves a special thanks for inspiring me to pursue a Ph.D. and starting my interest in geothermal power plants.

Thank you to Tara Walworth, Hilary Cullen, Teri Carey, and especially Polly Marion for going far beyond their responsibilities to keep the Energy Institute and the Earth-Energy IGERT program well organized.

My fellow Ph.D., M.S., and M.Eng. students at Cornell who directly contributed to this research deserve a special acknowledgement. Completing the work described in this thesis would not be possible without Mitchell Ishmael, Dr. Koenraad Beckers, Rachel Silverman, Lizeta Gkogka, Konstantios Vilaetis, and Dr. Adam Carr.

I appreciate the financial support for my research provided by the Cornell Energy Institute, Atkinson Center for a Sustainable Future, Department of Energy, Polish-American Fulbright Commission, Verizon Foundation and Verizon Wireless, ARPA-E, Geothermal Resources Council, and Cornell University Robert Frederick Smith School of Chemical and Biomolecular Engineering.

Thank you to the members of Tester group for making our lab in Snee Hall such a great place to be, for all the brainstorming sessions, and great lunchtime conversations. Special thanks go to Koenraad Beckers and Mitchell Ishmael for all the bike trips, driving with me across the U.S., and for helping me more times than I can remember.

Thank you to all Cornell friends especially Rambert, John, Nicole, Arna, Andrea, Adam, Tim, and George for all the joyful moments.

And most importantly thank you to Martina, Halina, Mirek, and Agnieszka for your love and support.

**TABLE OF CONTENTS**

**LIST OF FIGURES**

**LIST OF TABLES**

**LIST OF ABBREVIATIONS**

AFE - Authorizations for Expenditure

AWG - American Wire Gauge

Bbl - Standard oil barrel (42 U.S. Gallons)

BLS PPI - U.S. Bureau of Labor Statistics Producer Price Index for drilling oil, gas, dry, or service wells

CAP - Cornell Climate Action Plan

CEI - Cornell Energy Institute

CHP - Combined Heat and Power

DH - District Heating

DOE - Department of Energy

EGS - Enhanced Geothermal System

EIA - U.S. Energy Information Administration

EJ - Exajoule ($10^{18}$ J)

EOS - Equation of State

GDP - Gross Domestic Product

GEA - Geothermal Energy Agency

GEOPHIRES - GEOthermal Energy for the Production of Heat and Electricity Economically Simulated

GHG - Greenhouse Gases

GWP - Global Warming Potential

GUI - Graphical User Interface

HDR - Hot Dry Rock

HFO - Hydrofluoroolefin

HPLC - High Pressure Liquid Chromatography

HRSG - Heat Recovery Steam Generator

IEA - International Energy Agency

JAS - API Joint Association Survey on Drilling Costs

LCOE - Levelized Cost of Electricity

LCOH - Levelized Cost of Heat

M - Million

MCF - Thousand Cubic Feet

MD - Measured Depth i.e. length of wellbore measured along its path

MITDD - MIT Depth Dependent well cost index

MMBTU - Million British Thermal Units (approx. 1.06 GJ)

Ni-Cr - Nichrome

NPT - Non-Productive Time

NR - No Recuperator

OD - Outer Diameter

ODP - Ozone Depletion Potential

OECD - Organisation for Economic Co-operation and Development

ORC - Organic Rankine Cycle

O&M - Operation and Maintenance

PRT - Platinum Resistance Thermometer

PVT - Pressure-Volume-Temperature

R - Recuperator

REFPROP - NIST Reference Fluid Thermodynamic and Transport Properties Database

ROP - Rate of Penetration

Sc - Supercritical organic Rankine cycle

Sub - Subcritical organic Rankine cycle

## LIST OF SYMBOLS:

| | |
|---|---|
| $A$ - JAS Activity Adjusted index | [-] |
| $C$ - CEI Average index without correction for drilling activity | [-] |
| $C$ - Cost | [$] |
| $d$ - Measured well depth, MD | [m] |
| $\dot{E}$ - Exergy rate (maximum reversible work potential) | [kW] |

| | |
|---|---|
| $h$ - Mass enthalpy | [kJ/kg] |
| $I$ - CEI index corrected for drilling activity | [-] |
| $i$ - Discount rate | [%] |
| $J$ - CEI index without correction for drilling activity | [-] |
| $k$ – Permeability | [$m^2$] |
| $M$ - Molar mass or molecular weight | [g/mol] |
| $\dot{m}$ - Mass flow rate | [kg/s] |
| $\boldsymbol{R}$ - Specific gas constant | [kJ/kg-K] |
| RH - Relative humidity | [%] |
| $R^2$ - Coefficient of determination | [-] |
| $P$ - Cost | [$] |
| $P$ - Percentile | [-] |
| $P$ - Pressure | [bar] |
| $p$ - Probability | [-] |
| $s$ - Entropy | [kJ/kg-K] |
| $T$ - Temperature | [K or ºC] |
| $\dot{Q}$ - Heat flow rate | [kW] |
| $U$ - Overall heat transfer coefficient | [kW/$m^2$-K] |
| $\dot{W}$ – Power | [kW] |

$x$ - Mole fraction [-]

$x$ - Probabilistic well cost [$]

## LIST OF GREEK SYMBOLS

α - Shape parameter of gamma distribution function [-]

β - Rate parameter of gamma distribution function [-]

Δ – Difference [-]

δ - Overall uncertainty in the measured heat capacity [%]

$\eta$ - Efficiency [%]

Γ - Gamma function [-]

σ - Standard deviation [various]

Φ - Porosity [%]

## LIST OF SUBSCRIPTS

*c* - Critical point of working fluid

*cf* - Cooling fluid

*cond* - Condensing

*e* - Electric power

*hs* - Heat source

*in* – Inlet

*lit* - Literature value

*n* - Year

*net* - Accounting for the parasitic power consumption

*out* - Outlet

*p* - Pressure

*r* - Reduced, i.e., divided by the respective value at the critical point

*ref* - Reference year

*sv* - Saturated vapor

*th* - Thermal

*tri* - Triangular cycle

*u* - Utilization

*wf* - Working Fluid

*0* - Dead state

## LIST OF SUPERSCRIPTS

k - Depth interval as defined in JAS

*0* - Ideal gas state or the shift parameter in probabilistic distribution

* - Condition at which ORC plant achieves its maximum utilization efficiency

# 1 INTRODUCTION AND MOTIVATION

## 1.1 World energy demand: current situation and future trends

Access to energy is essential to the quality of our lives. Energy use determines both GDP and income growth, and the Energy Development Index (EDI) is strongly correlated with the Human Development Index (HDI) (Pachauri et al., 2012). Yet, 1.4 billion people in the World have no access to electricity and over 3 billion people rely on low-efficiency solid fuel stoves for cooking and space heating (Pachauri et al., 2012). Improving the living conditions in non-OECD countries will require increased energy use, and environmental and sustainability considerations will most likely limit our options. Despite a 10% decrease in energy intensity, the global primary energy demand increased by about one-third between 2000 and 2014 (ExxonMobil, 2016). It is expected, that this trend will continue in the next decades as showed in Figure 1-1.

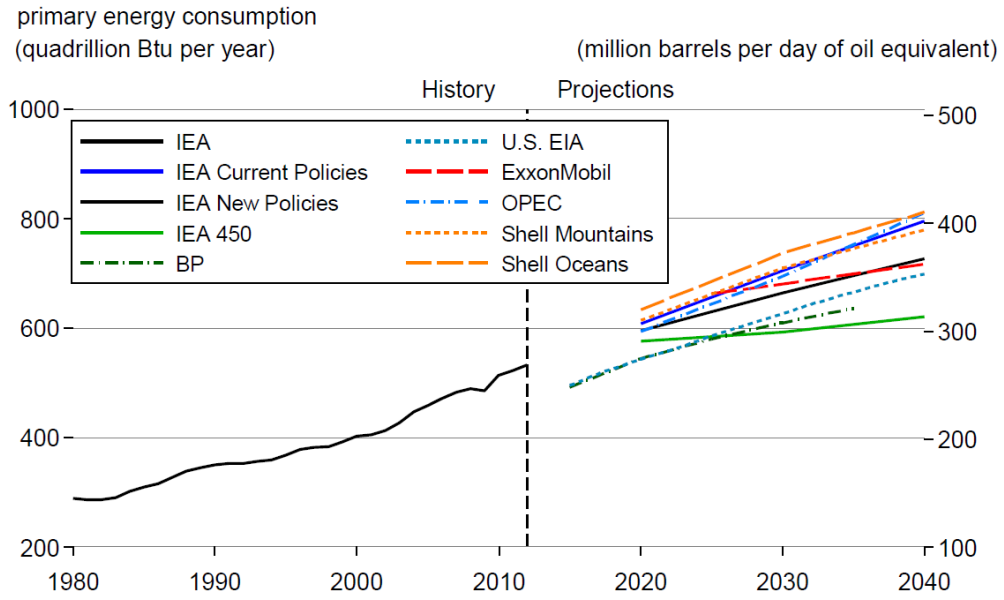


*Figure 1-1: Word's primary energy demand: history and forecasts (Newell et al., 2016)*

A diverse portfolio of energy solutions will be required to meet the growing energy demand. A large fraction of the new installed capacity is expected to come from low-carbon and renewable energy resources. The U.S. Energy Information Administration (EIA) estimates that the fastest growing energy sources in 2012-2040 will be renewables (2.6% increase per year), followed by nuclear (2.3% per year), and natural gas (1.9% per year) (EIA, 2016a). Among renewable energy sources, the highest growth rates are expected for solar (8.3% per year), followed by geothermal (6.5% per year) and wind energy (5.7% per year).

While wind and solar plants share many advantages, they are both intermittent sources of electricity with capacity factors of 0.2 to 0.4 (NREL, 2016). Due to their variable power output, at high market penetration rates they may require more robust transmission grid, distributed energy storage, or changes in consumer behavior. In contrast, geothermal energy is a baseload, dispatchable source of electricity with an average load factor of approximately 0.85 (NREL, 2016). In addition, geothermal energy can be used in co-generation (CHP) applications and

provide low-cost heat for direct-uses such as space heating, greenhouses, fish farming, or drying crops. Geothermal systems have very low operating costs (U.S. EIA, 2015) and at least an order of magnitude lower footprint compared to coal, solar, and wind plants (DiPippo, 2012). In addition, their $CO_2$ emissions are on average 3-9 times lower compared to fossil plants (The World Bank, 2016), and can be reduced to nearly zero by using closed-loop energy conversion systems.

## 1.2 Geothermal energy systems

Geothermal energy is a thermal energy stored in the subsurface rocks and fluids filling the pores and fractures in these rocks. It is continuously generated by the natural decay of radioactive isotopes ($^{40}K$, $^{238}Ur$, $^{235}Ur$, and $^{232}Th$) in the Earth's crust as well as transferred to the crust from the inner part of our planet. The driving force for this heat transfer is the geothermal gradient (ºC/km), one of three main parameters used to assess the quality of geothermal resources in a specific area.

The quality (or grade) of geothermal resources varies geographically as a result of variations in geology. While the average geothermal gradient is 25-30ºC/km, it can vary from as low as 5 ºC/km to, for localized thermal anomalies, over 200 ºC/km (Flovenz et al., 2000; Tissot and Welte, 1984). It addition to the geothermal gradient, resource quality depends on the permeability and porosity of reservoir rock. Permeability indicates rock's ability to let the fluid pass through, and porosity determines its natural fluid content. These three properties are used to describe the geothermal resource quality spectrum in Figure 1-2.

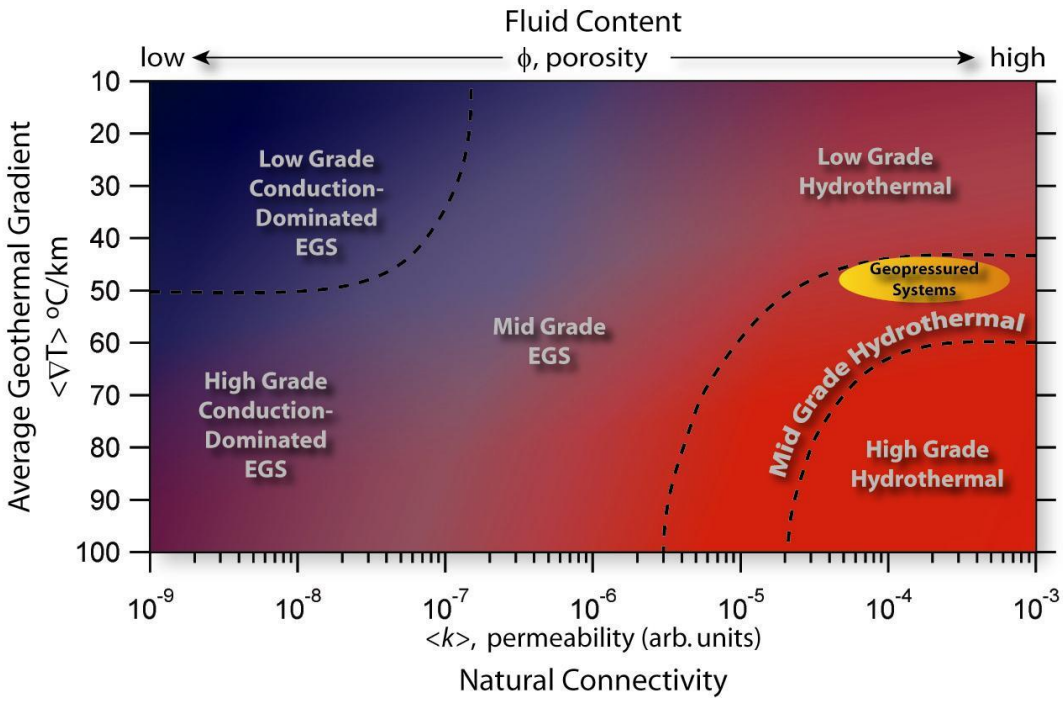


*Figure 1-2: Geothermal resource quality spectrum (Thorsteinsson et al., 2008)*

Based on the geologic setting, geothermal systems can be classified into four categories: hydrothermal, geopressured, magma, and conduction dominated (Tester et al., 2006). The conduction-dominated systems are also commonly known as Enhanced Geothermal Systems (EGS) or Hot Dry Rock.

The bulk of currently operating geothermal systems use high-grade hydrothermal resources characterized by high temperature gradients, high permeability, and the presence of in situ fluid. Hydrothermal systems are typically convection-driven and are located in volcanically active regions including parts of Iceland, Italy, Western U.S., Indonesia, and Philippines. They were the first type of geothermal resources to be commercially developed for a number of reasons: they are typically easier to identify due to surface manifestations (Hersir and Bjornsson, 1991),

require drilling shallower wells, often provide high well flow rates, and can use simple surface infrastructure such as dry steam of flash power plants. In locations where high-grade hydrothermal resources exist, geothermal systems are often the least expensive source of energy with Levelized Cost of Electricity (LCOE) of 0.03-0.06 $/kWh$_e$ (The World Bank, 2012; U.S. EIA, 2015). Hydrothermal resources are, however, spatially limited, and the largest high-grade hydrothermal fields have already been discovered. For geothermal energy to have a substantial contribution to the future global energy supply, it will require development of Enhanced (or Engineered) Geothermal Systems (EGS).

Enhanced Geothermal Systems lack sufficient permeability and/or in situ fluid which are present in conventional hydrothermal reservoirs. Instead, they are developed in dry and often impermeable rock by creating flow pathways using hydraulic stimulation methods. A conceptual view of a simple, two-well Enhanced Geothermal System is presented in Figure 1-3. To create an EGS reservoir, a first well is typically drilled through top layers of sedimentary rock into a low-permeability crystalline basement. The bottom section of the well, typically at 3-10 km depth is hydraulically stimulated, creating a network of interconnected fractures. The spatial extent of this network is determined using microseismic monitoring methods, and a second well is drilled to intersect the fractured reservoir. Once the system is completed, pressurized water or other heat transfer fluid such supercritical $CO_2$ is circulated through the subsurface loop consisting of injection well, fractured EGS reservoir, and production well. Thermal energy extracted by the fluid to the surface is used to generate electricity and/or for direct-use purposes.

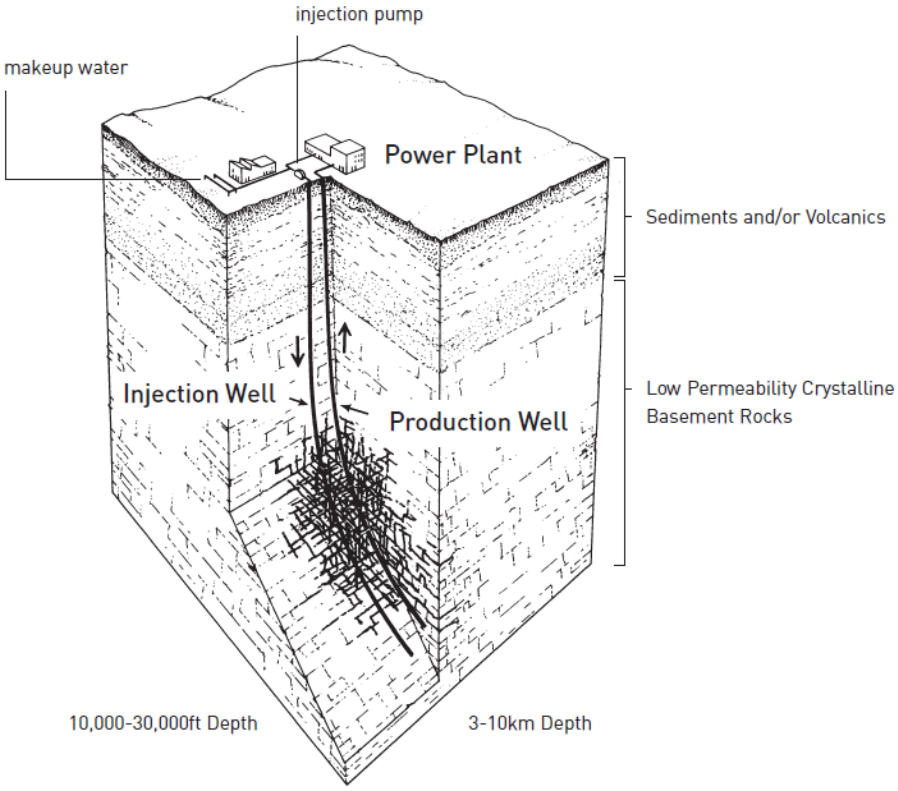


*Figure 1-3: A conceptual view of a two-well Enhanced Geothermal System (EGS)*

Because Enhanced Geothermal Systems are not limited to areas where natural geothermal systems exist, their overall potential is much greater. Technically recoverable U.S. EGS resources, estimated at 2% of the total thermal energy stored in rocks at 3-10 km depth, is $2.8*10^5$ EJ (Tester et al., 2006). That is almost 3000 times more than the 2015 total U.S. primary energy demand of 103 EJ (EIA, 2016b). With such an extensive resource base, Enhanced Geothermal Systems can become a long-term sustainable source of electricity and heat if the cost of mature EGS technology is sufficiently low.

In addition to the larger overall potential, EGS resources are more uniformly distributed compared to hydrothermal fields. As an example, Figure 1-4 shows the temperature at 4.5 km depth in the contiguous U.S, representing resources which are economically accessible with the current well drilling and completion technologies. While the high- (>200ºC) and medium-temperature (120-200ºC) resources are located predominantly in the Western part of the country, lower temperature resources suitable for direct use applications can be found almost anywhere in the U.S.

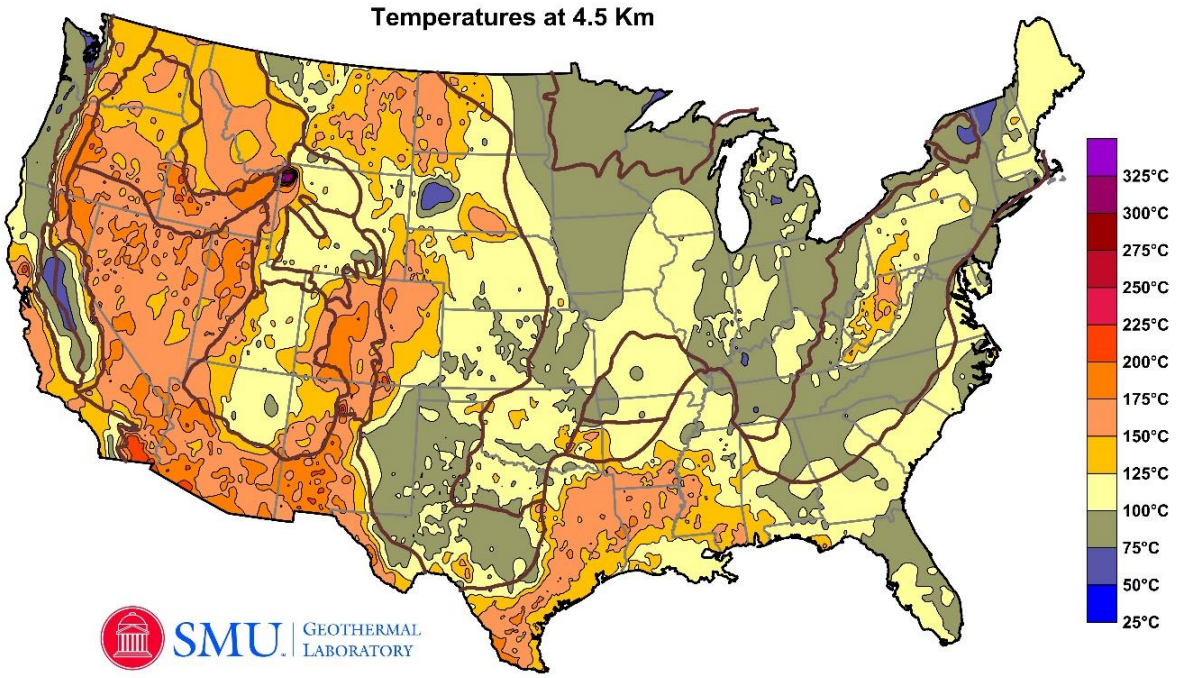


*Figure 1-4: Map of formation temperatures at 4.5km depth in the U.S. (Blackwell et al., 2011)*

While the EGS technology has not been implemented on a commercial scale yet, a number of successful, large-scale demonstration projects exist. Since the first EGS pilot project in Fenton Hill, New Mexico in 1974, a significant progress has been made in a number of key

development areas including directional drilling, controlled creation of large reservoir volumes, and circulating water with acceptable mass and pressure losses (Tester et al., 2006; U.S. DOE, 2010). In one of the most recent demonstration projects in Soultz, France, a 2 $km^3$ EGS reservoir was created at a 4-5 km depth, which was able to sustain production flow rates only 2 to 3 times lower from the commercial goals (Tester et al., 2006). While thermal recharge of conduction-dominated Enhanced Geothermal Systems is slower than for conventional convective systems, EGS reservoirs recover sufficiently to be used again after periods 2-4 times longer compared to their initial, multi-year use (Fox et al., 2013).

Currently, the main focus areas in EGS development are: 1) increasing production rates and avoiding premature reservoir cooling 2) controlled hydraulic stimulation to avoid noticeable seismic events and 3) reduction of capital cost and uncertainty by improved well drilling, hydraulic stimulation, and power conversion technologies.

## 1.3 Geothermal energy utilization: direct use and electricity generation

Geothermal energy has been used by humans for centuries, first as naturally occurring hot springs, and later in public baths and buildings located near the natural geothermal discharge areas. The modern use of geothermal energy began at the turn of XIX and XX century when the first geothermal electricity was generated in Larderello, Italy.

Today, the total installed capacity of deep geothermal systems is 12.7 $GW_e$ and 20.4 $GW_{th}$ for electric plant and direct-use applications, respectively (Bertani, 2016; Lund and Boyd, 2015). Geothermal electric capacity has been increasing at a steady, but rather slow rate of 3.2% per

year in 1984-2014 (Bertani, 2016; DiPippo, 2012), while the capacity of direct-use systems grew at much higher rate of 7.7% per year in 2010-2014 (Lund and Boyd, 2015).

The use of geothermal resources is dictated by both demand and the temperature of produced fluid. The low-temperature (<120ºC) resources are more suitable for direct-use applications whereas medium- and high-temperature fluids (120-200ºC and >200ºC, respectively) are typically used for generation of electricity and co-generation applications.

This quality-based approach is supported by the second law of thermodynamics which indicates that the higher temperature heat can be converted into work more effectively. It is also different from the way we use fossil fuels in our distributed energy systems, where the high-temperature thermal energy obtained during combustion is often downgraded to produce low-temperature heat for space heating or cooking. Such use of fossil fuels results in large destruction of exergy i.e. the potential to generate work.

As illustrated in Figure 1-5, the U.S. demand for low-grade heat is significant: of 100 EJ consumed in the U.S. in 2008, approximately 25 EJ could be delivered to the end-use as a low-temperature (<120ºC) thermal energy. The high-grade fuels burned for this purpose could be used more effectively to generate electricity or produce petrochemicals, and the low-temperature heat demand for space and water heating could be provided using low-grade renewable resources including geothermal energy.

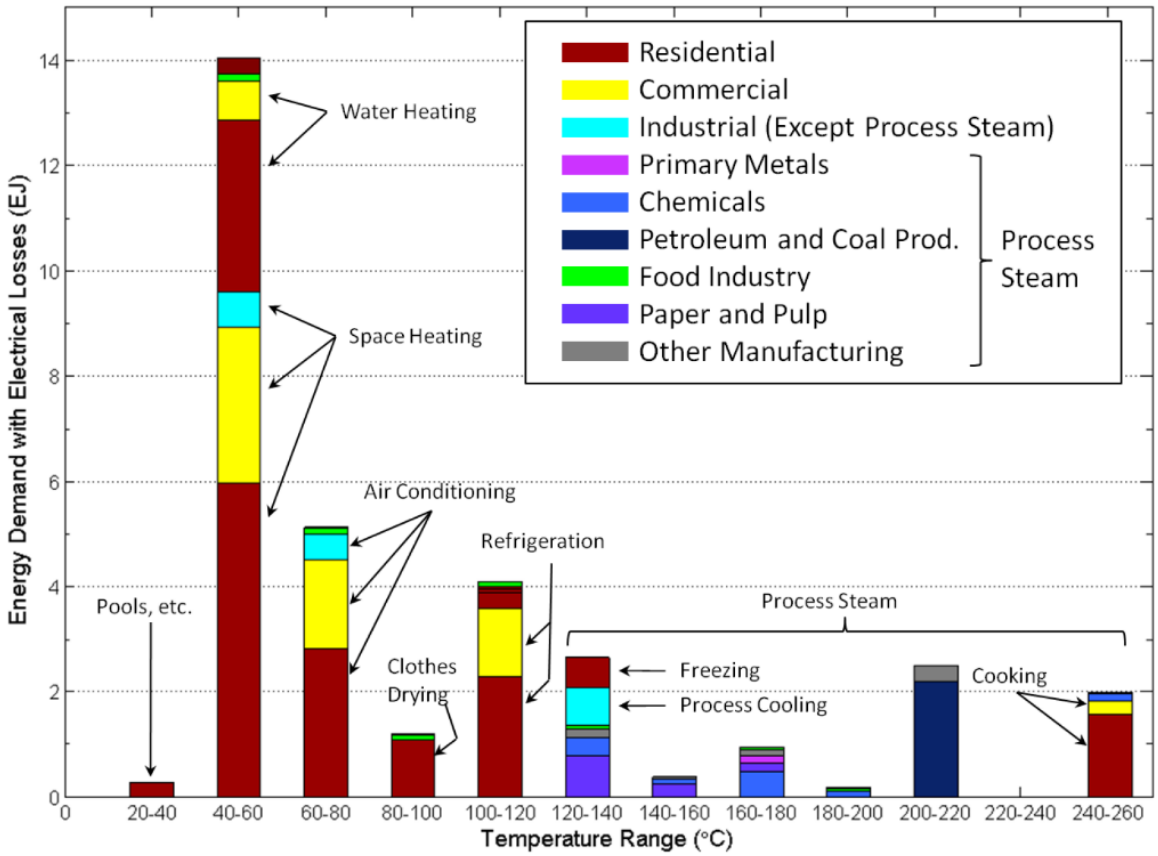


*Figure 1-5: Temperature spectrum of U.S. thermal energy use. The total energy demand in EJ (1EJ=$1^{18}$J) is plotted as a function of the end-use temperature (Fox et al., 2011).*

Direct use applications of geothermal energy include, but are not limited to geothermal heat pumps using borehole heat exchangers, space heating, bathing and swimming, greenhouse heating, and food drying (Lund and Boyd, 2015). Geothermal heat can also be used in cascaded direct-use systems, where the outlet stream from a higher-temperature process (e.g. space heating) is used as a heat input into a low-temperature process (e.g. soil heating in greenhouses or snow melting). Deep geothermal energy is particularly suitable for direct use applications with high load factors, because the operation and maintenance costs of geothermal systems are very low compared to their capital costs (U.S. EIA, 2015).

Geothermal resources at temperatures above 120ºC are typically used for electricity generation or combined heat and power (CHP). The main categories of geothermal power plants are presented in Figure 1-6 (DiPippo, 2012). The choice between individual technologies depends on the resource quality and, to a lesser extent, the stage of geothermal field development. Historically, simpler and less expensive energy conversion systems were typically used in the early phases of field development and more advanced solutions were added once the long-term reservoir behavior has been assessed.

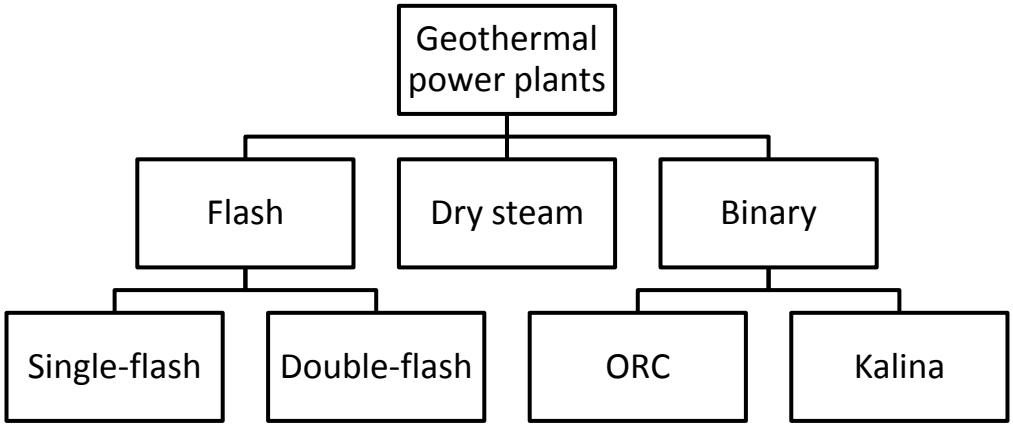


*Figure 1-6: Classification of geothermal power conversion cycles.*

Dry steam power plants are used to generate electricity from steam-dominated reservoirs. Steam-dominated geothermal systems are uncommon and, while the two largest geothermal areas in the World (The Geysers in California and Larderello in Tuscany) produce dry steam, it is unlikely that new large fields will be discovered. Geothermal dry steam power plants are very simple and consist of particulate removers, cyclone separators, steam turbines, and condensers (DiPippo, 2012).

Single- and double-flash power plants are used in liquid-dominated geothermal systems, in which production temperature exceeds 150ºC. In such systems, the geothermal fluid extracted from production wells undergoes an isenthalpic flashing process and is separated into saturated vapor and liquid in cyclone separators. The vapor is sent to the turbine and the saturated liquid can either be reinjected into the reservoir or, in a double-flash plant, undergo another flashing at a lower pressure to produce additional steam. After expanding saturated steam in a turbine, the low-pressure vapor-liquid mixture is condensed in a surface-type or direct-contact condenser and the heat of condensation is typically dissipated using a wet cooling tower.

Single- and double-flash plants are commonly used in hydrothermal fields and together they constitute 65% of the total geothermal capacity (DiPippo, 2012). They are, however, less suitable for Enhanced Geothermal Systems. The use of evaporative process to condense the steam means that less water is reinjected into the reservoir than is extracted from it. EGS systems typically have insufficient natural water inflow into reservoir, so the use of flash technology would require a significant source of make-up water, which is not always available.

As opposed to flash technology, binary power plants operate in a closed loop and often use air-cooled condensers, making them more suitable for many potential EGS locations. They typically generate electricity from 120-180ºC geothermal fluids, but can be economically used for lower-grade resources if a low-temperature heat sink is available (Aneke et al., 2011). They are also used instead of flash technology at higher heat source temperatures, if the geothermal fluid contains a high fraction of non-condensable gases ($CO_2$ and $H_2S$) or if flashing would result in scaling.

Binary power plants include Organic Rankine Cycle (ORC) and Kalina technologies. Both of them use low boiling-point working fluid operating in a closed loop, which indirectly exchanges heat with the geothermal fluid and the cooling fluid (air or water). ORC plants use organic working fluids (typically alkanes or hydrofluorocarbons), while Kalina plants use a water-ammonia mixture. While some researchers claimed significant efficiency advantage of the Kalina technology (Mlcak, 2004), both the analysis of an existing Kalina plant and the recent numerical evaluations have shown that it has a comparable efficiency to much simpler, more robust, and mature ORC technology (DiPippo, 2004; Walraven et al., 2013).

## 1.4 Techno-economic models of geothermal energy systems

Due to the large capital investments and uncertainties involved in geothermal projects, new developments should be carefully evaluated prior to and during the construction period. Such approach ensures an optimal configuration of geothermal system, an adequate long-term resource management, and reduction of the financial risk. To evaluate the economic feasibility of geothermal energy projects, a systems approach involving techno-economic modeling and optimization is often used.

A techno-economic model of geothermal energy system combines the thermal models of reservoir, geothermal wells, power plant and/or heat distribution system with the costs information about individual system components. The components of a techno-economic model of geothermal energy system are showed in Figure 1-7. The reservoir, wells, and surface infrastructure models need to be integrated into a larger superstructure, because they interact with one another. One example of such interaction is that between the resource temperature,

the depth of geothermal wells, and the efficiency of the power conversion system. Deeper wells provide higher production temperatures, which increases the efficiency of the power plant and reduces the specific cost of surface equipment (in $/kW). The drilling costs, however, increase exponentially with well depth (Lukawski et al., 2016) preventing geothermal developers from tapping very deep resources. In addition, the productivity of geothermal wells typically varies with depth as a result of differences in formation lithology. These and many other correlations are embedded in a techno-economic models of geothermal energy system. Such models can determine the optimum values of all design variables, including the depths of geothermal wells, and calculate the minimum levelized cost of electricity or direct-use heat.

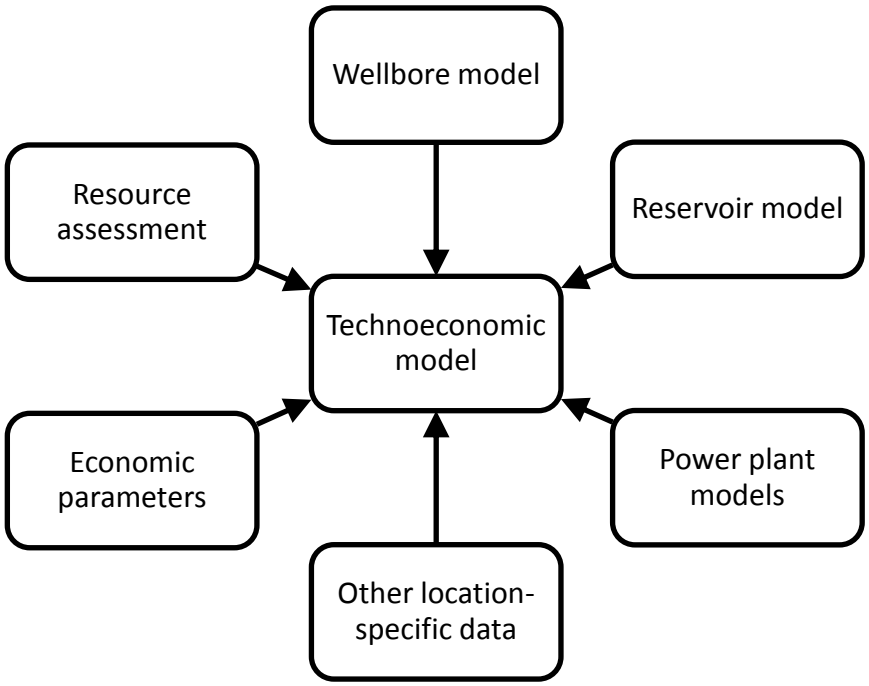


*Figure 1-7: Main components of a techno-economic model of a geothermal energy system*

A recently developed techno-economic model of geothermal energy systems named GEOPHIRES is essential to the work described in this thesis. GEOPHIRES integrates the

individual research projects described in this thesis into a larger structure and combines it with other required information to accurately model geothermal energy systems. Examples of research work described in this thesis which have been integrated into GEOPHIRES software include the efficiencies of geothermal power plants from Part I of this thesis and the geothermal well cost correlations described in Part III. The author assisted also with the development of other components of the GEOPHIRES software, such as multiple parallel fracture model (Fox et al., 2013), which are not included in this thesis.

GEOPHIRES was developed primarily by Koenraad Beckers at Cornell Energy Institute and has been extensively described in the literature (Beckers, 2016; Beckers et al., 2015, 2014, 2013; Reber et al., 2014). The acronym GEOPHIRES stands for **GEO**thermal energy for the **P**roduction of **H**eat and electricity (**IR**) **E**conomically **S**imulated, where 'IR' represents the electric current and resistance. GEOPHIRES is based on the earlier work in this area spanning from the Fenton Hill EGS project research (Armstead and Tester, 1987; Tester and Herzog, 1990) to the model developed for the 2006 EGS report produced by an MIT-led panel of experts (Tester et al., 2006).

In contrast to the previous models, GEOPHIRES allows the user to calculate not only the Levelized Cost of Electricity (LCOE) but also the Levelized Cost of Heat (LCOH) for direct-use and CHP applications. With 96 user-defined input parameters, and a choice of 4 reservoir models and 3 levelized cost models, this tool facilitates a lower-granularity analysis and optimization of EGS systems (Beckers, 2016).

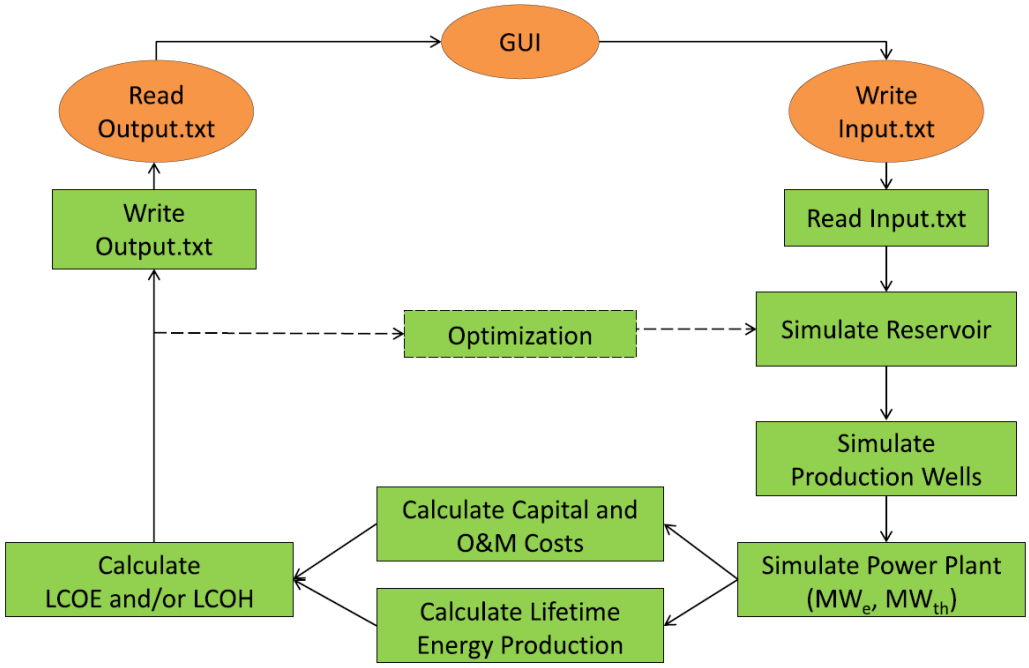


*Figure 1-8: Schematic of the operating procedure of the GEOPHIRES software. The procedures of Graphical User Interface (GUI) and FORTRAN code are shown in orange and green, respectively (Beckers, 2016).*

The calculation process of GEOPHIRES is presented in Figure 1-8. The software can be used to either calculate the technical and economic performance metrics of a specific geothermal system, or to optimize its design for a minimum LCOE or LCOH given the user-specified constraints. GEOPHIRES can be used either as a stand-alone software with a Graphical User Interface (GUI) or as a subroutine controlled by a different software. If used as a sub-routine, GEOPHIRES can become a powerful tool for assessing the economic feasibility of geothermal energy systems in multiple locations. An example of such analysis is the work by (Reber et al., 2014), who used a code in MATLAB software combined with GEOPHIRES and ArcGIS to evaluate the potential of geothermal district heating in New York and Pennsylvania. The authors

evaluated almost 3000 potential locations to identify the communities with the right combination of geothermal gradient, population density, energy demand, and climate to provide low LCOH. A graphical interpretation of their results is shown in Figure 1-9 (Reber et al., 2014).

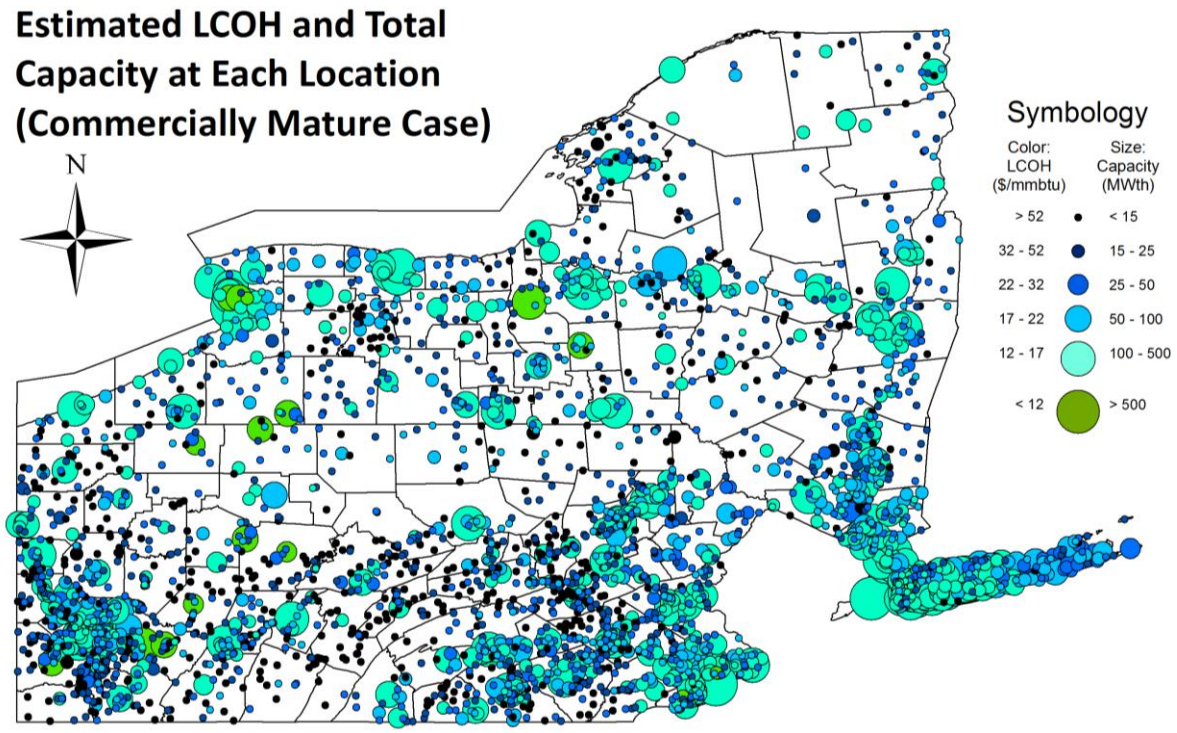


*Figure 1-9: Predicted levelized Cost of Heat (LCOH, $/MMBTU) and heat demand ($MW_{th}$) for EGS located in New York and Pennsylvania (Reber et al., 2014)*

## 1.5 Key research areas in geothermal energy systems

The rate of adoption of geothermal energy systems is slower compared to what could be expected based their dependability and the low cost of energy they can provide. While substantial improvements to hydrothermal technology have been made over the last 40 years

(U.S. DOE, 2010) and many initial concerns about the EGS reservoir performance have been resolved (Tester et al., 2006), the growth rate of geothermal electric capacity remains low at approximately 3% per year (DiPippo, 2012).

The main barrier to a broader adoption of geothermal energy systems is not technical, but rather financial. In resemblance to upstream oil and gas development, geothermal projects require substantial upfront investments in geophysical exploration and test drilling. These investments need to be made before the existence of resource is confirmed. If the discovered resource is insufficient to drill production wells and develop the surface infrastructure, the money spent on exploration is not recovered. This economic risk is often reflected in high interest rates for debt and equity for geothermal projects (The World Bank, 2012).

The most financially risky part of a geothermal project is the exploratory drilling. The first well in a hydrothermal field has an average success rate of 50% (IFC, 2013) and typically costs 2-8 million U.S. dollars (Lukawski et al., 2014). The success rate increases as more wells is drilled in a given field, but a study based on over 2600 hydrothermal wells showed that even during the development and operation drilling, 17-26% of the wells are unsuccessful (IFC, 2013).

To overcome the difficulty with securing a low-cost funding for geothermal energy development, the finance community needs a good understanding of the uncertainty and risk involved in these projects. This requires accurate predictive drilling cost models, which can estimate the cost and cost uncertainty of geothermal wells. Such models were developed as a part of this work and are discussed in Part I of this thesis.

In addition to providing more accessible project financing, a continued research and development efforts are needed in the key technical research areas including drilling, reservoir

engineering, and energy conversion technologies. Improvements in these fields would lead to lower cost of both EGS and hydrothermal systems and increased access to deeper resources.

Research in well drilling and completion is particularly important, because these activities comprise 35-40% of capital investment in hydrothermal systems (IFC, 2013) and up to 75% in low-grade EGS projects (Petty et al., 2009; Tester et al., 2006). Because of this high cost contribution, even small improvements in drilling technologies can have a large impact on the total project costs. Research and development in drilling methods involves both incremental improvements in the current technology as well as development of new, pioneering technologies. The former category includes roller cone drilling bits with higher penetration rates and longer lifetime, improved casing technologies, as well as sensors, electronics, and cementing methods suitable for extreme downhole temperatures (Tester et al., 2006). The revolutionary drilling technologies include thermal spallation drilling, mineral dissolution, and other methods aiming at increasing the penetration rates and reducing the bit replacement frequency in crystalline rock formations encountered in EGS projects (Augustine, 2009; Hillson and Tester, 2015; H. Thorsteinsson et al., 2008).

Research in reservoir engineering is needed to further increase the active volumes of EGS reservoirs by more effective hydraulic stimulation, while avoiding hydraulic short-circuiting or creating high-energy seismic events (Tester et al., 2006). Thermal-hydraulic models of geothermal reservoirs are also developed to model reservoir behavior over time, allowing us to better predict their lifetime and reduce the uncertainties associated with geothermal energy projects (Fox et al., 2013).

Lastly, continued research on power conversion systems is needed to improve the efficiency of low-temperature organic Rankine cycle (ORC) plants and to develop new power plant designs for ultra-high-temperature resources. Geothermal resources at temperatures close to or above the critical point of water (374ºC) may be available in the future from wells drilled near magma intrusions in volcanic systems. Such wells can provide an order of magnitude higher power output compared to the conventional hydrothermal resources and are currently developed as a part of the Icelandic Deep Drilling Project (Markusson and Hauksson, 2015).

The ongoing research in low-temperature ORC plants aims at increasing their efficiency and making their output less sensitive to the variations in ambient conditions. The proposed ways to improve the efficiency of ORC plants include improved selection of pure working fluids (Hung et al., 2010; Walraven et al., 2015), the use of working fluid mixtures (Andreasen et al., 2014; Chen et al., 2011), and supercritical ORCs, in which turbine inlet pressure exceeds the critical point of working fluid (Astolfi et al., 2014; Augustine et al., 2009). Although many studies evaluated performance of multiple working fluids in ORCs, a proper numerical analysis could be done only for a selected group of substances, for which accurate models describing pressure-volume-temperature (PVT) relations exist. Such models, referred to as equations of state (EOS) are often insufficiently accurate for modeling ORCs using less common pure fluids and most of fluid mixtures.

Providing means of assessing the performance of ORCs plants using less common working fluids would likely allow to identify new, more efficient ORC plant designs. This task is approached in this thesis in a two ways. Part I of this work discusses the methods which were developed to distinguish the most promising pure working fluids for which no accurate EOSs exist. These methods correlate specific thermodynamic properties of the working fluids, namely

their reduced ideal gas heat capacitates $C_p^0/R$ and critical temperatures $T_c$ with various ORC performance metrics. Part II of this work discusses thermophysical property measurements of fluid mixtures, which provide data for developing more accurate equations of state for fluid mixtures.

## 1.6 References


Andreasen, J.G., Larsen, U., Knudsen, T., Pierobon, L., Haglind, F., 2014. Selection and optimization of pure and mixed working fluids for low grade heat utilization using organic Rankine cycles. Energy 73, 204–213. doi:10.1016/j.energy.2014.06.012

Aneke, M., Agnew, B., Underwood, C., 2011. Performance analysis of the Chena binary geothermal power plant. Appl. Therm. Eng. 31, 1825–1832. doi:10.1016/j.applthermaleng.2011.02.028

Armstead, H.C.H., Tester, J., 1987. Heat Mining, First edit. ed. E. & F.N. Spon, London, New York.

Astolfi, M., Romano, M.C., Bombarda, P., Macchi, E., 2014. Binary ORC (Organic Rankine Cycles) power plants for the exploitation of medium-low temperature geothermal sources - Part A: Thermodynamic optimization. Energy 66, 423–434. doi:10.1016/j.energy.2013.11.057

Augustine, C., Field, R., DiPippo, R., Gigliucci, G., Fastelli, I., Tester, J., 2009. Modeling and Analysis of Sub- and Supercritical Binary Rankine Cycles for Low- to Mid-Temperature Geothermal Resources. Trans. - Geotherm. Resour. Counc. 33, 604–608.

Augustine, C.R., 2009. Hydrothermal Spallation Drilling and Advanced Energy Conversion Technologies for Engineered Geothermal Systems. Ph.D. Thesis, MIT. MIT.

Beckers, K.F., 2016. Low-temperature geothermal energy: systems modeling, reservoir simulation, and economic analysis. Cornell University.

Beckers, K.F., Lukawski, M., Anderson, B., Moore, M., Tester, J., 2014. Levelized costs of electricity and direct-use heat from Enhanced Geothermal Systems. J. Renew. Sustain. Energy 6. doi:10.1063/1.4865575

Beckers, K.F., Lukawski, M.Z., Aguirre, G.A., Hillson, S.D., Tester, J.W., 2015. Hybrid Low-Grade Geothermal-Biomass Systems for Direct-Use and Co-Generation: from Campus Demonstration to Nationwide Energy Player. Fortieth Work. Geotherm. Reserv. Eng. 1–11.

Beckers, K.F., Lukawski, M.Z., Reber, T.J., Anderson, B.J., Moore, M.C., Tester, J.W., 2013. Introducing Geophires V1.0: Software Package for Estimating Levelized Cost of Electricity and/or Heat From Enhanced Geothermal Systems. 38th Work. Geotherm.

Reserv. Eng.

Bertani, R., 2016. Geothermal power generation in the world 2010-2014 update report. Geothermics 60, 31–43. doi:10.1016/j.geothermics.2015.11.003

Blackwell, D., Richards, M., Frone, Z., Batir, J., Ruzo, A., Dingwall, R., Williams, M., 2011. Temperature at depth maps for the conterminous US and geothermal resource estimates, in: Geothermal Resources Council Transactions 35. GRC Record 1029452., pp. 1545–1550.

Chen, H., Goswami, D.Y., Rahman, M.M., Stefanakos, E.K., 2011. A supercritical Rankine cycle using zeotropic mixture working fluids for the conversion of low-grade heat into power. Energy 36, 549–555.

DiPippo, R., 2004. Second Law assessment of binary plants generating power from low-temperature geothermal fluids. Geothermics 33, 565–586. doi:10.1016/j.geothermics.2003.10.003

DiPippo, R., 2012. Geothermal Power Plants: Principles, Applications, Case Studies and Environmental Impact, 3rd ed. Butterworth-Heinemann.

EIA, 2016a. International Energy Outlook 2016.

EIA, 2016b. U.S. Energy facts [WWW Document]. URL http://www.eia.gov/energyexplained/index.cfm?page=us_energy_home (accessed 5.8.16).

ExxonMobil, 2016. The Outlook for Energy: A View to 2040. Irving, Texax.

Flovenz, O.G., Karlsdottir, R., Saemundsson, K., Smarason, O.B., Eysteinsson, H., Bjornsson, G., Bjornsson, T., 2000. Geothermal Exploration in Arskogsstrond, N-Iceland. World Geotherm. Congr. 2000 1133–1138.

Fox, D., Sutter, D., Beckers, K., Lukawski, M., Koch, D., Anderson, B.J., Tester, J.W., 2013. Sustainable heat farming: Modeling extraction and recovery in discretely fractured geothermal reservoirs. Geothermics 46, 42–54. doi:10.1016/j.geothermics.2012.09.001 accepted 24 September 2012

Fox, D.B., Sutter, D., Tester, J.W., 2011. The thermal spectrum of low-temperature energy use in the United States. Energy Environ. Sci. 4, 3731. doi:10.1039/c1ee01722e

Hersir, G.P., Bjornsson, A., 1991. Geophysical exploration for geothermal resources: principles and application. UNU Geothermal Training Programme, Reykjavik, Iceland.

Hillson, S.D., Tester, J.W., 2015. Heat Transfer Properties and Dissolution Behavior of Barre Granite as Applied to Hydrothermal Jet Drilling with Chemical Enhancement. Fortieth Work. Geotherm. Reserv. Eng. 1–9.

Hung, T.C., Wang, S.K., Kuo, C.H., Pei, B.S., Tsai, K.F., 2010. A study of organic working fluids on system efficiency of an ORC using low-grade energy sources. Energy 35, 1403–1411.

IFC, 2013. Success of Geothermal Wells: A Global Study. Washington, DC, USA.

Lukawski, M.Z., Anderson, B.J., Augustine, C., Capuano, L.E., Beckers, K.F., Livesay, B., Tester, J.W., 2014. Cost analysis of oil, gas, and geothermal well drilling. J. Pet. Sci. Eng. 118, 1–14. doi:10.1016/j.petrol.2014.03.012

Lukawski, M.Z., Silverman, R.L., Tester, J.W., 2016. Uncertainty analysis of geothermal well drilling and completion costs. Geothermics 64, 382–391. doi:10.1016/j.geothermics.2016.06.017

Lund, J., Boyd, T., 2015. Direct Utilization of Geothermal Energy 2015 Worldwide Review. Proc. World Geotherm. Congr. 25–29. doi:10.1016/j.geothermics.2011.07.004

Markusson, S.H., Hauksson, T., 2015. Utilization of the Hottest Well in the World , IDDP-1 in Krafla. World Geotherm. Congr. 2015 1–6.

Mlcak, H.A., 2004. An Introduction to the Kalina Cycle, in: PWR - Proceedings of the International Joint Power Generation Conference.

Newell, R.G., Qian, Y., Raimi, D., 2016. Global Energy Outlook 2015. doi:10.3386/w22075

NREL, 2016. Utility-Scale Energy Technology Capacity Factors [WWW Document]. Transparent Cost Database. URL http://www.nrel.gov/analysis/tech_cap_factor.html (accessed 4.8.16).

Pachauri, S., Rao, N., Nagai, Y., Riahi, K., 2012. Access to modern energy: Assessment and outlook for developing and emerging regions, UNIDO.

Petty, S., Bour, D., Livesay, B., Baria, R., Adair, R., 2009. Synergies and Opportunities Between EGS Development and Oilfield Drilling Operations and Producers. SPE 121165.

Reber, T.J., Beckers, K.F., Tester, J.W., 2014. The transformative potential of geothermal heating in the U.S. energy market: A regional study of New York and Pennsylvania. Energy Policy 70, 30–44. doi:10.1016/j.enpol.2014.03.004

Tester, J.W., Anderson, B.J., Batchelor, A.S., Blackwell, D.D., DiPippo, R., Drake, E.M., Garnish, J., Livesay, B., Moore, M.C., Nichols, K., Petty, S., Toksoz, M.N., Veatch, Ralph W, J., 2006. The Future of Geothermal Energy: Impact of Enhanced Geothermal Systems (EGS) on the United States in the 21st Century. MIT.

Tester, J.W., Herzog, H., 1990. Economic Predictions for Heat Mining: A Review and Analysis of Hot Dry Rock (HDR) Geothermal Energy Technology. Cambridge, Mass., USA.

The World Bank, 2012. Geothermal handbook: Planning and Financing Power Generation.

The World Bank, 2016. Greenhouse gases from geothermal power production.

Thorsteinsson, H., Augustine, C., Anderson, B.J., Moore, M.C., Tester, J.W., 2008. The impacts of drilling and reservoir technology advances on EGS. Thirty-ThirdWorkshop Geotherm. Reserv. Eng.

Thorsteinsson, H., Augustine, C., Anderson, B.J., Moore, M.C., Tester, J.W., 2008. The Impacts of Drilling and Reservoir Technology Advances on EGS Exploitation. Proceedings, Thirty-Third Work. Geotherm. Reserv. Eng. Stanford Univ. 14.

Tissot, B.P., Welte, D.H., 1984. Petroleum Formation and Occurrence, Second Revised and

Enlarged Edition. doi:10.1029/EO066i037p00643

U.S. DOE, 2010. A History of Geothermal Energy Research and Development in the United States. Washington, D.C., USA.

U.S. EIA, 2015. Levelized cost and levelized avoided cost of new generation resources in the annual energy outlook 2015.

Walraven, D., Laenen, B., D'haeseleer, W., 2013. Comparison of thermodynamic cycles for power production from low-temperature geothermal heat sources. Energy Convers. Manag. 66, 220–233.

Walraven, D., Laenen, B., D'haeseleer, W., 2015. Economic system optimization of air-cooled organic Rankine cycles powered by low-temperature geothermal heat sources. Energy 80, 104–113. doi:10.1016/j.energy.2014.11.048

# 2 OBJECTIVES AND APPROACH

## 2.1 Dissertation objectives

Successful operation of a geothermal energy system depends not only on the subsurface reservoir, but also on the geothermal wells and the surface infrastructure. Due to the complex interactions between the individual system components, geothermal systems often need to be modeled using an integrated systems approach. This thesis presents an example of such approach used to develop more efficient, less expensive, and less economically uncertain geothermal energy systems, including EGSs.

**The main objective of this thesis was to improve the competitiveness of geothermal energy systems by increasing their efficiency and reducing project risk. Within this topic, the specific goals of this work were to:**

1. Create guidelines for designing more efficient geothermal energy conversion and distribution systems
2. Quantify the costs and uncertainties associated with drilling and completion of geothermal wells

Both of these objectives are essential to accurate evaluation of EGS. In addition, geothermal wells and the surface infrastructure constitute a bulk of engineering work involved in creating geothermal energy systems.

Within the area of geothermal surface infrastructure, the primary focus of this work is on organic Rankine cycle (ORC) plants. ORC is the most promising heat-to-power conversion technology for low- and medium-grade EGS resources. While the ORC technology is well

established, it is continuously improved and even small efficiency gains can have a substantial effect on the economics of geothermal electricity generation. This work addresses a major limiting factor in the development of ORC plants - insufficiently accurate description of thermodynamic properties of many potential working fluids.

A second key research area in geothermal energy utilization is system integration and optimization. Geothermal power plants and district heating systems are both sub-components of a larger energy generation and distribution system. The proper integration of geothermal utilization systems with both subsurface reservoir and other energy sources can improve the performance of EGS and reduce the cost of energy.

Combined, the research on ORCs and system integration provide a comprehensive guideline for designing more efficient geothermal utilization systems. It is also one of two major paths towards the main goal of this work: improving the competitiveness of geothermal energy systems. The other path includes reduction of cost and economic uncertainty. Because well drilling typically constitutes the largest and most uncertain cost component of EGS, the focus on the last part of this thesis in on quantifying geothermal well costs.

In addition to serving a common goal, the individual chapters of this thesis are also integrated in a techno-economic EGS model named GEOPHIRES. This software uses efficiency and cost correlations from this thesis to model and optimize Enhanced Geothermal Systems.

## 2.2 Dissertation approach

The content of this dissertation is divided into three parts addressing various research objectives. Part I: Low Temperature Energy Conversion Systems, Part II: Measurements of Isobaric Heat Capacity of Fluids, and Part III: Drilling Costs of Geothermal, Oil, and Gas Wells.

Parts I and II both address the first goal of this work, which is to develop more efficient geothermal energy conversion and distribution systems. Each section uses a different approach to achieve the common goal. Whereas Part I employs numerical modeling and optimization methods to directly improve the energy conversion systems, Part II provides useful property measurements, which can indirectly benefit these power conversion systems by enhancing the accuracy of EOSs for working fluids.

Part I of this dissertation consists of two chapters: Chapter 3 focuses on developing guidelines for designing more efficient organic Rankine cycle (ORC) power plants. The main goal of this work is to correlate the efficiency of ORCs with the thermodynamic properties of working fluids. The developed methodology provides a way to estimate a number of performance metrics of ORC plants based only on the molecular structure of the working fluid and the parameters of heat source and heat sink. This approach can be used to analyze potential future working fluids, for which the existing EOSs are insufficiently accurate to perform regular cycle calculations. In addition, Chapter 3 analyzes performance of ORCs using multiple cycle configurations, working fluids, and parameters of heat source and heat sink. The developed correlations for efficiency of ORCs were validated using data from actual geothermal power plants and later used in the GEOPHIRES software.

Chapter 4 in Part I provides a broader view of the geothermal energy utilization systems. It evaluates the feasibility of integrating geothermal ORC plants and district heating systems into the existing energy infrastructure. A case study of a potential geothermal system at Cornell University is used to produce more generalized conclusions applicable to many communities in the Northeastern U.S. and beyond.

Part II of this dissertation facilitates the development of ORCs and other energy conversion and storage devices by providing accurate measurements of thermophysical properties of working fluids. In particular, measurements of isobaric heat capacity ($C_p$) were made for vapor, liquid, and in the supercritical region of pure fluids and fluid mixtures. To measure $C_p$ near the critical points of fluids with sufficiently high accuracy, a new type of measurement equipment, a fluid flow calorimeter, was designed, built, and tested. The $C_p$ measurements performed using the flow calorimeter can be used to validate the existing, and develop new equations of state, particularly for fluid mixtures.

Lastly, Part III of this dissertation addresses the second objective of this dissertation i.e. to quantify the costs and uncertainties associated with drilling and completion of geothermal wells. In chapter 6, the average geothermal well costs are evaluated as a function of well depth. Geothermal well costs are then compared to the current and historical costs of oil and gas wells. Besides evaluating the average well costs, Chapter 6 examines the learning curve effects related to drilling multiple similar wells within the same field.

Chapter 7 goes beyond the deterministic approach used in Chapter 6 by characterizing the uncertainty associated with the cost of drilling and completion of geothermal wells. The probability distributions of geothermal well costs are obtained using recent well records, a

predictive drilling cost model, and the Monte Carlo method. The correlations presented in Part III of this dissertation can be used to determine the economic feasibility of geothermal energy systems, assess the project risk, and facilitate investment decisions.

# Part I

# Low Temperature Energy Conversion Systems

# 3 ORGANIC RANKINE CYCLE (ORC) POWER PLANTS

## 3.1 Introduction

The most widely recognized and commercially mature technology for converting medium-temperature (120-180ºC) geothermal heat to electricity is the organic Rankine cycle (ORC). ORC power plants feature a design similar to conventional Rankine cycle plants, but use low-boiling point organic working fluids instead of water. Because of that, ORC plants achieve higher efficiency than steam cycles at low heat-source temperatures (Dai et al., 2009). Expanders in small ORC plants are also simpler and more efficient than comparable steam turbines, which made ORC a popular choice for small (<20 $MW_e$) biomass boilers and waste heat recovery systems.

Increased implementation of ORC technology has been supported by the research aimed at improving ORC plant performance through design modifications. Recent studies have focused on the selection of both pure working fluids (Hung et al., 2010; Saleh et al., 2007; Walraven et al., 2013) and multicomponent fluid mixtures (Andreasen et al., 2014; Chen et al., 2011; Heberle and Brüggemann, 2015), high-temperature ORC for waste heat recovery (Invernizzi et al., 2007) and biomass boilers (Martelli et al., 2015), and hybrid plants using more than one source of heat (Greenhut et al., 2010; Manente et al., 2011).

In several earlier investigations, ORC plants were optimized either to maximize their utilization (exergetic) efficiency or, if cost information was available, to either minimize their levelized cost of electricity (LCOE) (Augustine et al., 2009; Dai et al., 2009; Lukawski, 2009; Walraven

et al., 2013), minimize the total specific cost of the plant (Astolfi et al., 2014), or maximize the net present value (NPV) (Walraven et al., 2015). These studies compared the optimal operating parameters and various performance metrics of several organic working fluids and made recommendations for optimal cycle configurations. In addition, researchers performed parametric studies of ORCs to understand the impact of individual design parameters and to develop generalized design rules (Maraver et al., 2014).

A number of studies have made a distinction between wet and dry working fluids based on their behavior during isentropic expansion. With wet working fluids, the saturated vapor curve has a negative slope in temperature-entropy coordinates and thus an isentropic expansion of saturated vapor produces a vapor-liquid mixture. For dry working fluids, the saturation curve shows a positive slope over most of the range of interest and the expansion yields superheated vapor. This difference in behavior of various working fluids was linked to their molecular complexity and quantified using molecular mass, acentric factor, reduced ideal gas heat capacity, or directly by the slope of vapor saturation line (Chen et al., 2010; Invernizzi et al., 2007; Tester and Milora, 1977). Working fluids with dry expansion characteristics were shown to require less turbine inlet superheat (Chen et al., 2010; Tester and Milora, 1977) and provide higher thermal efficiency in cycles using heat recuperators (Invernizzi et al., 2007; Maraver et al., 2014).

The majority of previous studies looked at performance of multiple working fluids at one, specific set of heat source and sink temperatures. This research explores a range of heat source temperatures (100-230ºC), several cycle configurations and heat rejection conditions. Furthermore, this work goes beyond a mere parametric study given its main objective to correlate the thermodynamic properties of working fluids with their performance in ORCs. With such correlations, it should be possible to predict the efficiency of plants using new

working fluids, some of which may not have adequately characterized thermodynamic property correlations available for full cycle simulation. For example, accurate equations of state (EOSs) may not be available to develop precise numerical models of ORC plants. This work shows, that with the knowledge of only two thermodynamic parameters of a working fluid, namely, the ideal gas reduced heat capacity $C_p^0/\boldsymbol{R}$ and critical temperature $T_c$, it is possible to estimate a range of ORC plant performance metrics. Both $C_p^0/\boldsymbol{R}$ and $T_c$ have been tabulated for many substances and are widely available. Furthermore, they can be estimated for the remaining working fluids using molecular contribution methods, e.g., by Joback and Reid (1987) and by Poling et al. (2000). In this work, the value of ideal gas heat capacity $C_p^0$ was evaluated at a temperature corresponding to the arithmetic average of the heat sink temperature and the critical temperature of working fluid. The denominator in $C_p^0/\boldsymbol{R}$ denotes a specific gas constant.

This analysis begins with an introduction of the main ORC plant configurations and performance metrics in sections 3.2 and 3.3. Section 3.4 describes the numerical models of ORC plants used in this analysis, and section 3.5 contains the results of these models. In section 3.5.1, detailed results are presented for four ORC plant configurations and heat source temperatures from 100ºC to 230ºC using a single working fluid, R-134a. Section 3.5.2 provides results for same configurations of ORC plants, but using an alternative optimization function. The conclusions from section 3.5.1 are generalized in section 3.5.3 using results for 13 working fluids. Building on these results, various performance metrics of ORC plants are correlated with the thermophysical properties of working fluids in section 3.6. Lastly, section 3.7 quantifies the sensitivity of ORC plants to the heat rejection conditions.

## 3.2 Types of organic Rankine cycle (ORC) power plants

The operating principle of an ORC plant is presented in Figure 3-1.A. Thermal energy carried by a heat source fluid (hs) is transferred in a primary heat exchanger to a low-boiling-point working fluid. The working fluid vapor passes through a turbine where it expands and produces work. The working fluid is then cooled and condensed at a low pressure by dissipating heat to the cooling fluid (cf). After that, the working fluid is pressurized by a pump, and eventually returned to the primary heat exchanger. This cycle can be conveniently presented in pressure-enthalpy (P-h), temperature-enthalpy (T-h), or temperature-entropy (T-s) coordinates. The last set of coordinates (T-s) was chosen in Figure 3-2.A to highlight the near-isentropic expansion and compression processes. The most basic variation of ORC shown in Figure 3-1A and Figure 3-2.A is referred to as a subcritical (Sub) ORC, because the maximum pressure of working fluid is below the working fluid critical pressure $P_c$. The isothermal evaporation of working fluid in subcritical ORCs results in a large temperature mismatch between the heat source and the working fluid. This means that the log-mean temperature difference is large, which results in high irreversibility for the heat transfer process and reduces the maximum work potential (exergy) of the ORC working fluid (Bejan et al., 1996). To reduce this irreversibility and improve turbine power output, the maximum pressure in ORC can be increased above working fluid critical pressure. Such cycles are referred to as supercritical (Sc) ORC, and an example is of such cycle is presented in Figure 3-2.B. As a result of a higher maximum cycle pressure, the work consumed by the pump in supercritical ORC is significantly higher compared to a subcritical ORC, partially offsetting the increased turbine output (Tester and Milora, 1977).

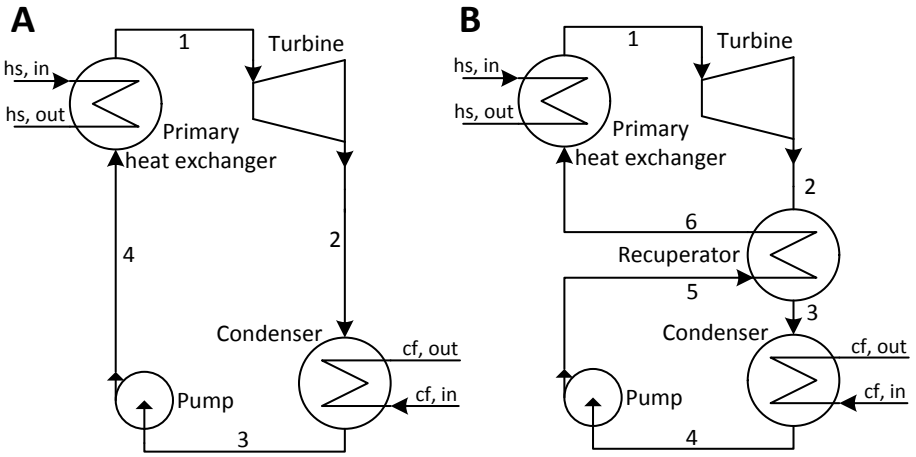


*Figure 3-1: Schematics of Organic Rankine Cycle (ORC) plants. Figure A: ORC plant with no recuperator (NR). Figure B: ORC plant with a heat recuperator (R).*

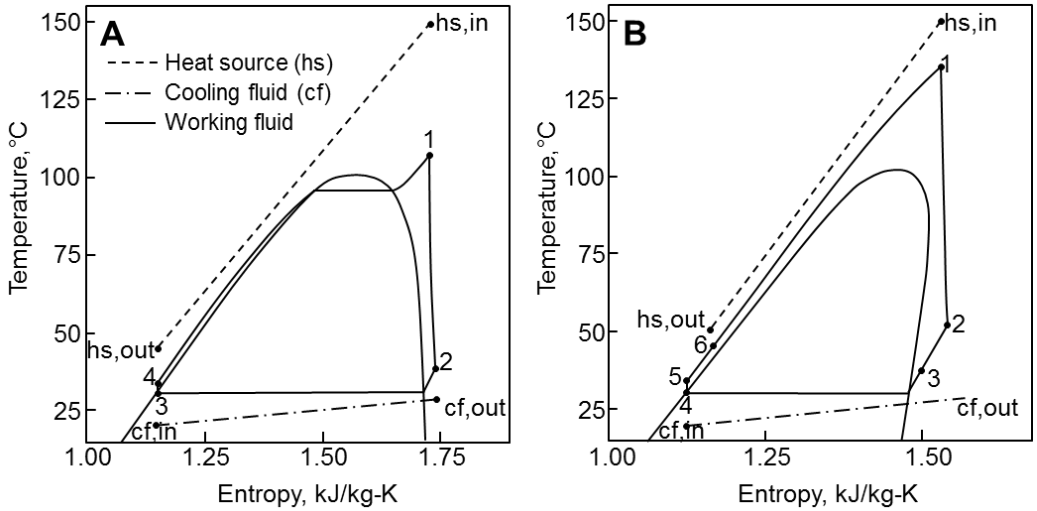


*Figure 3-2: Temperature-entropy (T-s) diagrams of ORC. Figure A: subcritical cycle with no recuperator (Sub-NR) using R-134a. Figure B: supercritical cycle with a recuperator (Sc-R) using R-227ea.*

ORC plants can use an additional heat exchanger called a recuperator. This component is an internal heat exchanger, as shown in Figure 3-1.B, and its effects are presented on a T-s diagram

in Figure 3-2.B. If the vapor at turbine exit (2) is superheated, a recuperator might be used to transfer a fraction of the vapor sensible heat (2→3) to the liquid working fluid (5→6) before it enters the primary heat exchanger. By doing that, the recuperator increases both the temperature of the heat source fluid leaving ORC plant (hs,out) and the thermal efficiency of the cycle (DiPippo, 2012; Invernizzi et al., 2007). However, a sufficient degree of superheat must be available for the recuperator to be practically feasible. In this work, cycles with recuperators are designated with (R) and cycles with no recuperators are abbreviated as (NR).

## 3.3 ORC performance metrics

Three types of efficiency are used in this analysis: utilization efficiency $\eta_u$, thermal efficiency $\eta_{th}$ and, as a reference, thermal efficiency of an ideal triangular cycle $\eta_{th,tri}$. Utilization efficiency, also commonly referred to as exergetic efficiency, is defined as the ratio of the net power output of the plant to the exergy rate of the incoming heat source fluid (DiPippo, 2004):

$$\eta_u = \frac{\dot{W}_{net}}{\dot{E}_{hs,in}} = \frac{\dot{W}_{net}}{\dot{m}_{hs} \cdot \left[h_{hs,in} - h_{hs,0} - T_0\left(s_{hs,in} - s_{hs,0}\right)\right]} \qquad (3\text{-}1)$$

where $\dot{m}_{hs}$ is the mass flow rate of the heat source fluid, $h_{hs}$ and $s_{hs}$ are the entropy and enthalpy, and the subscript *0* refers to the dead state (ambient) conditions. Utilization efficiency quantifies what fraction of the heat source thermodynamic potential is converted into useful work. As such, it can be used as a primary performance metric of ORC units, in which the heat source fluid leaving the plant is not used for any other purpose such as, e.g., district heating.

Thermal efficiency is the ratio of the net power output to the thermal power input into the cycle:

$$\eta_{th} = \frac{\dot{W}_{net}}{\dot{Q}_{in}} = \frac{\dot{W}_{net}}{\dot{m}_{hs} \cdot [h_{hs,in} - h_{hs,out}]} \quad (3\text{-}2)$$

Thermal efficiency determines what fraction of the heat withdrawn from the heat source is converted into electricity. It does not, however, quantify how much heat is taken out from the heat source fluid. Because of that, high thermal efficiency does not always correspond to high net power output. Thermal efficiency is a suitable performance metric for combined heat and power (CHP) plants, which utilize the heat source fluid leaving the ORC plant for direct use applications.

Lastly, the triangular (or trilateral) cycle is used as a reference ideal cycle, against which the thermal efficiencies of ORC plants can be compared (DiPippo, 2007). Triangular cycle is an equivalent of a Carnot cycle for heat sources with a finite and constant heat capacity. The temperature of the heat source fluid in an ideal triangular cycle is brought to the dead state temperature $T_0$ by reversible heat transfer to the working fluid. Thermal efficiency of ideal triangular cycle is expressed as (DiPippo, 2007):

$$\eta_{th,tri} = \frac{T_{hs,in} - T_0}{T_{hs,in} + T_0} \quad (3\text{-}3)$$

where all temperatures are absolute. The ratio of $\eta_{th}$ to $\eta_{th,tri}$ is referred to as relative efficiency $\eta_{rel}$ (DiPippo, 2007).

Other performance metrics used in this work include heat source outlet temperature $T_{hs,out}$, and specific heat exchange area $A_{hex}/P_{net}$. The latter is calculated as a ratio of combined heat transfer area of all heat exchangers in the cycle to the net power output of the ORC plant.

## 3.4 ORC models

### 3.4.1 Structure and assumptions of ORC models

The models of ORC plants used in this analysis were created with a goal to provide realistic performance figures and a fair comparison basis for different working fluids. The ORC plants were modeled in Aspen HYSYS v8.4 using pressure-volume-temperature (PVT) properties from REFPROP v8.0 equations of state (EOS) (Lemmon et al., 2013). Four different configurations of ORC plants were considered:

- Subcritical ORC with no heat recuperator (Sub-NR)
- Subcritical ORC including heat recuperator (Sub-R)
- Supercritical ORC with no heat recuperator (Sc-NR)
- Supercritical ORC including heat recuperator (Sc-R)

Simulations for heat source temperatures between 100ºC and 230ºC were run in 10ºC intervals. The base-case simulations were performed for ORC using a wet cooling tower (WCC), with 17ºC wet bulb temperature $T_0$ providing 20ºC cooling water at the condenser inlet. Additionally, section 3.7 presents sensitivity of the net power output to the dry bulb temperature and relative humidity, along with results for ORC using an air-cooled condenser (ACC). In ACC, the increase in air temperature was set at half of the temperature difference between the working fluid condensing temperature and the inlet air dry bulb temperature, which was previously found to maximize the net power output (Augustine et al., 2009). The dead state conditions for base-case ORC with wet cooling tower were set at 17°C and 1 bara.

Pinch point temperature differences of 3ºC were adopted for all heat exchangers with an exception of the ACC (Lukawski, 2009). The values of overall heat transfer coefficients $U$ for heat exchangers in subcritical cycles are obtained from (Lukawski, 2009), while $U$ for the

primary heat exchanger in supercritical cycles is estimated based on results from (Karellas et al., 2012a, 2012b; Lukawski, 2009). The estimated $U$ values for supercritical cycles suffer from increased uncertainty and should be calculated for each individual plant configuration during the more advanced design phases. The working fluid pressure drops in heat exchangers were ignored. This is also a simplification which should be addressed in final designs.

The isentropic efficiencies of turbines (dry-expansion) and pumps were set at 85% and 75%, respectively. They were assumed to be the same for all working fluids, and the effects of individual fluids properties on the isentropic turbine efficiency were ignored. In addition, the turbine efficiency was decreased if wet expansion occurred. Following the Baumann rule, isentropic efficiency was reduced by 1% for every percentage of average moisture present during expansion (DiPippo, 2012). In addition, the minimum turbine exhaust vapor quality was set at 0.9 to prevent blade erosion.

To enhance the stability of operation and avoid significant fluctuations in PVT properties occurring near the critical point, the maximum evaporation pressure in subcritical cycles was set at 90% of critical pressure $P_c$ (Augustine et al., 2009). In supercritical cycles, the minimum high pressure corresponds to 110% of $P_c$. The summary of the ORC model assumptions is presented in Table 3-1.

*Table 3-1: Summary of base-case ORC model specifications. Configurations denoted with asterisk are evaluated in sensitivity analysis in section 3.7. The reference sources listed in the text and the table provided a rationale for selection of base-case values for each parameter.*

| Design Parameter | Value/Properties |
|---|---|
| **1. Heat source** | |
| Substance | Liquid water |
| Temperature range | 100-230ºC |
| Pressure | 100 bara |
| **2. Heat exchangers** | |
| General characteristics | Countercurrent, single pass, split into 50 intervals with equal Δh |
| **2.1. Primary heat exchanger** | |
| Pinch point temperature difference | 3ºC |
| Hot end temperature approach | ≥5ºC |
| **2.1.1. Subcritical ORC** | |
| Maximum turbine inlet pressure | $0.9*P_c$ |
| Minimum turbine inlet vapor superheat | 1ºC |
| Preheater U | 1.1 kW/(m$^2$K) |
| Evaporator U | 2 kW/(m$^2$K) |
| Superheater U | 0.7 kW/(m$^2$K) |
| **2.1.2. Supercritical ORC** | |
| Minimum turbine inlet pressure | $1.1* P_c$ |
| Primary heat exchanger U | 1.3 kW/(m$^2$K) |
| **2.2. Recuperator (in Sub-R and Sc-R configurations)** | |
| Pinch point temperature difference | 3ºC |
| Recuperator U | 0.7 kW/(m$^2$K) |
| **2.3. Condenser and heat rejection system** | |
| **2.3.1. Water-cooled condenser with wet cooling tower (WCC) – base case** | |
| **Condenser** | |
| Pinch point temperature difference | 3ºC |
| Cooling water inlet temperature | 20ºC (6-34ºC)* |
| Cooling water temperature rise | 8ºC (Hensley, 2009) |
| Desuperheater U | 0.7 kW/(m$^2$K) |

| | |
|---|---|
| Condenser U | 1.6 kW/($m^2$K) |
| **Wet cooling tower** | |
| Inlet air dry bulb temperature | 24ºC (10-35ºC)* |
| Relative humidity of entering air | 50% (25%, 75%)* |
| Relative humidity of exiting air | 98% |
| Approach to wet bulb temperature | 3ºC (ASHRAE, 2010) |
| Wet bulb temperature rise | 7 ºC |
| Pressure rise of cooling fan | 170 Pa (Lukawski, 2009; Monroe, 1974) |
| Isentropic efficiency of fan | 0.65 (Lukawski, 2009) |
| Isentropic efficiency of circulation pump | 0.75 |
| Cooling water pressure drop | 1.5 bar |
| **2.3.2. Air-cooled condenser (ACC)*** | |
| Inlet air dry bulb temperature | 10-35ºC* |
| Air temperature rise | 0.5*($T_{cond}$-$T_{air,in}$) (Augustine et al., 2009) |
| Power consumption | 0.25 kW per kg/s of air flow<br>(Augustine et al., 2009; Manente et al., 2011) |
| **3. Expander** | |
| Isentropic efficiency | 85% for vapor-only expansion<br><85% when liquid present – Baumann rule<br>(Augustine et al., 2009) |
| Minimum exhaust vapor quality | 0.9 (Augustine et al., 2009) |
| Generator efficiency | 98% (Augustine et al., 2009) |
| **4. Working fluid pump** | |
| Isentropic efficiency | 75% (DiPippo, 2012) |

### 3.4.2 Optimization

All ORC plants were optimized with a goal of maximizing their utilization efficiency $\eta_u$, which is equivalent to maximizing their specific power output ($kW_e$ per kg/s of heat source fluid), for the given heat source inlet conditions. The BOX method available in Aspen HYSYS was used for this purpose (Aspen Technology, 2011). This method is based on the complex method by

Box (Box, 1965), the Downhill Simplex algorithm (Press et al., 1988), and the BOX algorithm (Kuester and Mize, 1973). The BOX algorithm is a slow, but robust method of finding the extrema of functions. It can also accommodate inequality constraints, such as minimum turbine exhaust vapor quality, or minimum heat source outlet temperature. The reliability of the optimization method was confirmed by systematically varying the initial values of the optimized variables and running the algorithm. The models always converged to the same solutions, independent of the initial values of the optimized variables.

Different variables were optimized depending on the type of cycle. In subcritical ORC models they included evaporation temperature, condensation pressure, and the difference between turbine inlet temperature and evaporation temperature, i.e., the turbine inlet superheat. In supercritical ORCs, optimized variables were: turbine inlet temperature, turbine inlet pressure and condensing pressure. The turbine exhaust vapor quality was constrained by the optimization procedure to values $\geq 0.9$.

### 3.4.3 Selection of working fluids

Working fluids were selected based on their availability, cost, and effects on health and environment. They were also chosen to represent a range of critical temperatures (66-174ºC), slopes of vapor saturation line (corresponding to wet, isentropic, and dry expansion), and several families of compounds (HFCs, HCFCs, PFCs, alkanes, and cycloalkanes). Table 3-2 lists the working fluids investigated in this analysis along with selected properties including: critical temperature ($T_c$) and pressure ($P_c$); molar mass ($M$); reduced ideal gas heat capacity ($C_p^0/\boldsymbol{R}$) evaluated at the average of working fluid critical temperature and the heat sink temperature; indication of fluid behavior during isentropic expansion (wet/isentropic/dry);

boiling point at atmospheric pressure ($T_{sv}$), ozone depletion potential (ODP), global warming potential (GWP), and fluid safety group according to the ASHRAE classification. The list includes high-GWP refrigerants such as R-134a or R-125 which, although still in common use, are phased down in the European Union and other countries (European Commision, 2016; Ingersoll Rand, 2014). They are expected to be replaced by the low-GWP working fluids listed in Table 3-2, such as propane, isobutane, and R-152a.

As indicated by the normal boiling point, none of the working fluids would create vacuum in condenser as long as condensing temperatures exceed 25ºC. This conservative design reduces the risk of air leakage into the system, and thus potential performance issues. In ASHRAE 34 standard, 'A' denotes low toxicity and '1', '2', and '3' indicate no flame propagation, lower flammability, and higher flammability, respectively. It should be noted that R-236ea has not been considered for supercritical configurations due to the limited range of EOS implemented in the REFPROP database.

*Table 3-2: Working fluids used in ORCs and their selected properties (ASHRAE, 2008; Calm and Hourahan, 2011; IPCC, 2007; Linde, 2015; Shengjun et al., 2011; UNEP, 2006).*

| Name | $T_c$ (°C) | $P_c$ (bar) | M (g/mol) | $C_p^0/R$ | Expansion type | $T_{sv}$ at 1 bar (°C) | ODP | GWP (100yr) | Safety group |
|---|---|---|---|---|---|---|---|---|---|
| R-125 | 66.0 | 36.2 | 120.0 | 11.8 | Wet | -48.4 | 0 | 3500 | A1 |
| R-218 | 71.9 | 26.4 | 188.0 | 18.5 | Dry | -37.1 | 0 | 8830 | A1 |
| R-143a | 72.7 | 37.6 | 84.0 | 9.8 | Wet | -47.5 | 0 | 4470 | A2 |
| R-32 | 78.1 | 57.8 | 52.0 | 5.4 | Wet | -51.9 | 0 | 675 | A2 |
| Propane | 96.7 | 42.5 | 44.1 | 9.6 | Wet | -42.4 | 0 | 3 | A3 |
| R-134a | 101.1 | 40.6 | 102.0 | 11.0 | Isentropic | -26.4 | 0 | 1430 | A1 |
| R-227ea | 102.8 | 29.3 | 170.0 | 17.5 | Dry | -16.7 | 0 | 3220 | A1 |
| R-152a | 113.3 | 45.2 | 66.1 | 8.9 | Wet | -24.3 | 0 | 124 | A2 |

| | | | | | | | | | |
|---|---|---|---|---|---|---|---|---|---|
| C3H6 | 125.2 | 55.8 | 42.1 | 7.9 | Wet | -32.8 | 0 | 20 | - |
| Isobutane | 134.7 | 36.3 | 58.1 | 13.4 | Dry | -12.1 | 0 | 20 | A3 |
| R-142b | 137.1 | 40.6 | 100.5 | 11.1 | Isentropic | -9.4 | 0.07 | 2310 | A2 |
| R-236ea | 139.3 | 34.2 | 152.0 | 17.0 | Dry | 5.9 | 0 | 1370 | - |
| R-245ca | 174.4 | 39.3 | 134.1 | 16.7 | Dry | 24.8 | 0 | 693 | A1 |

The reduced ideal gas heat capacity $C_p^0/\boldsymbol{R}$ is related to the slope of vapor saturation line on a T-s diagram and therefore affects the phase composition of the working fluid at turbine exhaust. Fluids with low $C_p^0/\boldsymbol{R}$ (<11) have a conventional Gaussian-like saturation curve, and isentropic expansion of saturated vapor results in a 2-phase mixture. Such working fluids are referred to as 'wet' and are represented in Figure 3-3 by R-32 and R-152a. 'Dry' working fluids such as R-227ea have high $C_p^0/\boldsymbol{R}$ (>11) and retrograde vapor saturation lines resulting in superheated vapor at the turbine exhaust. The fluids with $C_p^0/\boldsymbol{R}$ of approximately 11 have nearly vertical vapor saturation lines. These fluids are referred to as 'isentropic'.

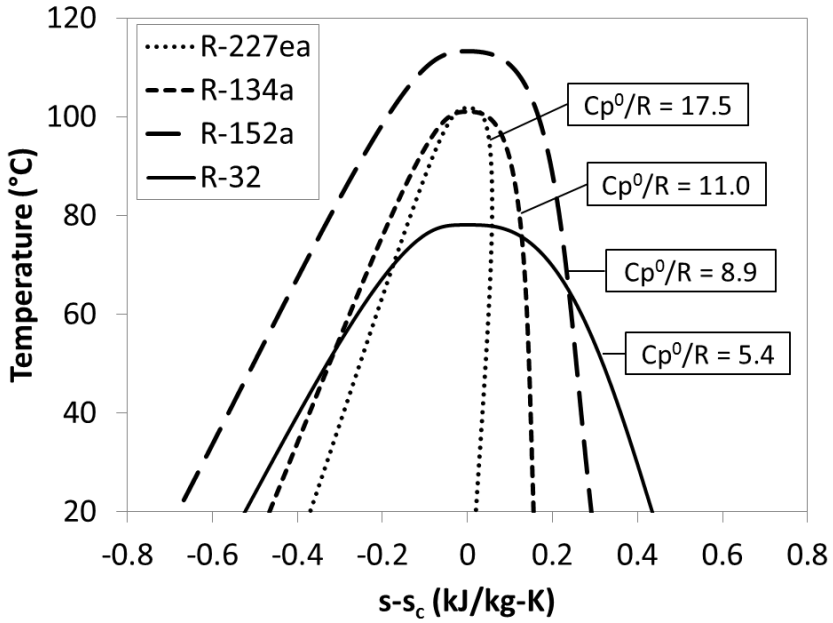


*Figure 3-3: Example of four working fluids representing a range of reduced ideal gas heat capacities $C_p^0/\boldsymbol{R}$. Dry working fluids with retrograde vapor saturation lines have high $C_p^0/\boldsymbol{R}$ (>11) and wet working fluids with Gaussian-shaped saturation lines have low $C_p^0/\boldsymbol{R}$ (<11).*

## 3.5 Results

The ORC models were validated by comparing their results with published values from an earlier study (Augustine et al., 2009). For this purpose, the heat rejection system and heat source parameters were modified to be consistent with those used in the previous analysis. For most configurations, the net power output reported in this work was 3-5% higher as a result of small differences in assumed efficiencies of individual ORC components. In one case, it was 15% higher as a result of finding better operating conditions corresponding to the global utilization efficiency maximum.

In addition, to examine the effects of various equations of state, the results obtained using REFPROP EOS were compared to those produced with other EOSs for a set of five common working fluids and all four investigated cycle configurations. REFPROP database contains high-accuracy, multiparameter EOSs based on Helmholtz free energy. The mean average percentage difference in net power output as compared to REFPROP EOS was: 1.1% for Peng-Robinson (PR), 1.4% for Soave-Redlich-Kwong (SRK), and 0.3% for Benedict-Webb-Rubin-Starling (BWRS). The relatively small differences in results obtained with various EOSs suggest that BWRS EOS can be used for the examined working fluids, temperatures, and pressures, if the REFPROP database is not available and the cubic EOS can be used for working fluid screening purposes. The accuracy of the examined EOS would likely be lower for many less common working fluids, which have not been examined in this work (Lemmon et al., 2013).

### 3.5.1 Detailed results for ORCs using R-134a working fluid

The selected parameters of optimized ORCs are presented in Figure 3-4 (A-H) using an example of R-134a working fluid. The conclusions, however, are broader and representative of the range of fluids explored in this work.

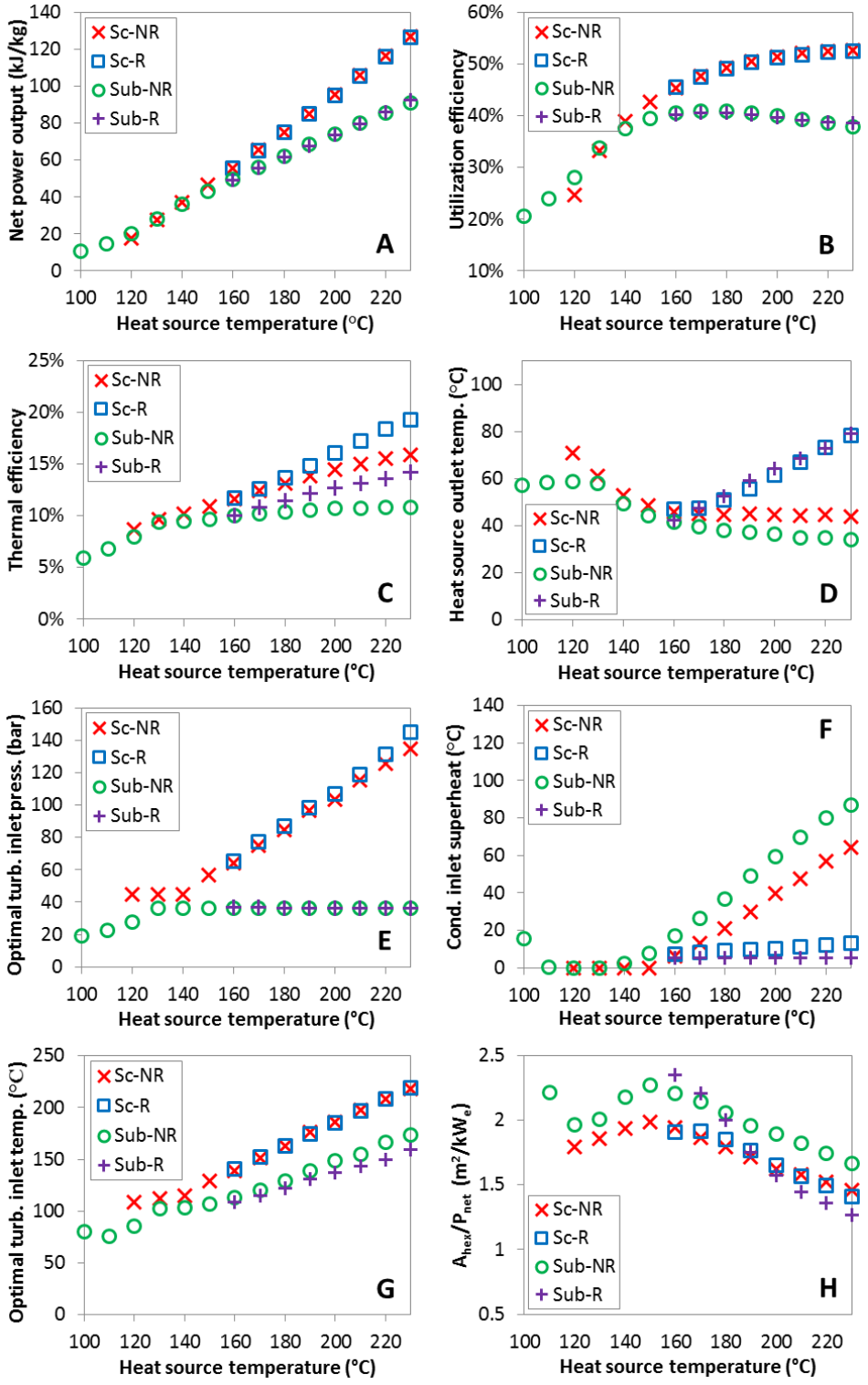


*Figure 3-4: (A-H) Selected parameters of four ORC plant configurations using R-134a are presented as functions of the heat source temperature. The cycles were optimized to maximize*

*the utilization efficiency for each resource temperature. The net power output in (A) is expressed per unit mass flow rate of the heat source fluid.*

As shown in Figure 3-4.A, supercritical cycles provide higher power output than subcritical ORC at medium and high heat source temperatures (e.g., for R-134a >140°C). This was not true at lower heat source temperatures less than 20 to 40°C above the working fluid critical temperature. The increased net power output of supercritical cycles translates into higher utilization efficiency presented in Figure 3-4.B. For R-134a the utilization efficiencies for subcritical and supercritical ORC achieve their respective maxima at different fluid heat source temperatures, namely, 175°C and 250°C, respectively. This feature is true for all working fluids. Furthermore, for any particular working fluid, the optimum temperature is always higher for supercritical cycles. This optimum heat source temperature is denoted as $T_{hs}$*.

In addition to higher utilization efficiency, supercritical cycles typically provide higher thermal efficiency than subcritical ORC, as shown in Figure 3-4.C. As a direct consequence of that, supercritical cycles can provide increased heat source outlet temperatures despite their higher net power outputs. In other words, supercritical ORCs not only produce more power than subcritical cycles, but do so while withdrawing less thermal energy from the heat source.

In the majority of the optimized cycles, temperature pinch (the lowest difference between the temperatures of two streams) occurs close to the cold end of primary heat exchanger. As a result, the heat source fluid is cooled to low temperatures, which may be troublesome in some applications. For example, in geothermal power plants excessive cooling of brine may induce scaling and reduce the heat transfer coefficient of the primary heat exchanger. In waste heat recovery applications, cooling gaseous heat sources below their dew points would lead to

condensation of corrosive liquids necessitating the use of more expensive materials in the preheater. These issues can be alleviated by installing a heat recuperator. Figure 3-4.C and Figure 3-4.D show that addition of heat recuperator results in increased thermal efficiency and heat source outlet temperature. The positive effects of using a recuperator increase with the heat source temperature and are higher in subcritical cycles compared to supercritical cycles. In supercritical ORCs, the higher pump pressure ratio results in a larger temperature increase across the pump. Because of that, less energy can be recovered from the superheated vapor leaving the expander in Sc-R cycles compared to Sub-R configurations.

The optimal turbine inlet pressures are presented in Figure 3-4.E. In subcritical cycles, turbine inlet pressure increases with the heat source temperature until it reaches the maximum allowable reduced pressure $P_r$ of 0.9. In supercritical cycles, optimum turbine inlet pressure corresponds to the minimum allowed $P_r$ of 1.1 at low heat source temperatures and increases if sufficiently high heat source temperatures (>140°C for R-134a) are available. The nearly linear increase in pressure for supercritical cycle at heat source temperatures from 140 to 200°C is an extension of the same trend for subcritical cycle from 100 to 130°C.

The implementation of the Baumann rule generally resulted in avoiding wet turbine expansions. In subcritical ORC, all optimized configurations have either saturated or superheated vapor at turbine exhaust. At low heat source temperatures (for R-134a <130°C), the optimization procedure selected a sufficient turbine inlet superheat to obtain saturated vapor at turbine exhaust. At higher heat source temperatures, turbine exhaust vapor becomes superheated. The optimal turbine inlet and outlet temperatures increase nearly linearly with the heat source temperature, as shown in Figure 3-4.G and Figure 3-4.F. In supercritical ORCs, there can be moisture present in turbine's exhaust if the heat source temperature is very low (e.g., for R-

134a <130°C). In these cases, however, supercritical cycles always provide lower power output than subcritical ORC and therefore would not be selected over the basic subcritical cycle.

Because supercritical cycles almost always provide a better temperature match between the heat source fluid and the organic working fluid, it is often thought that they require larger overall heat exchanger area compared to subcritical ORCs. Figure 3-4.H illustrates that the opposite is true. Subcritical ORCs have higher specific heat exchange area $A_{hex}/P_{net}$, which is defined as the ratio of the total heat transfer area of all heat exchangers in the cycle to the net power output. The high $A_{hex}/P_{net}$ in subcritical ORC is caused by the very large size of the preheater. To maximize the power output, optimization selects high evaporation pressures in subcritical ORCs, thus providing a very close temperature match in preheater (log-mean temperature difference, LMTD typically between 4 and 6ºC). Supercritical cycles provide a close temperature match between heat source and working fluid as well, but it is more uniformly distributed across the whole primary heat exchange path resulting in lower overall heat transfer area required. Interestingly, adding a recuperator to a subcritical cycle results in a decrease in the specific heat exchanger area. Despite being an added component, the recuperator reduces the duty of both the condenser and the preheater. Because the log-mean temperature difference of the recuperator is much higher than the preheater, this results in a lower total heat transfer area.

### 3.5.2 Results for ORCs using R-134a with an alternative objective function

To assess whether the larger heat transfer areas required by subcritical cycles are a result of specific assumptions made in this work, or a more general trend, an alternative optimization function was considered. While the remaining part of this chapter shows results for ORC plants

designed to maximize their utilization efficiency $\eta_u$, in this section the optimization procedure was set to minimize the specific heat exchanger area $A_{hex}/P_{net}$ instead.

Figure 3-5 shows, that even when using the minimum specific heat exchanger area as an optimization goal, supercritical cycles retain their advantages over subcritical ORCs in the form of higher net power output at most heat source temperatures and an increased thermal efficiency. Supercritical cycles also yield lower specific heat exchanger areas $A_{hex}/P_{net}$ as shown in Figure 3-5.H. This proves that the optimized subcritical cycles have large preheaters, even if the optimization procedure is set to reduce the heat exchanger sizes.

A comparison of Figure 3-4 and Figure 3-5 highlights the effects of using different objective functions to optimize the ORC plant design. Using minimum specific heat exchanger area instead of maximum utilization efficiency results, on average, in 19% drop in $A_{hex}/P_{net}$. This drop is accompanied by 10% average decrease in the net power output. Using minimum specific heat exchanger area as optimization function may be feasible if the heat input to the cycle is free as e.g. in a waste heat recovery plant. It would not be suitable, however, for geothermal power plants where the costs associated with extracting geothermal fluids are significant and the heat exchangers contribute a small fraction of the total system cost.

The operating parameters of cycles with minimum specific heat transfer areas $A_{hex}/P_{net}$ are quite different than for cycles with maximum utilization efficiency. The turbine inlet pressures in Figure 3-5 are much lower compared to Figure 3-4 and the turbine inlet temperatures are higher. As a result, cycles with minimum $A_{hex}/P_{net}$ have more superheat present at turbines exhaust. In configurations with recuperator, this either reduces the size of preheater or entirely eliminates it and the working fluid is preheated in recuperator. In supercritical cycles, low turbine inlet

pressures shown in Figure 3-5 increase the LMTD of preheater and reduce its size. In addition, cycles optimized for minimum $A_{hex}/P_{net}$ experience great increase in thermal efficiency if equipped with heat recuperator. Such cycles withdraw less heat from the heat source, but larger portion of this heat is converted into electricity. That makes them an interesting solution for combined heat and power (CHP) plants. For ORCs using R-134a with recuperator, the heat source outlet temperatures are in the 70-100ºC range, sufficiently high for many district heating systems.

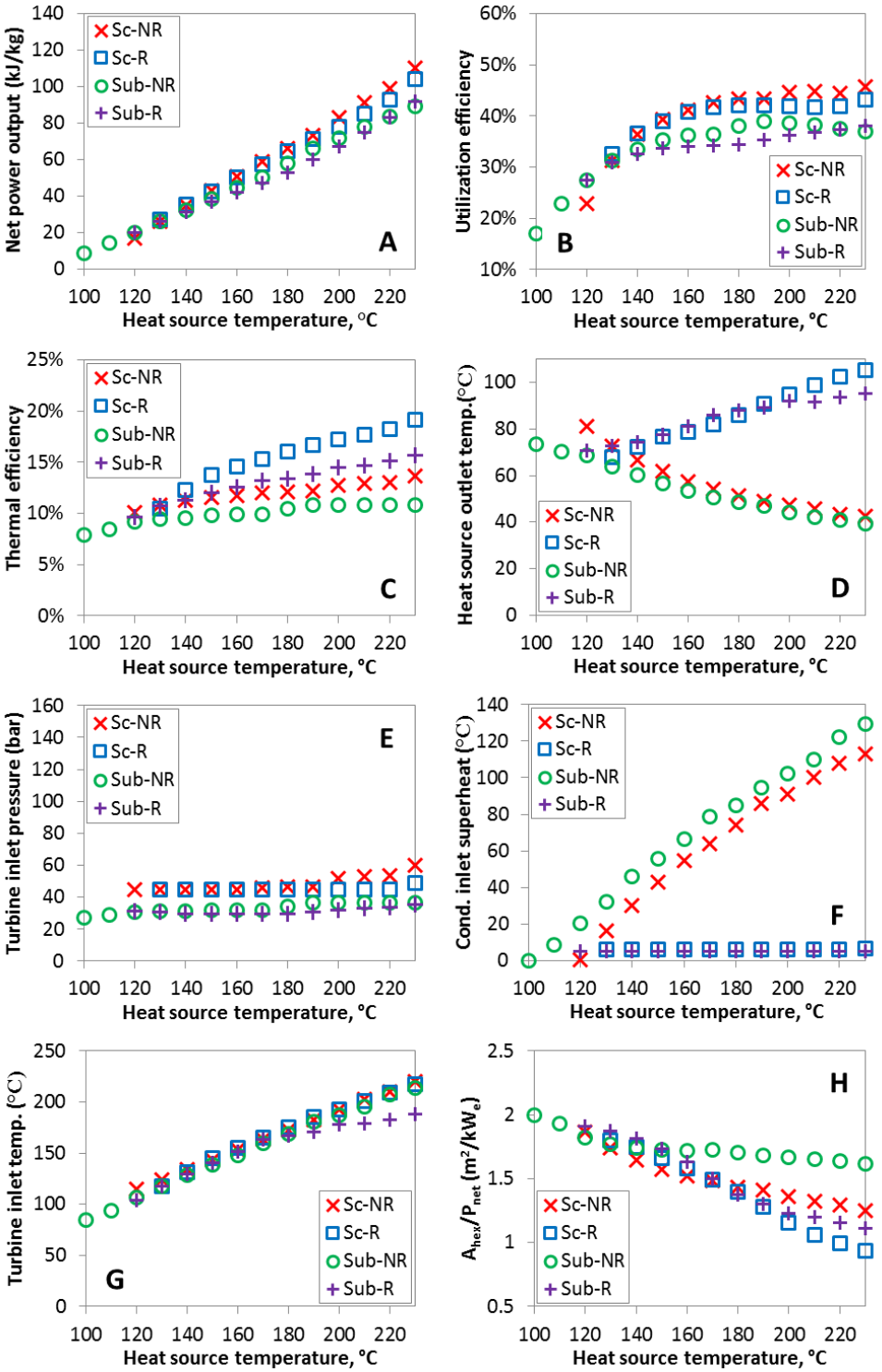


*Figure 3-5: (A-H) Selected parameters of four ORC plant configurations using R-134a are presented as functions of the heat source temperature. In contrast to Figure 3-4 and the rest of this article, these cycles were optimized to minimize the specific heat exchange area $A_{hex}/P_{net}$.*

### 3.5.3 Generalized results for multiple working fluids

The analysis described in the section 3.5.1 was performed for all 13 working fluids listed in Table 3-2. Figure 3-6 and Figure 3-7 show the utilization efficiencies of various working fluids as functions of heat source temperature for Sub-NR and Sc-NR cycles, respectively. Dotted and dashed lines mark the composite curves of maximum utilization efficiency for Sub-NR and Sc-NR cycles, respectively. In the considered temperature range, the most efficient Sc-NR cycles provide between 1% and 17%, and on average 7.5% higher utilization efficiency compared to the best Sub-NR cycles. The utilization efficiency curves for supercritical ORC are also less convex compared to the subcritical cycle. As a result, a single working fluid may be used near-optimally in a supercritical ORC over a broader range of heat source temperatures without sacrificing much in utilization efficiency. Fluids with high ideal gas reduced heat capacities $C_p^0/\boldsymbol{R}$ (R-218, R-227ea, R-236ea, R-245ca) yield higher utilization efficiencies compared to fluids with low $C_p^0/\boldsymbol{R}$ (R-32, R-152a, cyclopropane), particularly in the subcritical cycle.

The composite curves of maximum utilization efficiency 'Max Sub-NR' and 'Max Sc-NR' are composed of results for eight best performing working fluids. However, four working fluids (R-218, R-227ea, isobutane, and R-245ca) are sufficient to provide very high utilization efficiencies across the considered temperature spectrum. Some of the assessed low-GWP fluids (isobutane, R-142b, R-152a) perform well at heat source temperatures between 160 and 200°C, but they cannot match the performance of R-227ea and R-218 at low heat source temperatures and R-245ca above 200°C.

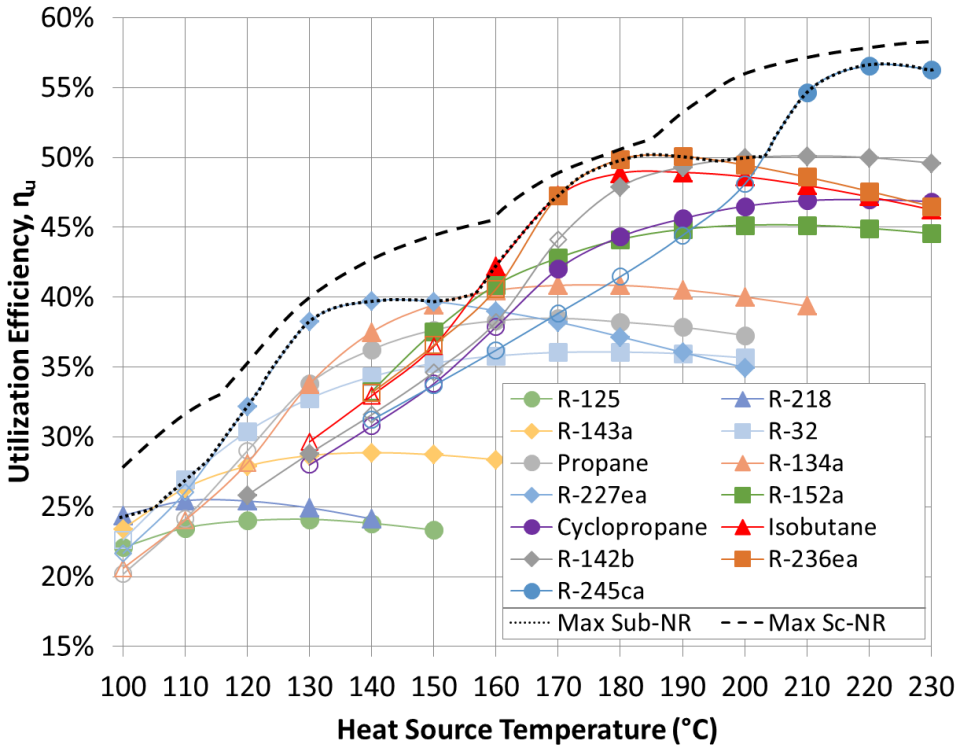


*Figure 3-6: Utilization efficiency of subcritical ORC with no recuperator (Sub-NR) using various working fluids. Filled markers represent configurations where turbine inlet pressure reached 0.9 of fluid critical pressure while empty markers represent cycles with optimal reduced turbine inlet pressures below 0.9. Dead state conditions $T_0$ and $P_0$ are 17°C and 1 bara.*

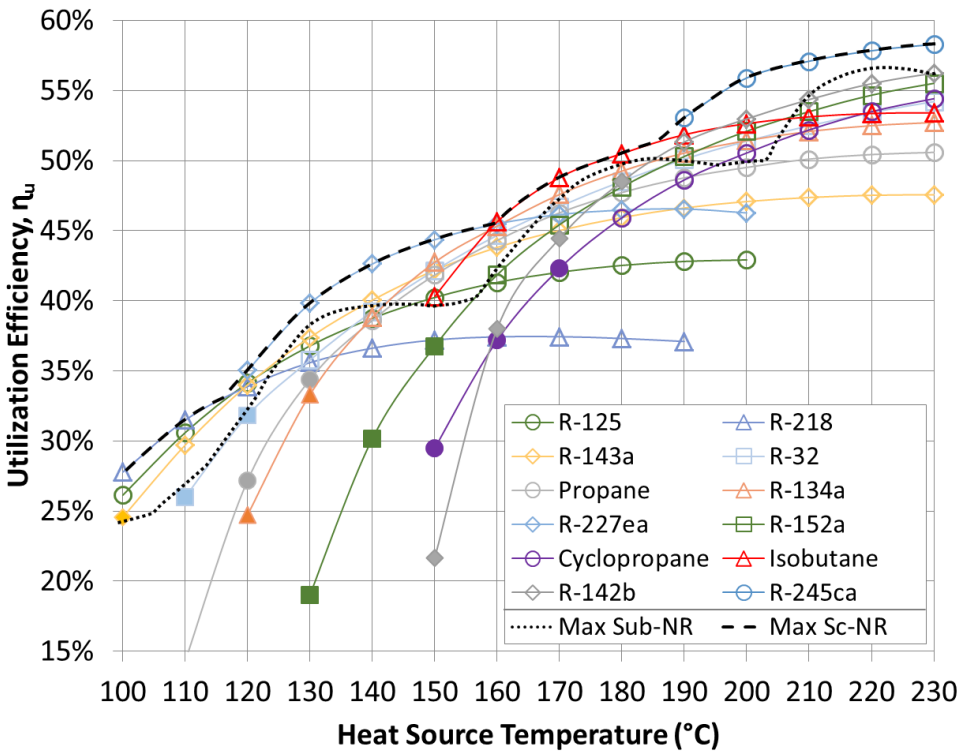


*Figure 3-7: Utilization efficiency of supercritical ORC with no recuperator (Sc-NR) using various working fluids. Filled markers represent configurations where optimal reduced turbine inlet pressure is 1.1, while empty markers represent cycles with reduced turbine inlet pressure above 1.1. Dead state conditions $T_0$ and $P_0$ are 17°C and 1 bara.*

For all of the heat source temperatures from 100 to 230 °C, the top-performing fluids in subcritical ORCs showed maximum utilization efficiencies when the reduced turbine inlet pressure was 0.9. This high evaporation pressure reduces exergy loss in the primary heat exchanger by providing a better temperature match in preheater and a lower enthalpy of vaporization. Configurations where the reduced turbine inlet pressure reached 0.9 are represented in Figure 3-6 with filled markers, while empty markers denote lower turbine inlet pressures. Depending on the working fluid used, reduced turbine inlet pressure of 0.9 is

achieved at absolute heat source temperatures of at least 1.06*$T_c$ to 1.09*$T_c$. This means, that in order to pre-screen fluids for maximum utilization efficiency in subcritical ORCs, it is enough to consider fluids with sufficiently low critical temperature and set their evaporation pressure at 90% of their critical pressure. The high evaporation pressures of well-performing subcritical ORCs also emphasize the need for an accurate determination of thermophysical fluid properties near their critical points.

For supercritical ORCs to reach high efficiency operation, the situation was different than for subcritical cycles. The supercritical ORCs reached their optimal performance when the reduced turbine inlet pressures were above 1.1. To illustrate this, cycles with optimal reduced turbine inlet pressures of 1.1 are indicated in Figure 3-7 by full markers and cycles with higher turbine inlet pressures are represented with empty markers.

The utilization efficiencies of the top-performing cycles with recuperators are not shown because they are typically only 0.5% lower than for cycles without recuperators. This small drop in power output is a combination of two factors: 1) a larger decrease in power due to shifting the location of the pinch point in the condenser leading to an increase in condensing pressure, and 2) a smaller increase in power due to the lower condenser duty and the resulting lower parasitic power consumption of the cooling tower. In actual plants, the power output of cycles with a recuperator would be even lower due to the pressure loss in the recuperator and resulting increased turbine backpressure. Depending on the working fluid used, each 0.1 bar increase in turbine backpressure would cause between 0.2% (for R-32) to 1.6% (for R-245ca) drop in utilization efficiency. The effects of pressure loss in recuperator would be more significant for fluids with high critical temperatures, which typically have low condensing pressures and high turbine exhaust volumetric flow rates.

Figure 3-8 shows the thermal efficiency of ORC plants with the highest utilization efficiencies. For each heat source temperature, thermal efficiency of both subcritical and supercritical cycles were presented for a comparison. ORC plants using a heat recuperator were included if the equivalent non-recuperated cycles had sufficiently hot turbine exhaust gases to transfer heat to the pressurized liquid working fluid. Thermal efficiency of ORC plants with a recuperator was on average 6.5% higher compared to equivalent cycles without recuperator. The increase in thermal efficiency was particularly high for dry fluids with high $C_p^0/\boldsymbol{R}$ and for heat source temperatures much above fluid critical temperature. As shown in the next section, the effects of adding a heat recuperator can be in fact predicted based on these three parameters: $C_p^0/\boldsymbol{R}$, $T_c$, and $T_{hs}$.

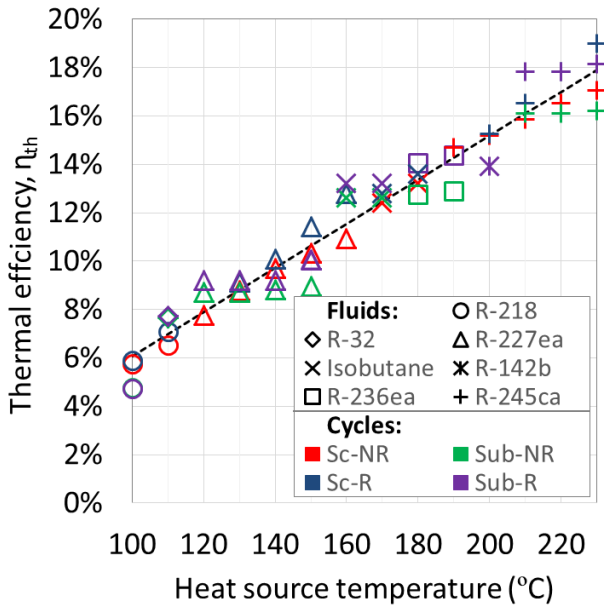


*Figure 3-8: Thermal efficiency of sub- and supercritical ORCs with and without heat recuperator as a function of heat source temperature. Results are presented only for working fluids with the highest utilization or exergetic efficiency for each heat source temperature. Marker colors indicate the types of cycles and the shapes determine the working fluids.*

The thermal efficiencies of ORC cycles were approximated in Figure 3-8 with the following linear trend:

$$\eta_{th} = 9.09 \cdot 10^{-4} \cdot T_{hs} - 0.03 \qquad (3\text{-}4)$$

where $T_{hs}$ is the heat source temperature in °C and the efficiency is given as a fraction. The fitted trend has a regression coefficient $R^2$ of 0.95 and a standard deviation of 0.8%. The thermal efficiencies of 5% to 19% presented in Figure 3-8 correspond to relative efficiencies $\eta_{rel}$ of 42% to 73% with an average of 63%. This figure is consistent with the reported 61% average relative efficiency of three existing ORC geothermal power plants using wet cooling towers (DiPippo, 2007). The relative efficiency of ORC plants increases with the heat source temperature, as the parasitic power losses and other irreversibilities contribute a smaller fraction of the heat input to the cycle.

## 3.6 Correlations between ORC performance and working fluid properties

Given the large number of potential ORC working fluids, it is useful to develop guidelines for their selection. Such guidelines could help to pre-screen working fluids for applications at specific heat source temperatures. This insight would be particularly helpful in analyzing less common fluids, for which the EOS are unavailable or inaccurate, making both numerical modeling of ORC and plant design a challenge. This section presents correlations for evaluating a number of ORC performance metrics based on the heat source temperature $T_{hs}$, the working fluid critical temperature $T_c$, and the ideal gas reduced heat capacity $C_p^0/\boldsymbol{R}$. This is the main and most novel contribution of this work. The correlated performance metrics include: heat source

temperature at which utilization efficiency is maximized $T_{hs}$*, sensitivity of utilization efficiency to the changes in heat source temperature, and the increase in both thermal efficiency $\eta_{th}$ and heat source outlet temperature $T_{hs,out}$ due to the addition of a heat recuperator. The last three correlations are new to this work.

Figure 3-6 and Figure 3-7 showed that each working fluid achieves its maximum utilization efficiency at a specific heat source temperature $T_{hs}$*. Following the methodology established by Tester and Milora (Tester and Milora, 1977), Figure 3-9 shows that the temperature $T_{hs}$* is strongly correlated with $C_p^0/\boldsymbol{R}$ and $T_c$ of the working fluid. Knowing both $C_p^0/\boldsymbol{R}$ and the critical temperature, one can accurately determine $T_{hs}$*. Supercritical cycles achieve their maximum utilization efficiencies at much higher heat source temperatures than subcritical ORC, especially when using wet working fluids such as R-32 or R-152a. The results for subcritical and supercritical cycles were approximated in Figure 3-9 with linear trends described by the following equation:

$$T_{hs}^* - T_c = a \cdot \frac{C_p^0}{R} + b \qquad (3\text{-}5)$$

Where constants *a* and *b* are: -4.5 and 121.5 for Sub-NR cycle and -9.73 and 250.7 for Sc-NR cycle, respectively. The trends fitted to data in Figure 3-9 provide reasonable $R^2$ values of 0.9 and 0.87 and standard deviations of 6.4°C and 15.3°C, respectively.

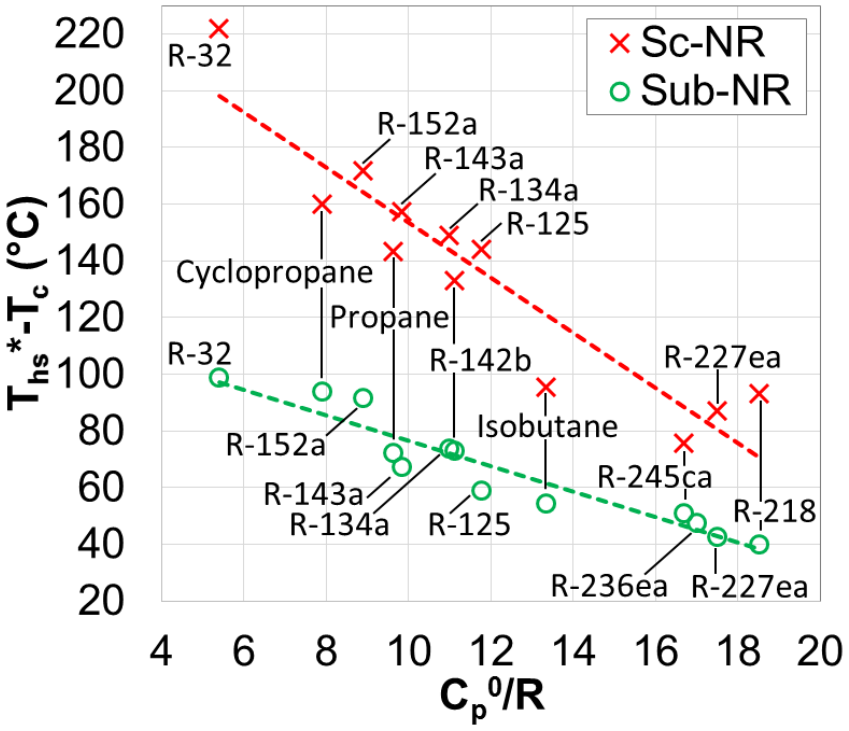


*Figure 3-9: Heat source temperatures $T_{hs}$* (relative to critical temperature $T_c$) at which the utilization efficiency is maximized for various working fluids. Results for subcritical (Sub-NR) and supercritical (Sc-NR) cycles are presented as functions of reduced ideal gas heat capacity $C_p^0/\boldsymbol{R}$.*

The scatter in results presented in Figure 3-9 is partially due to the assumption of an equal condenser pinch point temperature difference for all working fluids. This assumption led to small variations in the condensing temperatures of individual working fluids, a result of unequal vapor superheat at condenser inlet for different working fluids. The impact of this scatter is small, because the utilization efficiency curves presented in Figure 3-6 and Figure 3-7 are relatively flat near their maxima. If fact, utilization efficiencies at heat source temperatures predicted by the linear trends in Figure 3-9 are on average only 0.4% lower compared to the maximum utilization efficiencies obtained at $T_{hs}$*.

In this work, $C_p^0/\boldsymbol{R}$ of each working fluid was evaluated at a representative temperature corresponding to the arithmetic average of the heat sink temperature and fluid critical temperature. This temperature was selected to be consistent with the average slope of the vapor saturation line along turbine expansion path. Evaluating $C_p^0/\boldsymbol{R}$ at either the heat sink temperature or the critical temperature results in similar trends with average $R^2$ values of 0.83 and 0.89, respectively. The reduced ideal gas heat capacity proved to be a much better predictor of $T_{hs}$* than acentric factor or molar mass, for which equivalent correlations yielded $R^2$ values of only 0.18 and 0.55, respectively.

In addition to predicting the optimal heat source temperature $T_{hs}$*, the reduced ideal gas heat capacity allows one to estimate the utilization efficiency achieved at $T_{hs}$*, and the relative decrease in utilization efficiency which occurs if the heat source temperature is below or above $T_{hs}$*. Figure 3-6 showed that for subcritical ORCs, dry fluids with $C_p^0/\boldsymbol{R}$ above 11 (e.g., R-218, R-227ea, R-236ea, R-245ca) achieve higher utilization efficiencies, but over a narrower range of heat source temperatures. Wet fluids characterized by low $C_p^0/\boldsymbol{R}$ less than 11 (e.g., R-32, cyclopropane, R-152a) show lower, but more constant utilization efficiencies.

In Figure 3-10, the utilization efficiency of each working fluid in subcritical ORCs is presented at heat source temperatures 20°C above and 20°C below $T_{hs}$*. The utilization efficiencies are expressed as a percentage of the maximum utilization efficiency achieved at $T_{hs}$*, and presented as function of $C_p^0/\boldsymbol{R}$. At heat source temperatures 20°C below $T_{hs}$*, fluids with high $C_p^0/\boldsymbol{R}$ achieve only 88-92% of their maximum utilization efficiency, while fluids with low $C_p^0/\boldsymbol{R}$ achieve approximately 99% of their maximum utilization efficiency. For dry fluids, reducing the heat source temperature by 20ºC below $T_{hs}$* results in a poorer temperature match in the preheater, and thus less heat recovered from the heat source and a lower utilization efficiency.

An equivalent drop in the heat source temperature has a much smaller effect on the effectiveness of heat recovery in ORCs using wet working fluids. This discrepancy is due to the difference in optimal configurations of ORC plants using heat input at temperature $T_{hs}$*. Wet fluids require significant vapor superheat at turbine inlet and their evaporation temperature is much below the heat source temperature $T_{hs}$*, while dry fluids require little to no superheat, and their evaporation temperature is closer to $T_{hs}$*. Figure 3-10 shows, that at heat source temperatures 20°C above $T_{hs}$*, the decrease in utilization efficiency is far less significant than 20°C below $T_{hs}$*, but it is also correlated with $C_p^0/\boldsymbol{R}$.

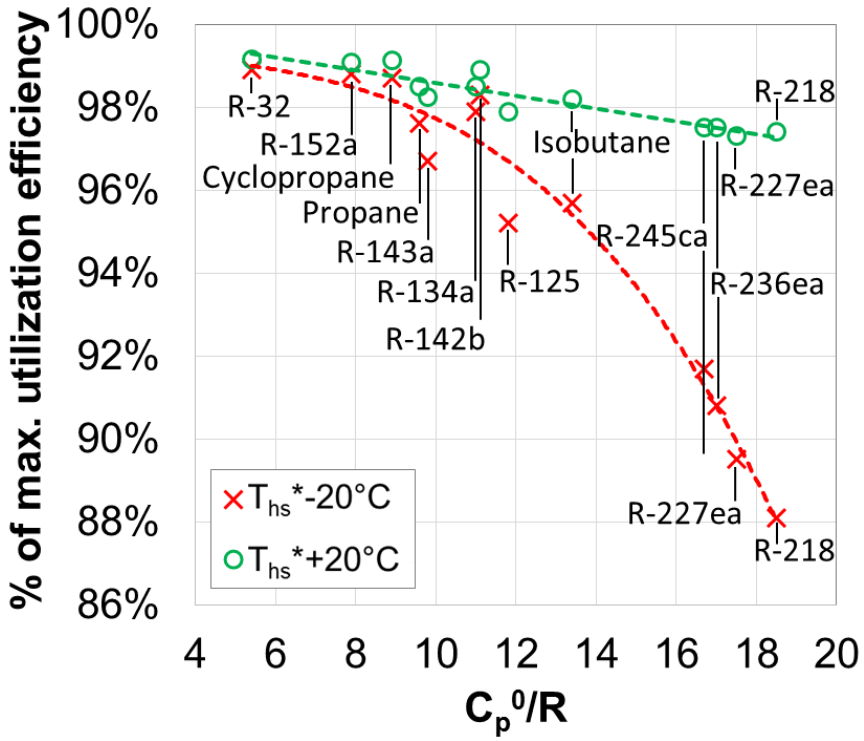


*Figure 3-10: Percentage of the maximum utilization efficiency achieved by individual working fluids at temperatures 20°C below and 20°C above the optimum resource temperature $T_{hs}$*. Results are for subcritical ORC without recuperator (Sub-NR)*

Polynomial trends fitted to the data in Figure 3-10 are described by the following equation:

$$\gamma = c \cdot \left(\frac{C_p^0}{R}\right)^3 + d \cdot \left(\frac{C_p^0}{R}\right)^2 + e \cdot \left(\frac{C_p^0}{R}\right) + f \qquad (3\text{-}6)$$

where $\gamma$ is the percentage of maximum utilization efficiency, and coefficients *c*, *d*, *e*, and *f* are listed in Table 3-3. The polynomial fits have reasonable correlation coefficients $R^2$ of 0.97 and 0.86 for 20ºC below and 20ºC above $T_{hs}$*, respectively.

*Table 3-3: Coefficients c-f used in Equation (3-6) and the standard deviations σ of the regressed data.*

| $T_{hs}$= | $T_{hs}$*-20°C | $T_{hs}$*+20°C |
|---|---|---|
| c | -3.04*10-5 | 0 |
| d | 3.7*10-4 | 0 |
| e | 2.91*10-3 | -1.55*10-3 |
| f | 1 | 1.002 |
| σ | 0.7% | 0.3% |

In addition to correlating the thermodynamic properties of working fluids with their performance in ORCs, rules-of-thumb may be useful for evaluating the effects of adding recuperators to ORC plants. For example, the increase in both the thermal efficiency $\eta_{th}$ and the heat source outlet temperature $T_{hs,out}$ due to the addition of a recuperator to supercritical ORC can be quantified using $C_p^0/\boldsymbol{R}$ and the difference between the heat source temperature and working fluid critical temperature ($T_{hs}$-$T_c$). These variables are correlated because the increases in $\eta_{th}$ and $T_{hs,out}$ are proportional to the degree of superheat present in turbine exhaust gases. This quantity is, in turn, determined by the turbine inlet temperature, the isentropic efficiency

of the turbine, and the ideal gas reduced heat capacity $C_p^0/\boldsymbol{R}$. In addition, the turbine inlet temperature is a nearly linear function of the heat source temperature for cycles which can accommodate a recuperator.

Figure 3-11 shows the increase in the heat source outlet temperature due to the addition of recuperator. This parameter is presented as a function of $C_p^0/\boldsymbol{R}$ and ($T_{hs}$-$T_c$). In Figure 3-11.A. results from the models are represented by the markers. They were approximated using a polynomial surface that is first-order in $C_p^0/\boldsymbol{R}$ and second-order in ($T_{hs}$-$T_c$). This correlation provides a reasonable coefficient of determination $R^2$ of 0.91, suggesting that the effects of using heat recuperators can be accurately predicted for other fluids for which the $C_p^0/\boldsymbol{R}$ and critical temperature are known. To better illustrate the accuracy of the fitted correlation, Figure 3-11.B and C show the results from ORC models using continuous lines and the corresponding predictions of the polynomial correlation using dashed lines. The data was split into two figures (B and C) to enhance the clarity and avoid overlap.

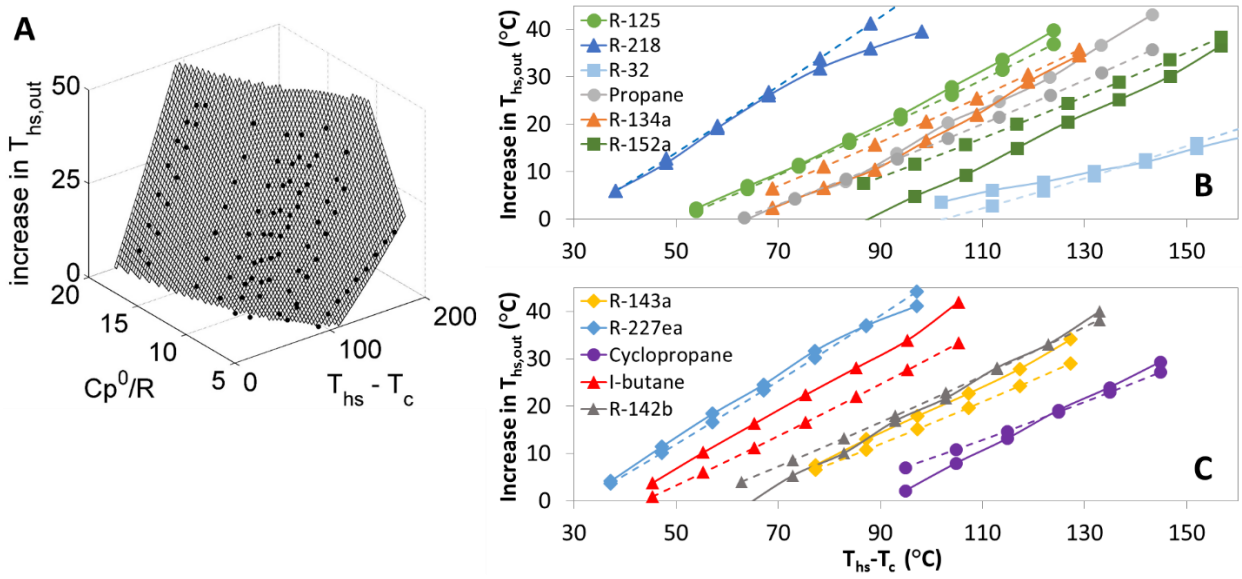


*Figure 3-11: Increase in the temperature of heat source fluid leaving ORC plant due to addition of a heat recuperator in supercritical ORC. Figure A: Markers represent results for individual working fluids. The surface in Figure A is a polynomial first-order fit in reduced ideal gas heat capacity $C_p^0/\boldsymbol{R}$ and second- order fit in the difference between heat source temperature and critical temperature of working fluid ($T_{hs}$-$T_c$). Figures B and C: Results from ORC models (continuous lines) are compared to the fitted correlation from Figure A (dashed lines).*

In a similar way, the increase in thermal efficiency provided by addition of recuperators to supercritical ORCs was quantified and presented in Figure 3-12. The regression coefficient $R^2$ for polynomial fitted to the data was 0.9.

The polynomial functions fitted to data in Figure 3-11 and Figure 3-12 are described by the following equation:

$$Z = A + B \cdot (T_{hs} - T_c) + C \cdot \left(\frac{C_p^0}{R}\right) + D \cdot (T_{hs} - T_c)^2 + E \cdot (T_{hs} - T_c) \cdot \left(\frac{C_p^0}{R}\right) \qquad (3\text{-}7)$$

where $Z$ is either the increase in heat source outlet temperature $T_{hs,out}$ or the absolute percentage point increase in thermal efficiency $\eta_{th}$. Constants A-E are listed in Table 3-4.

*Table 3-4: Coefficients A-E used in Equation (3-7) and the standard deviations σ of the regressed data.*

| Z= | Increase in $T_{hs,out}$ | Percentage point increase in $\eta_{th}$ |
|---|---|---|
| A | -25.09 | -0.03347 |
| B | -0.02852 | 0.0001015 |
| C | 0.3358 | 0.0007033 |
| D | 0.000634 | 1.332*10-7 |
| E | 0.03539 | 3.179*10-5 |
| σ | 3.6°C | 0.4% |

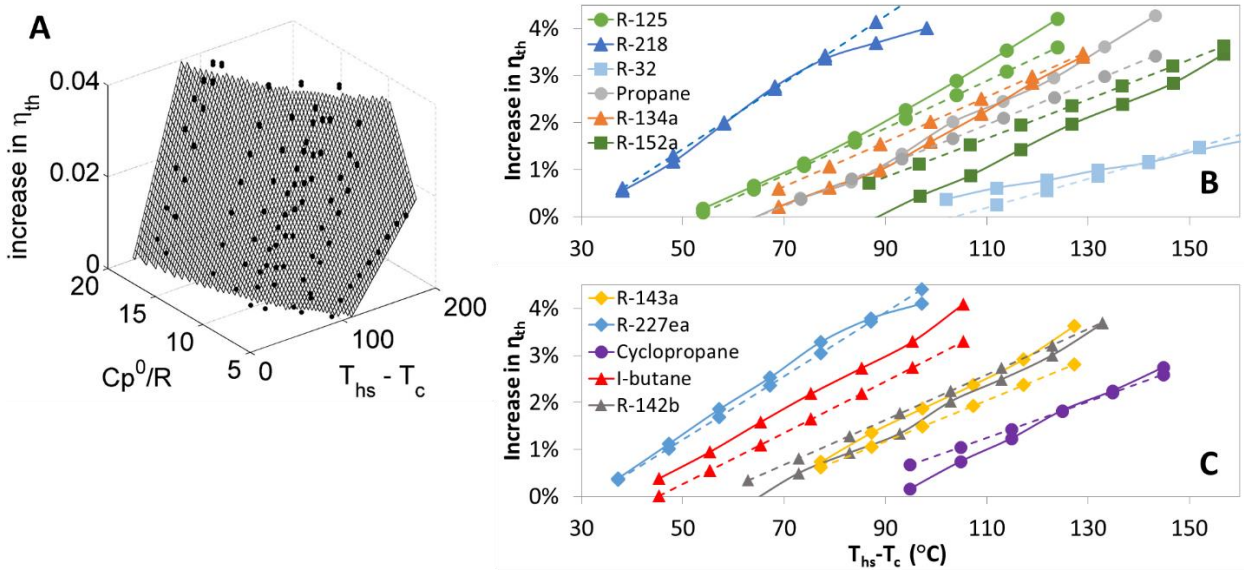


*Figure 3-12: Absolute percentage point increase in thermal efficiency due to addition of heat recuperator to supercritical ORCs. Figure A: Markers represent results for individual working fluids. Fitted surface is a polynomial first-order in $C_p^0/\boldsymbol{R}$ and second-order in ($T_{hs}$-$T_c$). Figures*

*B and C: Results from ORC models (continuous lines) are compared to the fitted correlation from Figure A (dashed lines)*

Results presented in Figure 3-11Figure 3-11 and Figure 3-12 suggest that dry fluids with reduced ideal gas heat capacities above 11 and critical temperatures at least 50-70°C below the heat source temperature would be particularly good candidates for Sc-R cycles used in combined heat and power (CHP) applications. The observed absolute increase in thermal efficiency of up to 4 percentage points is substantial because most of presented configurations have a base-case thermal efficiency between 10% and 20%.

## 3.7 Heat rejection systems

While the selection of a proper working fluid and its operating parameters is important, the largest variability in performance of existing ORC plants is due to the type of heat rejection system used. The choice between two most common solutions, a water cooled condenser (WCC) and an air cooled condenser (ACC), is typically made based on the availability of water and the regulatory environment. Therefore, the selection of heat dissipation system is often determined by the geographic location of the ORC plant and, unlike the type of working and its operating conditions, it is usually imposed on the ORC plant designers. The ORC models discussed in the previous sections used a WCC coupled with a wet, mechanical induced draft cooling tower. The inlet air dry bulb temperature was 24°C, wet bulb temperature $T_0$ was 17°C and the relative humidity was 50%. Figure 3-13 shows the sensitivity of the specific net power output (in $kW_e$ per kg/s of heat source fluid flow) to the changes in dry bulb temperature and relative humidity. In addition, it includes results for an ORC plant using an air cooled condenser

(ACC). The selected plant configuration uses a Sub-NR R-134a cycle and 150°C heat source temperature.

In moderate climates representative of the Eastern U.S. (15°C, 70% RH), a cycle with a WCC provides 25% higher power compared to an ACC plant. In warm, dry weather encountered in the Western U.S. (e.g., during an average summer afternoon in Reno, Nevada at 30°C and 20% RH), power output with WCC can be nearly double of that with ACC. This difference is due to both the higher parasitic power consumption of ACC fans and the increased condensing pressure caused by the ACC. At heat source temperatures below 150°, the power advantage of cycles with WCC is even greater than that presented in Figure 3-13.

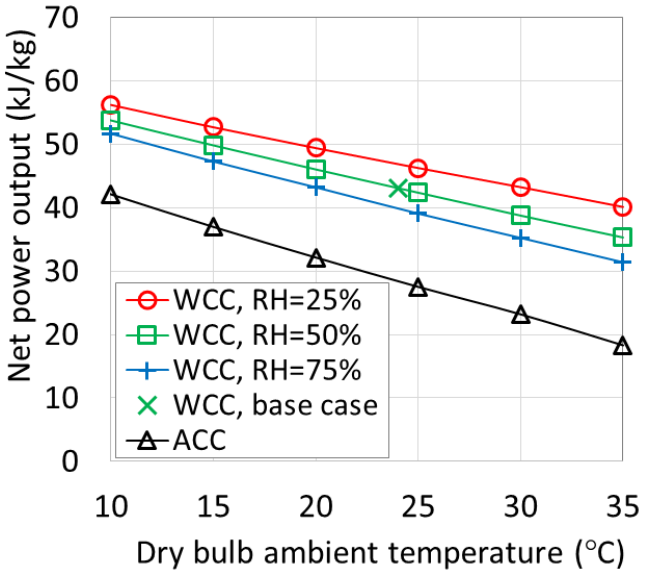


*Figure 3-13: Sensitivity of the specific net power output ($kW_e$/(kg/s) or kJ/kg of heat source fluid) to changes in dry bulb temperature and relative humidity (RH) for wet cooling tower (WCC) and air cooled condenser (ACC). Calculations were made for Sub-NR cycle using R-134a and heat source temperature of 150ºC*

## 3.8 Conclusions

This study analyzed four different ORC power plant configurations using heat sources from 100°C to 230°C, 13 different working fluids, and 2 types of heat rejection systems. The models employed were optimized for maximum utilization or exergetic efficiency and validated using results from previous numerical studies and performance data from actual ORC plants.

The key result of this work was correlating the efficiency of ORC plants with the thermodynamic properties of working fluids. Two selected fluid properties - reduced ideal gas heat capacity $C_p^0/\boldsymbol{R}$ and critical temperature $T_c$ can be evaluated from data or, for less characterized working fluids, using molecular contribution methods. Because of that, the correlations developed in this work can be used to pre-screen the potential ORC working fluids. It was shown that in ORC plants optimized for maximum utilization efficiency, $C_p^0/\boldsymbol{R}$ and $T_c$ can be used to accurately predict: 1) heat source temperature $T_{hs}$* at which a plant achieves its maximum utilization efficiency, 2) sensitivity of utilization efficiency to the changes in heat source temperature, and 3) increase in thermal efficiency and heat source fluid outlet temperature due to addition of a heat recuperator.

Furthermore, it was proven that supercritical ORCs provide up to 17% higher utilization efficiencies, increased thermal efficiencies, and smaller specific heat exchanger areas compared to subcritical ORCs. A single working fluid can be also effectively used in supercritical ORC over a broader range of heat source temperatures. Subcritical cycles, on the other hand, experience higher thermal efficiency increase when equipped with heat recuperators.

Adding a recuperator to the top performing sub- and supercritical configurations resulted, on average, in a 0.5% drop in net power output and a 6.5% increase in thermal efficiency. It also

increased the temperature of heat source fluid leaving ORC plant, which may help avoid scaling in geothermal ORC plants and condensation of flue gases in many heat recovery applications. Despite being an added capital cost component, a recuperator reduces the overall heat exchanger area in subcritical ORC as a result of lowering the heat duties of preheater and condenser and consequently decreases their sizes and capital costs.

The type of heat rejection system employed in the power cycle has a large impact on the efficiency of an ORC, especially for cycles utilizing low-temperature heat sources. In moderate climates, the use of an air cooled condenser results in only 20% penalty in net power output compared to a water cooled condenser. In warm and arid conditions, this difference increases to as much as 50%. From the efficiency standpoint, an evaporative cooling system is preferred over an air cooled condenser and should be used whenever cooling water is available.

## 3.9 Acknowledgements

This chapter is extensively based on the following journal article:

Lukawski, M., Tester, J., DiPippo, R., 2016. 'Impact of Molecular Structure of Working Fluids on Performance of Organic Rankine Cycles (ORCs)', Sustainable Energy & Fuels (submitted).

## 3.10 References

Andreasen, J.G., Larsen, U., Knudsen, T., Pierobon, L., Haglind, F., 2014. Selection and optimization of pure and mixed working fluids for low grade heat utilization using organic Rankine cycles. Energy 73, 204–213. doi:10.1016/j.energy.2014.06.012

ASHRAE, 2008. ANSI/ASHRAE Standard 34-2007: Designation and Safety Classification of Refrigerants.

ASHRAE, 2010. ASHRAE GreenGuide - The Design, Construction, and Operation of Sustainable Buildings.

Aspen Technology, 2011. Aspen HYSYS v 7.3 Unit Operations Guide.

Astolfi, M., Romano, M.C., Bombarda, P., Macchi, E., 2014. Binary ORC (Organic Rankine Cycles) power plants for the exploitation of medium-low temperature geothermal sources - Part B: Techno-economic optimization. Energy 66, 435–446. doi:10.1016/j.energy.2013.11.057

Augustine, C., Field, R., DiPippo, R., Gigliucci, G., Fastelli, I., Tester, J., 2009. Modeling and Analysis of Sub- and Supercritical Binary Rankine Cycles for Low- to Mid-Temperature Geothermal Resources. Trans. - Geotherm. Resour. Counc. 33, 604–608.

Bejan, A., Tsatsaronis, G., Moran, M., 1996. Thermal Design and Optimization. John Wiley & Sons, New York.

Box, M.J., 1965. A new method of constrained optimization and a comparison with other methods. Comput. J. 8, 42–52.

Calm, J.M., Hourahan, G.C., 2011. Physical, Safety, and Environmental Data for Current and Alternative Refrigerants. 23rd Int. Congr. Refrig. 22.

Chen, H., Goswami, D.Y., Rahman, M.M., Stefanakos, E.K., 2011. A supercritical Rankine cycle using zeotropic mixture working fluids for the conversion of low-grade heat into power. Energy 36, 549–555.

Chen, H., Goswami, D.Y., Stefanakos, E.K., 2010. A review of thermodynamic cycles and working fluids for the conversion of low-grade heat. Renew. Sustain. Energy Rev. 14, 3059–3067. doi:10.1016/j.rser.2010.07.006

Dai, Y., Wang, J., Gao, L., 2009. Parametric optimization and comparative study of organic Rankine cycle (ORC) for low grade waste heat recovery. Energy Convers. Manag. 50, 576–582.

DiPippo, R., 2004. Second Law assessment of binary plants generating power from low-temperature geothermal fluids. Geothermics 33, 565–586.

DiPippo, R., 2007. Ideal thermal efficiency for geothermal binary plants. Geothermics 36, 276–285.

DiPippo, R., 2012. Geothermal Power Plants: Principles, Applications, Case Studies and Environmental Impact, 3rd ed. Butterworth-Heinemann.

European Commision, 2016. EU legislation to Control F-gases [WWW Document]. URL http://ec.europa.eu/clima/policies/f-gas/legislation/index_en.htm (accessed 8.5.16).

Fox, D.B., Sutter, D., Tester, J.W., 2011. The thermal spectrum of low-temperature energy use in the United States. Energy Environ. Sci. 4, 3731. doi:10.1039/c1ee01722e

Greenhut, A.D., Tester, J.W., DiPippo, R., Field, R., Love, C., Nichols, K., Batini, F., Price, B., Gigliucci, G., Fastelli, I., 2010. Solar-Geothermal Hybrid Cycle Analysis for Low Enthalpy Solar and Geothermal Resources, in: Proceedings World Geothermal Congress 2010.

Heberle, F., Brüggemann, D., 2015. Thermo-Economic Evaluation of Organic Rankine Cycles for Geothermal Power Generation Using Zeotropic Mixtures. Energies 8, 2097–

2124.

Hensley, J.C., 2009. Cooling Tower Fundamentals, SPX Cooling Technologies, Inc. Overland Park, Kansas, USA. doi:10.1201/b11510-14

Hung, T.C., Wang, S.K., Kuo, C.H., Pei, B.S., Tsai, K.F., 2010. A study of organic working fluids on system efficiency of an ORC using low-grade energy sources. Energy 35, 1403–1411.

Ingersoll Rand, 2014. Climate Change Regulation and the Next Generation of Refrigerants [WWW Document]. URL http://www.trane.com/commercial/uploads/pdf/cso/138/Refrigerants.pdf (accessed 8.5.16).

Invernizzi, C., Iora, P., Silva, P., 2007. Bottoming micro-Rankine cycles for micro-gas turbines. Appl. Therm. Eng. 27, 100–110. doi:10.1016/j.applthermaleng.2006.05.003

IPCC, 2007. Changes in Atmospheric Constituents and in Radiative Forcing, in: Climate Change 2007: The Physical Science Basis. Cambridge University Press, Cambridge, UK, pp. 129–234. doi:10.1103/PhysRevB.77.220407

Joback, K., Reid, R., 1987. Estimation of Pure-Component Properties from Group-Contributions. Chem. Eng. Commun. 57, 233–243.

Karellas, S., Panousis, G., Leontaritis, A.-D., 2012a. Heat Transfer In Organic Rankine Cycle Applications, in: Advances in Industrial Heat Transfer. pp. 339–390.

Karellas, S., Schuster, A., Leontaritis, A.-D., 2012b. Influence of supercritical ORC parameters on plate heat exchanger design. Appl. Therm. Eng. 33-34, 70–76. doi:10.1016/j.applthermaleng.2011.09.013

Kestin, J. et al., 1980. Sourcebook on the Production of Electricity from Geothermal Energy. 997(DOE: Providence, RI, USA, 1980). U.S. Department of Energy.

Kuester, J.L., Mize, J.H., 1973. Optimization Techniques with Fortran, 1st ed. McGraw-Hill, NY, USA.

Lemmon, E.W., Huber, M., McLinden, M., 2013. NIST Standard Reference Database 23: Reference Fluid Thermodynamic and Transport Properties-REFPROP, Version 9.1.

Linde, 2015. Refrigerants Environmental Data: Ozone Depletion and Global Warming Potential. [WWW Document]. URL http://www.linde-gas.com/internet.global.lindegas.global/en/images/Refrigerants environmental GWPs17_111483.pdf (accessed 3.3.16).

Lukawski, M.Z., 2009. Design and Optimization of Standardized Organic Rankine Cycle Power Plant for European Conditions. M.S. Thesis, RES - The School For Renerable Energy Science.

Manente, G., Field, R., DiPippo, R., Tester, J.W., Paci, M., Rossi, N., 2011. Hybrid Solar-Geothermal Power Generation to Increase the Energy Production From a Binary Geothermal Plant, in: ASME 2011 International Mechanical Engineering Congress and Exposition. Denver, CO, pp. 109–119.

Maraver, D., Royo, J., Lemort, V., Quoilin, S., 2014. Systematic optimization of subcritical and transcritical organic Rankine cycles (ORCs) constrained by technical parameters in multiple applications. Appl. Energy 117, 11–29. doi:10.1016/j.apenergy.2013.11.076

Martelli, E., Capra, F., Consonni, S., 2015. Numerical optimization of Combined Heat and Power Organic Rankine Cycles - Part A: Design optimization. Energy 90, 310–328. doi:10.1016/j.energy.2015.06.111

Monroe, R.C., 1974. Fans Key to Optimum Cooling-Tower Design, Hudson Products Corporation. Houston, Tx, USA.

Poling, B., Prausnitz, J., O'Connell, J., 2000. The Properties of Gases and Liquids, 5th ed. McGraw-Hill.

Press, W., Teukolsky, S., Vetterling, W., Flannery, B., 1988. Numerical Recipes in C: The Art of Scientific Computing. Cambridge University Press.

Saleh, B., Koglbauer, G., Wendland, M., Fischer, J., 2007. Working fluids for low-temperature organic Rankine cycles. Energy 32, 1210–1221.

Shengjun, Z., Huaixin, W., Tao, G., 2011. Performance comparison and parametric optimization of subcritical Organic Rankine Cycle (ORC) and transcritical power cycle system for low-temperature geothermal power generation. Appl. Energy 88, 2740–2754. doi:10.1016/j.apenergy.2011.02.034

Tester, J., Milora, S., 1977. Geothermal Energy as a Source of Electric Power, MIT press. Cambridge, MA, USA.

Tester, J.W., Anderson, B.J., Batchelor, A.S., Blackwell, D.D., DiPippo, R., Drake, E.M., Garnish, J., Livesay, B., Moore, M.C., Nichols, K., Petty, S., Toksoz, M.N., Veatch, Ralph W, J., 2006. The Future of Geothermal Energy: Impact of Enhanced Geothermal Systems (EGS) on the United States in the 21st Century. MIT.

U.S. DOE, 2008. Waste Heat Recovery: Technology Opportunities in the US Industry.

UNEP, 2006. Montreal Protocol on Substancs That Deplete The Ozone Layer.

Walraven, D., Laenen, B., D'haeseleer, W., 2013. Comparison of thermodynamic cycles for power production from low-temperature geothermal heat sources. Energy Convers. Manag. 66, 220–233.

Walraven, D., Laenen, B., D'haeseleer, W., 2015. Economic system optimization of air-cooled organic Rankine cycles powered by low-temperature geothermal heat sources. Energy 80, 104–113. doi:10.1016/j.energy.2014.11.048

# 4 INTEGRATED GEOTHERMAL ENERGY UTILIZATION SYSTEMS: A CASE STUDY OF CORNELL UNIVERSITY

## 4.1 Introduction

The objective of Chapter 3 was to create guidelines for designing more efficient ORC power plants, which could improve the economic feasibility of geothermal energy systems. Equally important, however, is the integration of these power plants with the remaining components of geothermal energy systems. An advanced geothermal power plant designed in isolation may perform worse than a simpler unit, which was selected with consideration of the site-specific conditions including demand profile, operating conditions, and availability of other energy sources.

Geothermal power plants can be more effectively integrated into our energy systems by enhancing their load factors and by maximizing the geothermal resource utilization. The capital costs of geothermal systems are very high compared to their typical operation and maintenance (O&M) costs, so applications with high load factors typically provide better economic performance. Geothermal systems are preferably used as baseload sources of energy, but they can also be used economically in load-following applications if combined with other energy sources. In such hybrid energy systems, geothermal energy is used to meet the base-load energy demand and the variable load is provided by a peaking source of heat and/or electricity. The peaking energy system, using e.g. natural gas or biomass, typically has a lower capital cost and higher fuel cost compared to a geothermal system.

Geothermal systems benefit not only from increased load factors, but also from improved resource utilization. In many geothermal plants, spent geofluid is reinjected into the subsurface. This partially cooled geothermal brine could, however, become a heat source for direct-use applications in a combined heat and power (CHP) system. The performance of CHP systems could be further improved by using another process requiring even lower-temperature heat input. This method of using a single thermal energy source to supply a range of end-uses by utilizing the heat output from a higher-temperature process as a heat input into a lower-temperature process is called heat cascading or heat integration. By increasing the geothermal resource utilization, heat cascading can provide additional revenue streams and improve the project economics.

This chapter assesses the performance of low-grade Enhanced Geothermal Systems for direct-use and CHP applications. It also quantifies the technical and economic benefits of hybridization and heat cascading. To accomplish these goals, this work evaluates a proposed geothermal district heating (DH) network and a geothermal CHP system at Cornell University. The evaluated geothermal systems can be supported by a biomass boiler during periods of peak heat demand and are integrated with the existing natural gas CHP system at Cornell campus. While this analysis utilizes the Cornell University energy system as a model, many outcomes of the study are more general and representative of other locations in the Northeastern U.S. and beyond.

The Northeastern part of the United States, where Cornell University is located, is particularly suitable for geothermal direct-use and cogeneration applications due to limited availability of solar resources as well as high and relatively constant heating loads. In many areas of the Northeast, geothermal gradients reach 30-35°C/km (Shope et al., 2012). Using these resources

in electricity-only power plants would require drilling deep wells and yield high LCOE. Such geothermal gradients may, however, be sufficient for CHP and direct-use applications to be economically viable.

Cornell University with its average electricity demand of 30 $MW_e$ and a high annual heating demand of over 380 $GWh_{th}$, can be used as a model for many mid-sized communities in the Northeastern United States. Additional motivation for selecting it as a case study comes with the Cornell Climate Action Plan (CAP, Cornell University, 2009), which sets a goal for the Ithaca campus to become carbon neutral by 2050. The CAP provides a framework for gradual reduction in greenhouse gases (GHG) emissions. It also considers supplementing the efficient Cornell lake source cooling system with a heating system based on renewable resources, including low-temperature geothermal and biomass.

## 4.2 Existing energy system at Cornell

Cornell University campus covers an area of approximately 3 $km^2$ (745 acres). It includes facilities with a total net building area of 883,000 $m^2$ (9,500,000 sq. ft.). Its Northern latitude location results in 7182 annual standard heating degree-days and 315 cooling degree-days evaluated using 18.3°C (65°F) baseline (EERE, 2013). The total annual heat demand of Cornell campus is 382 $GWh_{th}$. Electricity demand is 250 $GWh_e$ annually, with the highest fluctuations occurring day to night rather than on a seasonal basis. Monthly heat demand of Cornell campus buildings was quantified using the data collected by Cornell Facilities and was found to vary from 11 to 53 $GWh_{th}$ as shown in Figure 4-1.

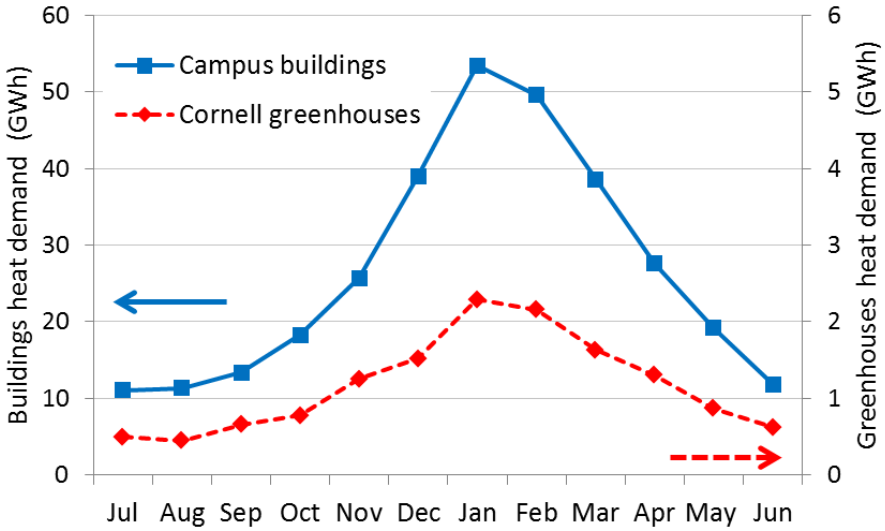


*Figure 4-1: Monthly heat demand of all Cornell University buildings at the Ithaca campus*

The Cornell greenhouses cover an area of 18,600 $m^2$ (200,000 sq. ft.). Their monthly heat consumption ranges from 0.45 $GWh_{th}$ in the summer to 2.3 $GWh_{th}$ in the winter. Greenhouses are primarily used for academic programs and research purposes.

The heat demand of the Cornell campus is covered by a steam district heating network powered by a cogeneration (CHP) plant. The cooling demand is mainly covered by chilled water supplied by a lake source cooling system (CU Energy and Sustainability, 2013). In addition, several absorption chillers are used around the campus, primarily for dehumidification of swimming pools.

Cornell University owns a state of the art natural gas combined cycle CHP plant, which has been fully operational since 2009. The schematic of the CHP plant is presented in Figure 4-2. The system utilizes two combustion turbines, each producing on average 14.3 $MW_e$. Turbines are fitted with heat recovery steam generators (HRSGs) producing on average a total of 34.8

$MW_{th}$. Gas turbines are designed to operate under full load and therefore cannot track changes in electric demand. If the heat demand exceeds the exhaust output of the gas turbines, duct burners installed in the HRSGs are used. Steam from the HRSGs is passed through two backpressure turbines (7.5 $MW_e$ total). It is then fed into the district heating network at temperatures between 160°C and 246°C (320-475°F) and pressures from 75 to 90 psia (5.2-6.2 bara). Lastly, an old, currently not used 58 $MW_{th}$ coal boiler can be used in case of high heating demand.

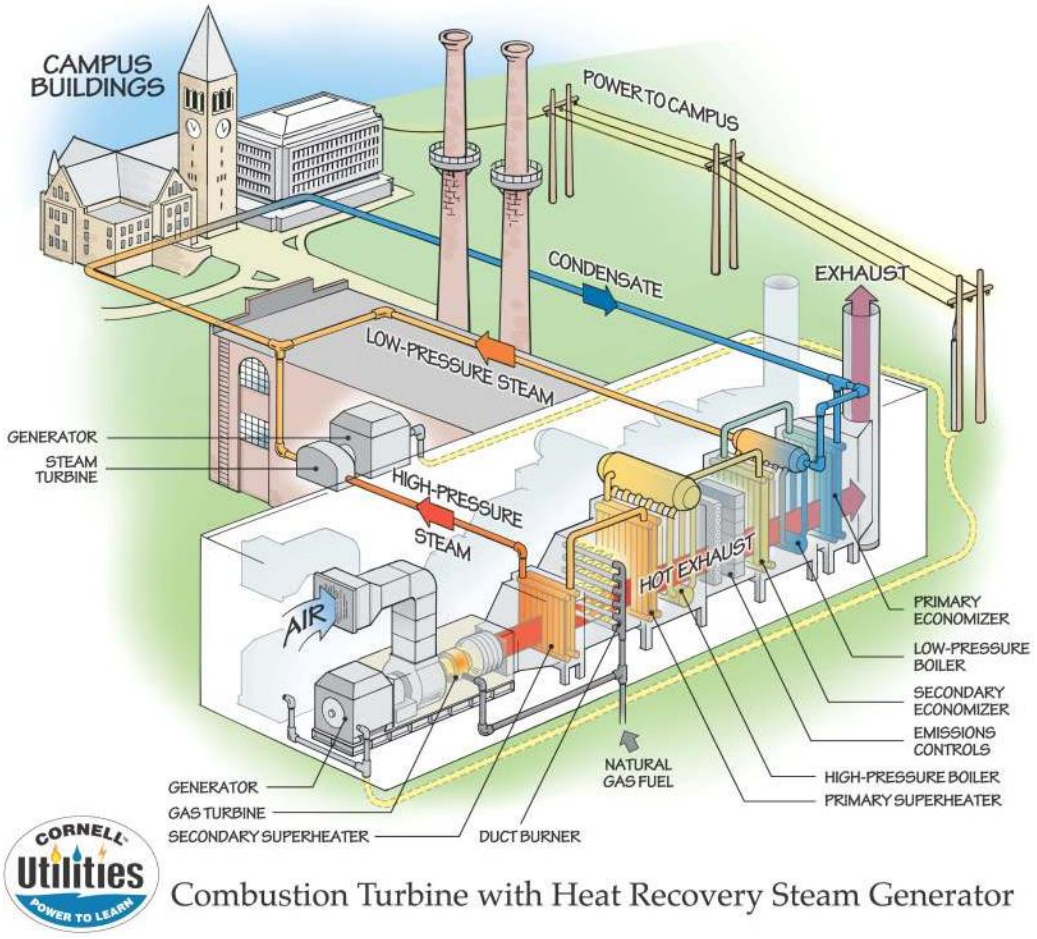


*Figure 4-2: Schematic of the existing CHP combined cycle power plant and district heating system at Cornell University.*

The existing power plant has an electrical efficiency of 34.5% and a thermal efficiency of 41.4%, which yield a combined energetic efficiency of 75.9%. The current system is capable of covering 90% of the peak heat demand at Cornell, and 70% of its total electricity demand. The heat deficit is covered by peaking boilers and remaining electricity is purchased from the grid.

District heat is delivered to the substations in campus buildings as a superheated steam. Approximately 18% of distributed heat is lost from the inefficient, 46 km (28.5 mi) long piping network (CU Facilities Services, 2013). In substations, heat exchangers transfer the heat to secondary hydronic loops, which supply energy needed for space heating, domestic hot water, and other uses. As district heating steam passes through the heat exchangers, it condenses and is eventually returned to the CHP plant.

The building heating systems are designed to operate at 82.2°C (180°F) secondary supply temperature and 72°C (165°F) secondary return temperature during the coldest days in a year. High space heating (secondary) temperatures impose a requirement of a relatively high district heating (primary) distribution temperature.

## 4.3 Proposed hybrid renewable energy system

The objective of this study was to design an efficient heat production and distribution system which uses geothermal and biomass resources to cover demand of a fraction of the Cornell campus. To do that, a fraction of the campus area, in which district heating piping would require considerable replacements within the next few years was isolated, and the existing heat distribution system was converted from steam to pre-insulated hot water piping. The chosen

area of North Campus and the Veterinary (Vet) School has a heat load corresponding to 26% of the whole campus demand, which was presented in Figure 4-1. This area is also adjacent to the greenhouses, which offer opportunity for heat cascading with their substantial demand for low-temperature heat.

The configuration of the proposed hybrid energy system is presented in Figure 4-3. The district heating network receives heat from the geothermal fluid, a biomass boiler, and a backup natural gas heat exchanger from the existing Cornell plant and distributes it to the optional ORC plant, substations in Cornell buildings, and the greenhouses.

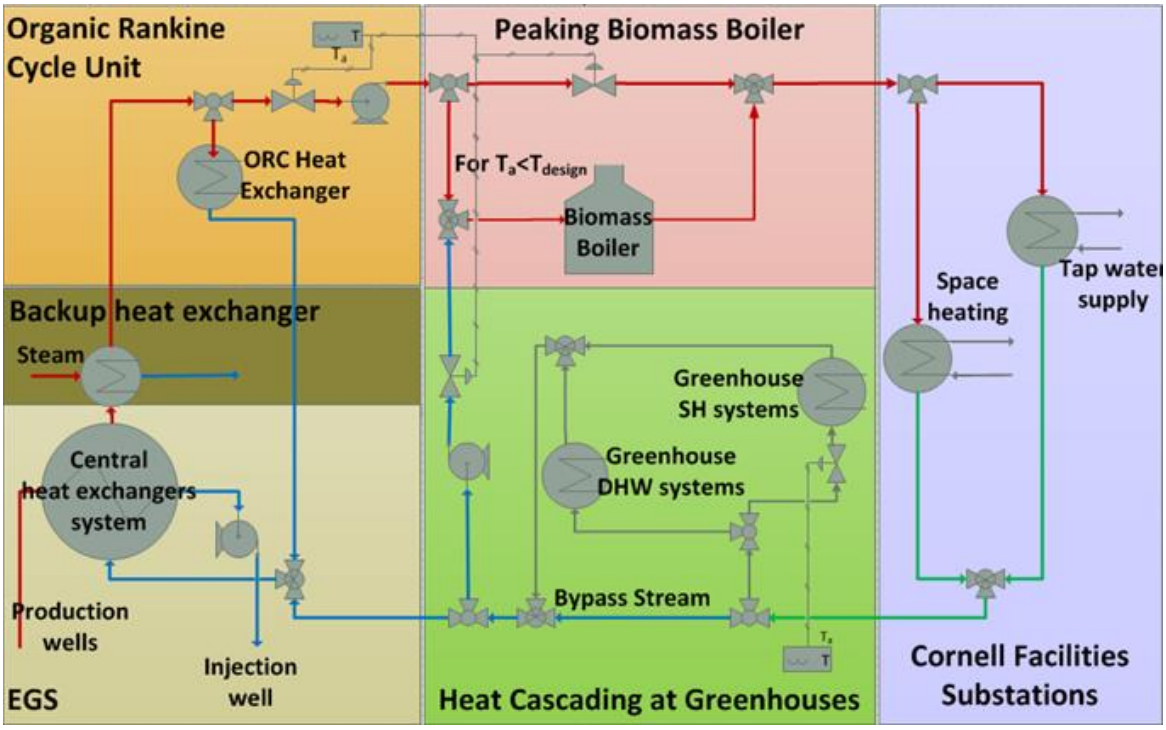


*Figure 4-3: Schematic of the proposed hybrid geothermal – biomass energy systems for Cornell. The 'DH' scenario does not include an ORC power plant. Red lines represent hot supply water and blue lines cold return water.*

The EGS reservoir was hydronically separated from the district heating (DH) network using a central heat exchanger installed in between production and injection wells. Although this solution introduces additional exergy (availability) loss, it prevents scaling and corrosion in the district heating network, allows for an easier control of the DH water temperature and flow rate, and facilitates system expansion in the future.

To further enhance reliability of the proposed design, a backup steam-to-water heat exchanger was included in the design. It allows the existing natural gas CHP plant to cover heat demand of the North Campus and the Vet School during the maintenance of the geothermal system.

Two possible design scenarios were considered:

1. 'DH': Geothermal energy was used only for district heating. This configuration does not include an Organic Rankine Cycle (ORC) power plant.
2. 'DH-ORC': Geothermal energy was used for both district heating and generation of electricity using an Organic Rankine Cycle power plant. The ORC unit operates during low heat demand using the excess heat from EGS.

In both cases, a torrefied biomass boiler can be used to increase the temperature of DH supply water during peak heat demand.

As shown in Figure 4-3, after receiving heat from geothermal fluid and combusted biomass, district heating water is pumped to building substations providing the heat required for space heating and domestic hot water needs. Approximately 30% of the district heating water returned from building substations is cascaded through greenhouses substations. The mixed return stream from substations in greenhouses and other Cornell facilities is then pumped to the central heat exchanger, which closes the cycle.

### 4.3.1 Heat distribution network

Because of low temperatures of economically accessible geothermal resources in the Northeast, the heat distribution system cannot use high-temperature steam as a transport medium. The proposed systems uses pressurized liquid water at temperatures between 90°C and 140°C (195-285°F). The minimum supply temperature in the DH network was constrained by the requirements of the existing space heating systems in the campus buildings. The DH supply temperature could be further lowered, which would increase the total efficiency of the system, but this would require significant amount of structural work and incurred costs in campus buildings. Thus, the existing components of space heating systems inside Cornell buildings such as radiators, pipes, valves, air ducts etc. were maintained. The existing substations were replaced with units using plate and frame water-to-water heat exchangers.

Approximately 20% of the district heating pipelines in the considered part of the network were replaced with pre-insulated pipes. Steam traps were removed and water circulation pumps were installed. The minimum mass flow rate in the DH network has been set at 30% of the nominal flow rate for a proper operation of the control valves and due to heat losses from supply pipes.

### 4.3.2 Greenhouses

The existing space heating systems in greenhouses are similar to the ones used in other campus buildings. They use 82.2°C (180°F) fluid, which requires high DH supply temperature. The existing installation was replaced with a low-temperature heating system consisting of soil heating system using fluid at 30-36°C (86-97°F) circulating in polyethylene tubes and a finned coil air heater. The proposed configuration is based on a study conducted at the Oregon Institute of Technology (Boyd et al., 2008). The proposed system requires district heating (DH)

temperature of less than 68°C (155°F) and thus can use the return DH water from other campus buildings as a heat source. Retrofitting low-temperature space heating systems in greenhouses requires less structural work and a lower capital investment compared to other Cornell buildings. Furthermore, soil heating is known to increase the productivity of plants.

### 4.3.3 Organic Rankine Cycle (ORC) power plant

The Organic Rankine Cycle unit used in 'DH-ORC' scenario operates only during low heat demand conditions. The unit is shut down if its heat input drops below 40% of the nominal value. Due to seasonal variations in available heat, two lower-capacity ORC plants were used instead of one big unit.

### 4.3.4 Torrefied biomass boiler

The torrefied biomass boiler was used to supplement the geothermal system when the ambient temperature drops below a certain value. This value is referred to as the design ambient temperature $T_{design}$ and is defined as the lowest outdoor temperature at which EGS can cover the total heat demand.

Biomass which underwent torrefaction – a low temperature pyrolysis – resembles coal and can be easily stored thanks to its hydrophobic properties. Possible feedstocks for torrefaction include all types of woody biomass, agricultural residues, and switchgrass. In principle, all or most of the biomass feedstocks required for torrefaction could be produced on Cornell's 14,000 acres of forest and agricultural land. The biomass could be torrefied and stored on campus property and combusted in the existing 58 $MW_{th}$ coal boiler.

### 4.3.5 System operation modes

The proposed system has four different operation modes depending on the ambient temperature. They are discussed below and presented in Figure 4-4. The nominal mass flow rate is defined as the district heating fluid flow rate in the third mode of operation as measured at the inlet manifold of the central heat exchanger.

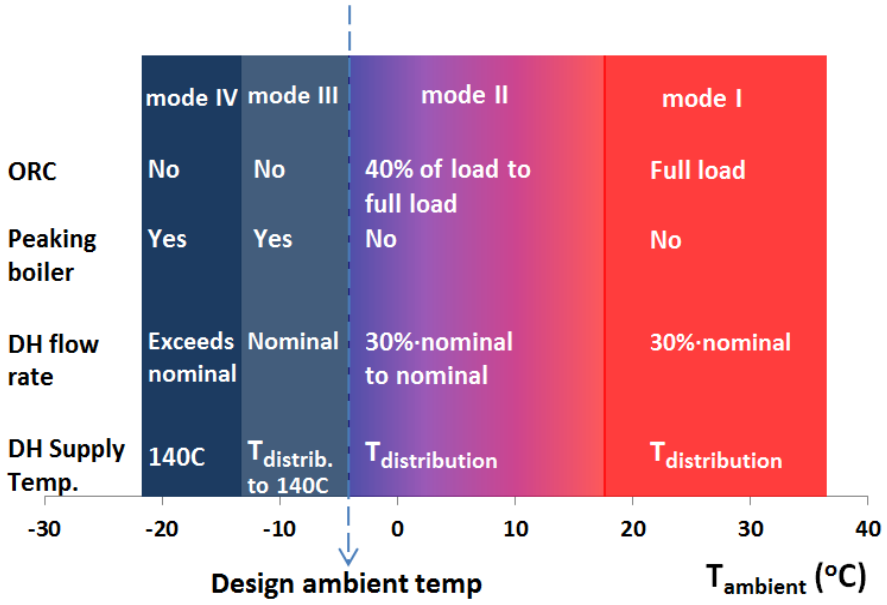


*Figure 4-4: Operation modes of the 'DH-ORC' system as a function of the ambient temperature. In the 'DH' scenario, operation modes are the same with exception of the ORC unit itself. Both design ambient temperature and the distribution temperature are chosen by the techno-economic optimization procedure.*

**Mode I:** ambient temperature is above the design ambient temperature $T_{design}$. No building space heating is required. The district heating system operates at minimum flow rate required by the domestic hot water demand. In the 'DH-ORC' scenario the ORC unit operates at its nominal heat input.

**Mode II:** ambient temperature is above $T_{design}$. The district heating network flow rate varies according to the heating load. The torrefied biomass boiler is not used. If an ORC unit is installed, its heat input gradually decreases with decreasing ambient temperature until it reaches 40% of the nominal value. Below 40%, the ORC plant is switched off.

**Mode III:** outdoor temperature is below $T_{design}$. The torrefied biomass boiler is used to increase the district heating distribution temperature up to 140°C (284°F). The district heating flow rate is kept at its nominal value. In 'DH-ORC' scenario the ORC unit is switched off.

**Mode IV:** ambient temperature is below $T_{design}$. The district heating supply temperature is kept at its maximum value allowed by the specifications of pre-insulated piping (140°C or 284°F). The district heating flow rate measured at the central heat exchanger is kept at its nominal value to provide acceptably high cooling of the geothermal fluid. The flow rate in the distribution system exceeds the nominal value, which is achieved by partially by-passing the central heat exchanger and providing additional heat input using the biomass boiler. The ORC unit is switched off.

## 4.4 Performance criteria

The performance of the proposed hybrid EGS-biomass systems was evaluated and compared to the existing Cornell energy system using the following metrics:

1. LCOE (Levelized cost of electricity, U.S. ¢/kWh) – an economic metric. The sold district heat is indirectly incorporated in LCOE by using heat credits.
2. Avoided natural gas consumption (MMBTU) – an environmental and economic metric
3. Avoided $CO_2$ emissions (tons $CO_2$/year) – an environmental metric

To calculate the avoided $CO_2$ emissions, the total $CO_2$ emissions resulting from covering Cornell's heating and electricity demand were evaluated, including electricity imported from the grid. Average emissions for New York State were assumed for the purchased electricity (NYISO, 2012).

Introducing an added capacity from the renewable energy systems can reduce the profitability of the existing natural gas CHP power plant by lowering its thermal load. Therefore, both the 'DH' and 'DH-ORC' scenarios were evaluated and optimized as a whole i.e. including the existing CHP natural gas power plant and the remaining steam district heating network. That is also the reason why the results are reported for the whole Cornell energy system and not its fraction which was converted to renewable resources. In order to determine the optimal system configurations, a techno-economic model of the proposed energy systems has been created. The three sections that follow describe the thermodynamic model of the Cornell energy system, the economic performance model, and the used optimization procedure.

## 4.5 Mathematical model of the hybrid energy system

A thermodynamic model of the proposed hybrid energy system was created in MATLAB software using previously developed methodology (Valdimarsson, 1993; Lukawski, 2010). This model evaluates the temperatures and mass flow rates of all streams presented in Figure 4-3 as a function of the ambient temperature. The main model outputs such as amount of delivered heat, natural gas consumption etc. were integrated over a period of one year using a typical annual outdoor temperature distribution for the Ithaca region (EERE, 2013). To

accomplish this, the campus heat demand was correlated with ambient temperature using 2008-2011 heat consumption and meteorological data (CU Facilities Services, 2013).

The model calculates both the required reservoir temperature and the geofluid flow rate based on a given heat load and a selected DH supply temperature. The DH supply temperature is chosen by the governing optimization procedure described in section 4.7. The district heating return temperature is then calculated using models of a space heating system and countercurrent heat exchanger. The space heating supply/return temperatures vary from 82°C/72°C at high heat demand to 71°C/65°C at low heat demand (CU Facilities Services, 2013).

### 4.5.1 District heating network

District heating system in the North Campus and Vet School areas was converted from steam to hot water. Replaced pipe diameters were selected to yield a moderate pressure drop of 160 Pa/m (Petitjean, 1994). Pressure losses and parasitic power requirements were evaluated using a Darcy-Weisbach equation. In addition, heat losses from the district heating network were calculated. The overall heat transfer coefficient for the segments of district heating piping which were converted from steam to hot water was very similar for the two fluids. Thus, the reduction in heat losses from these sections of the distribution network was almost entirely due to the lower temperature of the water compared to steam.

### 4.5.2 Enhanced Geothermal System (EGS)

The maximum flow rate of a single geothermal production well was set at 80 kg/s (Tester et al., 2006), which corresponds to an assumed commercially mature level for the EGS technology.

One injection well can be used in conjunction with up to two production wells. The geothermal gradient in Ithaca, NY was set at 30°C/km (Shope et al., 2012).

To simulate the lifetime of an EGS reservoir, a multiple parallel fracture model was used (Fox et al., 2013). This model evaluates the temperature within reservoir as a function of time. The analytical solution is based on Green's functions and utilizes a convolution integral to accommodate for variable geothermal fluid reinjection temperatures throughout the course of a year.

### 4.5.3 Organic Rankine cycle (ORC)

The ORC power plant was modeled in Aspen software as a subcritical cycle with recuperator and a wet cooling tower. The assumptions of the ORC model were the same as in Chapter 3 with exception of the heat sink temperatures obtained from the typical meteorological year (TMY3) data for the Ithaca region (EERE, 2013). The modeled ORC power plant uses R-32 working fluid, which provides high thermal efficiencies at heat source temperatures from 100°C to 140°C. While ORCs using other working fluids, e.g. R-227ea, may have higher utilization efficiencies than R-32, they withdraw more heat from the heat source fluid. This effect is undesirable in CHP applications, where the stream of heat source fluid leaving ORC plant is utilized in direct-use applications.

## 4.6 Economic evaluation

The numerical model of the proposed system incorporates an economic evaluation module. In this analysis, the annual discount rate was set at 6% and the payback time was assumed to be 20 years. The remaining economic assumptions are discussed below.

### 4.6.1 Capital investment costs

- Geothermal well drilling and completion costs were estimated using Equation (6-3) developed in chapter 6.
- ORC power plant cost: \$4000 per $kW_e$ of installed capacity.
- Pre-insulated district heating distribution piping costs were obtained from (Rafferty, 1996) and normalized to current year dollars using a plant construction cost index (Intratec, 2012).
- District heating circulation pumps: 150 \$/$kW_e$.
- Costs of heat exchangers were based on (Perry et al., 2008) and normalized to the current year dollars using a cost index.
- Costs of space heating systems in greenhouses were based on (Boyd et al., 2008).
- Component-specific factors were used to convert delivered-equipment costs to installed costs: 3.5 for heat exchangers and 4 for pumps (Perry et al., 2008).

### 4.6.2 Operation and maintenance (O&M) costs

- Natural gas price (as purchased by Cornell University): 4.5 \$/MMBTU.
- O&M costs of the existing natural gas CHP plant and DH system without fuel costs: 20 M\$ per year (approximately 3.4 ¢/kWh of delivered electricity and heat). The main cost component is the maintenance of the existing steam DH system.
- O&M costs of EGS system were obtained from (Tester et al., 2006).
- O&M costs of ORC power plant: 0.7 ¢/$kWh_e$ produced

- O&M costs of geothermal powered DH system using preinsulated hot water piping: 1 ₡/kWh$_{th}$ of delivered heat (IEA, 2011)
- Torrefied biomass purchase cost: $ 250 per ton, which is approximately $11.4 per GJ on the basis of higher heating value (Bergman et al., 2005)
- Electricity consumption of circulation pumps in the hydronic DH system: 8 ₡/kWh$_e$
- Heat credit: 7.56 ₡/kWh$_{th}$ (CU Facilities Services, 2013). Sold heat is incorporated as annual revenue and used to calculate the levelized cost of electricity (LCOE).

## 4.7 System optimization procedure

System design optimization was performed to minimize the levelized cost of electricity (LCOE), which is defined as:

$$LCOE = \sum_{t=1}^{n} \frac{\frac{[Investm. + O\&M + Fuel - Heat\ Credit]_t}{(1+i)^t}}{\frac{[\ Electric\ Power\ Generated]_t}{(1+i)^t}} \qquad (4\text{-}1)$$

Where *i* is the discount rate (6%) and *n* is the system lifetime (20 years).

A procedure in the MATLAB model selects the optimum system configuration by screening all allowed combinations of values for the variables. This simplified approach was chosen due to discrete nature of the problem and potential presence of local minima. The optimized variables include:

- Design ambient temperature $T_{design}$. It is the temperature at which the total campus heat demand is equal to the thermal capacity of the EGS system. A low design temperature increases the fraction of total energy demand covered by the geothermal system, but

reduces its capacity factor. A high design ambient temperature yields lower capital investment in EGS, but increases the amount of torrefied biomass required. Design outdoor temperature was varied from -21°C to 7°C (-6°F to 45°F).

- District heating distribution temperature was varied from 90°C to 140°C in 5°C steps.
- Approach temperature in the central heat exchanger was varied from 3°C to 15°C.

The MATLAB optimization procedure uses the following steps:

1. Selection of design ambient temperature and the district heating distribution temperature
2. Calculation of the temperatures and mass flow rates in all system components
3. Quantification of the capital investment and operating costs of the system
4. Internal optimization of the central heat exchanger. The approach temperature is selected to minimize the combined cost of geothermal wells and the central heat exchanger.
5. LCOE is calculated and the results are stored.
6. Procedure described in points 1-5 is repeated until all combinations of design ambient temperature and DH supply temperature are evaluated.
7. System design parameters corresponding to a minimum LCOE are selected.

## 4.8 Results

### 4.8.1 Optimal system configurations

The optimal design parameters minimizing the LCOE of the considered hybrid energy systems are presented in Table 4-1.

*Table 4-1: Optimal system operation parameters.*

| Scenario | DH | DH-ORC |
|---|---|---|
| Design ambient temperature, °C (°F) | -3.3 (26) | -12.2 (10) |
| DH distribution temperature, °C (°F) | 105 (221) | 120 (248) |
| Heat load w/o ORC, $GWh_{th}$/year | 92.7 | 93.7 |
| EGS thermal output, $GWh_{th}$/year | 88.6 | 209 |
| Torrefied biomass boiler thermal output, $GWh_{th}$/year | 4.1 | 0.2 |
| ORC electric output $GWh_e$/year | - | 8.3 |
| EGS capacity factor | 58.3% | 89.5% |
| Effective reservoir lifetime, years | 21 | 19 |

The economically optimal design of a direct-use system without an ORC unit corresponds to a relatively low distribution temperature of 105°C. In the 'DH-ORC' system, a distribution temperature of 120°C is selected, which is the lowest value allowed in this scenario. In both cases high costs of deep geothermal wells shifted the optimal system configuration towards a lower reservoir temperature and a lower district heating distribution temperature.

The ORC power plant operates on at least partial load for a large fraction of the year (84%) covering 3.3% of the campus electricity demand. The ORC increases the load factor of the EGS, which shortens the reservoir lifetime. Given that EGS capacity factor in 'DH-ORC' is 31% higher compared to 'DH' scenario, it may seem surprising that its reservoir lifetime is just 10% shorter. This is due to much higher seasonal load fluctuations in the 'DH' case. In the 'DH' scenario, after 21 years the model EGS reservoir can still meet the heat demand at the beginning of the heating season, but the production temperature becomes too low at the end of the winter.

The optimal design ambient temperatures of the two proposed systems are quite different: -3.3°C for the 'DH' and -12.2°C for the 'DH-ORC'. In the 'DH' system, the design outdoor

temperature is higher to avoid oversizing the geothermal heat source. Too many geothermal wells would result in a low capacity factor of the EGS and a high capital investment. In the 'DH-ORC' design, the geothermal heat source can be oversized to meet the heat demand at very low ambient temperatures. The additional heat extracted from subsurface is converted into work by the ORC power plant. Because ORC uses the geothermal heat at times when it is not needed for the space heating, the capacity factor of EGS in 'DH-ORC' scenario is very high at 89.5%. In the winter, when the ORC plant does not operate, the high thermal output of EGS reservoir almost eliminates the need for a peaking biomass boiler.

### 4.8.2 Economic and environmental impacts

Both proposed systems meet the heat demand of the Cornell campus. A summary of the economic and environmental impacts of transition to hybrid EGS-biomass systems is provided in Table 4-2. The results for both 'DH' and 'DH-ORC' configurations represent the whole campus energy system including the existing CHP natural gas plant and the remaining steam district heating network.

Implementation of the proposed EGS-biomass systems results in a 13%-15% reduction of $CO_2$ emissions and a 21% reduction in natural gas consumption at Cornell. Expressed on an annual basis, 560 Mscf less of natural gas can be used, which could save Cornell 2.55 M$/year. While achieving both of these goals, implementation of EGS increases the LCOE of the existing system by 0.72-0.81¢/$kWh_e$ (21-23%). The proposed systems require a 22 to 34 M$ capital investment. They cannot compete with the existing CHP plant on purely economic basis as long as social and environmental effects of fossil fuels consumption are not accounted for. The

primary reasons for this are a low natural gas price and high energy conversion efficiency of the existing state of the art CHP system at Cornell.

The LCOE for all three discussed energy systems is below the typical market prices. This is because of the pre-existing infrastructure at Cornell, which capital investment cost has only partially been included in the economic analysis.

*Table 4-2: System performance metrics*

| Scenario | Current System | DH | DH-ORC |
|---|---|---|---|
| Share of district heat supplied by | | | |
| Natural gas | 100% | 75% | 75% |
| EGS | 0% | 24% | 24.9% |
| Biomass | 0% | 1% | 0.1% |
| Performance metrics | | | |
| LCOE, ¢/kWh$_e$ | 3.5 | 4.22 | 4.31 |
| Capital investment, M$ | - | 22 | 34 |
| Produced electricity, GWh$_e$ | 221 | 192 | 200.3 |
| Purchased electricity, GWh$_e$ | 29 | 58 | 49.7 |
| Net annual $CO_2$ emissions, t/yr[1)] | 175,000 | 152,000 | 149,500 |
| Reduction in $CO_2$ emissions | - | 13.2% | 14.7% |
| Heat losses from the whole DH network | 18% | 15.7%[2)] | 16%[2)] |

[1)] Includes $CO_2$ emissions from the purchased electricity

[2)] Heat losses from part of the DH system, which was converted from steam to hot water are 7.2% and 8.4% for the 'DH' and 'DH-ORC' systems, respectively.

The influence of the design ambient temperature on the cost of electricity from the Cornell energy system is presented in Figure 4-5.

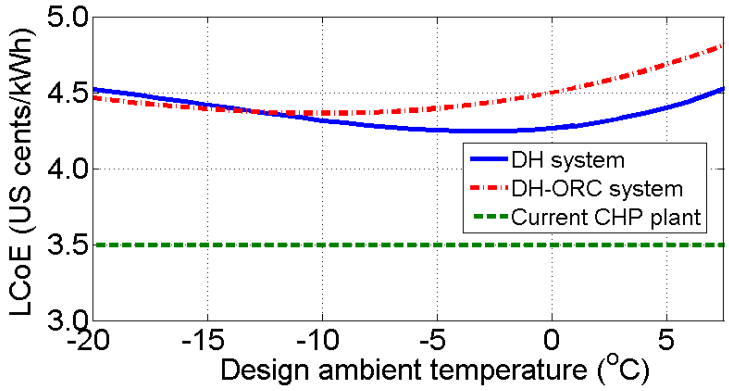


*Figure 4-5: Variation in the levelized cost of electricity with the design ambient temperature.*

With a limited number of existing Enhanced Geothermal Systems, the performance of subsurface reservoir remains uncertain. The presented analysis assumes that the EGS technology can provide well productivities, O&M costs, and reservoir lifetimes which are comparable to low-grade hydrothermal systems. A poor performance in any of these areas, which can be encountered particularly at the early stages of commercial-scale EGS development, would increase the LCOE. To quantify the impact of lower well productivities in the EGS, a sensitivity analysis was performed. The results are presented in Figure 4-6. While well productivity has an impact of the price of delivered end-product, a 50% reduction in the geothermal fluid mass flow rate only increases the LCOE about 10%. This low impact on the LCOE is partially due to the fact that only 24% of the district heating demand is supplied by the EGS. With a full conversion of Cornell Energy System to EGS, the economic impact of lower well productivities would be significantly greater.

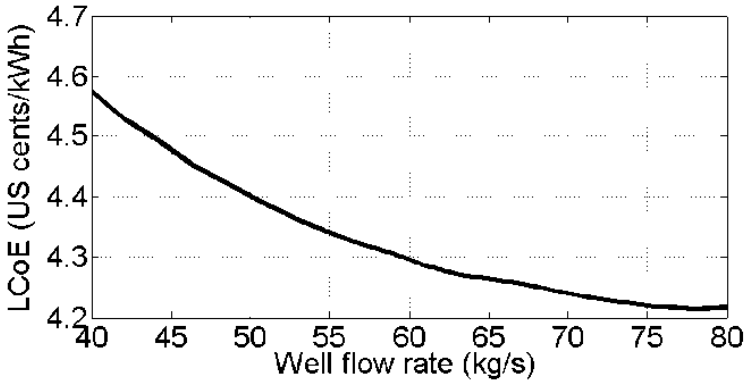


*Figure 4-6: Sensitivity of the levelized cost of electricity in the 'DH' scenario to geothermal well productivity.*

## 4.9 Conclusions

This work analyzed the viability of covering the energy demand of a fraction of the Cornell University campus with two of the most available and potentially economically feasible renewable resources in the Northeast: low-temperature geothermal and biomass. The proposed energy system is isolated from the existing Cornell CHP power plant, so it can also be potentially implemented in a similar form in other communities.

In the existing market of low natural gas prices it is difficult for low-grade geothermal district heating systems to replace the existing 80% efficient gas-fired combined cycle CHP plant on a purely economic basis. However, the proposed EGS achieve acceptable economic performance and provide buffer from the price volatility of fossil fuels. They can be economically superior to many other energy sources including decentralized coal and oil boilers. The advantage of hybrid geothermal-biomass systems would be the highest in locations where district heating systems are fueled by fossil fuel boilers.

Hybrid geothermal-biomass district heating systems have a significant advantage over combined cycle CHP plants in terms of $CO_2$ emissions. Implementation of the proposed systems results in a 13%-15% reduction of $CO_2$ output, while increasing the LCOE of Cornell energy system by only 0.72-0.81¢/kWhe.

Both heat cascading in greenhouses and load splitting between EGS and biomass boiler support lower investment costs and contribute to higher energy utilization. Further efficiency improvements can be achieved by retrofitting low-temperature space heating systems into the campus buildings. All new buildings should be designed to use such space heating systems as well. Transition to a low-temperature space heating would also result in a better cooling of the district heating water and thus provide improved utilization of the geothermal resource. This would be particularly important for expansion of the renewable heating system beyond the area described in this work, in which case no additional demand for low grade heat could be provided by the greenhouses.

## 4.10 Acknowledgements

The content of this chapter is based on the following publication:

Lukawski, M., Vilaetis, K., Gkogka, L., Anderson, B., Tester, J. (2013) "A Proposed Hybrid Geothermal-Natural Gas-Biomass Energy System for Cornell University. Technical and Economic Assessment of Retrofitting a Low-Temperature Geothermal District Heating System and Heat Cascading Solutions', Thirty-Eighth Workshop on Geothermal Reservoir Engineering, Stanford University, 2013

This work was done in collaboration with two M.Eng. students in Chemical Engineering at Cornell University: Lizeta Gkogka and Konstantinos Vilaetis. Both of them deserve a special recognition for their contributions to research on Cornell energy network, as well as design and optimization of the proposed hybrid renewable energy system.

## 4.11 References

Beckers, K. F., Lukawski, M. Z., Reber, T. J., Anderson, B. J., Moore, M. C., and Tester, J. W. (2013), "Introducing Geophires V1.0: Software Package for Estimating Levelized Cost of Electricity and/or Heat from Enhanced Geothermal Systems", Proceedings, Thirty-Eighth Workshop on Geothermal Reservoir Engineering, Stanford University, CA

Bergman, P. C., Boersma, A. R., Zwart, R.W., Kiel, J. H. (2005), "Torrefaction for biomass co-firing in existing coal-fired power stations", ECN Biomass, SenterNovem project no. 2020-02-12-14-001, Netherlands, 71p.

Boyd, T., Rafferty, K. (2008), "Geothermal Greenhouse Information Package", at <http://geoheat.oit.edu/pdf/green.pdf>

Cornell University (2009), Climate Action Plan, at <http://www.sustainablecampus.cornell.edu/climate>

Cornell University Energy and Sustainability (2013), How Lake Source Cooling Works, at <http://energyandsustainability.fs.cornell.edu/util/cooling/production/lsc/works.cfm>

Cornell University Facilities Services (2013), at <http://www.fs.cornell.edu/>

Cornell University Facilities Services (2013), Real Time Building Utility Use Data, at <http://portal.emcs.cornell.edu/>

EERE (The Office of Energy Efficiency and Renewable Energy, 2013), U.S. Department of Energy, EnergyPlus Energy Simulation Software, TMY3 (Typical Meteorological Year 3 Weather Data), at <http://apps1.eere.energy.gov/buildings/energyplus/weatherdata_about.cfm>

Fox, D. B., Sutter, D., Beckers, K. F., Lukawski, M. Z., Koch, D. L., Anderson, B. J., Tester, J. W. (2013), "Sustainable heat farming: Modeling extraction and recovery in discretely fractured geothermal reservoirs", Geothermics, 46, 42– 54

Fox, D.B., Sutter, D. and Tester, J. W. (2011), "The thermal spectrum of low-temperature energy use in the United States", Energy Environ. Sci., 4, 3731

IEA (International Energy Agency, 2011), "Geothermal Heat and Power: Technology Roadmap", Paris, France, 52 p.

Intratec (2012), Chemical Plant Construction Cost Index (IC Index), Intratec Knowledge Base, at <http://base.intratec.us/home/ic-index>

Lukawski, M. (2010), "Optimization of the Operation of Space Heating Systems Connected to District Heating for an Improved Cooling of the Primary Water" M.S. Thesis, AGH University of Science and Technology, Cracow, Poland, 84 p.

NYISO (New York Independent System Operator, 2012), at <http://www.nyiso.com/public/markets_operations/index.jsp>

Perry, R. H., Green, D. W. (2008), "Perry's chemical engineers' handbook", eight edition, McGraw-Hill, 2400 p.

Petitjean, R. (1994), "Total Hydronic Balancing: A handbook for design and troubleshooting of hydronic HVAC systems", Tour & Andersson AB, 485 p.

Rafferty, K. (1996), "Selected cost considerations for geothermal district heating in existing single-family residential areas", at <http://geoheat.oit.edu/pdf/tp93.pdf>

Shope, E. N., Reber, T. J., Stutz, G. R., Aguirre, G. A., Jordan, T. E., and Tester, J. W. (2012) "Geothermal Resource Assessment: A Detailed Approach to Low-Grade Resources in the States of New York and Pennsylvania." Proceedings, Thirty-Seventh Workshop on Geothermal Reservoir Engineering, Stanford University, CA

Tester, J. W., et al. (2006), "The Future of Geothermal Energy: Impact of Enhanced Geothermal Systems (EGS) on the United States in the 21st century", DOE contract DE-AC07-05ID14517, Boston, MA, 370 p.

Valdimarsson, P. (1993), "Modelling of Geothermal District Heating Systems", PhD Thesis, University of Iceland, Reykjavik, Iceland, 144 p.

# Part II

# Measurements of Isobaric Heat Capacity of Fluids

# 5 FLOW CALORIMETER FOR MEASURING ISOBARIC HEAT CAPACITY OF FLUIDS

## 5.1 Introduction

The further development of Organic Rankine Cycle (ORC) power plants requires an improved knowledge of the thermophysical properties of working fluids. Accurate prediction of the pressure-volume-temperature (PVT) properties of less common pure fluids could result in a discovery of new, more efficient refrigerants. In addition, better models of mixture properties would facilitate development of a new type of ORC plants, which achieves higher efficiency by using non-isothermal evaporation and condensation. Accurate characterization of fluid properties near the critical point and at supercritical conditions is particularly important, because the existing property models are often the less accurate at these conditions.

In addition to thermodynamic cycle design, there are many other reasons to continue the expansion of the thermodynamic property library. The progress of engineering and geosciences to ever more challenging conditions requires knowledge of fluid properties at high pressures and temperatures, often above the critical point. For example, deep subsurface conditions, like those encountered in oil and gas reservoirs, involve complex multi-component fluids at high temperatures and pressures. Other subsurface engineering applications such as carbon sequestration and EGS, provide additional motivation for thermophysical property characterization at supercritical conditions. Lastly, supercritical $CO_2$ fluid extractions commonly use co-solvents, such as light hydrocarbons or alcohols (Beckman, 2004; Brennecke

& Eckert, 1989), but the properties of such mixtures are not always sufficiently well determined.

For the engineering purposes, the PVT fluid properties are often described using equations of state (EOS). Equations of state are typically fit by regressing a functional model to experimental data. The accuracy and range of a given EOS, whether it is specific to a single fluid or a particular set of similar fluids, depends on the measured experimental properties on which it was built. In order to reliably predict properties, accurate experimental data are needed over a broad range of temperatures and pressures for pure fluids and fluid mixtures. Predictive accuracy of fluid properties is compromised when property data is sparse (e.g. for many fluid mixtures) or the thermophysical behavior of the fluid is difficult to measure (e.g. near a fluid's critical point). In addition, experimental data can provide insight into fluids' inter- and intramolecular interactions (Kutney, Reagan, Smith, Tester, & Herschbach, 2000). To validate and improve EOSs and further scientific understanding of the thermophysical behavior of supercritical fluids and fluid mixtures, accurate experimental measurements of thermodynamic properties are required for dense fluid mixtures over a range of temperatures and pressures.

Among the experimentally accessible thermodynamic properties, the measurement of isobaric heat capacity ($C_p$) is of particular importance because of its direct application in many engineering and heat exchange processes. The three predominate calorimetric methods for measuring a dense fluid's $C_p$ are Calvet calorimetry (Calvet & Prat, 1963; Dordain, Coxam, & Grolier, 1994), Workman calorimetry (Bishnoi, 1971; Boulton & Stein, 1993; Workman, 1930), and flow calorimetry (de Groot & Michels, 1948; Ernst & Hochberg, 1989; Ernst, Maurer, & Wiederuh, 1989; Rivkin & Gukov, 1968; San Jose, Mellinger, & Reid, 1976). Calvet calorimeters offer the advantage of an accurate differential measurement of heat capacity to a

known standard, while their shortcomings include a conversion from volumetric to massic heat capacity and an inevitable loss of fluid from the measurement cell when operated in a constant pressure mode. The Workman calorimeter measures the ratio of $C_p$ at the condition of interest to $C_p^*$ at a known, typically ideal, condition. By measuring a heat capacity ratio, Workman calorimetry offers a significant advantage by eliminating the necessity of a mass or volumetric flow rate measurement. Accurate knowledge of the measured fluid's heat capacity at a reference condition limits this method's effectiveness for fluid mixtures and less common pure fluids.

Flow calorimetry involves pumping fluid at a constant rate through a length of tubing at a specified temperature and pressure, delivering a known amount of thermal energy to that fluid, and measuring the resulting temperature rise. As implemented by Ernst and his co-workers (Ernst & Philippi, 1990; Ernst, Keil, Wirbser, & Jaeschke, 2001) and many other researchers (He, Su, Liu, Qi, & Lv, 2015; Miyazaki, Hejmadi, & Powers, 1980; Miyazawa, Kondo, Suzuki, & Sato, 2012; Saitoh, Sato, & Watanabe, 1989; Sandarusi, Mulia, & Yesavage, 1992; Segovia, Vega-Maza, Chamorro, & Martín, 2008; Zheng, Gao, Chen, Meng, & Wu, 2014), flow calorimetry is deployed as a robust absolute measurement of heat capacity, as opposed to the aforementioned measurement techniques which all reference a standard. The flexibility of the method necessitates additional measurements (particularly mass flow rate) and special attention to heat loss issues. It is worth noting that other types of flow calorimeters which do not employ absolute measurement techniques exist and include setups like the Picker flow calorimeter (Picker, Leduc, Philip, & Desnoyers, 1971) which uses a differential technique particularly well-suited for electrolyte mixtures.

This study focused on design, construction, and use of a flow calorimeter suitable for $C_p$, measurements of single-phase pure fluids and mixtures at sub- and supercritical conditions. The

calorimeter's accuracy is demonstrated for fluids and fluid mixtures over a wide range of temperatures (25–150 °C), pressures (1–300 bar), and densities. The basic accuracy of the calorimeter is estimated to be ±1%. A detailed description of the apparatus design and typical operating procedures follows. Measurements validating the operation of the calorimeter were done on pure carbon dioxide, pure methanol, and low mole fraction (1.27% and 1.42%) methanol in carbon dioxide mixtures. In the future, the calorimeter will be used to measure $C_p$ of promising low-GWP working fluids for ORC power plants and compression-refrigeration systems.

The work described in this chapter has been done in collaboration with Mitchel Ishmael. Both authors were involved in the conceptual design, building, and testing the calorimeter. In addition, Mitchel Ishmael has done a number of improvements to the system resulting in a substantial increase in the measurement accuracy and performed the final measurements and calculations for this work. The content of this chapter was previously published in the following article, which was written by both Mitchel Ishmael and Maciej Lukawski: Ishmael, M., Lukawski, M., Tester, J. (2016) Isobaric heat capacity (Cp) measurements of supercritical fluids using flow calorimetry: equipment design and experimental validation with carbon dioxide, methanol, and carbon-dioxide-methanol mixtures, *Journal of Supercritical Fluids*, 117.

## 5.2 Experimental method

### 5.2.1 Calorimeter operating principles

A flow calorimeter at steady state operating conditions approximates the thermodynamic definition of isobaric heat capacity ($C_p$) by replacing differential quantities with finite differences, as shown in Equation (1).

$$C_P(T,P,x) \equiv \left(\frac{\partial H}{\partial T}\right)_{P,x} \approx \left.\frac{\dot{Q}}{\dot{m}\Delta T}\right|_{low\ \Delta P} \qquad (5\text{-}1)$$

While maintaining a small pressure drop across the calorimeter, heat $(\dot{Q})$ is continuously added to a fluid at steady mass flow $(\dot{m})$ passing through the calorimeter, and the resulting temperature rise $(\Delta T)$ is measured. Equation (1) conveys some of the challenges of flow calorimetry: for an accurate measurement, the heat loss must be nearly eliminated or accurately quantified, the fluid must be well-mixed and its mass flow rate needs to be measured accurately, the pressure drop across the calorimeter must be small in order to approximate the isobaric condition, and the loss in accuracy due to approximating differentials with finite quantities needs to be addressed. The following sections describe the design of the experimental apparatus and the measurement methodology used in this study.

### 5.2.2 Description of the flow system

As shown in Figure 5-1, the dual syringe pump (1A) draws the compressible fluid, a 99.99% pure $CO_2$, from the gas cylinder (1B) and dispenses it through a check valve (1C) at a constant volumetric flow rate into one port of a mixing tee (1F). The second component, 99.9% pure methanol, enters through the other port of the mixing tee pumped by a reciprocating positive

displacement pump (1E), also operating at constant volumetric flow rate. The mass flow rate of the incompressible fluid is measured using a scale (1D) and a stop watch. The fluid mixture, exiting the mixing tee, enters a Coriolis mass flow meter (1G) where the mixture flow rate is measured. Next, the fluid passes through three sections of tubing placed inside of a temperature controlled fluidized alumina bath (1J): a preheat section, the calorimeter assembly, and an exhaust section. Preheat and exhaust tubing ensure temperature stability of the fluid at the inlet and outlet of the calorimeter assembly, and the thermal bath maintains a temperature stability of ±0.1 °C.

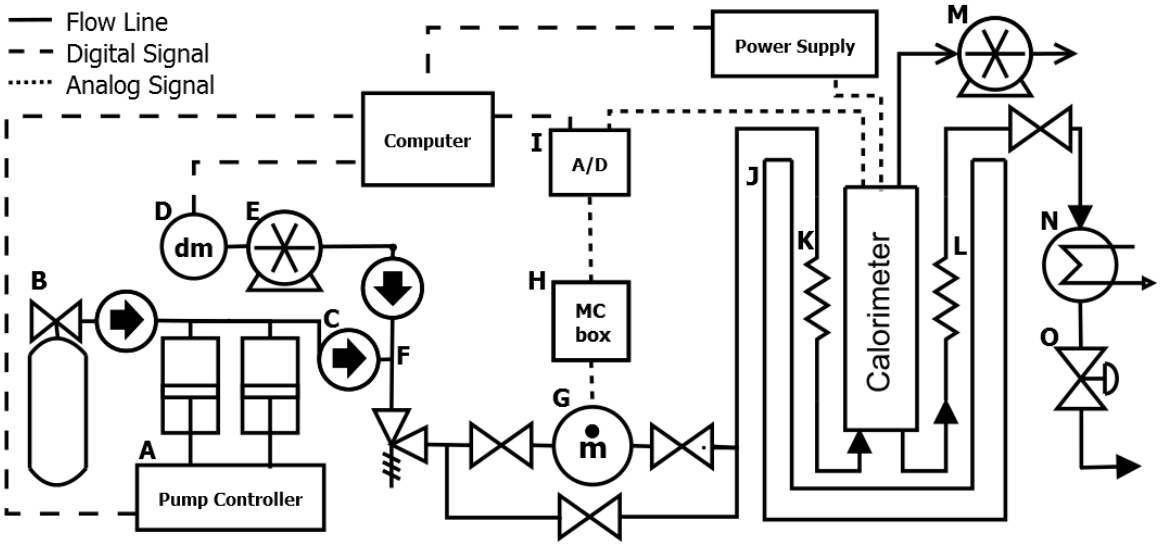


*Figure 5-1: Process flow diagram of the calorimeter system including dual syringe pump and controller (A), gas cylinder (B), check valve (C), mass balance (D), high pressure liquid chromatography (HPLC) pump (E), pressure relief valve (F), Coriolis mass flow meter (G), measurement conversion box (H), analog to digital conversion box (I), fluidized sand bath (J), vacuum pump (M), exhaust heat exchanger (N), and back pressure regulator (O).*

The calorimeter assembly, schematically detailed in Figure 5-2, consists of a U-tube (2B) placed inside a vacuum chamber (2C) held at 0.05 mbar by a vacuum pump. Two thermocouples (2A and 2I), placed at the inlet and outlet of the calorimeter, and a heating element (2F), near the bend of the U-tube, are kept in direct contact with the fluid being measured. A power supply provides electric current to the heating element made of Ni-Cr wire (2F) through insulated copper wires (2H). Pressure taps placed at the inlet and outlet of the calorimeter assembly are used to measure the absolute pressures. Back pressure regulators (1O) control and maintain the pressure in the flow system, and a series of regulators are used to let down the pressure before exhaust.

The main sub-components of flow calorimeter are listed in Table 5-1.

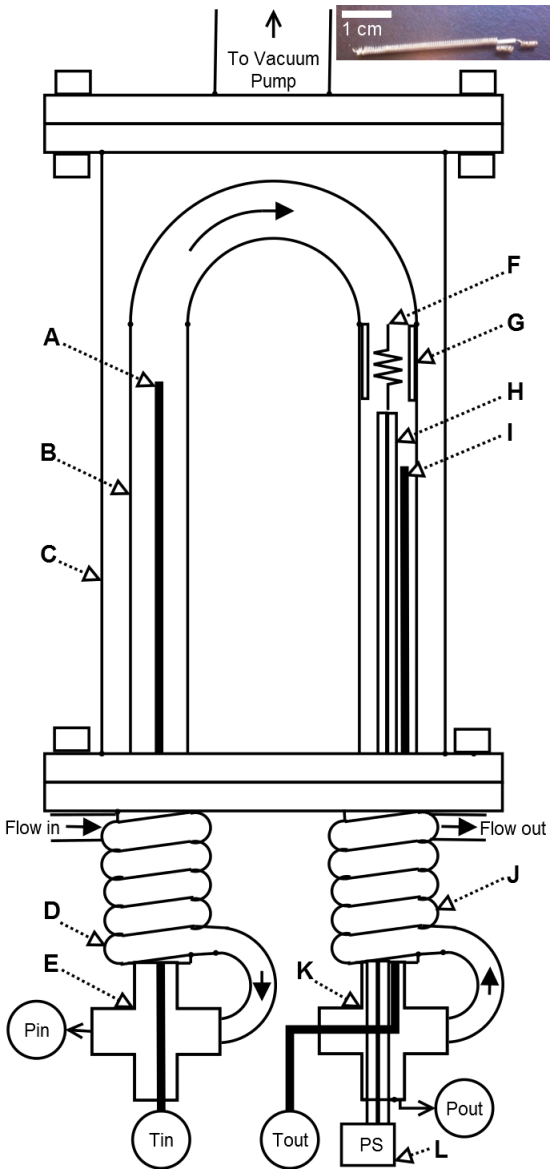


*Figure 5-2: Schematic of the calorimeter assembly: vacuum chamber, 6.35 cm OD (C), flow tubing, 0.64 cm OD (B), thermocouples (A and I), heating element/Ni-Cr resistor (F), ceramic insulation (G), 18 AWG copper wires attached to the heating element (H), inlet and outlet thermal equilibration length of tubing, 0.32 cm OD (D and J respectively), crosses at the inlet (E) and outlet (K), power supply (L, placed outside the heated bath). Inset: The custom-made Ni-Cr heating element.*

*Table 5-1: Selected sub-components used in the flow calorimeter*

| Component name | Supplier and model |
|---|---|
| Dual syringe pump ($CO_2$) | Teledyne ISCO 100DX, controller, and temperature control jackets cooled using refrigeration system |
| HPLC pump (methanol) | Agilent 218 solvent delivery pump |
| Coriolis mass flow meter | GE Rheonik RHM 015 |
| Alumina bath | Techne SBL-2D with TC-9D controller |
| Thermocouples | E-type, 1/16", Omega |
| Vacuum pump | Oerlikon Leybold |
| Power supply | Tektronix PWS4305 |
| Scale (methanol) | Mettler Toledo |
| Back pressure regulator | Equilibar EB1 |
| Heating element | 34 AWG bar Ni/Cr wire wound around 0.4 mm hollow alumina tube |
| Wires powering heating element | 18 AWG copper wires, 0.007" insulation |
| Flow tubing | Inconel, 1/4" tubing with 0.049" wall thickness |

A number of design measures have been incorporated into the system to increase the calorimeter's accuracy and decrease the measurement time. Heat losses were reduced by simultaneously lowering the driving forces for heat transfer and increasing the thermal resistance (Ernst et al., 1989; Rivkin & Gukov, 1968). Use of thin-walled (1.2 mm) 6.35 mm outer diameter Inconel tubing in the calorimeter reduced both heat conduction along the fluid flow path and the thermal inertia. The heating element, its connecting wires, and the thermocouples were placed in direct thermal contact with the fluid, decreasing heat loss and reducing the time needed to reach steady state during experiment typically to 1.5 minutes. Convective heat losses from the calorimeter's U-tube were curtailed by encasing it in a vacuum chamber. To reduce heat losses by radiation, the flow tubing has been thoroughly polished. In addition, any residual heat losses from the calorimeter were compensated by placing it in a

thermal bath held at the inlet temperature of the calorimeter, substantially lowering the thermal driving force for conduction, convection, and radiation to produce nearly adiabatic conditions inside the calorimeter.

The fluid must be properly mixed while maintaining a small pressure drop for Equation 1 to be valid. To assure efficient heat transfer between the heating element and the passing fluid, the bare Ni/Cr heater wire, shown inset in Figure 5-2, was wound in a coil to act as a turbulence promoter. The section of Inconel tubing where the measurements occur is short (0.4 m), and the consequential pressure drop, approximately 0.05 bar, is negligible.

### 5.2.3 Assessment of measurement uncertainty

The uncertainties of the constitutive measurements for calculating $C_p$ are listed in

Table 5-2 along with the uncertainty contributions resulting from assigning a measured $C_p$ value to a particular temperature, pressure, and composition.

*Table 5-2: The experimentally accessible properties required for a flow calorimetric determination of isobaric heat capacity. Contribution of each measured property to the overall measurement uncertainty is provided.*

| Measured Property | Property Range | Uncertainty contributions | Range uncertainty |
|---|---|---|---|
| Temperature | 60 - 200 °C | Platinum Resistance Thermometer (PRT) standard | ± 0.1 °C |
| | | Thermocouple stability and repeatability | ± 0.05 °C |
| Differential temperature | 2.0 - 3.5 °C | Observed average temperature difference inconsistency | ± 0.004 °C |
| Total mass flow rate | 12 - 19 g/min | Coriolis mass flow meter accuracy specification | ± 0.05 g/min |

| | | | |
|---|---|---|---|
| | | Signal drift for a constant flow rate | ± 0.06 g/min |
| Methanol mass flow rate | 0.1 - 0.15 g/min | Differential mass measurement of methanol component | ± 0.04 g |
| | | Stopwatch accuracy | ± 0.05 s |
| Pressure | 100 - 300 bar | Accuracy and repeatability of pressure transducer | ± 0.5 bar |
| Heater power | 1.1 - 2.2 W | Accuracy and stability of applied voltage and current | ± 0.002 W |

To reduce the temperature measurement uncertainty, the thermocouple located at the inlet of the calorimeter was calibrated with a platinum resistance thermometer (PRT) standard. The total uncertainty in this absolute temperature measurement is listed in Table 5-2 and includes uncertainties in the following: the PRT's ice point calibration, conversion of the PRT's resistance signal to temperature, analog to digital signal conversion of the PRT signal, and the repeatability of the thermocouple measurement in comparison to the PRT standard.

The difference in the fluid's temperature as it passes through the calorimeter, denoted as $\Delta T$ in Equation (1), is defined as the temperature of the fluid exiting the calorimeter minus the temperature of the fluid at the entrance to the calorimeter. This quantity is continuously monitored over the course of a heat capacity measurement. Sources of error, such as the Joule-Thomson effect or any measurement offsets between the thermocouples, are greatly reduced by comparing the temperature difference over two distinct periods of operation, when heat is being added to when it is not. Measurement of the temperature difference when heat is not being added to the fluid, termed a "blank experiment" by some authors (Ernst et al., 1989), significantly reduces many potential systematic errors. The observed temperature inconsistency, listed in Table 5-2, refers to a repeated experimental observation; the temperature

difference before heat ($\dot{Q}$) was applied was regularly unequal to the temperature difference after the heater was again off. The most likely cause of this temperature difference inconsistency is temperature fluctuations within the fluidized alumina bath.

Based on repeated $C_p$ measurements, an optimal induced temperature difference in the calorimeter was established to be 2.0–3.5 °C. This range represents a compromise between measurement uncertainty and resolution. The method of approximating the differential temperature increase with a finite temperature increase, as shown in Equation (1), results in an inherent error at conditions where $C_p$ shows strong dependence on pressure, temperature, and composition. This systematic error is particularly large in the vicinity of critical point, where physical properties show strong dependence on these variables. Depending on the sensitivity of the heat capacity function, one may incur significant errors by inducing too large a temperature change, as illustrated in Figure 5-3 for pure carbon dioxide.

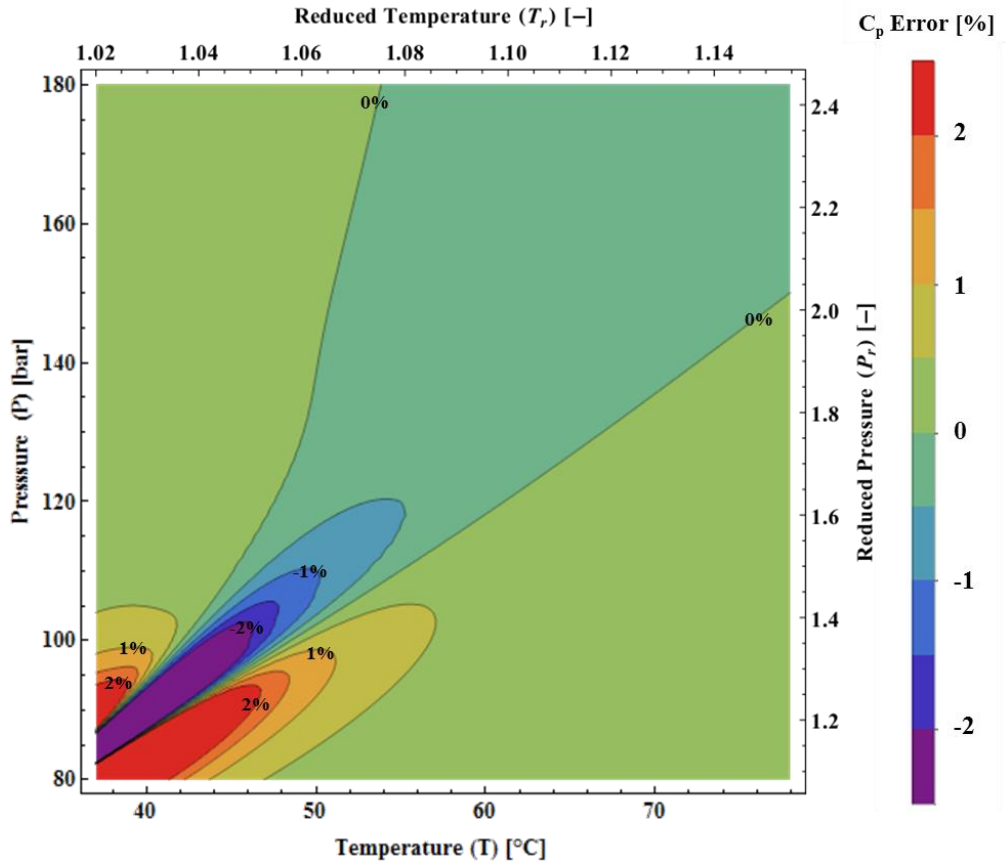


*Figure 5-3: Calculated systematic errors in heat capacity, shown as a percent error, due to replacement of a differential temperature rise in Equation 1 with a finite temperature rise, here $\Delta T$ = 4 °C. The Span and Wagner EOS (Lemmon, Huber, & McLinden, 2013; Span & Wagner, 1996) for carbon dioxide is treated as the true heat capacity function. Integral averages of heat capacity were calculated over the induced temperature rise and compared to the heat capacity value at the average temperature. A temperature rise of 4 °C was chosen based on existing calorimeters described in literature (Ernst et al., 1989; Rivkin & Egorov, 1959; Wu, Yu, Zhong, & Lin, 1995).*

A Coriolis mass flow meter was used to measure mass flow rate, eliminating the need for fluid density data. Accuracy specifications from the manufacturer were used and further in-house calibration was done to establish typical measurement drift. Mass flow rate of the fluid

mixture's less volatile component (methanol in this study) is taken by measuring the mass difference of the fluid reservoir with time.

The pressure transducer was installed as supplied from the manufacturer, with no further calibration done. The accuracy of the transducer includes additional uncertainty from analog to digital signal conversion.

The power supply to the heating element was calibrated with a highly accurate voltmeter. Uncertainty in the heater power, listed in Table 5-2, includes a correction for the additional resistance caused by the copper wire linking the power supply to the heating element.

As a next step, the overall uncertainty in measured heat capacity due to specifying a particular temperature, pressure, and composition was assessed. If a fluid's heat capacity is very sensitive to incremental changes in its temperature, pressure, and composition, the total $C_p$ uncertainty will be heavily influenced by the uncertainty in these three variables. To quantify this effect, experimental data as well as three different EOS models were used to evaluate the following partial derivatives for carbon dioxide, methanol, and carbon dioxide-methanol mixtures (De Reuck & Craven, 1993; Kunz & Wagner, 2012; Span & Wagner, 1996):

$$\left(\frac{\partial C_P}{\partial T}\right)_{P,x};\left(\frac{\partial C_P}{\partial P}\right)_{T,x};\left(\frac{\partial C_P}{\partial x}\right)_{T,P} \qquad (5\text{-}2)$$

Using these partial derivatives, all uncertainties in temperature, pressure, and composition have been converted into uncertainty in the measured heat capacity value. In regions where $C_p$ strongly fluctuates, such as the near critical region, the uncertainty increases by up to 2%. The partial derivatives in Equation (5-2 were also used to shift the experimentally measured values to round values of temperature, pressure, and composition that are listed in Table 5-3, Table

5-4, Table 5-5. The resulting shifts in the measured heat capacity values were insignificant when compared to the measurement uncertainty. Finally, in an effort to reduce the uncertainty from random noise, repeatability, and hysteresis, each experimental measurement was repeated three times.

To demonstrate that the calorimeter operated with negligible heat loss, heat capacity measurements of carbon dioxide were taken at a high temperature (150 ºC) where the fluid's heat capacity is relatively low (1.64 J/gK) and the partial derivatives of $C_p$ with respect to temperature and pressure are small. Keeping flow rate constant, different amounts of thermal energy were added to the fluid in order to vary the induced temperature rise. An increase in the observed heat capacity would indicate heat loss from the calorimeter due to the increased temperature difference between the calorimeter and its surroundings. Figure 5-4 verifies the near adiabaticity of the calorimeter because the heat capacity measurement shows no perceivable dependence on the induced temperature difference.

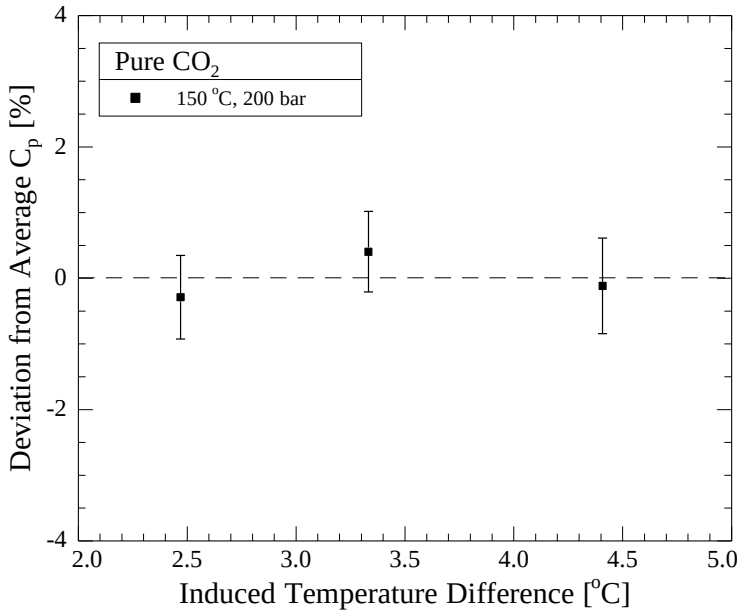


*Figure 5-4: Isobaric heat capacity measurements of pure carbon dioxide taken at 150 °C and 200 bar as a function of the induced temperature difference. The y-axis is the percent deviation of a singular experimental measurement from the average of all the measurements at this condition. The measurements shown here were taken at the same mass flow rate (10 g/min). With the induced temperature difference nearly doubled (4.4 ºC compared to 2.5 ºC), no appreciable change in the measured heat capacity was observed*

## 5.3 Results and discussion

The calorimeter's accuracy was verified with experimental measurements for both pure fluids and fluid mixtures. Carbon dioxide experiments were used to establish satisfactory measurement of the base quantities ($\dot{Q}, \dot{m}, \Delta T, P, and\ T$) because it is an extremely well characterized fluid (Span, 2013). Measurements of pure methanol, under fluid conditions very different to supercritical carbon dioxide, helped to demonstrate the calorimeter's versatility over a range of fluid densities. With regard to mixtures, the accuracy of controlling the fluid's

composition ($x$) and its effect on measured heat capacity were determined by comparing the results of measurements to the literature $C_p$ values of mixtures of methanol in carbon dioxide at low mole fractions of methanol (Boulton & Stein, 1993).

### 5.3.1 Physical calibration of the calorimeter

Following the practice established by other researchers (Rogers & Pitzer, 1981; Smith-Magowan & Wood, 1981; Vesely, Svoboda, & Pick, 1977; White & Downes, 1988), after determining the optimal ranges of mass flow rate, differential temperature, and heater power, a physical calibration of calorimeter was performed. Physical calibration accounts for non-idealities and systematic experimental errors present within the calorimeter which have not been mitigated by careful equipment design and operating procedures. Calibration was done by comparing 34 heat capacity measurements of pure $CO_2$ at 150 ºC and pressures between 100 and 300 bar to reference values calculated with the Span and Wagner EOS (Span & Wagner, 1996). Span and Wagner report an accuracy of ±0.6% for $C_p$ in this temperature and pressure region. Minimization of the absolute differences between experimental measurements and the EOS produced a 1.4% correction factor. All the heat capacity values presented in this chapter are 1.4% lower than the raw experimental measurements. Subsequent sections will demonstrate that this 1.4% physical calibration factor is largely independent of the temperature, pressure, and density for carbon dioxide, methanol, and carbon dioxide-methanol mixtures.

This work's calibration correction compares favorably with corrections of 2–15% reported by others (Fortier, Benson, & Picker, 1976; Rogers & Pitzer, 1981).

### 5.3.2 Measurements of pure carbon dioxide and pure methanol

The isobaric heat capacity of pure carbon dioxide was measured along 60, 90, 120, and 150 ºC isotherms for pressures ranging from 100 to 300 bar. The results are listed in Table 5-3 and plotted in Figure 5-5. The measurements of this study agree well with the high accuracy predictions of the Span & Wagner EOS (Span & Wagner, 1996) and experimental data collected by Ernst et al. (Ernst et al., 1989), as indicated by the mean percent errors of 0% and 0.3%, respectively. The Span and Wagner estimates are often taken as the standard reference values by numerous investigators. In nearly all cases, this study's measurements, the measurements by Ernst et al., and calculations from the Span & Wagner EOS, are within the estimated uncertainty bounds listed in Table 5-3. The 150 °C isotherm was used for physical calibration, therefore no estimate of measurement error was possible in that region. Measured heat capacity along the 60 °C isotherm tended to be larger than the associated literature values, while at 120 °C the measurements fell below the literature results. The small tendencies to overestimate or underestimate at these isotherms can likely be ascribed to random errors such as measurement drift or slight inaccuracies in calibration. The 60 °C isotherm corresponds to a reduced temperature of 1.1 for $CO_2$, proving this apparatus's ability to make accurate measurements proximate to the critical point, where $C_p$ maxima are large.

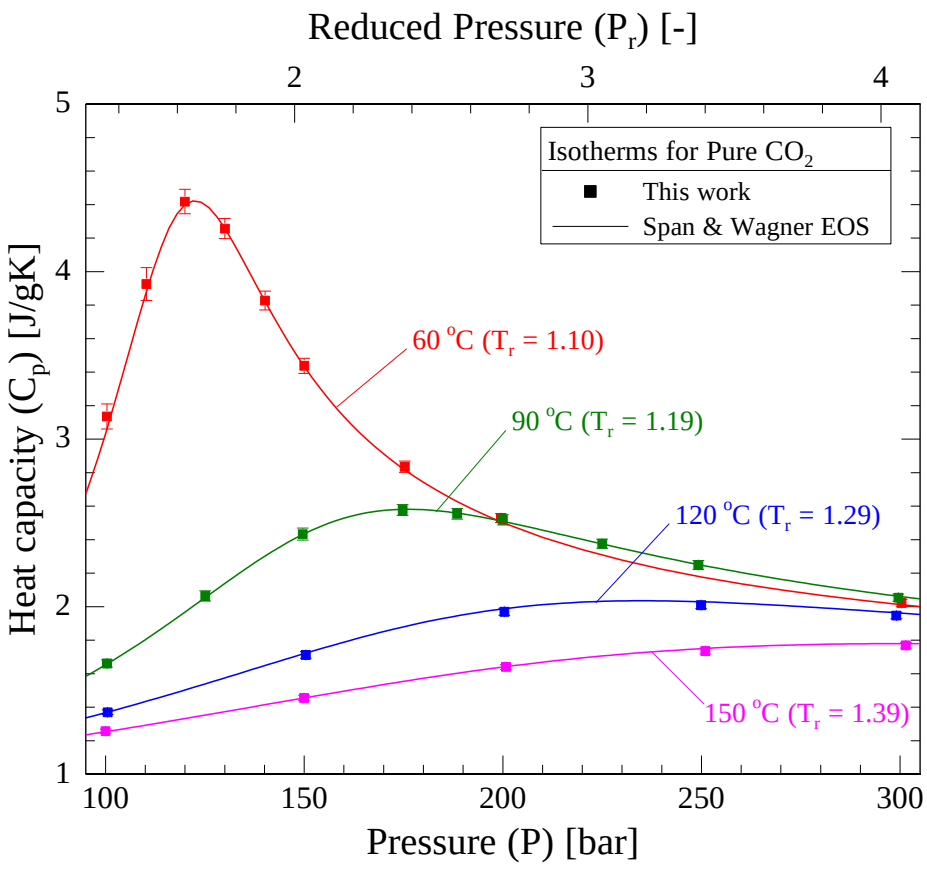


*Figure 5-5: Comparison of the measurements made in this work to reference values reported by Span and Wagner EOS (Span & Wagner, 1996). The data agrees with the Span and Wagner EOS values within the specified measurement uncertainty. Experimental measurements made by Ernst et al. corroborate the Span and Wagner EOS calculations (Ernst et al., 1989) in this supercritical region.*

*Table 5-3: Measured isobaric heat capacity values ($C_p$) of pure carbon dioxide from 60–150 ºC and 100–300 bar. The overall uncertainty ($\delta$) is presented as a percentage of the measured heat capacity. Presented as percent differences, the measurements made in this work are compared to the experimental measurements made by Ernst et al. and the Span and Wagner EOS ($C_{p,lit}$) (Ernst et al., 1989; Span & Wagner, 1996).*

| **Pure $CO_2$** |
|---|

| P [bar] | $C_p$ [J/gK] This Study | Estimated Uncertainty δ [%] | Comparison 100 ($C_{p,lit}$ - $C_p$)/$C_p$ | |
|---|---|---|---|---|
| | | | Ernst et al. | Span and Wagner EOS |
| **T = 60 °C (333 K)** | | | | |
| 100 | 3.08 | 2.4 | -0.2 | -1.6 |
| 110 | 3.88 | 2.5 | 0.9 | -0.7 |
| 120 | 4.39 | 1.7 | 1.0 | 0.3 |
| 130 | 4.26 | 1.4 | -0.3 | 0.1 |
| 140 | 3.83 | 1.5 | -0.4 | -0.1 |
| 150 | 3.44 | 1.3 | 0.0 | -0.1 |
| 175 | 2.84 | 1.2 | -0.5 | -0.7 |
| 200 | 2.52 | 1.0 | -1.4 | -0.9 |
| 300 | 2.02 | 1.1 | -1.2 | -0.5 |
| **T = 90 °C (363 K)** | | | | |
| 100 | 1.65 | 1.4 | 0.4 | 0.0 |
| 125 | 2.06 | 1.5 | 0.4 | -0.2 |
| 150 | 2.44 | 1.5 | 0.5 | -0.1 |
| 175 | 2.58 | 1.3 | 0.5 | 0.1 |
| 189 | 2.55 | 1.3 | - | 0.2 |
| 200 | 2.52 | 1.2 | -0.3 | -0.4 |
| 225 | 2.38 | 1.1 | 0.8 | -0.1 |
| 249 | 2.25 | 1.2 | 0.9 | 0.1 |
| 300 | 2.05 | 1.1 | 0.7 | 0.4 |
| **T = 120 °C (393 K)** | | | | |
| 100 | 1.37 | 1.0 | 0.1 | 0.2 |
| 150 | 1.71 | 1.2 | 1.3 | 0.7 |
| 200 | 1.97 | 1.1 | 1.5 | 1.0 |
| 250 | 2.01 | 1.0 | 1.0 | 1.0 |
| 300 | 1.95 | 1.0 | 0.9 | 0.8 |
| **T = 150 °C (423 K)** | | | | |
| 100 | 1.26 | 1.0 | - | -0.3 |
| 150 | 1.46 | 1.0 | - | -0.1 |

| | | | | |
|---|---|---|---|---|
| 200 | 1.64 | 0.9 | - | 0.0 |
| 250 | 1.74 | 1.0 | - | 0.8 |
| 300 | 1.77 | 1.0 | - | 0.5 |

Heat capacity measurements of pure methanol in both liquid and vapor states are listed in Table 5-4 and plotted in Figure 5-6. In the liquid state, this work's measurements agree to within to 2% with the EOS predictions reported by De Reuck & Craven (1993) and Lemmon, Huber, & McLinden (2013). Previous heat capacity measurements of liquid methanol at high temperatures (Boyette & Criss, 1988) show larger discrepancies compared to EOS predictions, on average 8% higher than our measured values. Given the uncertainty allocation for the methanol EOS in this region, the measurements of this work fit the EOS predictions well. Methanol's heat capacity in the vapor state is more accurately quantified by EOS, to within 1%. The *Cp* measurements in this study are 1% lower than the calculated methanol vapor *Cp*, which is within the 1.2% experimental uncertainty. The measurements for methanol conducted in this study confirm the accuracy of calorimeter across a broad range of fluid conditions.

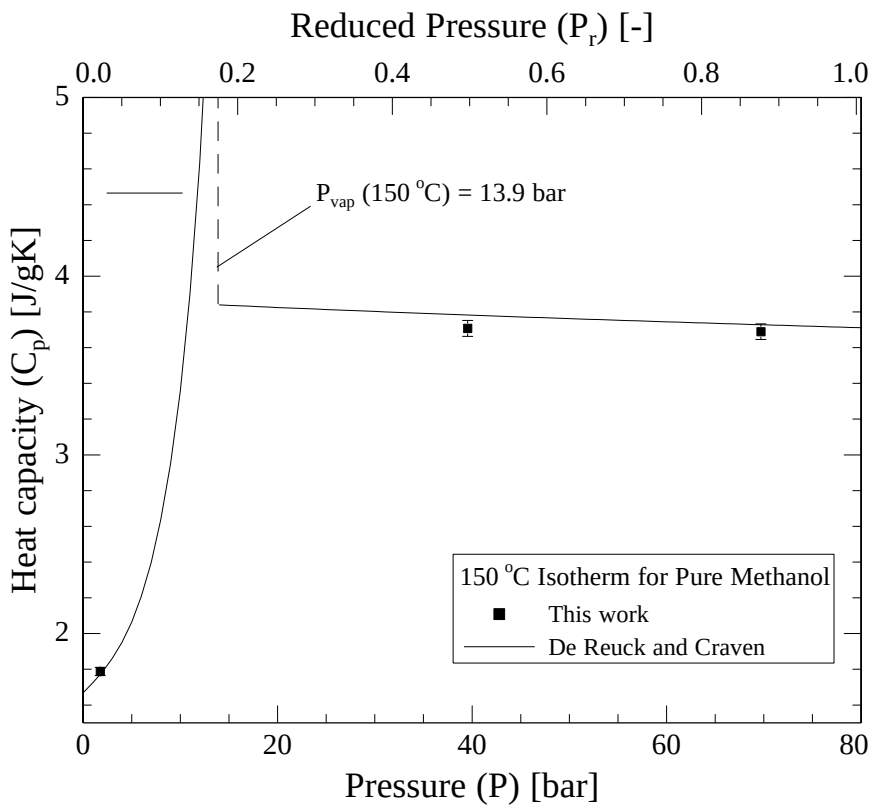


*Figure 5-6: Heat capacity measurements of pure methanol at 150 °C as a liquid, at approximately 40 bar and 70 bar, and as a vapor, at approximately 2 bar. The data agrees with the De Reuck and Craven EOS (De Reuck & Craven, 1993) within the specified measurement uncertainty and the accuracy of the EOS.*

*Table 5-4: Measured isobaric heat capacity ($C_p$) of pure liquid and vapor methanol at 150 °C. The overall uncertainty ($\delta$) is listed as a percentage of the measured heat capacity. The measurements made in this work are compared to the De Reuck and Craven EOS for methanol ($C_{p,lit}$) (De Reuck & Craven, 1993).*

| **Pure Methanol** | | | |
|---|---|---|---|
| **P [bar]** | **This Work $C_p$ [J/gK]** | **Estimated Uncertainty $\delta$ [%]** | **Comparison $100\ (C_{p,lit} - C_p)/C_p$** |
| | | | **De Reuck & Craven EOS** |

| T = 150 °C (423 K) | | | |
|---|---|---|---|
| 2 | 1.80 | 1.2 | -0.9 |
| 40 | 3.71 | 1.2 | 2.0 |
| 70 | 3.69 | 1.2 | 1.0 |

### 5.3.3 Measurements of carbon dioxide – methanol mixtures

Table 5-5 and Figure 5-7 compare the results of this work to the measurements made by Boulton and Stein on low mole fraction methanol in carbon dioxide mixtures (Boulton & Stein, 1993). The uncertainty in composition is estimated as ±4% of the methanol mole fraction. This large compositional uncertainty is due to the low methanol flowrate. The GERG-2008 EOS model results are presented as a comparison, because of the applicability of this EOS for $CO_2$ and existing mixing rules. Fitting of the GERG-2008 model to methanol-carbon dioxide data has occurred (Kunz & Wagner, 2012; Lemmon, Huber, & McLinden, 2013; Lemmon, 2015). Measured $C_p$ values agree favorably with reported values from Boulton and Stein. The measurement at 1.42% methanol, 50 °C, and 73 bar shows the largest deviation but still falls within the experimental uncertainty. Boulton and Stein's claimed uncertainties are shown in Figure 5-7. It is very likely that in this near critical region, where the isobaric heat capacity strongly fluctuates with small changes in temperature, pressure/density, and composition, their uncertainties should be increased beyond their basic ±1% estimate. In any case, the results of this study as well as those by Boulton and Stein agree to within their respective uncertainties.

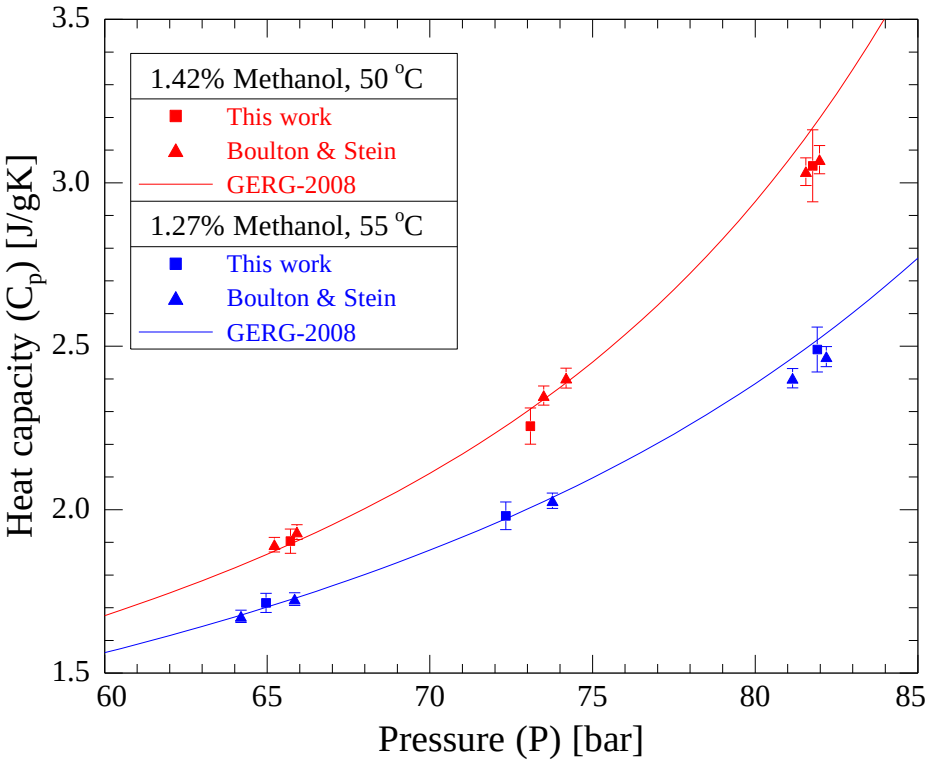


*Figure 5-7: Comparison of this study's measurements to Boulton and Stein's heat capacity measurements (Boulton & Stein, 1993) of low mole fraction methanol in carbon dioxide. The GERG-2008 EOS, the recommended EOS by REFPROP (Lemmon, Huber, & Mclinden, 2013), is compared to both sets of measurements (Kunz & Wagner, 2012).*

*Table 5-5: Measured isobaric heat capacity ($C_p$) of low mole fraction methanol-carbon dioxide mixtures at two isotherms. The overall uncertainty (δ) is listed as a percentage of the heat capacity. The measurements made in this work are compared to the measurements of Boulton and Stein and the GERG-2008 EOS ($C_{p,lit}$) (Boulton & Stein, 1993; Kunz & Wagner, 2012).*

| **Low Mole Fraction Methanol-$CO_2$ Mixtures** | | | | |
|---|---|---|---|---|
| **P [bar]** | **This Work $C_p$ [J/gK]** | **Estimated Uncertainty δ [%]** | **Comparison 100 ($C_{p,lit}$ - $C_p$)/$C_p$** | |
| | | | **Boulton & Stein** | **GERG-2008** |
| **T = 50 °C (323 K), x = 1.42% Methanol in $CO_2$** | | | | |

| | | | | |
|---|---|---|---|---|
| 66 | 1.91 | 1.9 | 1.1 | -0.9 |
| 73 | 2.24 | 2.5 | 3.4 | 2.2 |
| 82 | 3.11 | 3.5 | -1.2 | 2.5 |
| **T = 55 °C (328 K), x = 1.27% Methanol in $CO_2$** | | | | |
| 65 | 1.71 | 1.7 | -0.8 | -0.9 |
| 72 | 1.96 | 2.1 | -0.6 | 0.4 |
| 82 | 2.51 | 2.7 | -2.1 | 1.1 |

## 5.4 Conclusions and future work

Successful operation of flow calorimeters over a wide range of densities and viscosities is often a challenge due to variations in flow regimes, potential heat loss issues, and pressure drop difficulties. After careful design, construction, and calibration, the flow calorimeter detailed in this study achieved ±1% accuracy at temperatures from 25 to 150 °C and pressures from 1 to 300 bar for carbon dioxide, methanol, and carbon dioxide methanol mixtures. The experimental measurements presented here agree with the measurements made by Ernst et al. and Boulton and Stein for pure carbon dioxide and carbon dioxide-methanol mixtures, respectively (Boulton & Stein, 1993; Ernst et al., 1989). The extensive range of operating conditions and high accuracy of the calorimeter along with its flexibility for studying both pure fluids and mixtures make it a valuable tool for thermophysical property characterization of fluids at liquid, vapor, and supercritical conditions.

The next steps in this project will involve $C_p$ measurements of the proposed next generation working fluids for energy conversion systems. Many of the fluids currently used in ORC plants and vapor-compression refrigeration systems, including those listed in Table 3-2, have 100-

year horizon Global Warming Potentials (GWP) hundreds to thousands times higher than $CO_2$. It is likely, that in the near future only low-GWP working fluids will be permitted to use in energy conversion systems. One of the most commonly used working fluids in ORC plants, R-134a has a 100-year GWP of 1430. The current annual emissions of R-134a correspond to 0.2 gigaton of $CO_2$ equivalent, approximately 0.7% of $CO_2$ emissions from fossil fuel combustion (UNEP, 2010). Between 2006 and 2010, R-134a emissions have also been increasing at a high rate of approximately 10% per year. Approximately 60% of R-134a emissions come from mobile air-conditioning, with remaining contributions primarily from refrigeration, stationary air-conditioning, and foam products. The likely low-GWP replacement of R-134a is 2,3,3,3-tetrafluoropropene (HFO-1234yf), but its PVT properties are much more uncertain compared to R-134a. For example, the estimated uncertainty in $C_p$ for pure HFO-1234yf is 5% as compared to 0.5-1% for R-134a (Lemmon, Huber, & Mclinden, 2013). Developing more accurate EOS for HFO-1234yf would allow us to smoothen the transition to low-GWP working fluids and develop more efficient ORCs and refrigeration systems designed specifically for HFO-1234yf. Therefore, the next application of the described calorimeter will involve $C_p$ measurements of HFO-1234yf and its mixtures with $CO_2$.

## 5.5 Acknowledgements

The work described in this chapter has been done in collaboration with Mitchel Ishmael. Both authors contributed to conceptual design, building, and testing the calorimeter. In addition, Mitchel Ishmael has done a number of improvements to the system resulting in accuracy improvement and performed the final measurements and calculations for this work. The content

of this chapter was previously published in the following article, which was written by both authors:

Ishmael, M., Lukawski, M., Tester, J. (2016) Isobaric heat capacity (Cp) measurements of supercritical fluids using flow calorimetry: equipment design and experimental validation with carbon dioxide, methanol, and carbon-dioxide-methanol mixtures, *Journal of Supercritical Fluids*, 117, 2016

## 5.6 References


Beckman, E. J. (2004). Supercritical and near-critical CO2 in green chemical synthesis and processing. *Journal of Supercritical Fluids*, *28*(2-3), 121–191. doi:10.1016/S0896-8446(03)00029-9

Bishnoi, P. (1971). *Experimental heat capacities of carbon dioxide-methane mixtures at elevated pressures and the coorrelation of volumetric and thermal properties*. University of Alberta.

Boulton, J. R., & Stein, F. P. (1993). The constant pressure heat capacity of supercritical carbon dioxide-methanol and carbon dioxide-ethanol co-solvent mixtures. *Fluid Phase Equilibria*, *91*(1), 159–176. doi:10.1016/0378-3812(93)85086-2

Boyette, S., & Criss, C. M. (1988). Thermodynamic properties of methanol from 288 to 503 K and at 8.3 MPa. *Journal of Chemical & Engineering Data*, *33*(4), 426–429. doi:10.1021/je00054a011

Brennecke, J. F., & Eckert, C. A. (1989). Phase equilibria for supercritical fluid process design. *AIChE Journal*, *35*(9), 1409–1427. doi:10.1002/aic.690350902

Calvet, E., & Prat, H. (1963). *Recent progress in microcalorimetry*. John Wiley & Sons.

de Groot, S. R., & Michels, A. (1948). The Joule-Thomson Effect and the Specific Heat at Constant Pressure of Carbon Dioxide. *Physica*, *14*(4), 218 – 222.

De Reuck, K. M., & Craven, R. J. B. (1993). *Methanol, international thermodynamic tables of the fluid state, vol. 12*. Blackwell Scientific Publications.

Dordain, L., Coxam, J.-Y., & Grolier, J.-P. E. (1994). Measurements of isobaric heat capacities of gases from 323.15 to 573.15 K up to 30 MPa. *Review of Scientific Instruments*, *65*(10), 3263. doi:10.1063/1.1144560

Ernst, G., & Hochberg. (1989). Flow-calorimetric results for the specific heat capacity Cp of CO2, of C2H6, and of (0.5CO2 + 0.5C2H6) at high pressures. *J. Chem. Thermodynamics*, *21*, 407 – 414.

Ernst, G., Maurer, G., & Wiederuh, E. (1989). Flow calorimeter for the accurate determination of the isobaric heat capacity at high pressures; results for carbon dioxide. *The Journal of Chemical Thermodynamics*, *21*(1), 53–65. doi:10.1016/0021-9614(89)90007-4

Ernst, G., & Philippi, R. (1990). Flow-calorimetric results for the specific heat capacity Cp of water at high pressures between 20 and 50 MPa and temperatures between 298.15 and 673.15 K. *J. Chem. Thermodynamics*, *22*, 211 – 218.

Ernst, G., Keil, B., Wirbser, H., & Jaeschke, M. (2001). Flow-calorimetric results for the massic heat capacity Cp and the Joule–Thomson coefficient of CH4, of (0.85 CH4 + 0.15 C2H6), and of a mixture similar to natural gas. *The Journal of Chemical Thermodynamics*, *33*(6), 601–613. doi:10.1006/jcht.2000.0740

Fortier, J. L., Benson, G. C., & Picker, P. (1976). Heat capacities of some organic liquids determined with the Picker flow calorimeter. *The Journal of Chemical Thermodynamics*, *8*(3), 289–299. doi:10.1016/0021-9614(76)90108-7

He, M., Su, C., Liu, X., Qi, X., & Lv, N. (2015). Measurement of isobaric heat capacity of pure water up to supercritical conditions. *The Journal of Supercritical Fluids*, *100*, 1–6. doi:10.1016/j.supflu.2015.02.007

Kunz, O., & Wagner, W. (2012). The GERG-2008 wide-range equation of state for natural gases and other mixtures: An expansion of GERG-2004. *Journal of Chemical and Engineering Data*, *57*(11), 3032–3091. doi:10.1021/je300655b

Kutney, M. C., Reagan, M. T., Smith, K. A., Tester, J. W., & Herschbach, D. R. (2000). The Zeno (Z = 1) Behavior of Equations of State: An Interpretation across Scales from Macroscopic to Molecular. *The Journal of Physical Chemistry B*, *104*(40), 9513–9525. doi:10.1021/jp001344e

Lemmon, E. W. (2015). Private Communication, November 19, 2015. Thermophysical Properties Division, Nation Institute of Standards and technology (NIST).

Lemmon, E. W., Huber, M. L., & McLinden, M. O. (2013). *NIST Standard Reference Database 23: Reference Fluid Thermodynamic and Transport Properties-REFPROP, Version 9.1*. Gaithersburg.

Lemmon, E. W., Huber, M. L., & Mclinden, M. O. (2013). *NIST Standard Reference Database 23: Reference Fluid Thermodynamic and Transport Properties-REFPROP, Version 9.1*. Gaithersburg.

Miyazaki, T., Hejmadi, a. V., & Powers, J. E. (1980). A new high-pressure recycle-flow calorimeter and results of determinations with ethane. *The Journal of Chemical Thermodynamics*, *12*(2), 105–124. doi:10.1016/0021-9614(80)90122-6

Miyazawa, T., Kondo, S., Suzuki, T., & Sato, H. (2012). Specific heat capacity at constant pressure of ethanol by flow calorimetry. *Journal of Chemical & Engineering Data*, *57*, 1700–1707.

Picker, P., Leduc, P., Philip, P. R., & Desnoyers, J. E. (1971). Heat capacity of solutions by flow microcalorimetry. *J. Chem. Thermodynamics*, *3*, 631–642.

Rivkin, & Gukov. (1968). Experimental study of the isobaric specific heat of carbon dioxide at supercritical pressures. *Teploenergetika*, *15*(10), 72 – 75.

Rivkin, S. L., & Egorov, B. N. (1959). Experimental investigation of the heat capacity of heavy water. *Atomnaya Energiya*, *7*(5), 462–465.

Rogers, P. S. Z., & Pitzer, K. S. (1981). High-Temperature Thermodynamic Properties of Aqueous Sodium Sulfate Solutions. *Journal of Physical Chemistry*, *85*(4), 2886–2895. doi:10.1021/j150620a008

Saitoh, A., Sato, H., & Watanabe, K. (1989). A new apparatus for the measurement of the isobaric heat capacity of liquid refrigerants. *International Journal of Thermophysics*, *10*(3), 649–659.

San Jose, J. L., Mellinger, G., & Reid, R. C. (1976). Measurement of the Isobaric Heat Capacity of Liquids and Certain Mixtures above the Normal Boiling Point. *Journal of Chemical and Engineering Data*, *21*(4), 414–417.

Sandarusi, J. a., Mulia, K., & Yesavage, V. F. (1992). An automated flow calorimeter for the determination of liquid and vapor isobaric heat capacities: Test results for water and n-pentane. *Review of Scientific Instruments*, *63*(2), 1810. doi:10.1063/1.1143342

Segovia, J. J., Vega-Maza, D., Chamorro, C. R., & Martín, M. C. (2008). High-pressure isobaric heat capacities using a new flow calorimeter. *The Journal of Supercritical Fluids*, *46*(3), 258–264. doi:10.1016/j.supflu.2008.01.011

Smith-Magowan, D., & Wood, R. H. (1981). Heat capacity of aqueous sodium chloride from 320 to 600 K measured with a new flow calorimeter. *The Journal of Chemical Thermodynamics*, *13*(11), 1047–1073. doi:10.1016/0021-9614(81)90004-5

Span, R. (2013). *Multiparameter Equations of State*. *Journal of Chemical Information and Modeling* (Vol. 53). Springer. doi:10.1017/CBO9781107415324.004

Span, R., & Wagner, W. (1996). A new EOS for carbon dioxide covering the fluid region from the triple-point temperature to 1100K at pressures up to 800 MPa. *Journal of Physical and Chemical Reference Data*. doi:10.1063/1.555991

UNEP, 2011. HFCs: A Critical Link in Protecting Climate and the Ozone Layer.

Vesely, F., Svoboda, V., & Pick, J. (1977). Heat capacities of some organic liquids determined with the mixing calorimeter. *1st Czech. Conf. Calorimetry (Lect. Short Commun.)*, (15136), C9–1–C9–4.

White, D. R., & Downes, C. J. (1988). Heat loss corrections for heat capacity flow calorimeters. *Journal of Solution Chemistry*, *17*(8), 733–750. doi:10.1007/BF00647419

Workman, E. J. (1930). A new method of measuring the variation of the specific heats (Cp) of gases with pressure. *Physical Review*, *36*(6), 1083 – 1090.

Wu, Y., Yu, Q., Zhong, H., & Lin, R. (1995). A new flow calorimeter for the determination of the isobaric heat capacity of vapors. *Thermochimica Acta*, *254*, 93–101. doi:10.1016/0040-6031(94)02064-U

Zheng, Y., Gao, H., Chen, Q., Meng, X., & Wu, J. (2014). Isobaric heat capacity measurements of liquid HFE-7200 and HFE-7500 from 245 to 353 K at pressures up to 15 MPa. *Fluid Phase Equilibria*, *372*, 56–62. doi:10.1016/j.fluid.2014.03.017

# Part III

# Costs Analysis of Geothermal, Oil, and Gas Wells

# 6 AVERAGE COSTS OF GEOTHERMAL, OIL, AND GAS WELLS

## 6.1 Introduction

The first two parts of this dissertation focused on designing more efficient geothermal energy utilization systems. While the proposed developments in ORC technology would make geothermal energy systems more efficient and possibly less expensive, the economic feasibility of geothermal projects is largely defined by the drilling expenditures rather than by the power conversion systems. Well drilling and completion costs typically contribute to 30-60% of the total capital investment in hydrothermal power plants (Blankenship et al., 2005; Tester et al., 2006) and can exceed 75% for medium- and low-grade EGS (Petty et al., 2009). Drilling determines not only the cost, but also the risk associated with geothermal projects. Because of that, accurate well cost correlations are of a key importance to the techno-economic models of geothermal energy systems such as GEOPHIRES.

To assess a specific geothermal project, the cost calculations should be performed on an individual well basis. Such approach provides location-specific costs of materials and services, as well as well design and drilling rates, which are representative of the geologic setting. In many locations, however, the lack of historical well drilling records makes such approach impossible or inaccurate. Because of that, the existing well cost correlations are often based on wells drilled in multiple locations, and represent the average drilling and completion costs in a broader area. Such correlations for both hydrocarbon and geothermal wells are presented in this chapter. They can be used for general feasibility studies, economic comparisons with other

energy sources, and for designing more cost-effective geothermal energy systems. The presented correlations for the cost of geothermal wells were also embedded in the GEOPHIRES software.

Well drilling is an experience-based activity, so drilling multiple similar wells in the same field is likely to result in improved drilling performance and lower costs. Faster drilling in terms of overall penetration rates may be a consequence of optimized drill bit selection, better insight into the site's lithology, personnel training or simply elimination of past mistakes. Since well drilling and completion is usually the most expensive single component of both production of hydrocarbon fuels and geothermal energy, any cost improvements due to learning are meaningful and worth analyzing. Thus, an investigation of the application of the learning curve theory to drilling activities was also included in the analysis.

Various aspects of geothermal drilling have been analyzed in the past. Recent work is focused primarily on emerging drilling technologies (Blankenship et al., 2005; Rowley et al., 2000; Tester, et al., 2006; Thorsteinsson et al., 2008) and drilling and completion of EGS wells (GEECO et. al., 2012; Polsky et al., 2008; Tester, et al., 2006). A comprehensive overview of the geothermal drilling research activities was provided in 2010 by the U.S. Department of Energy (U.S. DOE, 2010). DOE report summarizes research programs in years 1976-2010 which had the biggest impact on geothermal drilling and logging technology, including particularly relevant to this study geothermal well models and cost models.

Costs associated with geothermal well drilling and completion have been analyzed to a low level of detail compared to hydrocarbon drilling. Many methods exist for evaluating drilling costs of oil and gas wells that include a treatment of complexity. These include, but are not

limited to Joint Association Survey (JAS), Mechanical Risk Index (MRI), Directional Difficulty Index (DDI) and Difficulty Index (DI) (Kaiser, 2007). The geothermal industry has not developed such analysis tools yet and the main focus so far has been on correlating drilling costs with well depth.

Historically, it is believed that there have been over 4000 geothermal wells drilled worldwide (Sanyal and Morrow, 2012), but their costs have rarely been published due to proprietary nature of the data. Furthermore, even if cost data were available, the number of geothermal wells drilled each year was considered insufficient to evaluate drilling costs as a function of well depth to a reasonable of statistical confidence (Augustine et al., 2006; Mansure and Blankenship, 2008; Mansure et al., 2006; Tester et al., 2006). Because of similarities between hydrocarbon and geothermal drilling processes, drilling cost trends for oil and gas wells have been commonly used to normalize the costs of geothermal wells drilled in the past to the current year (Augustine et al., 2006; Mansure and Blankenship, 2008; Mansure et al., 2006; Polsky et al., 2008; Sanyal and Morrow, 2012; Tester, et al., 2006). This dissertation shows, that such approach is no longer possible, because the changes in the costs of geothermal wells are not correlated with the evolution of oil and gas well prices.

Several geothermal drilling cost trends have been developed in the past. A well cost index first created by Tester and Milora (Milora and Tester, 1976) and later refined by Herzog and Tester (Tester and Herzog, 1990) allowed for comparison of the historical costs of drilling hydrothermal, EGS, and hydrocarbon wells. The index was used to convert the costs from nominal to real dollars, which provided a common basis for comparison. The cost trend was based on JAS database of U.S. onshore oil and gas wells. Augustine et al. (Augustine et al., 2006) as a part of the 'Future of Geothermal Energy' assessment (Tester et al., 2006) expanded

Herzog and Tester's analysis up to 2003. The new well cost index named MIT Depth Dependent (MITDD) index assigned a separate trend to each of nine well depth intervals listed in the JAS.

Geothermal well completion costs were also analyzed by others (Mansure and Blankenship, 2008; Mansure et al., 2006; Mansure and Blankenship, 2005). They used the Producer Price Index for drilling oil, gas, dry, or service wells from the U.S. Department of Labor, Bureau of Labor Statistics (BLS PPI) to escalate the historical cost of hydrocarbon and geothermal wells (U.S. BLS, 2013). Due to its simplicity, availability, and regular updates this index has been commonly used in other reports (Augustine et al., 2010; Bloomfield and Laney, 2005; GeothermEx, 2004) and techno-economic models such as Geothermal Electricity Technology Evaluation model (GETEM) (Entingh et al., 2006). Mansure and Blankenship normalized the costs of 33 geothermal wells from Sandia National Laboratory database and used them to generate a correlation describing the cost of geothermal wells as an exponential function of their depth (Mansure and Blankenship, 2008). In addition to providing a comprehensive description of the factors driving geothermal well costs, the authors emphasized the need for collecting more drilling cost records, particularly for wells drilled in the 21st century. Development of a more rigorous methodology than BLS PPI was suggested to account for the changes in well design that occurred over the last several decades. Both of these challenges are addressed in this work.

The abovementioned statistical analyses yield average drilling and completion costs expressed as functions of the well depth. They do not account for complexity of drilling environment nor any other factors affecting well costs other than depth. If any site-specific information is available, predictive methods utilizing detailed drilling cost models are more suitable. Such a predictive geothermal cost model, WellCost Lite, has been developed by Bill Livesay and co-

workers at Sandia National Laboratory (Tester et al., 2006). WellCost Lite is an Excel based model that calculates the time and cost to drill and complete each casing interval. The program allows the specification of location-dependent parameters such as rate of penetration, drilling bit lifetime, casing program, trouble time, rig rate, and mobilization and demobilization costs (Augustine et al., 2006).

Analyses of learning processes in oil and gas drilling have been by far more common than in geothermal industry. For example, Brett and Millheim (Brett and Millheim, 1986) analyzed the records of over 2000 oil and gas wells distributed among more than 30 onshore and offshore fields. Like other studies (Ikoku, 1978; Kravis et al., 2004), they used a simple learning model in which drilling time decreases exponentially with the number of similar wells drilled in a sequence. Drilling time drops until it reaches a minimum level corresponding to technical capabilities of a drilling company in a specific area. The rate at which this technical limit is approached was defined as learning rate.

An equivalent analysis of the learning process for geothermal drilling is difficult to perform because of small sample sizes and higher heterogeneity of geothermal formations. Recent publications indicate a high learning potential of specific geothermal fields, namely, an increase in the average rate of penetration of 30% within the Salak field in from 2004 to 2008 (Prihutomo and Arianto, 2010) and of 100% in the Kamajong field between the early exploratory drilling and 45th well (Sanyal and Morrow, 2012). In geothermal drilling, learning effect improvements were more commonly expressed in terms of thermal of electric power output per well (Sanyal and Morrow, 2012; Stefansson, 1992). Such a definition of the learning curve is an evaluation of the success of geologic and geophysical surveys, but is not a direct measure of drilling performance. The cost of drilling successful and unsuccessful wells can be very similar. Success

in geothermal drilling should be rather determined by both thermal/electric capacity of a well and its cost. Overall, no extensive economic analysis of learning curves in geothermal drilling has been performed.

The work presented in this chapter extends the knowledge on the average geothermal and hydrocarbon well costs by correlating these costs with the measured depth and degree of drilling experience in a given area. This chapter is organized as follows: section 6.2 includes the analysis of current oil and gas well drilling and completion costs, followed by a description of a newly developed hydrocarbon well cost index based on JAS data reported between 1976 and 2009. Section 6.3 discusses drilling and completion costs of geothermal wells. Section 6.4 concludes the chapter with a statistical analysis of learning potential in well drilling. The monetary value of learning is determined by comparing the costs of exploratory and development hydrocarbon wells.

## 6.2 Oil and gas wells drilling and completion costs

### 6.2.1 Current costs of oil and gas wells

Following Augustine et al. (Augustine et al., 2006), the presented well cost analysis is based on U.S. onshore oil and gas wells reported in the API JAS (American Petroleum Institute, 1976-2009). The JAS is an annual publication reporting U.S. oil and gas drilling expenditures. It determines the average drilling costs based on 40% to 60% of wells drilled each year (Kaiser, 2007). Wells are broken down based on geographic location (onshore, offshore), state, well class (oil, gas, dry) and type (exploratory, development). Dry holes are defined as wells which are not productive enough to be completed. The well data are split into nine intervals based on

the measured depth (MD) i.e. the length along the wellbore path. Total annual drilled footage and costs are reported for each depth interval with no distinction between vertical, directional, and horizontal wells. The most recent issue of JAS includes data for the year 2009.

Measured depth is the primary, but not the only factor affecting drilling expenditures. Well cost also strongly depends on the geological formation. Geological setting determines penetration rates, number of casing strings and frequency of drilling string failures (Kaiser, 2007). However, no single parameter can accurately describe drilling complexity (Mansure et al., 2006). The JAS uses a 11-parameter model to correlate the well cost with field characteristics (Kaiser, 2007). Unfortunately, the mathematical functions used by the JAS have not been published and restrictions on data availability make parametric analysis of drilling cost impossible.

The average costs of U.S. onshore oil and gas wells in 2009 are listed in Table 6-1 and plotted in Figure 6-1. The average well cost in each depth interval was obtained by dividing the total drilling expenditure by the number of wells. Cost per meter is calculated as the total drilling expenditure over the total annual oil and gas well footage. Offshore wells, dry holes, and sidetracks are omitted from the analysis. Figure 6-1 depicts nonlinear variation in well cost with measured depth. Deep wells are disproportionately more expensive compared to shallow ones. They require more time to drill due to increased tripping, trouble, and casing time. Risk of overpressure in deep formations creates a need for more casing strings, which increases both material costs and non-rotating time (Tester et al., 2006). As drilling depth increases, contractors are more likely to encounter abrasive rocks, high temperatures, and reservoirs rich in $CO_2$ and $H_2S$ (Kaiser, 2007).

*Table 6-1: Average 2009 U.S. onshore oil and gas well depth and cost obtained from API JAS. Data include both vertical and directional wells.*

| Depth interval (MD*) | | Average depth (MD*) | | Average cost per foot in 2009 ($/ft.) | | |
|---|---|---|---|---|---|---|
| feet | meters | feet | Meters | Oil | Gas | Oil and gas |
| 1250 – 2499 | 381 – 761 | 1822 | 555 | 301 | 385 | 341 |
| 2500 – 3749 | 762 – 1142 | 3102 | 945 | 249 | 322 | 288 |
| 3750 – 4999 | 1143 – 1523 | 4392 | 1339 | 267 | 273 | 270 |
| 5000 – 7499 | 1524 – 2285 | 6365 | 1940 | 435 | 440 | 438 |
| 7500 – 9999 | 2286 – 3047 | 8673 | 2643 | 540 | 606 | 587 |
| 10000 – 12499 | 3048 – 3809 | 11027 | 3361 | 621 | 636 | 631 |
| 12500 – 14999 | 3810 – 4571 | 13602 | 4146 | 951 | 797 | 861 |
| 15000 – 17499 | 4572 – 5333 | 16111 | 4911 | 1367 | 1019 | 1091 |
| 17500 – 19999 | 5334 - 6096 | 18789 | 5727 | 1055 | 890 | 991 |

*Measured depth – length of wellbore measured along drilling trajectory

Analysis of the JAS data shows that since year 1984, wells listed in the 3750 – 4999 ft. (1143 – 1524 m) category had the lowest cost per unit length among all depth intervals. This depth corresponds to an optimum between the depth-dependent costs components (drilling, casing, cementing, and trouble) and relatively constant pre-spud expenditures. Between 1976 and 2008, drilling and completion cost per meter was the highest for the deepest wells in the 17500 – 19999 ft. (5334 – 6096 m) category. In 2008 and 2009, the maximum cost per meter shifted to a lower depth interval. This is likely a result of higher contribution of horizontal wells and improved drilling practices.

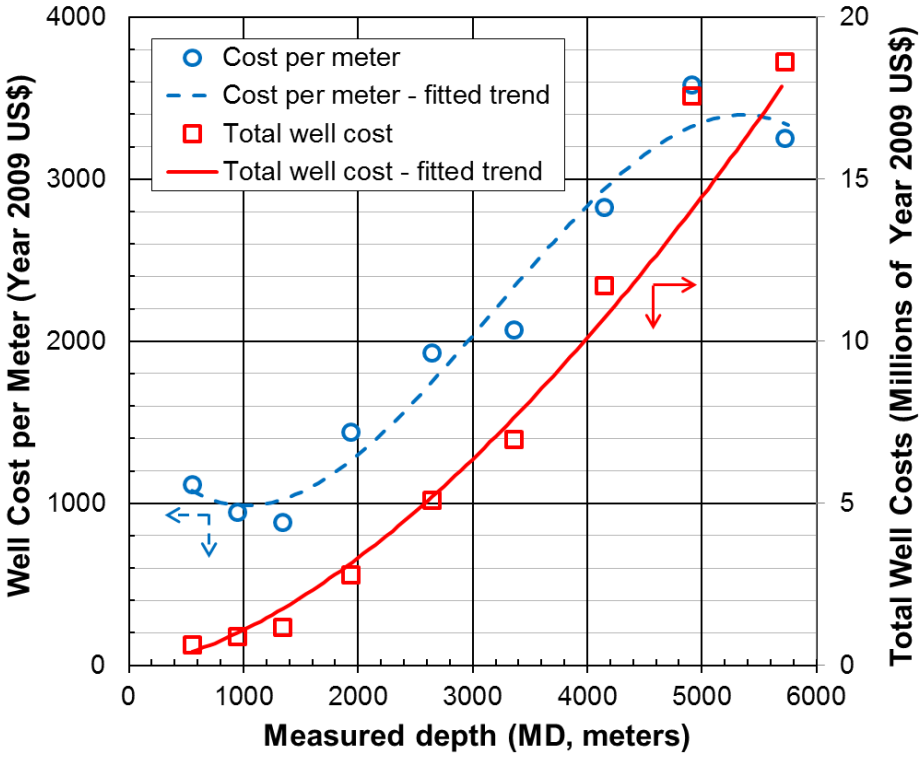


*Figure 6-1: Drilling and completion costs of U.S. onshore oil and gas wells in 2009.*

Previous studies expressed the average well costs as an exponential function of well depths (Augustine et al., 2006; Mansure and Blankenship, 2008; Tester, et al., 2006). Until 2003 the correlation coefficient $R^2$ for exponential curve fit to the JAS oil and gas data was at least 0.98. After 2003, improvements in drilling technology made the exponential function less suitable for describing well completion costs resulting in $R^2$ value of 0.95 in 2009. Thus, the following power curve fit with $R^2$ of 0.97 is used to more accurately describe average oil and gas well completion cost in 2009:

$$Oil\ and\ gas\ well\ cost = 1.65 \cdot 10^{-5} \cdot (MD)^{1.607} \qquad (6\text{-}1)$$

where the well cost is in millions of 2009 U.S. dollars and MD is a measured depth of well in meters. This correlation is presented in Figure 6-1.

Analysis of 1976-2009 JAS data shows that companies are drilling deeper and more complex oil and gas wells. As depicted in Figure 6-2, the average depth of oil and gas wells has been increasing since 1989. While MD corresponding to 25$^{th}$ percentile remained almost constant since 1976, improved technology has allowed us to target deeper resources, continuously increasing the median and third quartile. A decreasing discrepancy between the average and median well depths indicates that well depth distribution is becoming less positively skewed. An accurate drilling cost index needs to account for these significant variations in the average well depth.

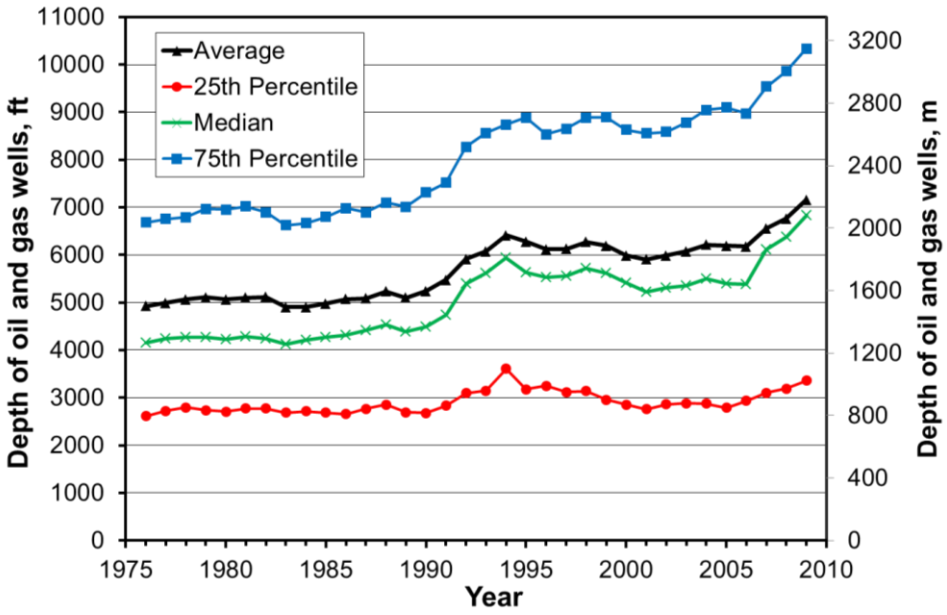


*Figure 6-2: Depth of oil and gas wells as reported by API JAS. First quartile, median and third quartile were calculated assuming a uniform distribution of well depths within each depth interval.*

### 6.2.2 Development of the CEI oil and gas well cost index for years 1976-2009

A well cost index is required to make comparisons between the cost of wells drilled in different points in time. It can be used to express past drilling expenditures in current year (real) dollars. This section explains how the Cornell Energy Institute (CEI) well cost index was created and adjusted for yearly changes in drilling activity. The CEI index is based on 1976-2009 API JAS data and extended methodology used previously to develop MITDD index (Augustine et al., 2006). The CEI index consists of nine separate trends for different depth intervals. In contrast to the MITDD, the CEI index is based on cost per foot and not cost per well. This modification increased the accuracy of index by counteracting annual changes in average well depth within each depth interval. Variations in average well depth in years 1976 – 2009 vary from 2% for deep 12500-14999 ft. (3810 – 4572 m) wells to 8.5% for the shallow 1250 – 2499 (281 – 762 m) wells. Following the MITDD, the CEI index is referenced to 1977 i.e. its value for each depth interval is set to 100 in 1977.

To present a general well cost trend and to adjust the CEI index for changes in drilling activity, the CEI Average well cost index was created. The CEI Average index was created by summing the CEI cost indices for all depth intervals, each with a weight corresponding to its contribution to the total drilling expenditure in 2009. This index is less accurate than the depth-dependent CEI index as it consists of a single trend. To validate the CEI index, it was compared with two other drilling cost trends: the JAS Activity Adjusted drilling cost index and the Bureau of Labor Statistics Producer Price Index for Oil, Gas, Dry and Service Wells (U.S. BLS, 2013) referred to as BLS PPI. The JAS Activity Adjusted index is annually published by API. An 11-parameter algorithm is used to correct the cost trend for yearly variations in drilling activity including type, location and depth of wells (Kaiser, 2007). In the JAS Activity Adjusted index, the

average well costs in the previous years are recalculated by keeping these 11 parameters constant to the recent 2009 year survey (American Petroleum Institute, 1976-2009). Rigorous methodology involved in data collection and processing makes the JAS Activity Adjusted index the most accurate single-trend well cost index. However, it does not capture significant variations in cost trends among different well depths. The JAS Activity Adjusted index reaches back only to the year 2000. The BLS PPI reaches back to 1986, but it is based on less rigorous methodology.

A comparison of the three discussed drilling cost trends is presented in Figure 6-3. The effect of inflation on drilling and completion costs was eliminated by using the GDP price index (U.S. Office of Management and Budget, 2013). An inflation adjusted well cost index shows how the cost of oil and gas well drilling changed with respect to other goods and services. Both the BLS PPI and JAS Activity Adjusted indices were normalized to the CEI Average index in the year 2000. The JAS index shows a rapid increase in hydrocarbon well costs in 2004 and another, more significant rise in 2006-2008. The BLS PPI does not capture the latter trend, underestimating the 2000-2009 cost escalation by 135%. The CEI index overestimates the drilling and completion costs, but shows a similar trend to the JAS Activity Adjusted index. Divergence is likely to be caused by an increasing share of horizontal wells. While in the year 2000 horizontal wells contributed to only 4% of total wells drilled, 5% of footage and 10% of cost, by 2009 the respective numbers increased to 22%, 33% and 48%. In 2009, horizontal wells had an average 78% higher MD and 90% higher cost per meter compared to vertical wells (American Petroleum Institute, 1976-2009)

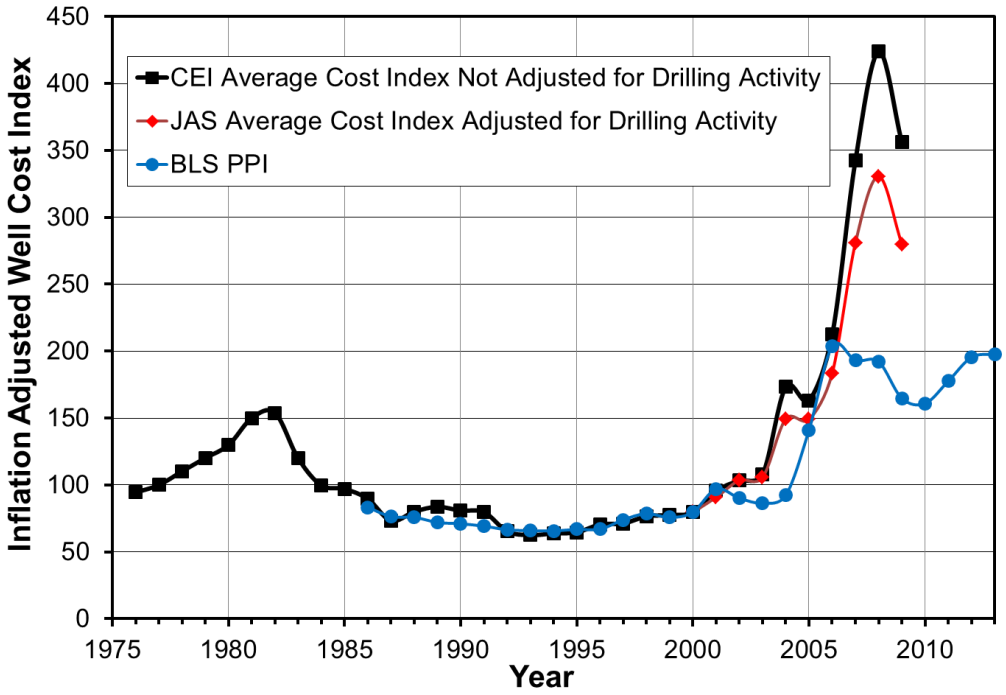


*Figure 6-3: Comparison of CEI Average well cost index before adjusting it for changes in drilling activity with two other indices: Bureau of Labor Statistics Producer Price Index for Oil, Gas, Dry and Service Wells (BLS PPI), and JAS Activity Adjusted Index. All three indices are adjusted for inflation using the GDP deflator.*

The CEI index was adjusted to compensate for changes in drilling activity between 2000 and 2009. The CEI depth-dependent index was adjusted to make the CEI Average index converge with the JAS Activity Adjusted index. The following normalization formula assigned a higher CEI index correction factor to depth intervals, which experienced the highest increase in cost since 2000:

$$I_n^k = J_{ref}^k + \left(J_n^k - J_{ref}^k\right) \cdot \left(\frac{A_n - A_{ref}}{C_n - C_{ref}}\right) \qquad (6\text{-}2)$$

Where: *I,J,A,* and *C* are various forms of CEI and JAS cost indices, *k* is the well depth interval, and *n* and *ref* represent the index year and reference year, respectively. Full explanation of these terms is provided in the 'list of symbols' section.

### 6.2.3 CEI oil and gas well cost index – results and discussion

The Cornell Energy Institute (CEI) well cost index based on nominal dollars and corrected for post-2000 changes in drilling activity (later simply referred to as the CEI index) is presented in Figure 6-4 and Table 6-2. Although the tabulated index values include four significant figures, this precision should not be confused with accuracy. The CEI index shows high variations in cost trends for different depth intervals. The first drilling cost peak occurred in 1982 and was caused by the events following the 1979 Iranian revolution. Between 1976 and 1982, the index for deep (over 12500 ft.) wells increased twice as much as for shallow, up to 5000 ft. wells. After 1982 indices for deep wells began to drop and by 1986 the medium (5000-12500 ft.) and shallow well indices were effectively the same. Since then, prices of shallow and medium-deep wells have escalated at rates much higher compared to deep wells. This increasing affordability to drill deep is an indicator of improvements in the drilling technology. This trend is likely to slow down or reverse after 2009 as a result of increased demand for large 1000-2000 hp drilling rigs (RigData, 2010). Such units are more suitable for directional drilling in shale formations. The major differences between the CEI cost trends for various depth intervals indicate that any depth-independent well cost index is likely biased. Even activity-adjusted indices will under- or overestimate drilling expenditures depending whether they are applied to deep or shallow wells.

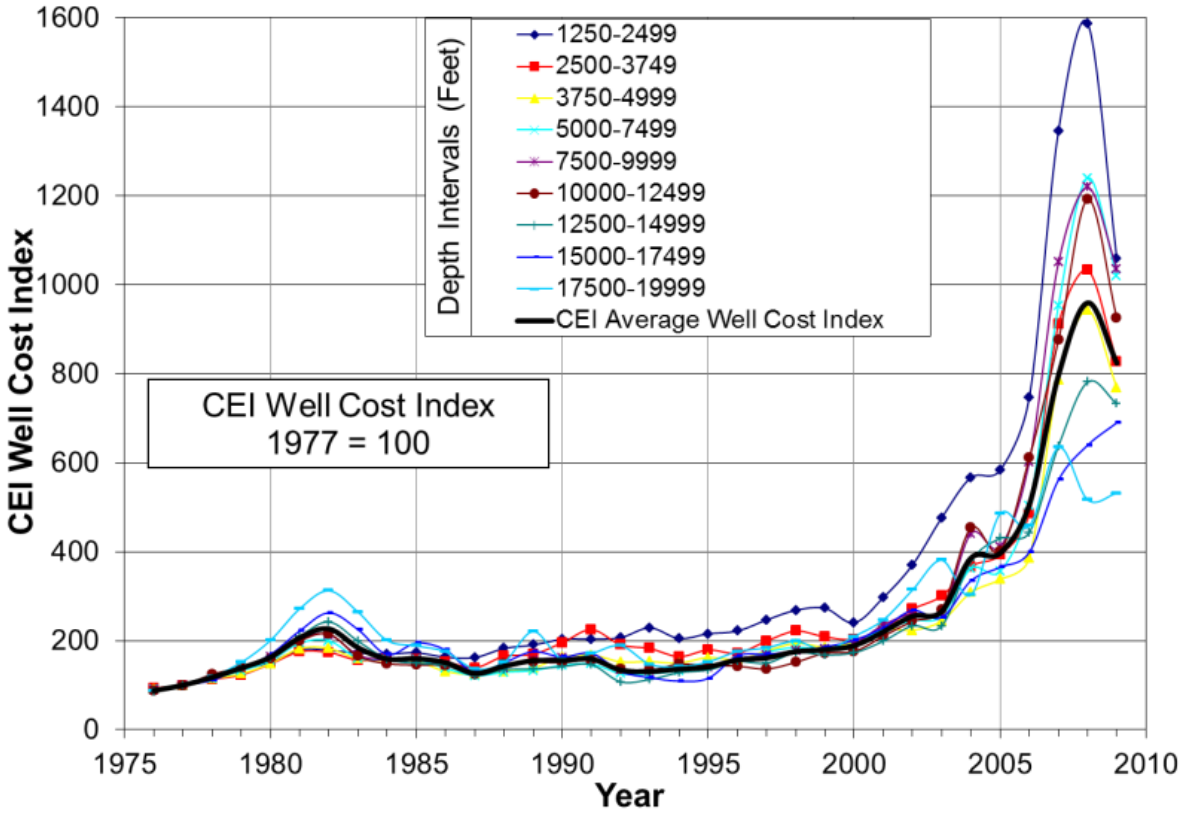


*Figure 6-4: CEI and CEI Average well cost indices (1977 = 100). Both indices are adjusted for changes in drilling activity after year 2000.*

*Table 6-2: Values of Cornell Energy Institute (CEI) well cost index for the period 1976-2009. The CEI index has been adjusted for changes in drilling activity since 2000.*

| Year | CEI Well Cost Index | | | | | | | | | |
|---|---|---|---|---|---|---|---|---|---|---|
| | CEI Average | Measure depth (MD) interval (feet) | | | | | | | | |
| | | 1250-2499 | 2500-3749 | 3750-4999 | 5000-7499 | 7500-9999 | 10000-12499 | 12500-14999 | 15000-17499 | 17500-19999 |
| | | Measured depth (MD) interval (meters) | | | | | | | | |
| | | 381-761 | 762-1142 | 1143-1523 | 1524-2285 | 2286-3047 | 3048-3809 | 3810-4571 | 4572-5333 | 5334-6096 |
| **1976** | 87.9 | 92.0 | 93.9 | 91.0 | 90.8 | 88.5 | 86.5 | 85.9 | 87.6 | 88.0 |
| **1977** | 100.0 | 100.0 | 100.0 | 100.0 | 100.0 | 100.0 | 100.0 | 100.0 | 100.0 | 100.0 |
| **1978** | 117.7 | 119.6 | 112.9 | 114.4 | 114.8 | 119.9 | 123.7 | 114.0 | 111.2 | 118.9 |

| | | | | | | | | | | |
|---|---|---|---|---|---|---|---|---|---|---|
| **1979** | 138.7 | 135.6 | 123.2 | 125.6 | 132.4 | 141.5 | 140.8 | 136.8 | 139.2 | 151.2 |
| **1980** | 163.0 | 151.6 | 147.9 | 148.8 | 155.6 | 163.5 | 160.3 | 162.4 | 169.0 | 200.8 |
| **1981** | 206.8 | 180.1 | 175.1 | 182.4 | 194.5 | 203.9 | 201.0 | 209.4 | 222.0 | 271.7 |
| **1982** | 226.7 | 178.4 | 173.8 | 182.7 | 200.0 | 213.9 | 216.3 | 242.4 | 262.7 | 312.4 |
| **1983** | 184.4 | 172.5 | 156.4 | 159.1 | 160.8 | 168.0 | 167.1 | 199.1 | 225.0 | 264.5 |
| **1984** | 159.1 | 170.1 | 159.6 | 156.1 | 157.7 | 155.9 | 149.3 | 158.7 | 168.8 | 200.6 |
| **1985** | 159.8 | 172.8 | 157.4 | 153.6 | 157.4 | 156.5 | 146.0 | 149.6 | 195.0 | 188.4 |
| **1986** | 150.9 | 163.2 | 152.8 | 131.0 | 138.1 | 146.8 | 144.8 | 145.3 | 179.1 | 175.2 |
| **1987** | 126.8 | 162.2 | 139.2 | 124.4 | 121.4 | 129.4 | 124.4 | 121.3 | 127.5 | 136.8 |
| **1988** | 142.9 | 182.6 | 165.1 | 131.3 | 129.2 | 139.1 | 147.6 | 134.9 | 150.5 | 151.8 |
| **1989** | 155.2 | 190.4 | 169.6 | 139.0 | 133.1 | 156.4 | 152.1 | 136.3 | 175.5 | 220.6 |
| **1990** | 155.6 | 203.2 | 195.6 | 163.2 | 144.9 | 161.7 | 151.4 | 141.9 | 163.2 | 157.2 |
| **1991** | 159.2 | 203.9 | 225.0 | 168.0 | 147.5 | 158.0 | 154.9 | 146.0 | 171.6 | 171.3 |
| **1992** | 133.9 | 206.9 | 190.8 | 152.7 | 126.2 | 134.3 | 134.9 | 107.6 | 130.7 | 188.7 |
| **1993** | 130.9 | 228.9 | 182.6 | 153.1 | 125.4 | 132.7 | 133.6 | 113.0 | 117.1 | 147.0 |
| **1994** | 136.4 | 205.0 | 164.3 | 150.0 | 132.7 | 138.3 | 146.1 | 128.3 | 109.1 | 141.9 |
| **1995** | 141.1 | 215.7 | 179.4 | 162.3 | 146.3 | 140.9 | 143.4 | 134.5 | 115.5 | 152.3 |
| **1996** | 156.9 | 221.8 | 172.1 | 157.6 | 153.4 | 159.3 | 142.8 | 153.0 | 165.8 | 175.8 |
| **1997** | 161.4 | 246.7 | 199.3 | 177.1 | 174.3 | 167.8 | 137.1 | 149.6 | 169.6 | 184.1 |
| **1998** | 175.7 | 268.5 | 221.7 | 194.1 | 185.1 | 177.8 | 151.9 | 173.6 | 175.8 | 198.9 |
| **1999** | 180.1 | 272.9 | 208.6 | 186.2 | 181.3 | 182.1 | 171.2 | 168.2 | 186.2 | 179.0 |
| **2000** | 189.0 | 240.4 | 203.4 | 197.2 | 194.2 | 194.1 | 176.5 | 173.1 | 201.1 | 209.8 |
| **2001** | 220.2 | 297.2 | 227.9 | 226.2 | 225.9 | 235.5 | 201.4 | 199.2 | 229.4 | 246.9 |
| **2002** | 255.3 | 370.6 | 270.9 | 223.7 | 245.2 | 261.2 | 244.0 | 233.4 | 268.1 | 314.2 |
| **2003** | 266.0 | 476.2 | 300.8 | 244.7 | 255.3 | 262.8 | 263.8 | 233.2 | 252.3 | 381.0 |
| **2004** | 385.7 | 566.8 | 366.8 | 308.5 | 362.0 | 441.0 | 387.3 | 378.9 | 334.8 | 302.8 |
| **2005** | 396.9 | 583.5 | 392.7 | 337.9 | 356.0 | 410.9 | 368.0 | 430.0 | 365.1 | 485.5 |
| **2006** | 505.6 | 746.5 | 485.4 | 386.0 | 503.3 | 602.2 | 527.8 | 443.2 | 398.8 | 457.9 |
| **2007** | 797.0 | 1346.0 | 910.9 | 785.8 | 953.5 | 1050.3 | 726.9 | 637.7 | 561.5 | 634.5 |
| **2008** | 959.7 | 1587.9 | 1033.5 | 942.8 | 1240.1 | 1219.5 | 936.7 | 781.5 | 639.6 | 516.5 |
| **2009** | 824.0 | 1059.8 | 827.7 | 769.0 | 1020.6 | 1035.4 | 732.2 | 733.0 | 690.1 | 531.8 |

The 2003-2008 drilling cost increase can be compared to post-1979 price escalation by accounting for the inflation. The effects of inflation were eliminated by using GDP deflator (U.S. Office of Management and Budget, 2013), as shown in Figure 6-5. In terms of real values, the 2008 drilling costs peak is approx. 2.7 times higher than in 1982. The CEI Average index quadrupled between 2003 and 2008, while the disruptive events of 1979 resulted in an increase of only 28%.

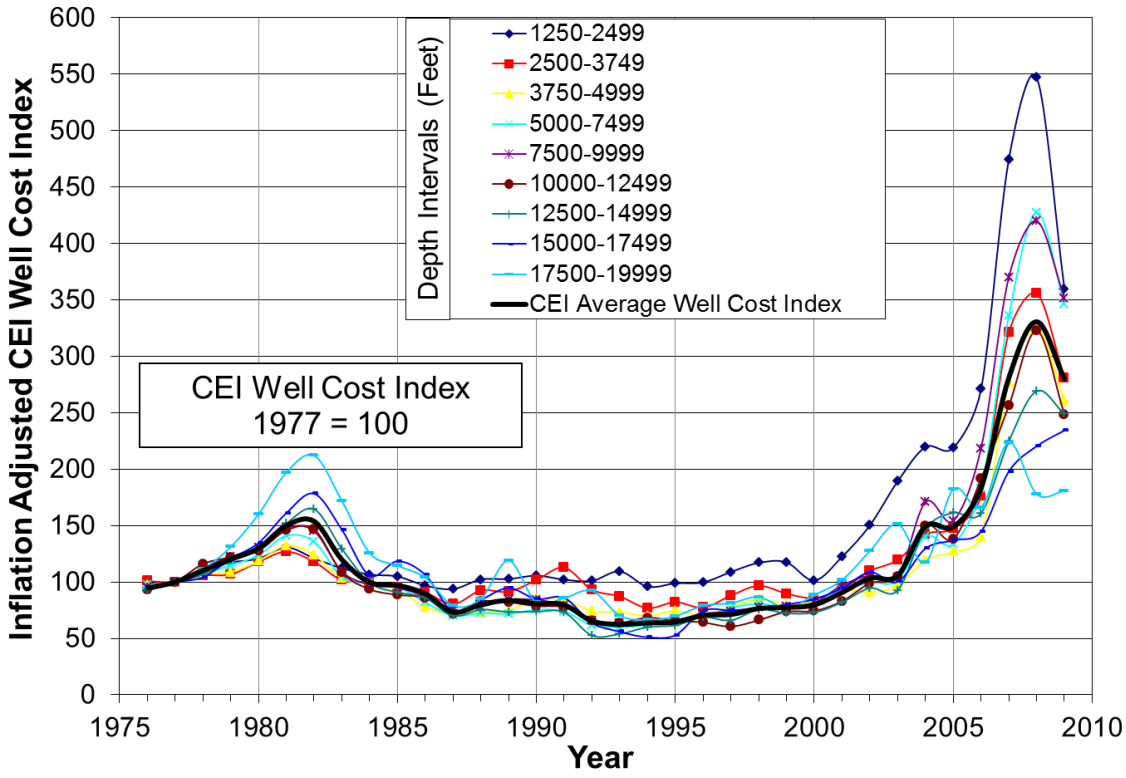


*Figure 6-5: CEI and CEI Average well cost indices (1977 = 100). Both indices are adjusted for inflation using GDP deflator and changes in drilling activity.*

### 6.2.4 Factors driving the 2003-2008 escalation of oil and gas well costs

The CEI drilling index evaluates, but does not explain the unprecedented 2003-2008 increase in oil and gas well completion costs. To elucidate this process, the CEI index was correlated with the main economic parameters affecting drilling and completion costs. These include oil and gas prices as well as cost and availability of major well services and consumables. The historical cost trends were adjusted for inflation by using the GDP deflator (U.S. Office of Management and Budget, 2013), so that costs could be compared on a consistent basis and presented in terms of current (real) dollars.

The increase in well cost between 2003 and 2008 was a response to strong oil and gas prices. The 2004 peak was caused by the high cost of natural gas in the U.S. The 2006-2008 trend was driven by both price of crude oil increasing from $40.7/bbl. in December 2004 to the maximum of $133.6/bbl. in June 2008 (U.S. Energy Information Administration, 2013a), as well as natural gas averaging at a high level of $7.8/MCF in the same period.(U.S. Energy Information Administration, 2013b) Prior to mid-2009, the U.S. market was dominated by natural gas drilling, as shown in Figure 6-6. Since 2009, increased production from unconventional plays resulted in an oversupply of natural gas. The saturation of the gas market shifted the drilling activity to liquid-rich unconventional gas formations. As a result, the share of gas rigs dropped from 80% in mid-2009 to 30% in mid-2012 (Baker Hughes, 2013). From 2010 to 2012, the cost of drilling in the U.S. has likely been driven by global crude prices rather than by domestic natural gas prices.

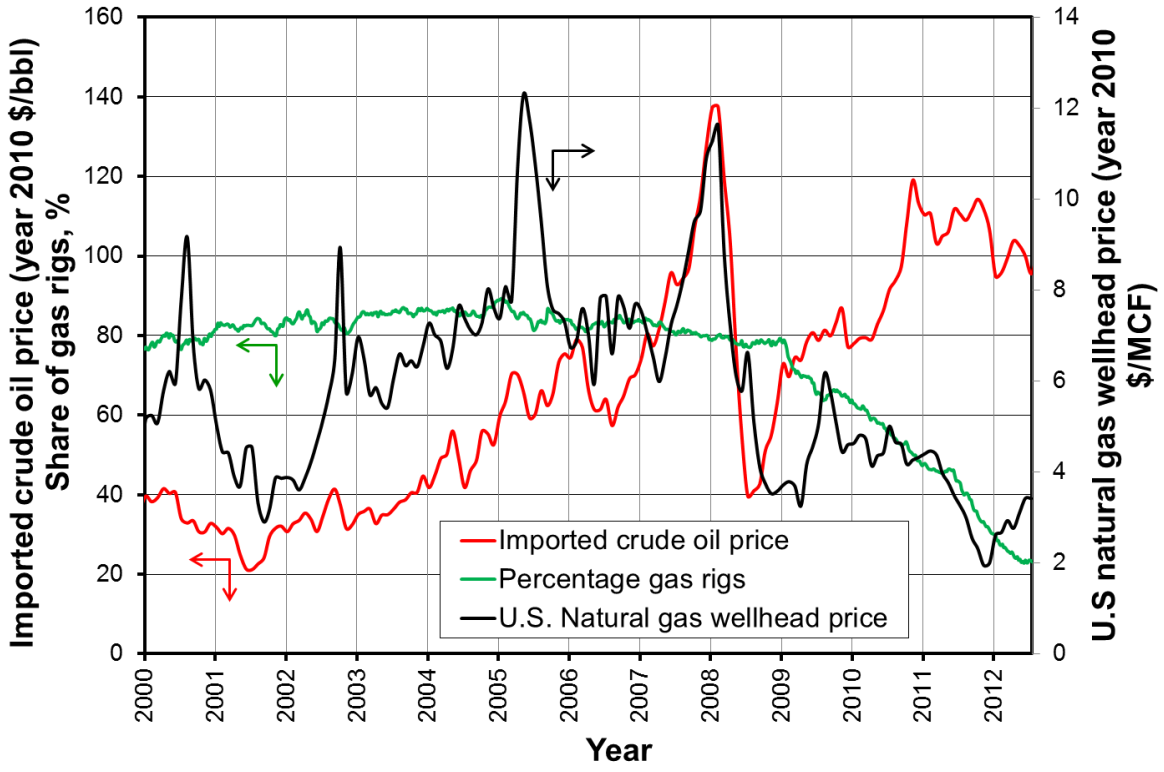


*Figure 6-6: U.S. natural gas wellhead prices and imported oil prices. The ratio of the number of gas rigs to the total onshore oil and gas rigs is based on Baker Hughes data. Indices on abscissa denote mid-years (June).*

In addition to the prices of crude oil and natural gas, well expenditures are affected by the costs of services and materials used to drill and complete the wells. Three primary cost components of oil and gas wells are drilling services, casing consumables, and cementing. The latter two are presented in the form of producer price indices (U.S. BLS, 2013) and are compared to the CEI Average index adjusted for drilling activity, shown in Figure 6-7. Since 1995, the cost escalation rates of both casing and cement were below the CEI drilling index. While increasing steel prices contributed to the 2004 well cost peak, the disruptive event of 2006-2008 cannot be explained by an increased cost of casing or cement.

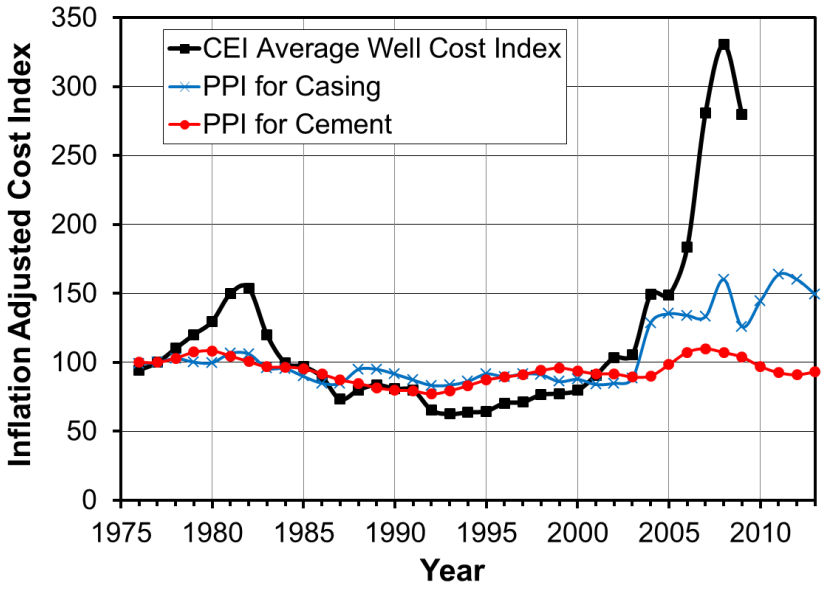


*Figure 6-7: Producer price indices (PPI) for casing ('Iron, steel pipe and tube from purchased steel') and cement ('Cement manufacturing') as compared to CEI Average well cost index.*

As shown in Figure 6-7, the drilling cost escalation rates were negative for 10 years following the 1982 peak. Despite increases in the late 90s', well completion costs expressed in real dollars did not reach their 1977 value until year 2002. During this period rig rates were very low, often below the amortization costs of a new rig (Mansure and Blankenship, 2008). Operators survived by salvaging parts from decommissioned rigs (Mansure and Blankenship, 2008; Tester et al., 2006). Low demand and day rates resulted in 84% drop in the number of U.S. onshore rigs between 1982 and 1999, as shown in Figure 6-8. Strong oil and gas prices in the 2000s' encouraged operators to commission 1250 new units between 1999 and 2008, tripling the 1999 active rig count. The insufficient supply of drilling rigs during the period of increased demand triggered the post-2003 increase in rig rental rates.

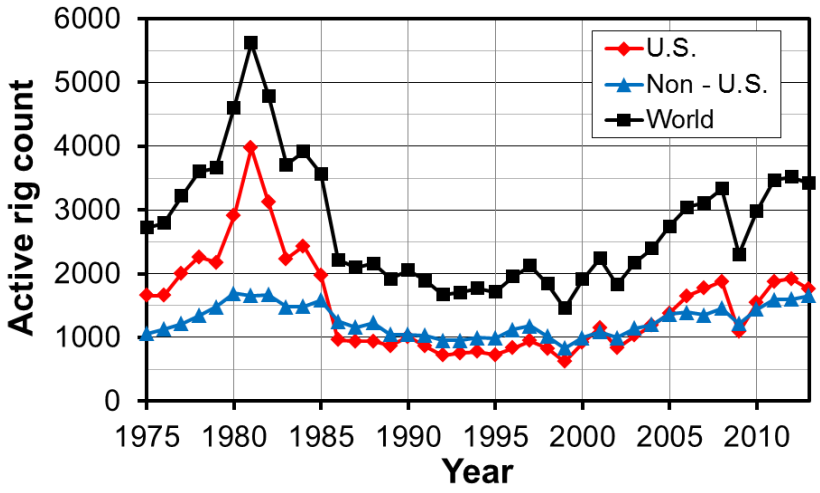


*Figure 6-8: Onshore active drilling rig count in the U.S. and worldwide.*

The 2008 and 2011 U.S. rig counts may seem insignificant compared to 1982 level, but the drilling performance improved considerably over this period. To evaluate this process, the average number or wells per rig and annual footage per rig were calculated based on 1976-2009 JAS and Baker Hughes records (American Petroleum Institute, 1976-2009; Baker Hughes, 2013). As Figure 6-9 shows, an average active rig in 2009 drilled twice the number of wells and triple the footage compared to 1982. Thus, despite the lower rig count, current drilling capacity is higher than in 1982.

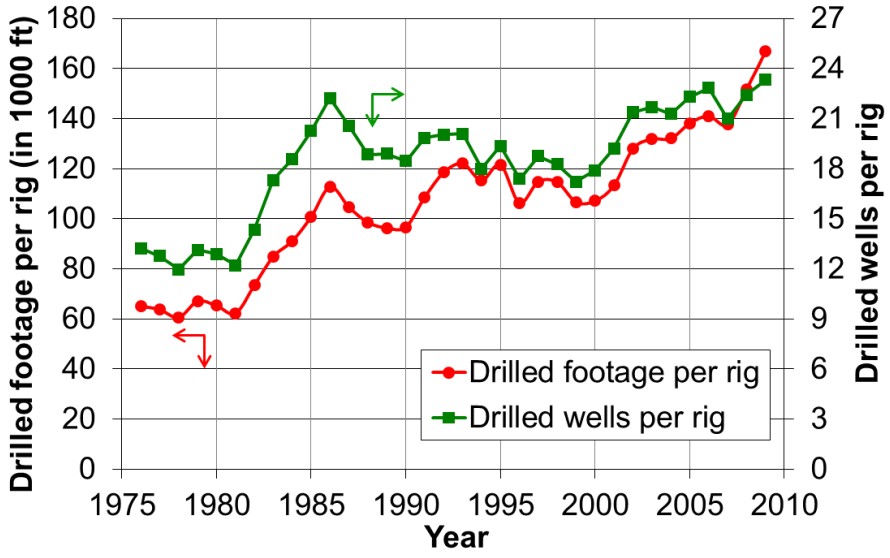


*Figure 6-9: U.S. Onshore drilling performance of active oil and gas rigs in years 1976 - 2009.*

More direct evidence of the relation between 2003-2008 drilling cost increase and rig availability is found in rig utilization. While in mid-2004 only 52% of fleet was in use, in the 2006-2008 period rig utilization increased to 78-92% (RigData, 2010). The 2008 financial crisis and low fuel prices brought the U.S. rig utilization to 58% in late 2009, resulting in 15% lower well costs compared to mid-2008 as estimated by the CEI well cost index.

## 6.3 Geothermal wells drilling and completion costs

Current geothermal drilling technology has evolved from a combination of oil and gas and hydrothermal drilling practices due to similarity of equipment and materials. Modified oil and gas rigs are often used to develop geothermal resources (Binder, 2007; Blankenship et al., 2005). Rig alterations are required mainly because of different geologic settings. While oil and gas are typically found in sedimentary formations, geothermal lithologies include much harder,

abrasive, and fractured rocks. Geothermal formations consisting of igneous rocks interlayered with sediments are usually more difficult and slower to drill which affects costs.

Geothermal regimes are often underpressured and their porosity and permeability can vary by orders of magnitude within a few meters of depth (Blankenship et al., 2005; Tester, et al., 2006). This variability may result in the loss of circulation which contributes an average of 10-20% of the costs of the well (Blankenship et al., 2005). Higher lithological heterogeneity and well integrity issues encountered in geothermal drilling require that wells are stabilized using multiple casing intervals. The increased number of casing strings in shallow geothermal wells results in higher drilling times and costs compared to oil and gas completions. This correlation is reversed for deep resources. The risk of overpressure in deep oil and gas aquifers is much higher compared to geothermal reservoirs, which are typically hydrostatic or underpressured (Tester et al., 2006). Tapping overpressured hydrocarbon reservoirs may result in more casing strings and trouble time than required for drilling a geothermal well of similar depth.

Geothermal regimes are always hot and require the use of special logging devices and mud coolers. Annuli of geothermal wells have to be completely filled with cement due to thermal expansion of casing and well integrity issues. Oil and gas wells have lower requirements with only the bottom 500 to 1000 ft. (150 to 300 m) of annuli cemented in place (Tester et al., 2006). Geothermal wells need a non-standard casing if the brine is very corrosive due to increased contents of $CO_2$, $H_2S$ or other dissolved species. Such casing may also be required in some oil and gas wells in corrosive or sour gas environment.

Finally, the economically feasible mass flow rates of geothermal brine are much higher compared to hydrocarbon wells. Geothermal wells have higher completion diameters (7” to 9-

5/8" perforated casing, liner, or open hole) compared to oil and gas wells (4-1/2" to 5" perforated casing) (Bush and Siega, 2010; Tester et al., 2006). Higher diameters reduce penetration rates and require larger drilling bits, more powerful rigs, and more steel and cement to complete. Altogether, shallow geothermal drilling (<3000 m) is more technically complex than oil and gas drilling. In contrast, deep hydrocarbon wells (>5000 m) tapping overpressured reservoirs are likely to be more challenging than deep EGS wells.

In this section, the influence of the abovementioned factors on the drilling and completion costs was considered by comparing the cost of geothermal wells to the cost of oil and gas wells. Several methods were used to infer the cost of geothermal wells. An extensive database of 104 hydrothermal and EGS wells drilled between 1972 and 2002 and 42 wells drilled between 2008 and 2013 has been assembled. These data are presented in Table 6-3. In addition to reported costs of actual geothermal wells, the predicted costs of 29 hydrothermal and EGS wells were also included in Table 6-3. Because of limited geothermal drilling activity in the U.S. and the confidential nature of drilling costs, the data presented also include non – U.S. wells. 126 elements in this data set represent individual geothermal wells and the remaining 20 give average costs and depths of multiple similar wells drilled in one field within short period of time.

*Table 6-3: Summary of actual and predicted completed geothermal wells costs.*

| Well ID | Depth (m) | Depth (ft.) | Cost when drilled (M$) | Year drilled | Cost year 2009 (M$)* | Comments |
|---|---|---|---|---|---|---|
| **EGS Actual Costs** | | | | | | |
| GT-1 | 732 | 2402 | 0.06 | 1972 | 1.29 | Fenton Hill, New Mexico, USA |

| | | | | | | |
|---|---|---|---|---|---|---|
| GT-2 | 2932 | 9619 | 1.90 | 1974 | 30.41 | (Tester and Herzog, 1990) |
| EE-1 | 3064 | 10052 | 2.30 | 1975 | 22.77 | |
| EE-2 | 4660 | 15289 | 7.30 | 1980 | 29.81 | |
| EE-3 | 4250 | 13944 | 11.50 | 1981 | 40.26 | |
| EE-3a | 4572 | 15000 | 5.16 | 1988 | 23.66 | |
| RH-11 (low) | 2175 | 7136 | 1.24 | 1981 | 6.51 | Rosemanowes, Cornwall, UK (Tester and Herzog, 1990)<br><br>Low: 1 USD = 1 GBP<br>High: 1.6 USD= 1 GBP |
| RH-11 (high) | 2175 | 7136 | 1.98 | 1981 | 10.41 | |
| RH-12 (low) | 2143 | 7031 | 1.24 | 1981 | 6.51 | |
| RH-12 (high) | 2143 | 7031 | 1.98 | 1981 | 10.41 | |
| RH-15 (low) | 2652 | 8701 | 2.25 | 1985 | 14.88 | |
| RH-15 (high) | 2652 | 8701 | 3.60 | 1985 | 23.81 | |
| GPK3 | 5101 | 16736 | 6.57 | 2003 | 17.97 | Soultz, France. No trouble costs.<br>1 USD = 1.13 EUR (Baria, 2005) |
| GPK4 | 5100 | 16732 | 5.14 | 2004 | 10.60 | |
| Habanero 2 | 4725 | 15502 | 6.30 | 2004 | 12.99 | Australia. No trouble costs.<br>USD = 0.724 AUD (Wyborn, 2005) |
| **EGS Predicted Costs** | | | | | | |
| UK 1 | 6000 | 19685 | 8.42 | 1985 | 23.78 | 1 USD = 1 GBP (Shock, 1987) |
| Utah 1 | 3657 | 11998 | 3.36 | 1987 | 19.76 | Roosevelt Hot Springs, (Bechtel National Inc., 1988) |
| Japan 1 | 3000 | 9843 | 6.00 | 1985 | 39.69 | (Hori, 1986) |
| Entingh 1 | 3000 | 9843 | 6.90 | 1984 | 45.82 | (D. Entingh, 1987) |
| Entingh 2 | 3000 | 9843 | 3.80 | 1984 | 25.24 | |
| Entingh 3 | 3000 | 9843 | 3.00 | 1984 | 19.92 | |
| Heat Mining 1 | 3000 | 9843 | 3.00 | 1984 | 19.92 | (Armstead and Tester, 1987) |
| **U.S. Hydrothermal Actual Wells** | | | | | | |
| Geysers 1 | 1800 | 5906 | 0.49 | 1976 | 5.46 | (Milora and Tester, 1976) |
| Geysers 2 | 3048 | 10000 | 2.28 | 1989 | 10.95 | (Batchelor, 1989) |
| Geysers 3 | 3491 | 11452 | 2.66 | 1994 | 13.33 | (GeothermEx, 2004) |
| Geysers 4 | 2858 | 9378 | 2.18 | 1992 | 16.84 | |
| Geysers 5 | 3027 | 9932 | 2.92 | 1995 | 21.46 | |
| Geysers 6 | 2947 | 9670 | 3.76 | 1992 | 29.02 | Depth is for deepest of 3 legs and cost is for all 3 legs (GeothermEx, 2004) |
| Geysers 7 | 2590 | 8496 | 2.22 | 1992 | 17.12 | (GeothermEx, 2004) |
| Geysers 8 | 3307 | 10850 | 2.35 | 1992 | 12.77 | |
| Geysers 9 | 2874 | 9429 | 3.24 | 1992 | 24.97 | Well has 3 legs (GeothermEx, 2004) |

| | | | | | | |
|---|---|---|---|---|---|---|
| Geysers 10 | 2334 | 7658 | 0.82 | 1986 | 5.80 | (GeothermEx, 2004) |
| Geysers 11 | 2277 | 7471 | 1.19 | 1985 | 7.69 | |
| Geysers 12 | 3233 | 10606 | 2.49 | 1986 | 12.58 | |
| Geysers 13 | 1703 | 5588 | 0.80 | 1986 | 5.93 | |
| Geysers 14 | 2780 | 9120 | 1.97 | 1988 | 14.66 | |
| Geysers 15 | 2088 | 6849 | 1.42 | 1987 | 11.92 | |
| Imperial Valley | 1600 | 5249 | 0.17 | 1976 | 1.85 | (Milora and Tester, 1976) |
| Medicine Lake | 2592 | 8503 | 3.79 | 2002 | 15.02 | (GeothermEx, 2004) |
| SSU3 1 | 2134 | 7000 | 3.58 | 1988 | 28.24 | Unocal, avg. of 2 producers (GeothermEx, 2004) |
| Vulcan 1 | 1219 | 4000 | 1.77 | 1985 | 8.87 | Magma, avg. of 7 producers (GeothermEx, 2004) |
| Hoch 1 | 1524 | 5000 | 3.08 | 1987 | 22.45 | Magma, avg. of 7 producers (GeothermEx, 2004) |
| Elmore 1 | 1829 | 6000 | 2.86 | 1987 | 24.02 | Magma, avg. of 8 producers (GeothermEx, 2004) |
| Leathers 1 | 2286 | 7500 | 2.97 | 1988 | 22.78 | Magma, avg. of 7 producers (GeothermEx, 2004) |
| SSU3 2 | 2134 | 7000 | 1.52 | 1988 | 11.98 | Unocal, avg. of 7 injectors (GeothermEx, 2004) |
| Vulcan 2 | 1219 | 4000 | 1.42 | 1985 | 7.13 | Magma, avg. of 5 injectors (GeothermEx, 2004) |
| Hoch 2 | 1524 | 5000 | 1.54 | 1987 | 11.22 | Magma, avg. of 4 injectors (GeothermEx, 2004) |
| Elmore 2 | 1829 | 6000 | 1.77 | 1987 | 14.85 | Magma, avg. of 4 injectors (GeothermEx, 2004) |
| Leathers 2 | 2286 | 7500 | 2.51 | 1988 | 19.22 | Magma, avg. of 4 injectors (GeothermEx, 2004) |
| HFC 1 | 1829 | 6000 | 1.90 | 1984 | 12.32 | HGC, avg. of 21 wells (GeothermEx, 2004) |
| SIGC 1 | 1524 | 5000 | 1.02 | 1993 | 6.70 | Ormat, avg. of 11 producers (GeothermEx, 2004) |
| SIGC 2 | 1524 | 5000 | 0.87 | 1993 | 5.71 | Ormat, avg. of 10 injectors (GeothermEx, 2004) |
| Ormesa I - 1 | 1524 | 5000 | 0.85 | 1986 | 5.65 | Ormat, avg. of 19 producers (GeothermEx, 2004) |
| Ormesa I - 2 | 1524 | 5000 | 0.55 | 1986 | 3.67 | Ormat, avg. of 13 injectors (GeothermEx, 2004) |
| Ormesa II - 1 | 1524 | 5000 | 0.84 | 1987 | 6.09 | Ormat, avg. of 7 producers (GeothermEx, 2004) |
| Ormesa II - 2 | 1524 | 5000 | 0.81 | 1987 | 5.93 | Ormat, avg. of 4 injectors (GeothermEx, 2004) |

| | | | | | | |
|---|---|---|---|---|---|---|
| SNL – US | 2627 | 8618 | 1.76 | 1997 | 10.86 | (Mansure, 2004) |
| **Non – U.S. Hydrothermal Actual Wells** | | | | | | |
| El Salvator 1 | 1459 | 4788 | 1.80 | 1998 | 7.13 | Directional well (GeothermEx, 2004) |
| El Salvator 2 | 1608 | 5276 | 2.02 | 1997 | 11.83 | |
| El Salvator 3 | 1600 | 5250 | 1.83 | 1997 | 10.73 | |
| El Salvator 4 | 1628 | 5341 | 1.76 | 1997 | 10.31 | Vertical well (GeothermEx, 2004) |
| El Salvator 5 | 1646 | 5399 | 2.05 | 1997 | 12.02 | Directional well (GeothermEx, 2004) |
| El Salvator 6 | 1507 | 4944 | 1.69 | 1998 | 6.71 | |
| El Salvator 7 | 1556 | 5104 | 2.14 | 1998 | 11.81 | |
| El Salvator 8 | 1601 | 5253 | 3.09 | 1997 | 18.08 | |
| El Salvator 9 | 750 | 2461 | 1.73 | 1999 | 6.72 | Vertical well (GeothermEx, 2004) |
| El Salvator 10 | 650 | 2133 | 1.21 | 1997 | 5.19 | |
| El Salvator 11 | 2331 | 7648 | 2.57 | 1998 | 14.95 | Directional well (GeothermEx, 2004) |
| El Salvator 12 | 2432 | 7979 | 2.34 | 1998 | 13.65 | |
| El Salvator 13 | 2495 | 8186 | 2.21 | 1999 | 12.56 | |
| El Salvator 14 | 2157 | 7077 | 3.91 | 1997 | 22.86 | |
| El Salvator 15 | 2292 | 7520 | 2.96 | 1998 | 17.23 | |
| El Salvator 16 | 2179 | 7149 | 3.68 | 1998 | 20.29 | |
| El Salvator 17 | 2326 | 7630 | 3.19 | 1998 | 15.35 | |
| El Salvator 18 | 2208 | 7244 | 3.21 | 1998 | 17.71 | |
| El Salvator 19 | 2342 | 7684 | 2.53 | 1998 | 14.74 | |
| El Salvator 20 | 750 | 2461 | 0.98 | 1998 | 3.88 | Vertical well (GeothermEx, 2004) |
| El Salvator 21 | 2590 | 8498 | 2.15 | 1998 | 12.53 | Directional well (GeothermEx, 2004) |
| El Salvator 22 | 2500 | 8203 | 2.56 | 1997 | 15.82 | Vertical well (GeothermEx, 2004) |
| El Salvator 23 | 504 | 1653 | 1.23 | 1998 | 4.84 | Directional well (GeothermEx, 2004) |
| El Salvator 24 | 614 | 2015 | 0.85 | 1998 | 3.34 | |
| El Salvator 25 | 650 | 2133 | 1.11 | 1998 | 4.38 | |
| El Salvator 26 | 2045 | 6709 | 0.96 | 1997 | 5.63 | Vertical well (GeothermEx, 2004) |
| El Salvator 27 | 733 | 2406 | 1.00 | 1998 | 3.93 | |
| El Salvator 28 | 2428 | 7966 | 2.58 | 1999 | 14.64 | Directional well (GeothermEx, 2004) |
| Azores | 1135 | 3724 | 1.89 | 2000 | 7.69 | (GeothermEx, 2004) |
| Guatemala 1 | 200 | 655 | 0.24 | 1999 | 0.93 | |
| Guatemala 2 | 608 | 1996 | 0.45 | 1999 | 1.76 | |
| SNL – Non-US | 2317 | 7603 | 1.54 | 1996 | 10.00 | |

| | | | | | | |
|---|---|---|---|---|---|---|
| SNL – Non-US | 2374 | 7789 | 1.73 | 1997 | 10.67 | Sandia National Laboratories (Mansure, 2004) |
| SNL – Non-US | 2377 | 7800 | 1.38 | 1996 | 8.95 | |
| SNL – Non-US | 2739 | 8986 | 1.87 | 1997 | 11.52 | |
| SNL – Non-US | 2760 | 9055 | 1.32 | 1997 | 8.15 | |
| SNL – Non-US | 2807 | 9210 | 2.98 | 1996 | 19.36 | |
| SNL – Non-US | 2819 | 9249 | 0.92 | 1997 | 5.65 | |
| SNL – Non-US | 2869 | 9414 | 1.03 | 1996 | 6.69 | |
| SNL – Non-US | 3021 | 9912 | 1.06 | 1996 | 6.89 | |
| SNL – Non-US | 3077 | 10096 | 1.51 | 1996 | 7.76 | |
| **Hydrothermal Predicted Wells** | | | | | | |
| IV-FL | 1829 | 6001 | 1.12 | 1986 | 8.30 | Meridian predictions of hydrothermal wells from IMGEO (geothermal cost of model) database (Entingh, 1989) |
| IV-BI | 2743 | 8999 | 0.96 | 1986 | 6.74 | |
| BR-FL | 2438 | 7999 | 1.22 | 1986 | 8.58 | |
| BR-BI | 914 | 2999 | 0.56 | 1986 | 3.01 | |
| CS-FL | 3048 | 10000 | 2.03 | 1986 | 10.28 | |
| CS-BI | 914 | 2999 | 0.58 | 1986 | 3.12 | |
| YV-FL | 1524 | 5000 | 0.91 | 1986 | 6.69 | |
| YV-BI | 152 | 499 | 0.41 | 1986 | 2.64 | |
| GY-DS | 3048 | 10000 | 1.16 | 1986 | 5.84 | |
| ***Wells drilled in or after year 2008*** | | | | | | |
| **HDR predicted** | | | | | | |
| Thermasource | 6096 | 20000 | 21.34 | 2008 | - | (Polsky et al., 2008) |
| Impact Tech. 1 | 6401 | 21000 | 27.01 | 2012 | - | (GEECO et. al., 2012), costs evaluated using WellCost Lite |
| Impact Tech. 2 | 6401 | 21000 | 22.18 | 2012 | - | |
| Impact Tech. 3 | 9144 | 30000 | 31.80 | 2012 | - | |
| WellCost Lite 1 | 2438 | 8000 | 4.54 | 2012 | - | WellCost Lite (Livesay, 2012) Well configurations with 8-1/2 and 10-5/8 final bit diameter were designed for each depth. Wells are non-optimal and trouble free. |
| WellCost Lite 2 | 2438 | 8000 | 5.0 | 2012 | - | |
| WellCost Lite 3 | 2438 | 10000 | 5.14 | 2012 | - | |
| WellCost Lite 4 | 2438 | 10000 | 5.5 | 2012 | - | |
| **U.S. Hydrothermal Actual** | | | | | | |
| LC-US 1 | 1052 | 3450 | 3.11 | 2009 | - | (Capuano Jr., 2012) |
| LC-US 2 | 1222 | 4010 | 3.96 | 2009 | - | |
| LC-US 3 | 1234 | 4050 | 4.35 | 2009 | - | |

| | | | | | | |
|---|---|---|---|---|---|---|
| LC-US 4 | 1561 | 5120 | 2.9 | 2010 | - | |
| LC-US 5 | 1862 | 6110 | 3.35 | 2010 | - | |
| LC-US 6 | 1173 | 3850 | 1.75 | 2011 | - | |
| US-1 | 3299 | 10825 | 13.54 | 2009 | - | Individual U.S. hydrothermal wells |
| US-2 | 2568 | 8425 | 7.26 | 2009 | - | |
| US-3 | 2323 | 7622 | 5.37 | 2009 | - | |
| US-4 | 2806 | 9205 | 7.44 | 2013 | - | |
| US-5 | 2514 | 8247 | 4.91 | 2011 | - | |
| US-6 | 2517 | 8258 | 5.29 | 2012 | - | |
| US-7 | 939 | 3080 | 2.02 | 2011 | - | |
| US-8 | 1065 | 3493 | 1.85 | 2011 | - | |
| US-9 | 1309 | 4294 | 2.58 | 2011 | - | |
| US-10 | 3582 | 11753 | 8.15 | 2010 | - | |
| US-11 | 3761 | 12340 | 7.67 | 2010 | - | |
| US-12 | 3562 | 11687 | 9.60 | 2010 | - | |
| US-13 | 3041 | 9976 | 7.64 | 2010 | - | |
| **Non – U.S. Hydrothermal Actual** | | | | | | |
| MBB-2 | 1840 | 6037 | 6.42 | 2011 | - | Indonesia, Wayang Windu field (Prihutomo et al., 2012) |
| MBB-3 | 1930 | 6332 | 4.16 | 2011 | - | |
| MBB-6 | 2450 | 8038 | 7.12 | 2011 | - | |
| WWA-5 | 1550 | 5085 | 3.46 | 2011 | - | |
| WWA-6 | 1460 | 4790 | 3.27 | 2011 | - | |
| MBB-4 ST2 | 1914 | 6280 | 5.86 | 2011 | - | Indonesia, Wayang Windu field (Prihutomo, 2012) |
| MBB-5 ST1 | 1916 | 6286 | 5.46 | 2011 | - | |
| MBE-4 | 1600 | 5249 | 3.83 | 2011 | - | |
| MBE-5 | 2288 | 7507 | 7.43 | 2011 | - | |
| WWT-2 | 2100 | 6890 | 5.95 | 2011 | - | |
| AWI 7-8 | 2819 | 9250 | 3.59 | 2008 | - | Indonesia, Salak field (Prihutomo and Arianto, 2010) |
| AWI 20-1 | 2704 | 8872 | 6.50 | 2008 | - | |
| New Zealand 1 | 2306 | 7566 | 2.94 | 2008 | - | Avg. of 9 wells (Bush and Siega, 2010) |
| New Zealand 2 | 2087 | 6847 | 3.82 | 2008 | - | Avg. of 4 wells (Bush and Siega, 2010) |
| New Zealand 3 | 2794 | 9167 | 6.86 | 2008 | - | Avg. of 6 wells (Bush and Siega, 2010) |

To determine the applicability of CEI index to geothermal wells, the costs of geothermal wells completed between 1972 and 2002 were normalized to 2009 U.S. dollars. A 7% cost escalation rate was assumed for the 1972-1976 period. Normalized costs of historical wells were compared to nominal (non-normalized) costs of most recent geothermal wells drilled between 2008 and 2013. In Figure 6-10 the cost-depth data obtained for actual and predicted geothermal wells are plotted on a semi-logarithmic scale. Hydrothermal wells are denoted with dots and EGS wells with triangles. Solid markers symbolize actual costs and empty markers represent predicted (modeled) costs. Costs of geothermal wells drilled before 2007 were updated to US$ (yr. 2009) using CEI drilling cost index and are denoted with various colors except from black. Cost of geothermal wells drilled between 2008 and 2012 were not normalized to yr. 2009 and are denoted with black markers.

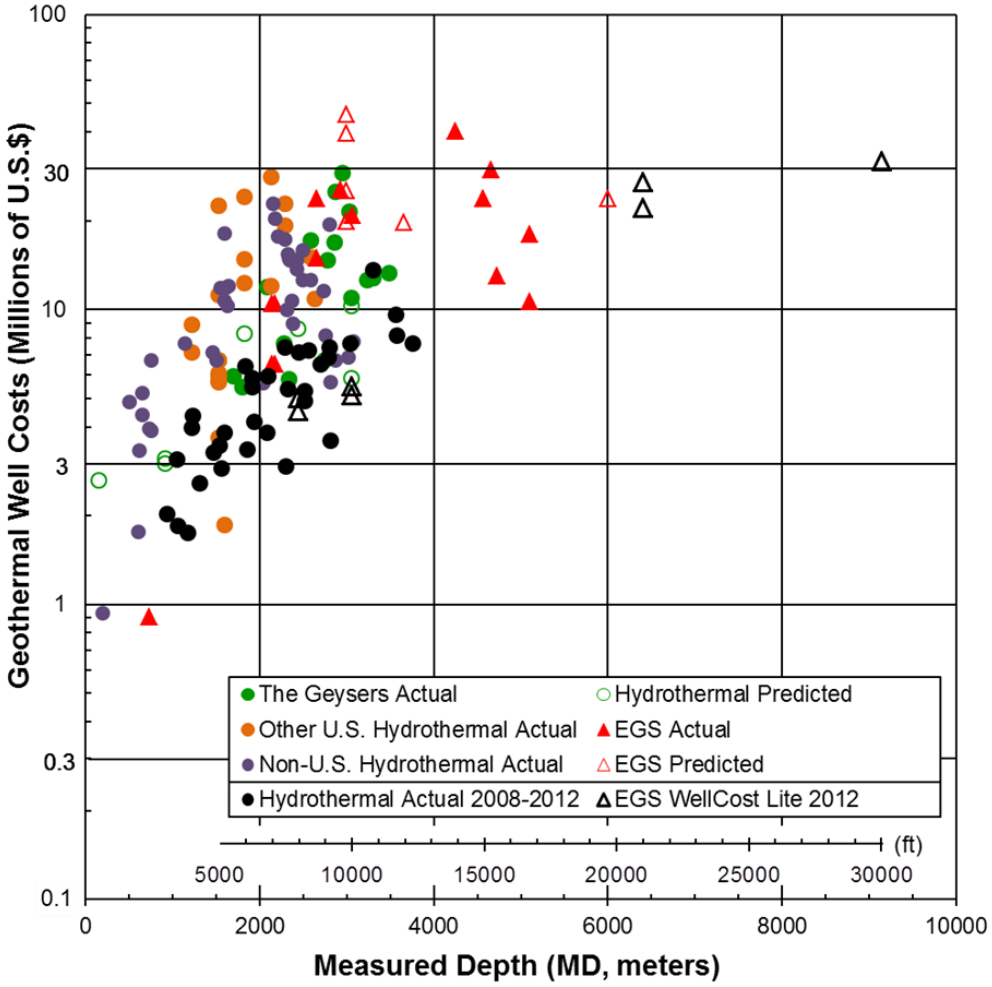


*Figure 6-10: Geothermal well drilling and completion costs as a function of measured well depth. Costs of recently drilled or modeled wells (in black) are compared to costs of historical wells normalized to U.S. $ (yr. 2009) using CEI index (in other colors).*

The historical costs of geothermal wells normalized using the CEI index are generally greater than the real current geothermal well costs. This shows that neither the CEI, nor any other cost index based on oil and gas wells can consistently be used to represent changes in geothermal well costs. Since 1976, the cost of geothermal wells escalated at lower rates compared to oil and gas wells. It was likely due to more extensive geothermal drilling technology

improvements. Furthermore, geothermal well costs are also correlated less with observed fluctuations in oil and gas prices.

Current geothermal well costs are more accurately represented by the 2008-2013 well records and WellCost Lite model predictions for EGS wells. Figure 6-11 shows geothermal well costs (in black) as compared to hydrocarbon well costs (in red) represented by the average 2009 JAS oil and gas drilling costs (full red markers) and a set of records for individual ultra-deep oil and gas wells (blank red markers). The costs of individual ultra-deep hydrocarbon wells drilled in the early 2000s' (Tester, et al., 2006) were normalized to 2009 using the CEI index. Actual costs of hydrothermal wells drilled between 2008 and 2013 are presented in nominal US$. Costs of EGS wells are predicted using WellCost Lite model and are presented in US$ (2012).

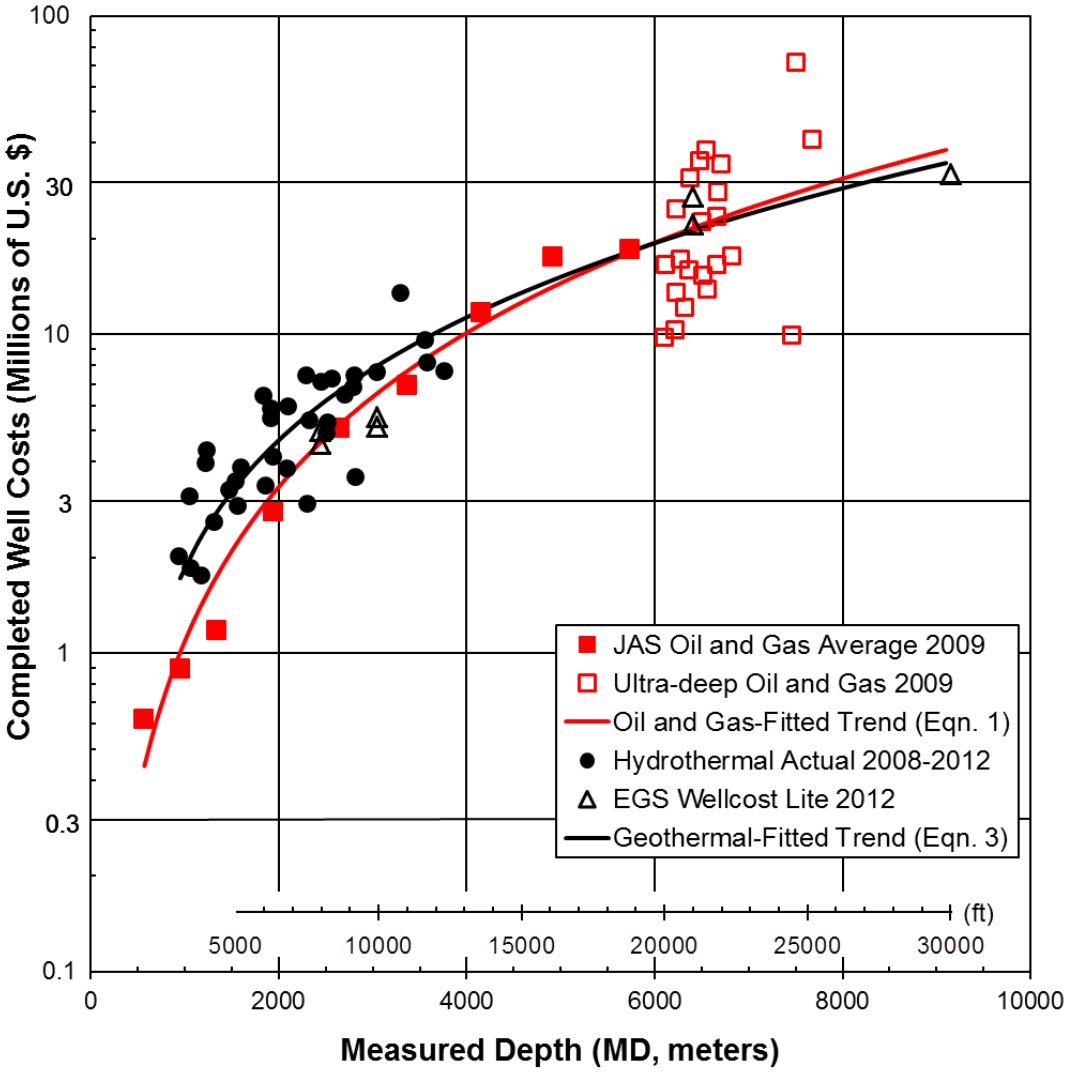


*Figure 6-11: Geothermal well costs (in black) compared to average 2009 oil and gas well costs (in red). See text for more details.*

The average current costs of geothermal wells can be reasonably well approximated by a following equation with a correlation coefficient $R^2$ of 0.92:

$$Geothermal\ well\ cost = 1.72 \cdot 10^{-7} \cdot (MD)^2 + 2.3 \cdot 10^{-3} \cdot MD - 0.62 \qquad (6\text{-}3)$$

where well cost is in millions of U.S. dollars and MD is a measured depth of well in meters. This correlation is presented in Figure 6-11.

The recently drilled hydrothermal wells between 1 and 4 km have typically been more expensive than oil and gas wells of the same depth. On average, 2 km (6560 ft.) and 3 km (9840 ft.) geothermal wells are 40% and 23% more expensive than hydrocarbon wells, respectively. The predicted costs of deep EGS wells (>6000 m) are up to 10% lower than the JAS oil and gas average and lay within the observed scatter of ultra-deep oil and gas wells.

The large scatter in reported well costs has been observed before in geothermal drilling (Mansure et al., 2006). Wide distribution of well costs is typical even for the very mature hydrocarbon drilling industry (McIntosh, 2010) as proven by the ultra-deep well records shown in Figure 6-11. Cost dispersion may be partially explained by the variability in lithology of geothermal formations. Previous studies found a spread in geothermal well drilling costs within a single field to be over 10% lower compared to multi-field data (Mansure et al., 2006). Another reason for the scatter may be inconsistency in the methods used to report costs among various drilling companies. Moreover, the analyzed geothermal wells includes both standard (9-5/8”), as well as large-diameter (13-3/8” casing) wellbores, the latter of these being approximately 30% more expensive (Bush and Siega, 2010).

The cost distribution of post-2007 hydrothermal wells at a specified depth has a positive skew, which is characteristic of drilling activities (McIntosh, 2010). Geothermal drilling costs are unlikely to be normally distributed. Skewed probability density function such as gamma, log-normal, or Weibull with a long tail representing uncommon, very expensive wells is more suitable.

## 6.4 Learning effects in well drilling and completion

Reflecting on previous field-specific analyses of learning potential (Brett and Millheim, 1986; Ikoku, 1978), this section provides an attempt to generate a more general learning correlation. The following analysis evaluates the learning potential in hydrocarbon well drilling, based on the current and historical JAS cost data. Learning potential is defined in terms of cost ratio of an average development well to an average exploratory well, both of which have same measured depth.

The first well in an oil and gas field is drilled with a limited prior knowledge about the formation characteristics. Thus, exploratory wells drilled in unproven areas are inherently more risky and likely to take more time to drill. They are often among the most expensive wells in a drilling campaign. Development wells tapping identified reserves should be less expensive as a result of increased experience of the operator.

The learning potential analysis for oil and gas wells is based on the JAS records from 15 years in between 1989 and 2009. Drilling cost per meter was calculated separately for each year, type of well (exploratory, development), and each of the nine CEI index depth intervals. The exploratory wells in the JAS database include new-field wildcats, deeper- and shallower-pool tests and outposts (extensions). Development wells comprise wells drilled to produce oil and gas from reservoirs discovered by previous drilling (American Petroleum Institute, 1976-2009). To enhance the correlation accuracy, the minimum number of exploratory wells drilled in one year within each depth interval was set to 30. Cost ratios of development and exploratory wells in all 15 years were compared and similar trends were observed. All calculated values of

specific drilling and completion costs in nominal dollars per meter were then normalized to 2009 dollars using the CEI index.

The normalized costs of exploratory and development wells, as a function of their measured depth, are presented in Figure 6-12. The scatter in costs of shallow and medium-deep development wells is lower than for exploratory wells. Due to larger numbers of development wells, their drilling and completion costs are typically closer to average well costs represented by the CEI index. Thus, normalized costs of development wells from various years show less spread compared to exploratory wells. High-order polynomial curves were fitted to data in Figure 6-12. These curves represent average costs of exploratory and development oil and gas wells as a function of measured depth. Learning potential is presented in Figure 6-12 in the form of development to exploratory well cost ratio, which varies from 0.82 to 1.03 with an average value of 0.92. This indicates that on average, onshore oil and gas development wells are 8% less expensive than exploratory wells. Statistically, moderately deep and deep oil and gas wells (2000-5000 m) have the highest learning potential with development wells being 7%-18% less expensive than exploratory wells.

This statistically determined learning potential is less optimistic compared to results presented earlier by Brett and Millheim for oil and gas wells (Brett and Millheim, 1986). These authors determined the average learning rate in terms of drilling time. They estimated that the 3$^{rd}$ and 10$^{th}$ development wells should take typically 75% and 50% of the time required to drill the 1$^{st}$ development well, respectively. Such learning performance would result in more than 8% average cost difference between exploratory and development wells as determined in this study.

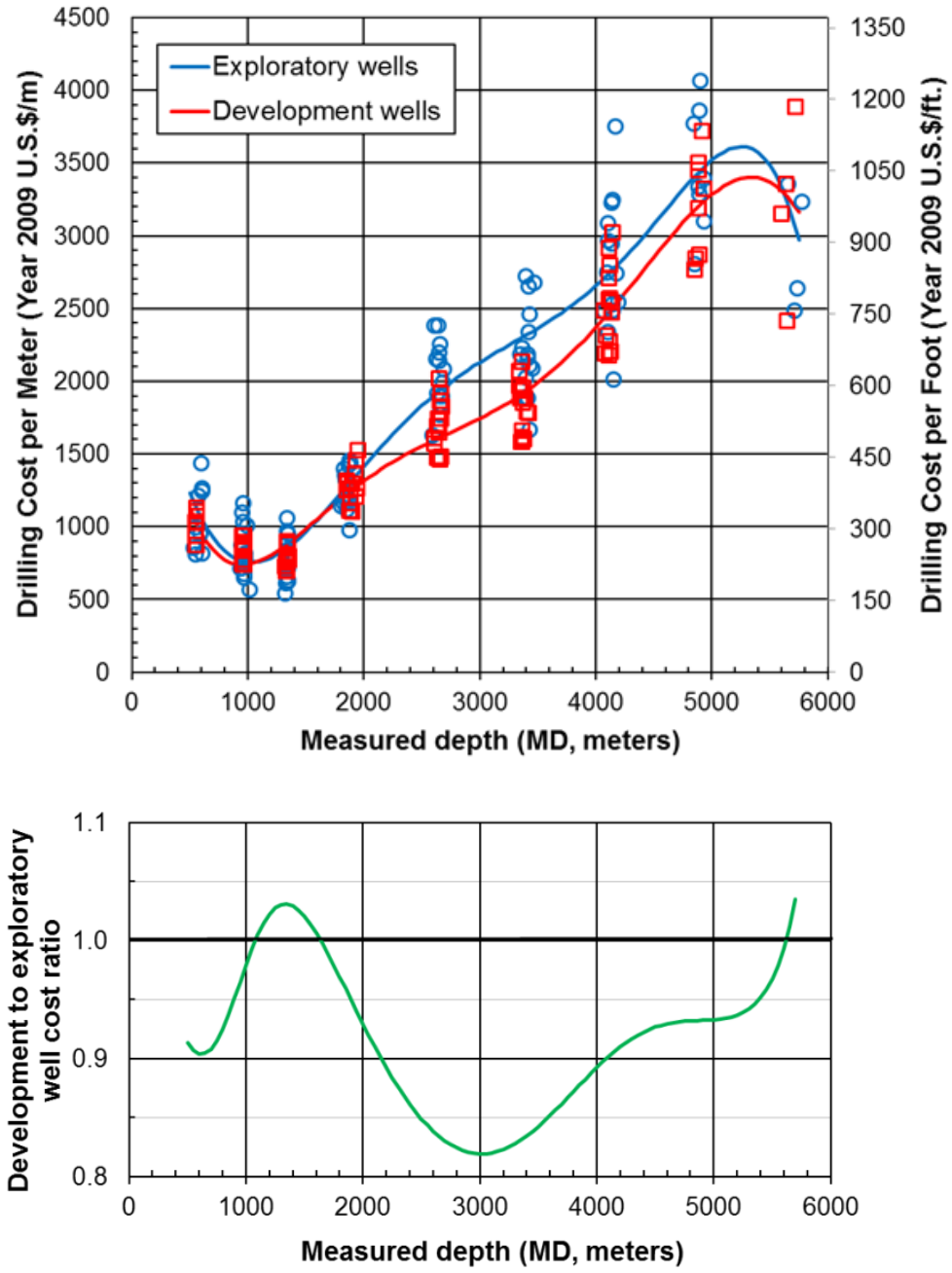


*Figure 6-12: Above: Average drilling and completion costs per meter of exploratory and development oil and gas wells. Below: Ratio of cost of an average hydrocarbon development well to an average exploratory well as a function of the measured depth.*

One possible explanation of the discrepancy in learning potential between this study and previous analyses is that learning curve papers often show a state-of-art learning performance instead of average improvement. The fields chosen for such studies are likely to be the ones in which enhancement in penetration rates has been previously observed. This s average results for the U.S. onshore oil and gas drilling, but may be biased by the differences in design of exploratory and development wells. Most exploratory wells are vertical, while many development wells are directional or horizontal (Kaiser, 2007). Exploratory wells may also have a small diameter or shorter cement sheath.

The learning curve in hydrocarbon drilling would be a rather conservative estimate of geothermal drilling performance improvement. Learning potential in the geothermal industry is likely to be higher as geothermal formations have less homogenous and predictable lithology than sedimentary formations. Geothermal wildcats often have more casing strings compared to development wells of the same depth. This ensures well stability in an unknown environment, but increases capital investment.

To estimate geothermal learning potential, the drilling performance reported by Brett and Millheim (Brett and Millheim, 1986) was used. Reported improvements in drilling time were converted to well costs by evaluating the time-dependent cost components of geothermal wells. Analysis of a detailed cost component spreadsheet for a 20000 ft. EGS well (Polsky et al., 2008) shows that time-dependent costs correspond to approximately 50% of total geothermal well completion costs. This number was used to express the reported range of learning performance (Brett and Millheim, 1986) in terms of costs. Results show that with 'industry average' learning rate, the $5^{th}$ geothermal development well drilled in a given field is likely to cost no more than 80% of the first well as presented in Figure 6-13. Such improvement rates have been observed

in geothermal drilling, where development wells are often 25% less expensive compared to exploratory wells (Capuano Jr., 2012).

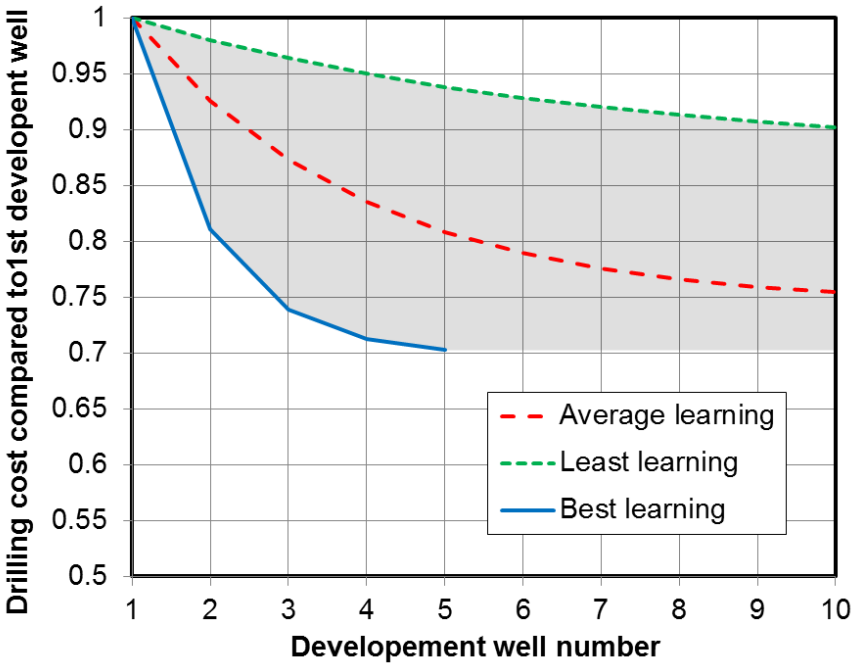


*Figure 6-13: Estimated learning curve in geothermal drilling. These estimates are based on reported range of improvements in drilling time of oil and gas wells and cost breakdown for geothermal drilling.*

## 6.5 Conclusions

In general, operators are pursuing deeper and more difficult drilling programs to extract resources from oil, gas, and geothermal reservoirs. Improved drilling technology has reduced the rate at which well costs increase with depth. The current average cost of onshore oil and gas wells is described as a power function of its measured depth while drilling expenditures incurred in specific years are compared using a well cost index. A newly developed cost index (CEI)

accounts for yearly changes in depth and type of U.S. onshore oil and gas wells. The CEI trend offers superior accuracy and the longest lifespan (1976-2009) among available oil and gas well cost indices. It shows that oil and gas well completion costs increased by over 250% between 2003 and 2008, followed by a modest 15% drop in 2009.

The statistical analysis of learning potential in hydrocarbon drilling indicated that an average onshore development well would be estimated to be 8% cheaper than the exploratory well of the same depth.

This work showed, that the practice of using oil and gas well cost indices to normalize the geothermal well costs is no longer valid. The improvements in geothermal well drilling technology and the volatility of oil markets led to much lower geothermal well cost escalation rates compared to oil and gas drilling. Despite the differences in geologic conditions, the larger completed diameters, and the increased complexity of drilling geothermal wellbores compared to hydrocarbon wells, the costs of geothermal and oil and gas wells are similar.

## 6.6 Acknowledgements

I greatly appreciated the help from Dr. Brian Anderson in obtaining the JAS reports, from late Bill Livesay in providing the WellCost Lite models, and from Rachel Silverman in collecting a fraction of the geothermal well cost data. This chapter is extensively based on the following publication:

Lukawski, M., Anderson, B., Augustine, C., Capuano, L., Beckers, K., Livesay, B., Tester, J., 2014. Cost Analysis of Oil, Gas, and Geothermal Well Drilling, Journal of Petroleum Science and Engineering 118, 1-14.

## 6.7 References


American Petroleum Institute, (API), 1976-2009. Joint Association Survey on Drilling Costs. Washington, DC, USA.

Armstead, H.C.H., Tester, J.W., 1987. Heat Mining. E.F. Spon, London, UK.

Augustine, C., Tester, J.W., Anderson, B., Petty, S., Livesay, B., 2006. A Comparison of Geothermal with Oil and Gas Well Drilling Costs, in: Proceedings, Thirty-First Workshop on Geothermal Reservoir Engineering, Stanford University. Stanford, CA, USA, p. 15.

Augustine, Chad, Anderson, A., Young, K.R., 2010. Updated U. S. geothermal supply curve, in: Proceedings, Thirty-Fifth Workshop on Geothermal Reservoir Engineering, Stanford University. Stanford, CA, USA, p. 16.

Baker Hughes, 2013. Rotary Rig Count [WWW Document]. URL http://investor.shareholder.com/bhi/rig_counts/rc_index.cfm (accessed 6.5.13).

Batchelor, A.S., 1989. Geoscience Ltd., Falmouth, U.K., personal communication, 12.1989.

Bechtel National Inc., 1988. Hot Dry Rock Venture Risks and Investigation. Final report for the U.S. Department of Energy, under contract DE-AC03-86SF16385. San Francisco, CA, USA.

Binder, J., 2007. New Technology Drilling Rig, in: Proceedings European Geothermal Congress 2007. Unterhaching, Germany, p. 4.

Blankenship, D.A., Wise, J.L., Bauer, S. J., Mansure, A. J., Normann, R.A., Raymond, D.W., LaSala, R.J., 2005. Research Efforts to Reduce the Cost of Well Development for Geothermal Power Generation, in: 40th U.S. Symposium on Rock Mechanics (USRMS). p. 10.

Bloomfield, K., Laney, P., 2005. Estimating Well Costs for Enhanced Geothermal System Applications. Idaho National Laboratory Report for the U.S Department of Energy. Contract DE-AC07-05ID14517 95.

Brett, J., Millheim, K., 1986. The Drilling Performance Curve: A Yardstick for Judging Drilling Performance. SPE 15362 12.

Bush, J., Siega, C., 2010. Big Bore Well Drilling in New Zealand – A Case Study, in: Proceedings World Geothermal Congress 2010. Bali, Indonesia, p. 7.

Capuano Jr., L.E., 2012. President/CEO Capuano Engineering Consultants, personal communication, 15.08.2012.

Entingh, D., 1987. Historical and Future Cost of Electricity from Hydrothermal Binary and Hot Dry Rock Reservoirs, 1975-2000. Alexandria, VA, USA.

Entingh, D., 1989. Meridian Corporation, Alexandria, VA., personal communication, 11.1989.

Entingh, D.J., Mines, G.L., Nix, G., Mansure, A., Bauer, S., Petty, S., Livesay, B. J., 2006. DOE Geothermal Electricity Technology Evaluation Model (GETEM): Volume I – Technical Reference Manual.

Fox, D., Sutter, D., Beckers, K., Lukawski, M., Koch, D., Anderson, Brian J, Tester, J.W., 2013. Sustainable heat farming: Modeling extraction and recovery in discretely fractured geothermal reservoirs. Geothermics 46, 42–54.

GEECO (Gas Equipment Engineering Corporation) et. al., 2012. Baseline System Costs for 50 MW Enhanced Geothermal System - A Function of: Working Fluid, Technology, and Location. Final Report for the U.S. Department of Energy, DE-EE0002742 143.

GeothermEx, 2004. New Geothermal Site Identification and Qualification. California Energy Commision Report 264.

Hori, Y. et al., 1986. On Economics of Hot Dry Rock Geothermal Power Station and related documents. Japan.

Ikoku, C.U., 1978. Application of Learning Curve Models to Oil and Gas Well Drilling. SPE 7119 12.

Kaiser, M.J., 2007. A Survey of Drilling Cost and Complexity Estimation Models. International Journal of Petroleum Science and Technology 1, 1–22.

Kravis, S., Irrgang, R., Scott, P., Lollback, P., 2004. The Trouble Probability Plot : A New Measure of Drilling Maturity. SPE 89959 12.

Mansure, A. J., 2004. Sandia National Laboratories, personal communication, 12.04.2004.

Mansure, A. J., Bauer, S. J, Livesay, B.J., Petty, S., 2006. Geothermal Well Cost Analyses 2006. Geothermal Resources Council Transactions 30, 271–276.

Mansure, A. J., Blankenship, D.A., 2008. Geothermal Well Cost Analyses 2008. Geothermal Resources Council Transactions 32, 43–48.

Mansure, Arthur J., Blankenship, D., 2005. Geothermal Well Cost Analyses 2005. Geothermal Resources Council Transactions 29, 515–520.

McIntosh, J., 2010. The Future Ain't What It Used to Be , Or Is It? Journal of Petroleum Technology 62, 48–50.

Milora, S., Tester, J.W., 1976. Geothermal Energy as a Source of Electric Power. MIT Press, Cambridge, MA, USA.

Petty, S., Bour, D., Livesay, B., Baria, R., Adair, R., 2009. Synergies and Opportunities Between EGS Development and Oilfield Drilling Operations and Producers. SPE 121165.

Polsky, Y., Capuano, L.J., Finger, J., Huh, M., Knudsen, S., Mansure A J, Raymond, D., Swanson, R., 2008. Enhanced Geothermal Systems (EGS) Well Construction Technology Evaluation Report. Sandia report SAND2008-7866 108.

Prihutomo, M.J., 2012. Star Energy Geothermal (Wayang Windu), Ltd, personal communication, 23.10.2012.

Prihutomo, M.J., Arianto, S., 2010. Drilling Performance Improvements of Salak Geothermal Field, Indonesia 2006 - 2008, in: Proceedings World Geothermal Congress 2010. Bali, Indonesia, p. 10.

Prihutomo, M.J., Hartono, Y., Samosir, J., Abanes, R., 2012. Extended Reach and High Inclination Drilling Geothermal Well in Wayang Windu, in: Proceedings, Thirty-Seventh Workshop on Geothermal Reservoir Engineering, Stanford University. Stanford, CA, USA, p. 10.

RigData, 2010. Land Rig Newsletter. Day Rate Report 20, 1–18.

Rowley, J., Saito, S., Long, R., 2000. Advanced Drilling System For Drilling Geothermal Wells- An Estimate of Cost Savings. Geothermal Resources Council Transactions 24, 87–92.

Sanyal, S.K., 2005. Sustainability and Renewability of Geothermal Power Capacity. Proceedings World Geothermal Congress 2005 Antalya, Turkey.

Sanyal, S.K., Morrow, J.W., 2012. Success and the Learning Curve Effect in Geothermal Well Drilling – a Worldwide Survey, in: Proceedings Thirty-Seventh Workshop on Geothermal Reservoir Engineering, Stanford University. Stanford, CA, USA, p. 8.

Stefansson, V., 1992. Success in geothermal development. Geothermics 21, 823–834.

Tester, J.W., Herzog, H., 1990. Economic Predictions for Heat Mining: A Review and Analysis of Hot Dry Rock (HDR) Geothermal Energy Technology. Cambridge, MA, USA.

Tester, J. W., Anderson, B. J., Batchelor, A.S., Blackwell, D.D., DiPippo, R., Drake, E.M., Garnish, J., Livesay, B.J., Moore, M.C., Nichols, K., Petty, S., Taksoz, M.N., Veatch, R.W.J., 2006. The Future of Geothermal Energy: Impact of Enhanced Geothermal Systems (EGS) on the United States in the 21st Century. Boston, USA.

Thorsteinsson, H., Augustine, C., Anderson, B. J., Moore, M.C., Tester, J.W., 2008. The Impacts of Drilling and Reservoir Technology Advances on EGS Exploitation. Proceedings, Thirty-Third Workshop on Geothermal Reservoir Engineering, Stanford University 14.

U.S. Bureau of Labor Statistics (BLS), 2013. Producer Price Indices (PPI): “Drilling oil, gas, dry, or service wells PCU21311121311101”; “Iron, steel pipe and tube from purchased steel, PCU331210331210”; “Cement manufacturing PCU327310327310” [WWW Document]. URL http://www.bls.gov/ppi/#tables

U.S. Department of Energy Geothermal Technologies Program, 2010. Drilling 1976-2006: A History of Geothermal Energy Research and Development in the United States.

U.S. Energy Information Administration (EIA), 2013a. Short-term Energy Outlook Real and Nominal Prices: Imported Crude Oil Prices [WWW Document]. URL http://www.eia.gov/forecasts/steo/realprices/ (accessed 5.15.13).

U.S. Energy Information Administration (EIA), 2013b. U.S. Natural Gas Wellhead Prices [WWW Document]. URL http://www.eia.gov/dnav/ng/ng_pri_sum_dcu_nus_m.htm (accessed 5.15.12).

U.S. Office of Management and Budget, 2013. Section 10, Table 10.1 - Gross Domestic Product and Deflators Used in the Historical Tables: 1940–2018 [WWW Document]. Budget of the United States Government. URL http://www.whitehouse.gov/omb/budget/Historicals

# 7 UNCERTAINTY ANALYSIS OF GEOTHERMAL WELL DRILLING AND COMPLETION COSTS

## 7.1 Introduction

The work described in Chapter 6 evaluated the average well costs as a function of well depth, but provided little information about the well cost uncertainty. While Figure 6-11 was used to illustrate the average well costs, it also show that two geothermal wells with similar depths may have significantly different costs. The average well costs are useful for comparing geothermal energy with other energy sources and for creating wise energy policies. This information is, however, insufficient for the finance industry, which cares about the economic risks of individual geothermal projects. Gaining an understanding of the drilling cost uncertainty could help geothermal developers in securing low-interest financing by reducing the infrastructure risks. Therefore, characterization of geothermal well drilling costs and uncertainty are critical to the growth and expansion of geothermal development, particularly for lower-grade, deeper resources.

Geothermal well costs were evaluated as a function of depth by a number of authors (Augustine et al., 2006; Lukawski et al., 2014; Mansure and Blankenship, 2013; Tester et al., 2006). The work described in Chapter 6 and a recent publication (Lukawski et al., 2014) as well as the previous study (Augustine et al., 2006) provided predictions for the average costs of geothermal wells at depths ranging from 3,000 to 30,000 ft. (910 to 9,100 m). They did not characterize the range of uncertainty around these average costs. Both studies point to the limited availability

of geothermal drilling data as the reason for taking this deterministic approach. The first publication to consider uncertainty as part of the EGS well costing calculation was (Yost et al., 2015). The authors used a computer program called Decision Aids for Tunneling (DAT) to model distributions of costs and times associated with each step of well drilling and completion. The overall cost of each drilling or completion activity was represented as a function of a fixed material cost, an hourly cost, and a time required for that activity. Uncertainty was factored into these equations by inputting probability distributions for all costs and times, which were obtained from the Sandia geothermal well database (Polsky et al., 2008). This yielded a method for calculating overall well cost probability distribution. However, the analysis by (Yost et al., 2015) is based on one EGS well and does not account for non-productive time (NPT). It also assumes that individual well cost components are not correlated with each other. This assumption may not always be valid; e.g. volumes of drilling mud and cement are often correlated since they are both affected by the frequency and severity of circulation loss events.

The approach of this work builds upon past methodologies to quantify the cost uncertainty of 8,000-15,000 ft. (2,400-4,600 m) deep EGS wells located in the U.S. While these depths may seem low compared to those presented in Chapter 6, approximately 70% of EGS wells drilled in the past fall within this range (Breede et al., 2013). In contrast the previous studies (Augustine et al., 2006; Lukawski et al., 2014; Mansure and Blankenship, 2008), this work presents probability distributions of well costs instead of a single, average drilling cost. This work builds on the probabilistic approach introduced by (Yost et al., 2015) by accounting for the non-productive time, including the correlations between individual well cost components, and most importantly by analyzing a range of EGS well depths instead of a single 20,000 ft. (6,100 m) well.

Correlations presented in this chapter can be used to determine the cost probability distributions for wells of any measured depth (MD) within the 8,000-15,000 ft. (2,400-4,600 m) range, assess the project risk, and facilitate investment decisions. To enhance the accuracy of the data set, only the most recent well cost data from the U.S. geothermal industry was incorporated, from the period of 2009 to 2013. The used well cost database includes fourteen hydrothermal wells drilled in the Western U.S. in similar geologic conditions, EGS wells from previous publications (Baker Hughes, 2012), and EGS wells designed in WellCost Lite for the purpose of this study. The well cost records were analyzed to: 1) determine the main variables influencing the costs of drilling and completing geothermal wells, 2) obtain the probability distribution of each of these variables, and 3) identify significant correlations between these variables. These distributions and correlations were then input to WellCost Lite, a predictive drilling cost model, using Monte Carlo method to obtain the probability distribution for the overall well cost as a function of depth.

The geothermal wells analyzed in this work were drilled in or designed for locations in the United States. Consequently, this analysis uses U.S. drilling, labor, and material costs. Similarly to the previous chapter, this analysis uses wells drilled in various locations. This introduces an additional scatter to the well cost database due to the differences in formation lithology and various location-specific costs such as rig rates. However, while the cost differences between individual geothermal fields are important, accounting for them reduces the overall cost variability by only 11% (Mansure et al., 2006). With a more extensive well cost database, presented methodology could also be used to produce more accurate correlations for individual geologic provinces.

## 7.2 Methodology

The overview of used methodology is presented as a flowchart in Figure 7-1. First, detailed well data for this study were gathered from several sources, including ten EGS wells modeled in WellCost Lite software. The well expenditures were evaluated using 2012 costs for individual well services and consumables. Other well cost data sources included fourteen actual hydrothermal wells drilled in the Western U.S. in similar geologic settings from 2008 to 2013 and eight EGS wells whose costs were estimated by drilling engineers (Baker Hughes, 2012). Table 7-1 provides a list of these wells with summary statistics that include drilling cost, depth, year drilled, and total drilling days.

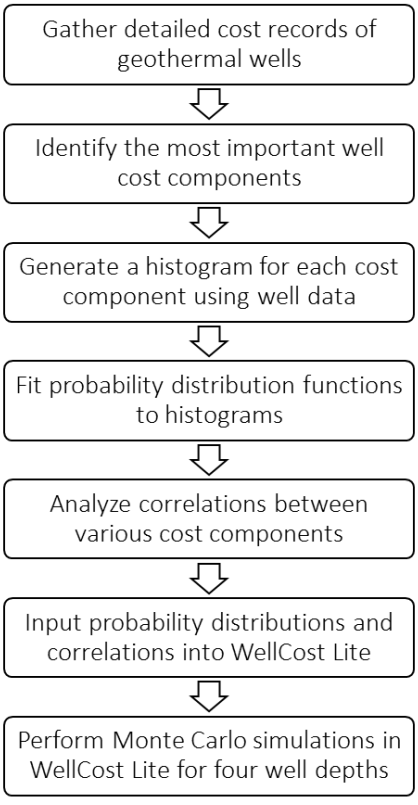


*Figure 7-1: Flowchart representing the used methodology*

*Table 7-1: List of geothermal wells with detailed cost data used in the probabilistic well cost study*

| Well name | Depth (m) | Depth (ft.) | Cost ($M) | Year | Well type | Total days |
|---|---|---|---|---|---|---|
| U.S. Hydrothermal 1 | 2,588 | 8,490 | 3.87 | 2003 | Production | 184 |
| U.S. Hydrothermal 2 | 3,041 | 9,976 | 7.64 | 2010 | Production | 110 |
| U.S. Hydrothermal 3 | 3,299 | 10,825 | 13.54 | 2009 | Injection | 162 |
| U.S. Hydrothermal 4 | 2,568 | 8,425 | 7.26 | 2009 | Injection | 91 |
| U.S. Hydrothermal 5 | 2,323 | 7,622 | 5.37 | 2009 | Injection | 65 |
| U.S. Hydrothermal 6 | 2,806 | 9,205 | 7.44 | 2013 | Injection | 86 |
| U.S. Hydrothermal 7 | 2,514 | 8,247 | 4.91 | 2011 | Injection | 58 |
| U.S. Hydrothermal 8 | 2,517 | 8,258 | 5.29 | 2012 | Injection | 64 |
| U.S. Hydrothermal 9 | 939 | 3,080 | 2.02 | 2011 | Injection | 57 |
| U.S. Hydrothermal 10 | 1,065 | 3,493 | 1.85 | 2011 | Injection | 28 |
| U.S. Hydrothermal 11 | 1,309 | 4,294 | 2.58 | 2011 | Injection | 50 |
| U.S. Hydrothermal 12 | 3,582 | 11,753 | 8.15 | 2010 | Injection | 109 |
| U.S. Hydrothermal 13 | 3,761 | 12,340 | 7.67 | 2010 | Injection | 102 |
| U.S. Hydrothermal 14 | 3,562 | 11,687 | 9.21 | 2010 | Injection | 128 |
| WellCost Lite EGS 1 | 2,438 | 8,000 | 4.54 | 2012 | Production | 41 |
| WellCost Lite EGS 2 | 3,048 | 10,000 | 5.14 | 2012 | Production | 52 |
| WellCost Lite EGS 3 | 3,658 | 12,000 | 6.92 | 2008 | Production | 56 |
| WellCost Lite EGS 4 | 4,572 | 15,000 | 8.09 | 2008 | Production | 59 |
| WellCost Lite EGS 5 | 2,438 | 8,000 | 6.27 | 2008 | Production | 51 |
| WellCost Lite EGS 6 | 3,048 | 10,000 | 7.57 | 2008 | Production | 55 |
| WellCost Lite EGS 7 | 3,658 | 12,000 | 8.38 | 2008 | Production | 60 |
| WellCost Lite EGS 8 | 4,572 | 15,000 | 9.15 | 2008 | Production | 66 |
| WellCost Lite EGS 9 | 2,438 | 8,000 | 5.01 | 2012 | Production | 45 |
| WellCost Lite EGS 10 | 3,048 | 10,000 | 5.50 | 2012 | Production | 46 |
| Baker Hughes EGS 1 | 2,286 | 7,500 | 5.70 | 2012 | Vertical | 75 |
| Baker Hughes EGS 2 | 3,048 | 10,000 | 6.71 | 2012 | Vertical | 89 |
| Baker Hughes EGS 3 | 2,950 | 9,678 | 6.54 | 2012 | 45˚ Well | 95 |
| Baker Hughes EGS 4 | 3,333 | 10,935 | 7.53 | 2012 | 45˚ Well | 102 |
| Baker Hughes EGS 5 | 4,090 | 13,420 | 8.10 | 2012 | 45˚ Well | 115 |
| Baker Hughes EGS 6 | 3,927 | 12,885 | 9.29 | 2012 | 90˚ Well | 112 |
| Baker Hughes EGS 7 | 3,775 | 12,385 | 9.17 | 2012 | 90˚ Well | 107 |

| | | | | | | |
|---|---|---|---|---|---|---|
| Baker Hughes EGS 8 | 5,604 | 18,385 | 12.65 | 2012 | 90˚ Well | 145 |

Itemized costs for each well were grouped according to 24 categories commonly used in authorizations for expenditure (AFE) - the term for drilling cost worksheets used in the industry. These 24 cost categories were then sorted by their contribution to the total well cost. A representative itemized well cost breakdown from an 8,000 ft. (2,400 m) EGS well is shown in Figure 7-2. Within each of these cost categories, data were organized by the well interval. Then individual cost components comprising each cost category were divided by interval depth or required time, yielding specific costs in $/ft. or $/day. These specific costs were then sorted into bins and plotted in histograms to reveal the shape of their probability distributions. Figure 7-3 shows an example of such a histogram for depth-normalized drill bit cost. Using these histograms, supplemented by advice from geothermal drilling engineers, each cost component was approximated by a common distribution functional form, such as normal, triangular, or Weibull. For example, the depth-normalized drill bit cost was approximated by a normal probability distribution, shown by the fitted curve in Figure 7-3. The type of probability distribution fitted to each cost category and the parameters of each distribution are listed in Table 7-2. This table includes the distributions for the fourteen most important categories, each of which is responsible for 2.5% or more of total well cost, as shown in Figure 7-2. In reality, the WellCost Lite model contains a much more detailed and complex cost breakdown, with many of these fourteen basic categories containing several sub-categories. A total of 45 sub-categories were modeled with fitted distributions in WellCost Lite. In addition, some costs were not characterized probabilistically due to insufficient detail of the data sets, or because of their

very low contribution to the total well cost. These items are treated as constants and are labeled "deterministic" in Table 7-2.

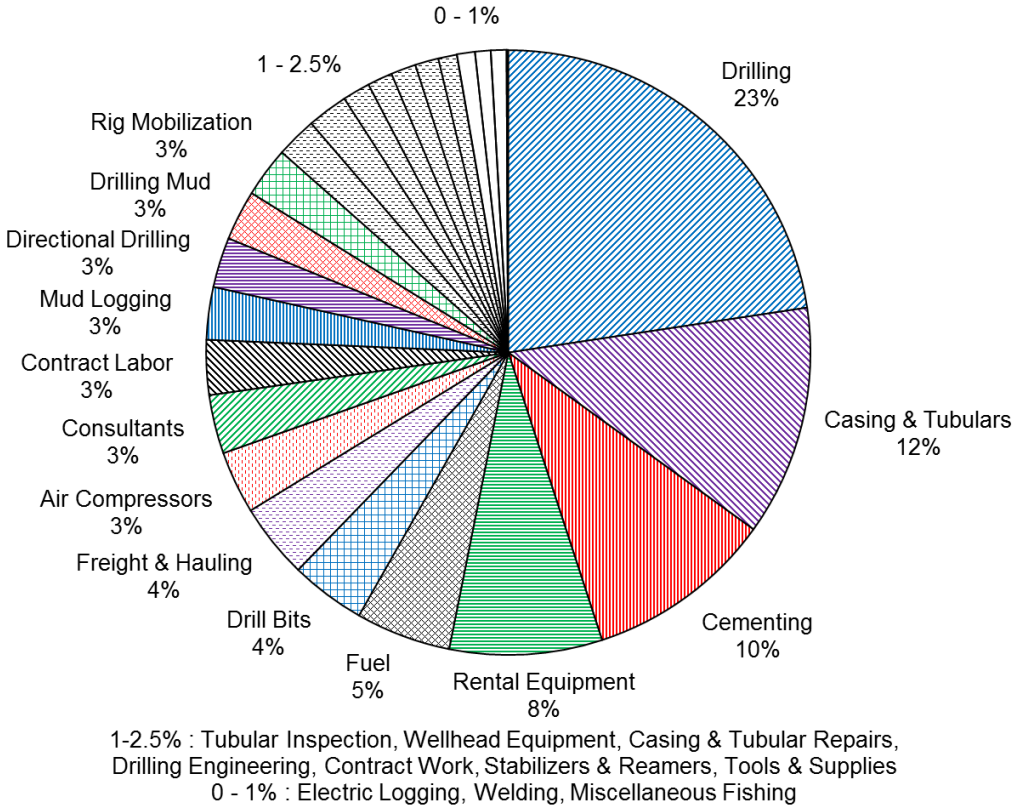


*Figure 7-2: Contribution of individual cost categories for an EGS well with a measured depth (MD) of 8,000 ft. (2,400 m)*

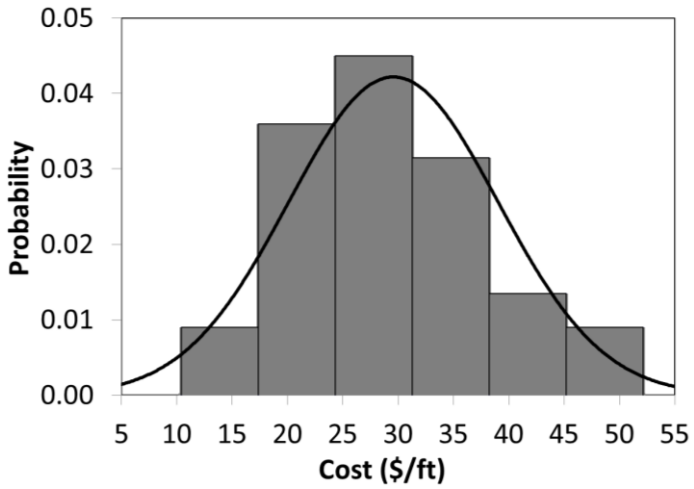


*Figure 7-3: Example probability distribution of individual well cost component: normalized drill bit cost ($ per ft. of MD)*

*Table 7-2: Probability distributions of most important well cost factors*

| Factor | Unit | Per Interval | Distribution | Parameters |
|---|---|---|---|---|
| Rate of Penetration (ROP) | ft./hr | Yes | Lognormal | Interval 1: μ = 14, σ = 10<br>Interval 2: μ = 12, σ = 8<br>Interval 3: μ = 11, σ = 3<br>Interval 4: μ = 9, σ = 1 |
| Rig Rental Cost | $/day | No | Triangular | Min = 18,000; Mode = 20,000; Max = 23,000 |
| Casing Cost | $/ft. | Yes | Normal | μ = casing weight in lb/ft; σ = 10% of μ |
| Cement | $/ft. | Yes | Triangular | Min = 40; Mode = 120; Max = 220 |
| Rental Equipment | $/day | No | Uniform | Min = 588; Max = 9,218 |
| Fuel | $/gal | No | Deterministic | 4.5 |
| Drill Bits | $/bit | Yes | Normal | μ = 25,000; σ = 8,000 |
| Freight & Hauling | $/day | Yes | Deterministic | 700 |
| Air Compressors | $/hr | Yes | Uniform | Min = 50; Max = 60 |
| Consultants | $/day | No | Deterministic | 400 |
| Contract Labor | $ | Yes | Triangular | Min = 10000; Mode = 23000; Max =35000 |

| | | | | |
|---|---|---|---|---|
| Mud Logging | hr | Yes | Triangular | Interval 1: 0<br>Interval 2 - 4: (Min = .0005;<br>Mode = .0008; Max = .0012)*MD |
| Directional Drilling | $ | Yes | Normal | 0.25*number of drilling days*<br>*(μ = 13,000; σ =3,000) |
| Drilling Mud | $/hr | Yes | Lognormal | μ = 50; σ = 25; shift = 60 |
| Rig Mobilization | $ | No | Deterministic | 200,000 |

As a next step, the categories with the highest contributions to the total well cost were searched for evidence of correlations between variables. The Pearson correlation coefficients (r) between main parameters affecting the overall well cost were calculated. These parameters included: rate of penetration (ROP), interval depth, number of drill bits used, and the costs of mud, cement, and directional drilling. The correlation coefficients were calculated between both individual parameters for various well intervals (e.g. ROPs in intervals 2 vs. 3), as well as between various cost components for the same well interval (e.g. mud cost vs. cement cost in interval 3). Including such correlations is a crucial step in quantifying the uncertainty because a mishap or holdup encountered during drilling is rarely a random, isolated event. Rather, it is a symptom of a larger issue such as unfavorable geological conditions or less experienced drilling crew. Such problems may affect many aspects of drilling and will likely drive up costs across several categories. For example, extraordinarily high drilling mud costs are often a symptom of significant loss of circulation, which is caused by a highly permeable formation section. Under such conditions, it is likely that cement costs would be similarly affected, as cement would also be lost to the formation. Therefore, one would expect to see a positive correlation between drilling mud and cement costs, and failing to account for this correlation would lead to an underestimation of uncertainty in the total well cost. Analysis of the most

influential cost categories yields seven statistically-significant (p-value<0.1) linear correlations listed in Table 7-3.

*Table 7-3: Statistically-significant correlations between individual well cost components are quantified using Pearson correlation coefficient (r), coefficient of determination ($r^2$), and p-value.*

| Variable Y | Variable X | r | $r^2$ | p-value |
|---|---|---|---|---|
| Mud (Interval 3) | Cement (Interval 3) | 0.86 | 0.75 | 0.0001 |
| Mud (Interval 4) | Cement (Interval 4) | 0.78 | 0.61 | 0.0015 |
| Cement (Interval 1) | Depth (Interval 1) | 0.70 | 0.50 | 0.0072 |
| Mud (Interval 1) | Cement (Interval 1) | 0.65 | 0.42 | 0.0162 |
| Mud (interval 2) | Cement (Interval 2) | 0.56 | 0.31 | 0.0472 |
| Cement (Interval 2) | ROP (Interval 2) | -0.52 | 0.27 | 0.0711 |
| ROP (Interval 2) | Depth (Interval 2) | -0.49 | 0.24 | 0.0885 |

Several of the correlations in this table are between mud and cement, confirming that they may be treated as paired variables following the logic presented above. The correlations between these two variables are also presented in Figure 7-4. A correlation is also observed between cement cost and depth of the first interval, as the volume of cement would be affected by the interval length. The negative correlations between the rate of penetration (ROP) and depth, as well as between cement and ROP, both agree with our expectations. At greater depths, the driller is more likely to encounter lower penetration rates and trouble, whether because of geology or equipment failures, causing the ROP to decrease. In the cases where ROP decreases due to circulation problems, the cement cost will increase, as cement may be lost to the formation in the same well interval.

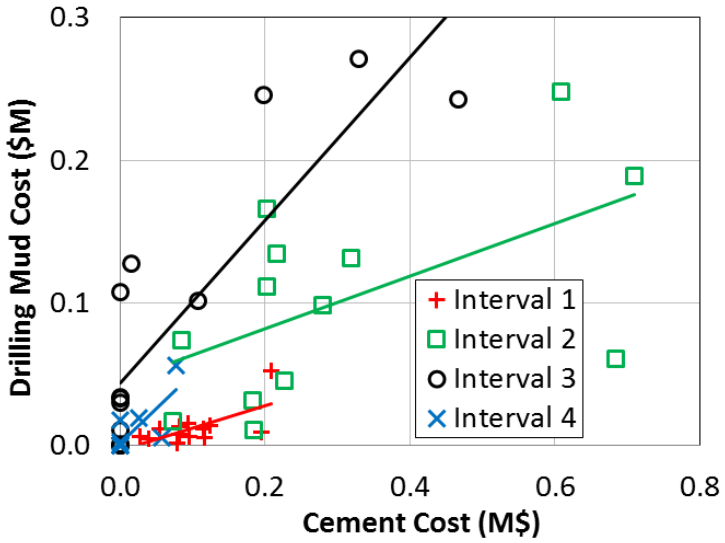


*Figure 7-4: Linear correlations between the costs of drilling mud and cement are fitted to hydrothermal well data.*

Many of the correlations presented in Table 7-3 and Figure 7-4 have low coefficient of determination ($r^2$) values, indicating that there is a substantial scatter and that just a fraction of variability in cost component Y can be explained by the values of cost component X. While the variables in Table 7-3 are not as well correlated as many engineering variables, the drilling process is stochastic and inherently harder to predict than many physical phenomena.

Upon characterizing the probability distributions of individual cost factors and finding the most significant correlations between them, these functions were implemented in the WellCost Lite model using Monte Carlo simulator @RISK (Palisade Corporation, 2015). @RISK software allows the user to input probability distributions into cells in a WellCost Lite spreadsheet and to perform a Monte Carlo simulation yielding total well cost distribution. The WellCost Lite worksheets were completed for four well designs with depths of 8,000 ft. (2,400 m), 10,000 ft. (3,000 m), 12,000 ft. (3,700 m), and 15,000 ft. (4,600 m). Each of these wells has 3 casing

strings (surface, intermediate, and production) in addition to conductor casing. The last well section is drilled open hole with an 8-1/2" diameter. Deep wells with abnormal pore pressures or significant lost circulation could require another drilling casing or liner, resulting in more complex and expensive designs. For each of the 4 well models in WellCost Lite, 45 probability distributions, the most significant of which are listed in Table 7-2, were input along with the correlations listed in Table 7-3. In order to prevent the simulation from producing unrealistically high results, all continuous distributions were truncated with a lower boundary at P1 (first percentile) and an upper boundary at P99 (ninety-ninth percentile). Monte Carlo simulations with 100,000 iterations were run for each of the 4 well depths, yielding the overall well cost distributions.

## 7.3 Results

The cumulative probability curves for the overall cost of 8,000-15,000 ft. (2,400-4,600 m) wells are presented in Figure 7-5. The results of the Monte Carlo simulations performed on the four WellCost Lite models were approximated using fitted probability distribution curves. Several functional forms (normal, log-normal, gamma, logistic, Weibull, gamma, triangular) were examined and gamma distribution was determined to be the best fit for all of the simulation results. Figure 7-5Figure 7-5 shows the comparison of the cumulative well cost probabilities obtained from the Monte Carlo simulations (in red) with the fitted gamma distributions (in black). The coefficients of determination for the fitted gamma functions were at least 0.998.

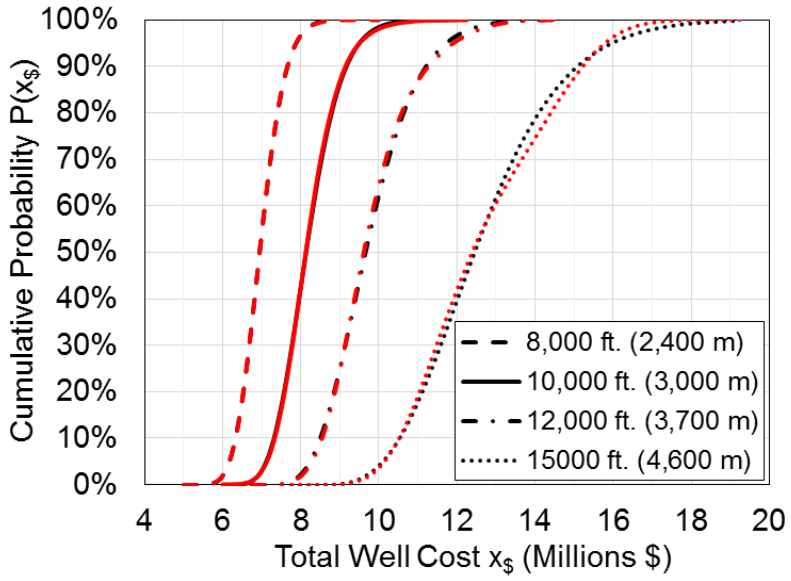


*Figure 7-5: Cumulative probability distribution $P(x_{\$})$ of the total cost of 8,000-15,000 ft. (2,400-4,600 m) geothermal wells. Results of the Monte Carlo simulations in WellCost Lite (in red) are approximated with gamma functions (in black).*

The gamma functions expressing the cumulative well cost probability in Figure 7-5 are presented as probability density functions in Figure 7-6. The curves in Figure 7-6 may be viewed as histograms, where each curve corresponds to a specific well depth and the area under each curve equals 1.

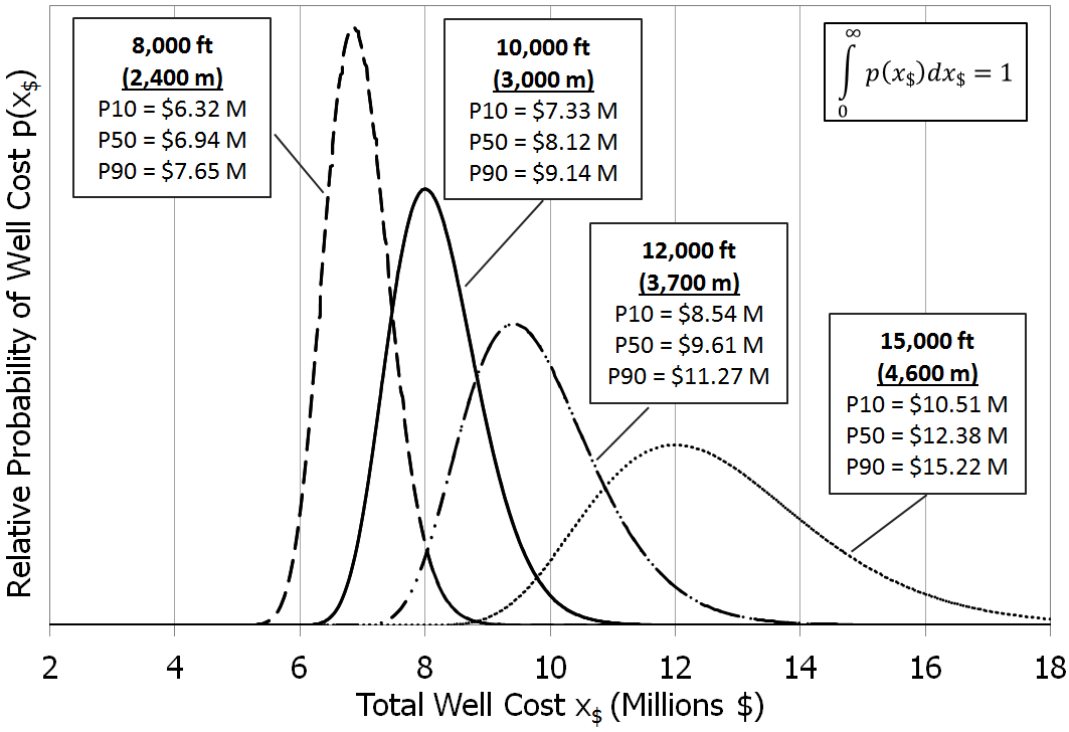


*Figure 7-6: The probability of occurrence of a specific well cost p(x$) versus well cost is presented for wells with 4 different measured depths (MD).*

As expected, the curves shift to the right (higher well cost) with increasing well depth. The probability distributions for deep wells are wider and less peaked, indicating increased well cost uncertainty. While for an 8,000 ft. (2,400 m) well, tenth percentile (P10) and ninetieth percentile (P90) correspond to 91% and 110% of the median (P50) cost, for a 15,000 ft. (3,000 m) well they represent 85% and 123% of P50, respectively. All four distributions have a positive skew, i.e. the tail on the right side of the mean is longer than that on the left, and the skewness increases with the well depth. This is due to a higher likelihood of trouble in deeper wells. It also indicates that deeper wells are more likely to become 'black swans' – rare, expensive, and hard-to-predict wells.

The gamma probability distributions presented in Figure 7-6 take the form:

$$p(x_\$) = \frac{\beta^\alpha}{\Gamma(\alpha)}(x_\$ - x_0)^{\alpha-1}e^{-\beta(x_\$ - x_0)} \quad (7\text{-}1)$$

Where $\alpha$ is the shape parameter, $\beta$ is the rate parameter, $x_\$$ is the well cost in U.S. dollars, $x_0$ is the shift (i.e. the y-intercept of the fitted distribution) in U.S. dollars, and $\Gamma$ is the gamma function defined as:

$$\Gamma(\alpha) = \int_0^\infty z^{\alpha-1}e^{-z}dz \quad (7\text{-}2)$$

The input parameters for the gamma probability distributions are given in Table 7-4.

*Table 7-4: Parameters for gamma distributions describing total well costs*

| Depth (ft.) | α | β | $x_0$ (shift) |
|---|---|---|---|
| **8,000** | 34.295 | 89,420 | 3,900,000 |
| **10,000** | 14.188 | 193,900 | 5,450,000 |
| **12,000** | 8.830 | 363,100 | 6,570,000 |
| **15,000** | 7.620 | 658,400 | 7,640,000 |

For practical purposes, it is useful to provide equations for well cost distributions at all depths within the 8,000-15,000 ft. (2,400-4,600 m) range, to allow drilling engineers and investors to easily estimate the magnitude of cost uncertainty for any given well depth. The following equation was obtained by interpolation of results for four geothermal wells presented in Figure 7-5 and Figure 7-6, as well as Table 7-4. The equation can be used to evaluate $\alpha$, $\beta$, and *shift* parameters for wells with measured depths from 8,000 ft. to 15,000 ft. (2,400 to 4,600 m):

$$y = A \cdot d^3 + B \cdot d^2 + C \cdot d + D \qquad (7\text{-}3)$$

Where *y* represents the parameter in question (either *α*, *β*, or *shift*) and *d* represents measured well depth (MD) in meters. The values of constants A through D are listed in Table 7-5. When using data from Table 7-4 and Table 7-5 it is essential to use all significant figures, and not to extrapolate the results outside of the 8,000-15,000 ft. (2,400-4,600 m) depth range. All parameters of the gamma distribution can then be predicted with an error of less than 0.5%.

*Table 7-5: Constants used as an input to Eqn. (7-3) for evaluating α, β, and shift parameters as functions of measured well depth (MD)*

| y | A | B | C | D |
|---|---|---|---|---|
| **α** | -6.986E-09 | 8.3695E-05 | -3.3377E-01 | 4.518E+02 |
| **β** | -2.676E-05 | 3.3170E-01 | -1.0420E+03 | 1.046E+06 |
| **Shift** | 0 | -4.870E-01 | 5.164E+03 | -5.783E+06 |

In order to compare the results of this work with previous publications, the predicted minimum well cost (Pmin), tenth percentile (P10), median (P50), ninetieth percentile (P90), and the maximum (Pmax) were plotted as functions of well depth in Figure 7-7 and Figure 7-8. Also displayed are average geothermal and oil and gas well costs from (Lukawski et al., 2014), which were presented in Chapter 6.

Although the 8,000-15,000 ft. (2,400-4,600 m) well depth range investigated in this study may seem low compared to the depths considered in the previous chapter, approximately 70% of the existing EGS wells fall into this depth range (Breede et al., 2013). Probabilistic analysis of shallower and deeper wells is currently limited by the availability of detailed drilling records,

but may become possible as more geothermal wells are drilled or their cost data are shared within the industry.

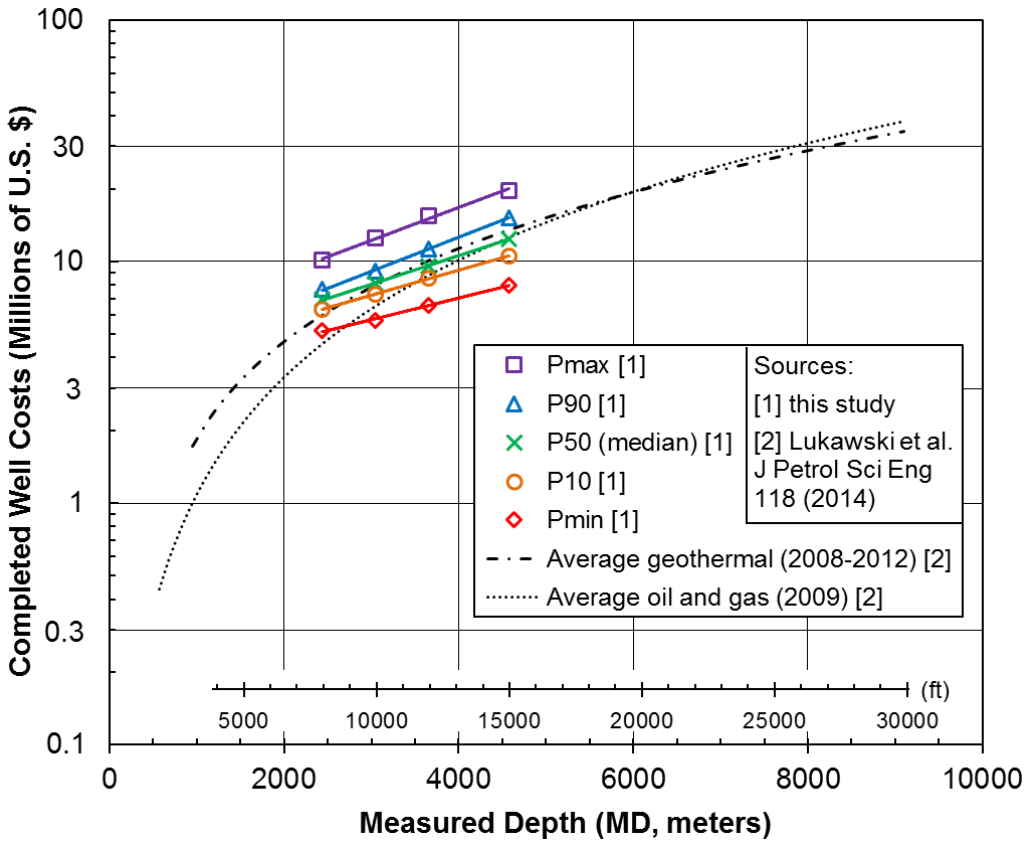


*Figure 7-7: Semi-log graph of geothermal well cost curves from this chapter compared to average geothermal and hydrocarbon well costs from Figure 6-11, also presented in Lukawski et al. (2014)*

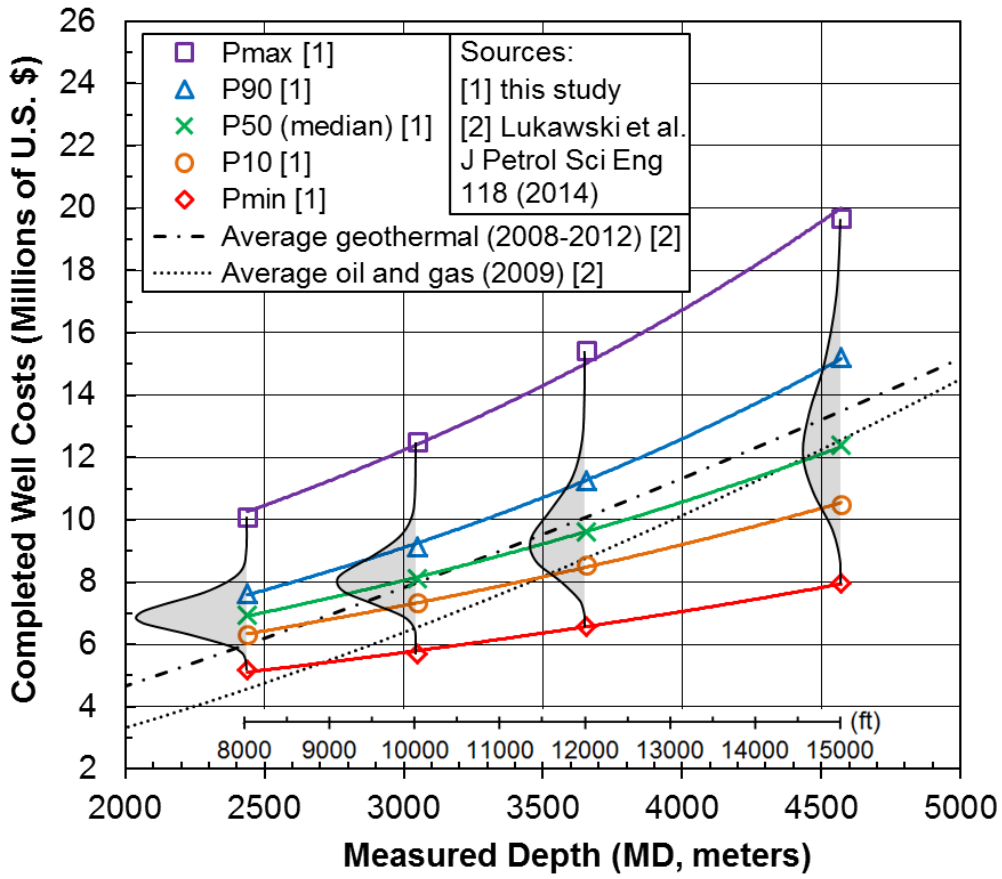


*Figure 7-8: Results from Figure 7-7 plotted on a linear graph. The grey shaded areas denote cost probability distributions for four geothermal wells as described by Eqn. (7-1)*

As shown in the previous analyses (Augustine et al., 2006; Lukawski et al., 2014; Mansure and Blankenship, 2013), the increase in cost of geothermal wells with depth is stronger than linear. In this study, the median well costs, Pmin, P10, P90, and Pmax are approximated as exponential functions of depth and presented as colored lines in Figure 7-7 and Figure 7-8:

$$\Phi = a \cdot exp(b \cdot d) \qquad (7\text{-}4)$$

where $\Phi$ is the completed well cost in U.S. dollars (2012), $d$ is the measured depth (length of the borehole along its path) in meters, and the values of constants $a$ and $b$ are given in Table 7-6. All five exponential fits have coefficients of determination of at least 0.995.

*Table 7-6: Constants used as an input to Eqn. (7-4) to produce correlations for well cost curves presented in Figure 7-5 and Figure 7-6.*

| Φ | a | b |
|---|---|---|
| **Pmin** | 3.09 | 2.06E-04 |
| **P10** | 3.54 | 2.39E-04 |
| **P50 (median)** | 3.56 | 2.72E-04 |
| **P90** | 3.44 | 3.25E-04 |
| **Pmax** | 4.78 | 3.13E-04 |

The average geothermal well cost curve from Figure 6-11 falls within the uncertainty range of the simulation results as shown in Figure 7-7 and Figure 7-8. For 8,000 ft. (2,400 m) and 15,000 ft. (4,600 m) wells, this curve indicates costs that are 13% below and 9% above the median well cost (P50) from the probabilistic analysis, respectively. This difference may be attributed to the specific design of the four geothermal wells used in this study, and to the advancements in drilling technology. While all four wells modeled in this study have 3 casing intervals, some actual geothermal wells may require an additional casing string or liner. The deeper the well is, the more likely it is to need an additional casing interval. An added intermediate liner would increase the median cost of 12,000 ft. (3,700 m) and 15,000 ft. (4,600 m) wells by approximately 15%, thus reducing the mismatch between the results of this study and the work presented in Chapter 6. The low slope of the median (P50) cost curve also reflects the recent

decrease in drilling cost at greater depths. Drilling deep wells has become more affordable largely due to the advancements in drilling technology including high-temperature electronics, improved roller cone bits, and availability of large, >1500 hp drilling rigs.

While most recent geothermal well costs fall within the range estimated in this study, individual wells may be cheaper than Pmin or more expensive than Pmax. Well cost may fall below the minimum curve for two reasons, neither of which can be easily predicted in a general model such as WellCost Lite. First, as a result of poor management practices, developers may use excess materials, such as casing, left over from a previous well without reporting their costs in the AFE. The second potential source is learning: as a developer drills many wells within the same geothermal field, a model of the sub-surface geology is developed so that future wells can be strategically placed to avoid undesirable features, and the selection of well design, drilling methods, and operations can be optimized to reduce the risk and improve performance for the specific geology. As the developer learns and understands the nature of the field, consecutive wells can typically be drilled and completed faster and with less non-productive time (NPT). Well costs may also exceed the Pmax values presented in Figure 7-7 and Figure 7-8 since it is impossible to predict the absolutely worst case scenario corresponding to Pmax (McIntosh, 2010).

Finally, the results of the Monte Carlo simulations determined which cost factors hold the most influence over the well cost uncertainty. Figure 7-9 shows the tornado diagram of the most influential drilling cost parameters for an 8,000 ft. (2,400 m) geothermal well in order of decreasing uncertainty. Some of these parameters are listed individually for each drilling interval. Each bar represents the deviation from the mean well cost brought about by a swing through the full range of possible values for the corresponding variable. According to this

diagram, the most important factors in determining uncertainty are the rate of penetration (ROP), cost of cement and drilling bits, rig day rate, and drilling mud cost. This list remains consistent for deeper wells, with the exception that drilling mud becomes less important, while directional drilling and trouble both move significantly higher on the list. These changes are reasonable because both directional drilling and trouble costs increase with depth, and they also become less predictable due to a wide range of geological conditions encountered at greater depths.

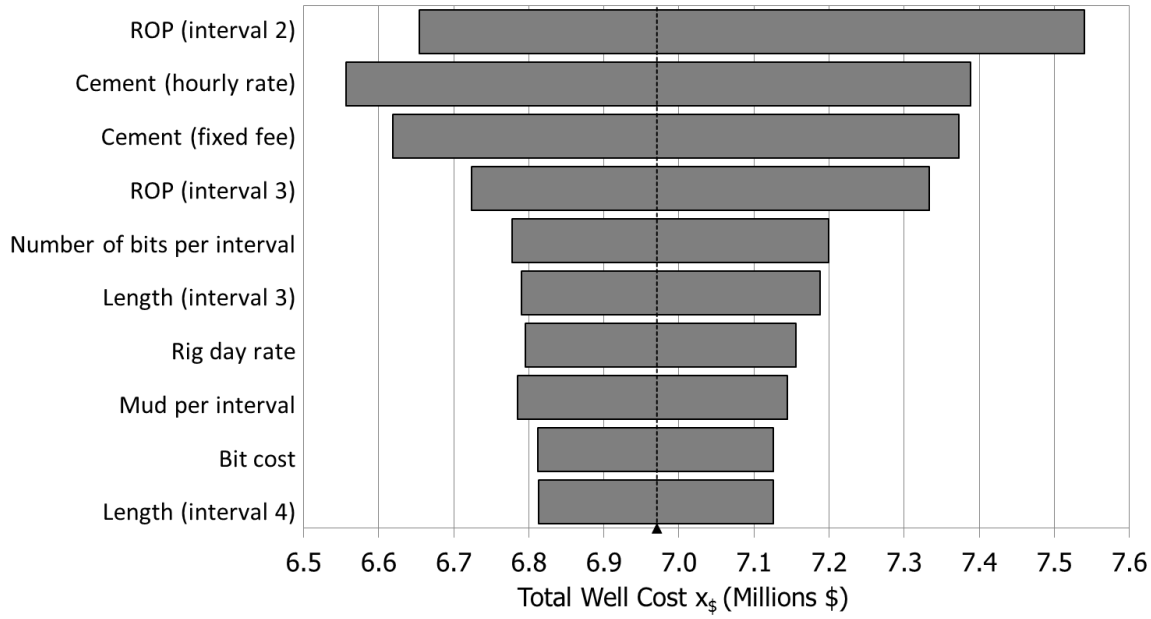


*Figure 7-9: Leading factors contributing to cost uncertainty of an 8,000 ft. (2,400 m) geothermal well. The inputs were ranked by their effect on the output mean.*

## 7.4 Conclusions

The cost uncertainty of 8,000 ft. (2,400 m) to 15,000 ft. (4,600 m) EGS wells was quantified using a Monte Carlo method and the predictive drilling cost model WellCost Lite. The results

of this work are presented in the form of equations which can be used by drilling engineers, researchers, and investors to estimate the probability distribution of geothermal well costs. The median well costs obtained with the probabilistic approach match closely the average well costs from Chapter 6, which were based on a larger number of geothermal wells.

Quantitatively, the results display three trends, which are characteristic of drilling activities:

1. Well costs increase exponentially with depth as a result of the more difficult drilling environment.
2. Uncertainty of well cost increases with depth due to increased likelihood of trouble and less predictable drilling conditions.
3. Deep wells have more positively-skewed cost probability distributions. As a result of increased trouble time, probability distributions for deep wells have long, narrow tails stretching far into the high cost region.

The last two characteristics have been quantified in literature for oil and gas wells, but never before for geothermal boreholes.

The main limitations of this work and other analyses in this field result from the limited access to geothermal well cost data. Although it is believed that more than 4,000 geothermal wells have been drilled historically worldwide (Sanyal and Morrow, 2012), costs on less than 5% of them have been published. Detailed well costs required for probabilistic studies are even scarcer. In addition to refining the presented cost estimates, a larger well cost database could make it possible to extend this analysis beyond the 8,000-15,000 ft. (2,400-4,600 m) depth range. Moreover, it is likely that many well cost components treated as uncorrelated in this study would actually become correlated if a larger data set were available. Including such

additional correlations would increase the well cost uncertainty. Having a larger geothermal well database would also improve our insight into the costs of trouble events and, in particular, rare and expensive 'worst case' scenarios. In addition, no distinction has been made between drilling costs in different geologic provinces. This is an obvious simplification, as drilling times and costs highly depend on subsurface characteristics, which vary geographically.

At a time when much of the world is searching for reliable renewable energy sources and geothermal is often marginalized due to high and uncertain capital investment costs, evaluation of drilling cost uncertainty could greatly contribute to the advancement of geothermal energy as a base-load, sustainable source of heat and electricity.

## 7.5 Acknowledgements

This chapter is extensively based on the following publication:

Lukawski, M.*, Silverman, R.*, Tester, J., 2016. Uncertainty Analysis of Geothermal Well Drilling and Completion Costs, Geothermics 64, 382–391 (*equal contribution authors)

My co-author, Rachel Silverman deserves special thanks for her contributions to gathering geothermal well cost data, numerical analysis, and co-writing the manuscript.

## 7.6 References

Augustine, C., Tester, J., Anderson, B., 2006. A Comparison of Geothermal with Oil and Gas Well Drilling Costs, in: Proceedings, Thirty-First Workshop on Geothermal Reservoir Engineering, Stanford University. Stanford, CA, USA, p. 15.

Baker Hughes, 2012. Enhanced Geothermal Systems Directional Well Costing. Sandia National Laboratories, PO No: 1290712.

Beckers, K.F., Lukawski, M., Anderson, B., Moore, M., Tester, J., 2014. Levelized costs of

electricity and direct-use heat from Enhanced Geothermal Systems. J. Renew. Sustain. Energy 6. doi:10.1063/1.4865575

Breede, K., Dzebisashvili, K., Liu, X., Falcone, G., 2013. A systematic review of enhanced (or engineered) geothermal systems: past, present and future. Geotherm. Energy 1. doi:10.1186/2195-9706-1-4

Brett, J., Millheim, K., 1986. The Drilling Performance Curve: A Yardstick for Judging Drilling Performance. SPE 15362 12.

EIA, 2015. Total energy statistics [WWW Document]. URL http://www.eia.gov/totalenergy/data/annual/index.cfm (accessed 9.13.15).

GEA, 2014. 2014 Annual U.S. & Global Geothermal Power Production Report.

Gerber, L., Marechal, F., 2012. Design of Geothermal Energy Conversion SystemsWith a Life Cycle Perspective. Proc. Thirty-Seventh Work. Geotherm. Reserv. Eng. Stanford Univ.

Lukawski, M.Z., Anderson, B.J., Augustine, C., Capuano, L.E., Beckers, K.F., Livesay, B., Tester, J.W., 2014. Cost analysis of oil, gas, and geothermal well drilling. J. Pet. Sci. Eng. 118, 1–14. doi:10.1016/j.petrol.2014.03.012

Mansure, A.J., Bauer, S.J., Livesay, B.J., Petty, S., 2006. Geothermal Well Cost Analyses 2006. Geotherm. Resour. Counc. Trans. 30, 271–276.

Mansure, A.J., Blankenship, D.A., 2008. Geothermal Well Cost Analyses 2008. Geotherm. Resour. Counc. Trans. 32, 43–48.

Mansure, A.J., Blankenship, D.A., 2013. Geothermal Well Cost Update 2013. GRC Trans. 37, 629–632.

McIntosh, J., 2010. The Future Ain't What It Used to Be , Or Is It? J. Pet. Technol. 62, 48–50.

Palisade Corporation, 2015. @Risk software.

Petty, S., Bour, D., Livesay, B., Baria, R., Adair, R., 2009. Synergies and Opportunities Between EGS Development and Oilfield Drilling Operations and Producers. SPE 121165.

Polsky, Y., Capuano, L.J., Finger, J., Huh, M., Knudsen, S., Mansure A J, Raymond, D., Swanson, R., 2008. Enhanced Geothermal Systems (EGS) Well Construction Technology Evaluation Report. Sandia Rep. SAND2008-7866 108.

Reber, T.J., Beckers, K.F., Tester, J.W., 2014. The transformative potential of geothermal heating in the U.S. energy market: A regional study of New York and Pennsylvania. Energy Policy 70, 30–44. doi:10.1016/j.enpol.2014.03.004

Sanyal, S.K., Morrow, J.W., 2012. Success and the Learning Curve Effect in Geothermal Well Drilling – a Worldwide Survey, in: Proceedings Thirty-Seventh Workshop on Geothermal Reservoir Engineering, Stanford University. Stanford, CA, USA, p. 8.

Tester, J., Reber, T., Beckers, K., Lukawski, M., Camp, E., Aguirre, G.A., Jordan, T., Horowitz, F., 2015. Integrating Geothermal Energy Use into Re-building American Infrastructure. Proc. World Geotherm. Congr. 2015.

Tester, J.W., Anderson, B.J., Batchelor, A.S., Blackwell, D.D., DiPippo, R., Drake, E.M., Garnish, J., Livesay, B., Moore, M.C., Nichols, K., Petty, S., Toksoz, M.N., Veatch, Ralph W, J., 2006. The Future of Geothermal Energy: Impact of Enhanced Geothermal Systems (EGS) on the United States in the 21st Century. MIT.

Yost, K., Valentin, A., Einstein, H.H., 2015. Estimating cost and time of wellbore drilling for Engineered Geothermal Systems (EGS) - Considering uncertainties. Geothermics 53, 85–99. doi:10.1016/j.geothermics.2014.04.005

# 8 OVERALL CONCLUSIONS AND RECOMMENDATIONS FOR THE FUTURE RESEARCH

## 8.1 Conclusions

This thesis used a multidisciplinary approach to quantify and improve technical and economic performance of geothermal energy utilization systems. This goal was achieved by developing more efficient energy conversion methods as well as providing accurate data for the techno-economic EGS software GEOPHIRES.

This work aimed to improve the organic Rankine cycle (ORC) technology by providing a new approach to working fluid selection. First, it correlated the efficiency of optimized ORC plants with two thermodynamic properties of working fluids: reduced ideal gas heat capacity $C_p^0/\boldsymbol{R}$ and critical temperature $T_c$. Both of these properties have been tabularized for many working fluids and can be estimated for the remaining substances using molecular contribution methods. Because of that, the developed correlations can be used to compare performance of various working fluids based only on their molecular structures. This may allow researchers to screen potential ORC working fluids, many of which may not have sufficiently well described thermodynamic properties to be analyzed using conventional methods.

Because the thermodynamic correlations developed in Chapter 3 provide only approximate results, an in-depth analysis of the less common ORC working fluids will require accurate equations of state (EOS). The flow calorimeter described in Chapter 5 provided isobaric heat capacity ($C_p$) measurements, which can be used to improve the accuracy of EOS. Due to careful design, construction, and calibration, the flow calorimeter achieved ±1% measurement

accuracy at temperatures from 25 to 150 °C and pressures from 1 to 300 bar. The equipment was validated using measurements for carbon dioxide and methanol at vapor, liquid, and supercritical conditions. Most importantly, the calorimeter can be used for measurements of fluid mixtures and in the vicinity of critical point, where EOS are typically less accurate.

In addition to designing more efficient energy conversion cycles, geothermal utilization systems can be improved by better system integration. The case study of a hybrid geothermal-biomass district heating for Cornell University highlighted the importance of heat integration and hybridization in geothermal direct-use applications. Both heat cascading and the use of a peaking biomass boiler lowered the levelized cost of energy and increased geothermal resource utilization. At the current natural gas prices below $5/MMBTU, geothermal heating systems cannot economically complete with the existing combined cycle CHP plants in the Northeastern U.S. They do, however, provide an acceptable economic performance, greatly reduce the $CO_2$ emissions, and would limit our exposure to the volatility of natural gas prices.

The main objective of this work was to make geothermal utilization systems more competitive in the energy market. This can be achieved by increasing their efficiency, but also by improved assessment of project economics. The key process determining the cost and risk of geothermal projects is well drilling and completion. This work assessed the costs of geothermal wells as a function of their depth. It showed, that despite the differences in well design, the costs of geothermal and oil and gas wells are similar. The geothermal well cost distributions presented in Chapter 7 can be used by drilling engineers, researchers, and investors to estimate the well cost uncertainty. The analysis showed that the range of possible well costs increases with well depth as a result of more difficult drilling environment. Deep wells also typically have more positively-skewed cost probability distributions due to higher likelihood of trouble.

To explore the similarities between geothermal and hydrocarbon well drilling, this study included also an analysis of oil and gas well costs. A new well cost index was developed, which describes year-to-year fluctuations in well drilling and completion costs. This index was based on tens of thousands of onshore oil and gas wells drilled in the U.S. each year from 1976 to 2009. It offers a superior accuracy and the longest lifespan among available well cost indices.

## 8.2 Recommendations for the future work

For Enhanced Geothermal Systems (EGS) to become a major source of energy, it will require further research, development and demonstration activities. The main technical limitations of EGS have been addressed since the pilot project in Fenton Hill in 1970s. However, the key performance metrics of EGS reservoirs including active volume and productivity will need to increase before EGS technology becomes commercial. This will require continued support for demonstration-scale EGS projects.

The research on improving efficiency and reducing cost of geothermal utilization systems is also essential to the success of EGS. The work on ORC power plants presented in this thesis was limited to pure working fluids, but could be extended to include non-azeotropic mixtures. The use of multicomponent working fluids would provide non-isothermal evaporation and condensation in ORC without the need to increase cycle pressure beyond critical. The resulting lower exergy losses in heat exchangers and pumps would increase the cycle efficiency.

The use of multi-component working fluids in ORCs requires development of more accurate EOS. To provide the experimental data needed for fitting EOS, the flow calorimeter will be used to measure $C_p$ of promising working fluid mixtures. The next measurements will be done

for HFO-1234yf and its mixtures with $CO_2$. The HFO-1234yf is a likely future replacement for R-134a, which is commonly used in ORCs, refrigeration, and air conditioning systems. HFO-1234yf has a 100-year global warming potential of 4 as compared to 1430 for R-134a, but its thermophysical properties are not as well defined, especially in the near-critical region.

The analysis of proposed renewable heating system for Cornell University provided a basis for the future work in this area. Some of the introduced solutions were used in the follow-up studies in our group to evaluate the potential for direct-use of geothermal resources in the U.S. Northeast. To implement a demonstration-scale geothermal project at Cornell, it will require a more accurate cost analysis and a detailed system design. The probabilistic well cost estimates developed in Chapter 7 could also provide a better estimate of the economic uncertainty of the project. For the well depths considered at Cornell (3.7-4.2 km), the P10 and P90 costs would be up to 15% lower and 20% higher than median (P50) cost, respectively.

Finally, there are many ways in which the geothermal well cost analysis performed in this study could be extended. The scope and accuracy of presented work was limited by the availability of geothermal well cost data. With more extensive well database, future studies could be performed for individual geologic provinces or even specific geothermal fields. Additional well cost records would also refine the probabilistic well cost estimates by providing additional correlations between individual well cost components and improving estimates of the trouble time. Future research could also better address the cost reduction potential due to drilling multiple wells in the same field. The current estimates are based on oil and gas industry and are likely different from the geothermal practice. Lastly, the well cost estimates should be regularly updated to reflect the changing market trends.